T.C
GAZİANTEP UNIVERSITY
GRADUATE SCHOOL OF HEALTH SCIENCES

DETECTION OF SMALL ORGANIC MOLECULES WITH THREE-DIMENSIONAL BIOMOLECULE-BASED BIOSENSORS USING BIOINFORMATICS APPLICATIONS

İmren BAYIL

Ph.D. THESIS

DEPARTMENT OF BIOINFORMATICS AND COMPUTATIONAL BIOLOGY

SUPERVISOR
Assoc. Prof. Dr. Tuğba TAŞKIN TOK

Gaziantep
2023

T.C
GAZIANTEP UNIVERSITY
INSTITUTE OF HEALTH SCIENCES
DEPARTMENT OF BIOINFORMATIC AND COMPUTATIONAL BIOLOGY

DETECTION OF SMALL ORGANIC MOLECULES WITH THREE DIMENSIONAL BIOMOLECULE-BASED BIOSENSORS USING BIOINFORMATICS APPLICATIONS

İmren BAYIL

Thesis Defense Date:13.07.2023

Approval of the Health Sciences Institute;

Assoc. Prof. Dr. Davut Sinan KAPLAN
Director of Graduate School Health Science

I certify that this thesis satisfies all the requirements as a thesis for the degree of Doctor of Philosophy

Assoc. Prof. Dr. Tugba TAŞKIN TOK
Head of the Department of Bioinformatic and Computational Biology

I certify that this thesis satisfies all the requirements as a thesis for the degree of Doctor of Philosophy.

Assoc. Prof. Dr. Tugba TAŞKIN TOK
Thesis Supervisor

This thesis has been read and accepted, in scope and quality, as a thesis for the degree of Doctor of Philosophy.

Examining Committee Members	Signature
Assoc. Prof. Dr. Tugba TAŞKIN TOK	
Assoc. Prof. Dr. Belgin ÖZER	
Assoc. Prof. Dr. Necla BENLİER	
Prof. Dr. Zafer ÇETİN	
Assoc. Dr. Tuba DENKÇEKEN	

DECLARATION

I hereby affirm that all of the information contained in this document was obtained and presented in accordance with academic regulations and ethical standards. I also certify that, as required by these rules and standards of conduct, I have appropriately cited and referenced all materials and results that are not my own.

2023

İmren BAYIL

ACKNOWLEDGEMENTS

I firstly give my special thanks to my Ph.D. thesis advisor, Assoc. Prof. Dr. Tuğba TAŞKIN TOK for her great contribution during the whole phase of my thesis and her kindness and patience during the course of my Ph.D. studies.

I would like to thank the Presidency of the Council of Higher Education (YOK), of which I am proud to be a scholarship holder within the scope of the 100/2000 YOK Doctoral Scholarship Program, for their financial and moral support during my doctoral studies.

The numerical calculations reported in this thesis were partially performed at TUBITAK ULAKBIM, High Performance and Grid Computing Center (TRUBA resources). In addition, three-dimensional structure prediction in this thesis was performed with a one-month demo version license of the Schrodinger program.

I would like to thank my professor, Assoc. Prof. Dr. Necla BENLIER and Assoc. Prof. Dr. Belgin OZER who evaluated the progress of my thesis study.

I would like to thank my dear friend Aysegül BARAN, who has been with me in all my troubles and happiness, who has made this difficult process beautiful, with whom we have accumulated many beautiful memories, who has always been with me in both my happiness and sadness, and I believe that our friendship will last forever, for her unique help and support.

I would like to express my endless gratitude to my beloved mother Saide Melek BAYIL and my father Mehmet BAYIL for their love, sacrifice, material, and moral support throughout my education life, and I would like to dedicate this study, especially to my precious mother, whom I have an infinite love with all my heart, and for her great patience during the doctorate period.

TABLE OF CONTENTS

SYMBOLS AND ABBREVIATIONS

Å	Angstrom
a_i	Acceleration of the particle
b_0	Bonds
cal	Calori
E	Energy
fs	Femto second
F_i	Force
IC_{50}	Inhibitor concentration-half maximum
K	Kelvin
kcal	Kilocalories
K_i	Inhibition Constant
mol	Molar
m_i	Particle of mass
nM	Nanomolar
ns	Nanosecond
µM	Micromolar
T	Temperature
V	Potential Energy
ΔG	Binding Energy
π	Pi
kB	Boltzmann Constant
n	Torsion angle
δ	Dihedral angles

θ_0	Balance angle
ε	Epsilon
ω_0	Improper Dihedral angles
$r_{1,3:0}$	Urey Bradley 1,3-term
ADT	AutoDock Tools
2D	Two Dimensions
3D	Three Dimensions
B3LYP	Becke-Three Parameter Lee, Yang, Parr Density Function
BPA	BPA-binding Aptamer
BPA	Bisphenol A
Charmm	Chemistry at Harvard Macromolecular Mechanics
DLG	Digital Line Graph
DCCM	Dynamical Cross-Correlation Matrix
DNA	Deoxyribonucleic Acid
DFT	Density Functional Theory
EDC	Endocrine-Disrupting Compound
EM	Energy Minimization
GROMACS	Groningen Machine for Chemical Simulations
HF	Hartree-Fock
MD	Molecular Dynamic
MM	Molecular Mechanic
MM/PBSA	Macromolecular Mechanies/Poisson-Boltzmann Surfqace
NPT	Isothermal-Isobaric ensemble, moles (N), pressure (P) and temperature
NVT	Amount of substance (N), Volume (V), and Temperature
PCA	Principal Component Analysis
PBC	Periodic Boundary Condition

PME	Particle Mesh Ewald
RNA	Ribonucleic Acid
RG	Radius of Gyration
RMSD	Root Mean Square Deviation
RMSF	Root Mean Square Fluctuations
SS-DNA	Single-Stranded Deoxyribonucleic Acid
TIP3P	Three-Point Transferable Intermolecular Point
QM	Quantum Mechanism

LIST OF FIGURES

LIST OF TABLES

ABSTRACT

DETECTION OF SMALL ORGANIC MOLECULES WITH THREE-DIMENSIONAL BIOMOLECULE-BASED BIOSENSORS USING BIOINFORMATICS APPLICATIONS

İmren BAYIL
Ph.D Thesis, Department of Bioinformatics and Computational Biology
Supervisor: Assoc. Prof. Dr. Tuğba TAŞKIN TOK
June 2023, 237 pages

Endocrine-disrupting chemicals (EDCs) are an array of compounds, either synthetic or naturally occurring, that have the ability to mimic or interfere with the normal hormonal activity within the body upon exposure. The genesis of these substances is attributed to the consumption of polluted water, inhalation of polluted air, consumption of contaminated food, or exposure to polluted soil. As a result, biosensors have been constructed for the purpose of rapid and targeted detection of endocrine-disrupting compounds (EDCs) in environmental samples. Biosensors employ aptamers, which are biological recognition elements, in their production. Aptamers have emerged as a promising substitute for various applications, exhibiting superiority over numerous biomolecules due to their inherent advantages such as enhanced stability, reusability, artificial synthesis, and prolonged preservation. Aptamer biosensors serve a crucial role in the detection of small molecules due to these characteristics. Due to the intricacy of aptamer structure, their elucidation by conventional methods is extremely challenging. This circumstance has led to the development of three-dimensional aptamer structures based on various models and techniques. This study aims to provide an approach to predicting the 3D structures of the SS-DNA required for this sequence by initially selecting an aptamer sequence showing biosensor properties specific to BPA, one of the endocrine-disrupting chemicals detected in water samples in the literature. The present study aims to elucidate the intermolecular mechanisms and binding affinity between aptamers and endocrine-disrupting chemicals through the utilization of bioinformatics techniques such as molecular docking, molecular dynamics simulation, and binding energies. Furthermore, a comparative analysis of the reliability of different modeling programs and force fields will be conducted by assessing their correlation with experimental results reported in the literature. The results of our study using these computational strategies will provide useful information to reveal the intermolecular mechanisms and affinity required for aptamer-based biosensors and to develop a new aptamer for aptamer-based biosensors in a shorter time and at a lower cost.

Keywords: Aptamer, Binding energy, Endocrine disruptive chemicals, molecular docking, molecular dynamic simulation

ÖZET

BİYOENFORMATİK UYGULAMALAR KULLANILARAK ÜÇ BOYUTLU BİYOMOLEKÜLLER TEMELLİ BİYOSENSÖRLER İLE KÜÇÜK ORGANİK MOLEKÜLLERİN TESPİT EDİLMESİ

İmren BAYIL
Doktora Tezi, Biyoenformatik ve Bilişimsel Biyoloji Anabilim Dalı
Tez Danışmanı: Doç. Dr. Tuğba TAŞKIN TOK
Haziran 2023, 237 sayfa

Endokrin bozucu kimyasallar (EDC'ler), vücut tarafından alındığında hormonların normal işleyişini taklit eden veya engelleyen sentetik veya doğal kimyasallardır. Bu maddelerin ortaya çıkması, kirlenmiş suyun içilmesi, kirlenmiş havanın solunması, gıdaların yutulması veya kirlenmiş toprakla temas sonucu gerçekleşir.Bu nedenle, çevresel örneklerde EDC'lerin hızlı ve yerinde tespitini araştırmak için biyosensörler geliştirilmiştir. Bu biyosensörlerin üretimi için biyolojik tanıma elemanları olan aptamerler kullanılmaktadır..aptamerler, gelişmiş stabilite, yeniden kullanılabilirlik, yapay sentez ve uzun süreli koruma gibi doğal avantajları nedeniyle çok sayıda biyomoleküle göre üstünlük sergileyerek çeşitli uygulamalar için umut verici bir alternatif olarak ortaya çıkmıştır..Bu özellikleri sayesinde aptamer biyosensörler küçük moleküllerin tespitinde önemli rol oynamaktadır. Aptamerlerin yapısının karmaşıklığı nedeniyle, geleneksel yollarla aydınlatılmaları çok zordur. Bu durum aptamer yapılarının farklı model ve yöntemler kullanılarak üç boyutlu yapılarının geliştirilmesine yol açmıştır. Bu çalışma, başlangıçta literatürde su örneklerinde tespit edilen endokrin bozucu kimyasallardan olan BPA ya özgü biyosensör özelliği gösteren aptamer dizilimi seçilerek,başlangıçta bu dizilim için gerekli olan SS-DNA nın 3D yapılarını tahmin etmek için bir yaklaşım sağlamayı amaçlamıştır. Biyoinformatik yöntemlerden moleküler kenetlenme ve moleküler dinamik simülasyonu ve bağlanma enerjileri uygulanarak, modellediğimiz aptamerler ile endokrin bozucu kimyasallar arasındaki moleküller arası mekanizmaların ve bağlanma afinitesinin ortaya çıkarılarak, literatürdeki deneysel sonuçla iyi bir korelasyon verip vermediği karşılaştırarak hangi modelleme programının ve hangi kuvvet alanının daha güvenilir olduğu tartışılacaktır. Bu hesaplama stratejilerini kullanarak yaptığımız çalışmanın sonuçları, aptamer tabanlı biyosensörler için gerekli olan moleküller arası mekanizmaları ve afiniteyi ortaya çıkarmak ve aptamer tabanlı biyosensörler için daha kısa sürede ve daha düşük maliyetle yeni bir aptamer geliştirmek için yararlı bilgiler sağlayacaktır.

Anahtar Sözcükler: Aptamer, Bağlanma enerjisi, moleküler kenetlenme, Endokrin bozucu kimyasallar, Moleküler dinamik simülasyon

1. INTRODUCTION AND AIM

Exogenous substances or mixtures of substances that impact the functions of the endocrine system and result in unfavorable health outcomes in both the organism and its offspring are referred to as endocrine disruptors. It is widely believed that these substances have the potential to interfere with fundamental physiological processes, including but not limited to growth, stress response, gender development, reproductive capacity, insulin production, utilization, and metabolic rate, by perturbing the endocrine equilibrium. Moreover, individuals are exposed to these compounds on a daily basis. Endocrine disruptors can be of human, animal, and plant origin, as well as synthetic and industrial chemical origin (1).

People often think that they can only get these chemicals through the contaminated soil and water near the factory. Yet they are exposed to these chemicals every day. For example, canned food, baby bottles, toys, cosmetics, shampoos, all products in plastic, cleaning products, all technological products in our homes, armchairs, new cars, refrigerators, drinks and water in plastic, many ready-made foods and pesticides, and vegetables and fruits due to the plastic containers in which they are stored also contain endocrine disruptors. The majority of antibiotic drugs used by humans are also endocrine disruptors. Additionally, it has also been used in practically every agricultural product and meat crop.

There is hardly anyone in the world who has not been exposed to endocrine disruptors. These chemicals have been detected in the blood of even Eskimos. 90% of the flame retardants, phthalates, antibacterial agents, and bisphenol compounds found in plastic items have been found in people's blood in studies conducted in American society (2).

In short, it is thought to pose a great threat to humans. For this reason, it is very difficult to be completely isolated from endocrine-disrupting products at this age. Examining the harms of these chemicals to health with the methods known in toxicology does not give accurate results. Because these chemicals, even in very small doses, can cause serious damage to health through the hormonal system, Their effects can occur after years, and as a result of a long-term follow-up, some harms can be understood. Exposure can cause diabetes, obesity, cancer, and other chronic diseases over the years (3).

Today, there is a demand for new analytical devices that can provide fast and reliable data to detect these chemicals, as these chemicals are on the rise and have worrying health and environmental consequences. This monitoring is not possible with conventional analytical methods. Early detection requires new analytical instruments with high sensitivity, linearity, and a shorter reaction time. In this sense, biosensors seem to be the technology of choice. Compared to traditional methods, biosensors have superior advantages such as being fast, inexpensive, practical, allowing direct analysis, and being portable. Biosensors are widely used in this field due to their advantages, such as their low cost, fast reaction time, and portability. Traditional methods, on the other hand, can be very time-consuming and require a lot of equipment.

A biosensor is a device that can generate a quantifiable response due to the chemical reactions of biomolecules. Typically, it comprises two fundamental constituents, namely a biological receptor and a transmitter. Bioreceptors exhibit a high degree of specificity towards the target molecule, thereby facilitating the binding event, which is subsequently translated into a detectable signal by the transducer. Thus, molecular recognition forms the basis of the biosensor principle. For this reason, biological recognition elements are critical for the fabrication of biosensors. Because the molecular sensing element coupled to the transducer is responsible for the analytical performance of biosensors.

Aptamers are preferred as biorecognition agents for the detection of endocrine-disrupting chemicals. Aptamers are a class of molecules that exhibit high specificity and affinity for their targets. These molecules are typically composed of oligonucleotides, such as RNA and SS DNA, or peptide molecules. Aptamers' specific three-dimensional structures enable them to bind to their targets with high precision. Aptamers exhibit a high degree of specificity towards a wide range of targets, encompassing particles, organic dyes, amino acids, nucleotides, RNA, biological cofactors, tiny organic compounds, fatty acids, peptides, contaminants, enzymes, development factors, transcription variables, antibodies, viral proteins and/or components, mitochondria, and bacteria. Aptamers have become an ideal alternative for biosensors as they offer several advantages such as shorter selection times, unlimited shelf life, low cost, robustness, and reusability (4-5).

This study aims to provide a proposal for forecasting the three-dimensional configurations of SS DNA necessary for aptamer sequences, which we initially acquired from the literature.

Since the structure of the aptamers is very difficult to illuminate in conventional ways and only a very few aptamers have been illuminated, their three-dimensional structure has been modeled using different modeling techniques.

Thus, by applying molecular dynamics and molecular docking simulations based on bioinformatics methods to how it formed a linkage mechanism with the target molecule, the intermolecular mechanisms and the binding affinity between the aptamer and endocrine disrupting chemicals, which have been modeled, will be revealed, and it is hoped to enable the integration of them into biosensor devices.

In our study, the best aptamer conformation and the stability of the system between the target and the aptamer will be analyzed in more detail with the molecular dynamics simulation studies that we have applied and compared with the experimental results in the literature to reveal which modeling program is more reliable, and as a result, it will help us to design a new aptamer for aptamer-based biosensors in a shorter time and at a lower cost.

2. GENERAL INFORMATION

2.1. An Overview Of Biosensors

A biosensor is an autonomous and integrated device that can furnish precise numerical or qualitative analytical data by utilizing a biological recognition element, also known as a biochemical receptor, which is in direct spatial proximity to a transmitter element (6). An additional frequently employed characterization of biosensors pertains to their function as analytical instruments that rely on a bioreceptor to detect biologically significant analytes, utilizing either an electrical or optical readout (7). Figure 2.1 illustrates that biosensors consist of diverse constituents, including bioreceptors, biorecognition elements, transducers, and detectors. Typically, these constituents are integrated into a device that encompasses a data processor and a signal amplifier.

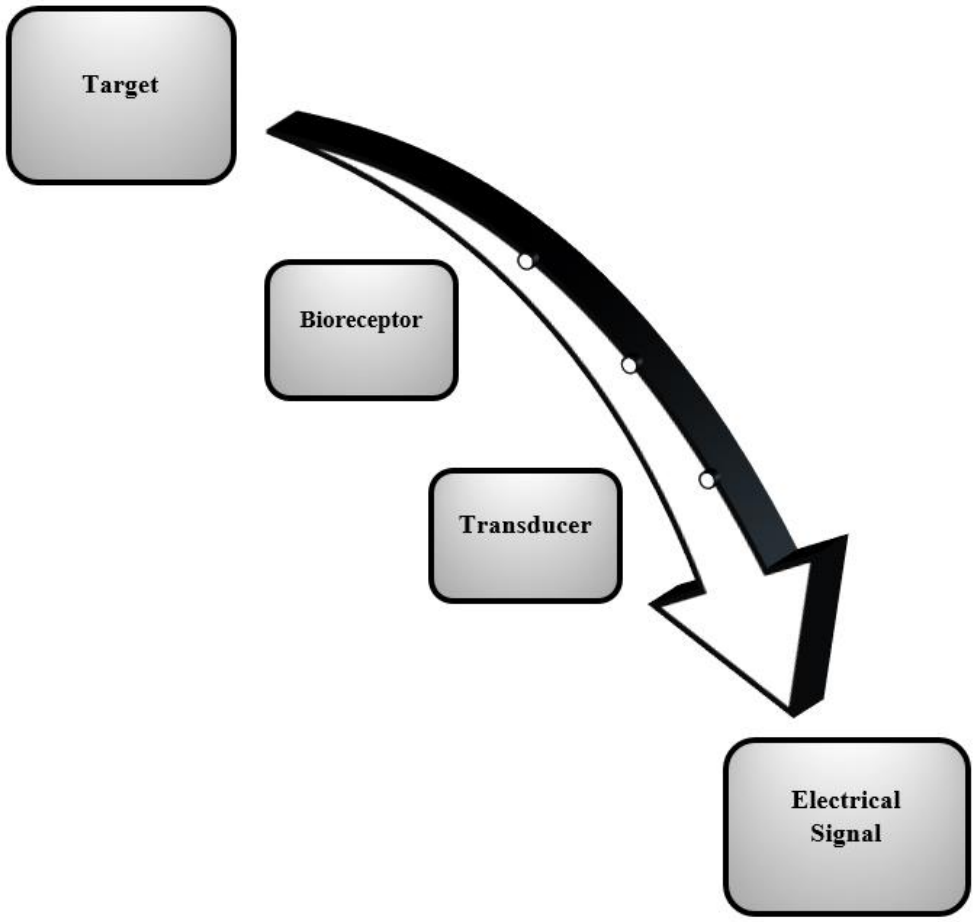

Figure 2.1. Illustration of a biosensor in diagram form.

The aforementioned biosensor is depicted in the schematic diagram, which is primarily segmented into three distinct sections.

2.1.1. Bioreceptor: A bioreceptor refers to a molecule that originates from a biological source and exhibits specific recognition toward the analyte. Receptors encompass a variety of entities, including enzymes, mitochondria, aptamers, DNA, and antibodies. Receptors encompass a variety of biological entities, including enzymes, cells, aptamers, DNA, and antibodies. The phenomenon of bio-recognition refers to the generation of signals, such as light, warmth, pH, charge, or weight alteration, resulting from the interaction between the bioreceptor and the analyte.

2.1.2. Transducer: The transducer component within biosensors is responsible for translating the signal resulting from the interaction between the analyte and bioreceptor into a quantifiable output. The majority of transducers generate optical or electrical signals that typically exhibit a correlation with the quantity of relationships that contact the analyte and bioreceptor.

2.1.3. **Electrical Signal:** This component constitutes a biosensor subsystem that facilitates the processing of the transduced signal and its subsequent preparation for display. The system is comprised of intricate electronic circuitry that executes signal conditioning functions, including signal amplification and conversion from traditional to electronic format Following this, the display unit of the biosensor measures and expresses the processed signals in numerical values (8).

2.2 A Brief Historical Background of Biosensor

The notion of a biosensor has been present since ancient times. The earliest documented instance of a biosensor can be traced back to 1906, when Cremer made the observation that the electric potential generated between segments of an aqueous solution separated by a glass membrane is proportional to the concentration of an acid present in the solution (8). The concept of pH was introduced by Soren Peder Lauritz Sorensen in 1909, and subsequently, an electrode was devised by Hughes in 1922 to measure pH (9). The advent of a "true biosensor" in 1959 can be attributed to Leland C. Clark, Jr., who is widely recognized as the "father of biosensors". Clark devised a glucose oxidase electrode sensor, as depicted in the accompanying figure, to identify glucose in biological specimens by detecting the existence of hydrogen peroxide or oxidase.

Subsequent to that, significant advancements have been achieved in the creation of biosensors with exceptional sensitivity and specificity (6-10).

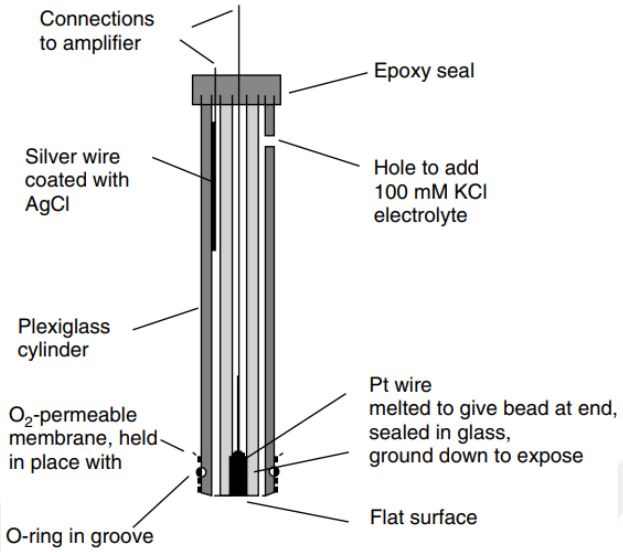

Figure 2.2. Schematic of Clark oxygen electrode (7).

2.2.1. The Biosensor of Compare to Conventional Methods

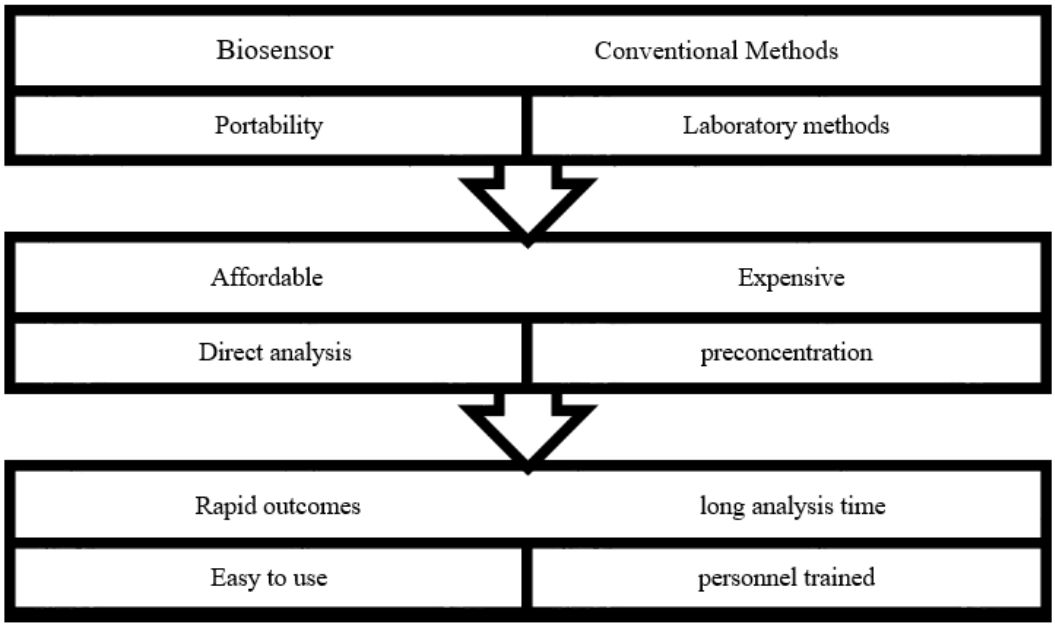

Figure 2.2.1. In comparison to traditional approaches, the biosensor.

2.3. Principle and Working of Biosensor

2.3.1 Principle of Biosensor

Figure 2.1 illustrates that a biosensor is comprised of a bioreceptor and a transducer. The bioreceptor utilized in biosensors may encompass a diverse range of entities such as enzymes, antibodies, living cells, and tissues, among others. The transducer employed in such systems may include electric current, electric potential, and other analogous mechanisms. Figure 2.3.1 presents a comprehensive compilation of the various potential receptors and transducers.

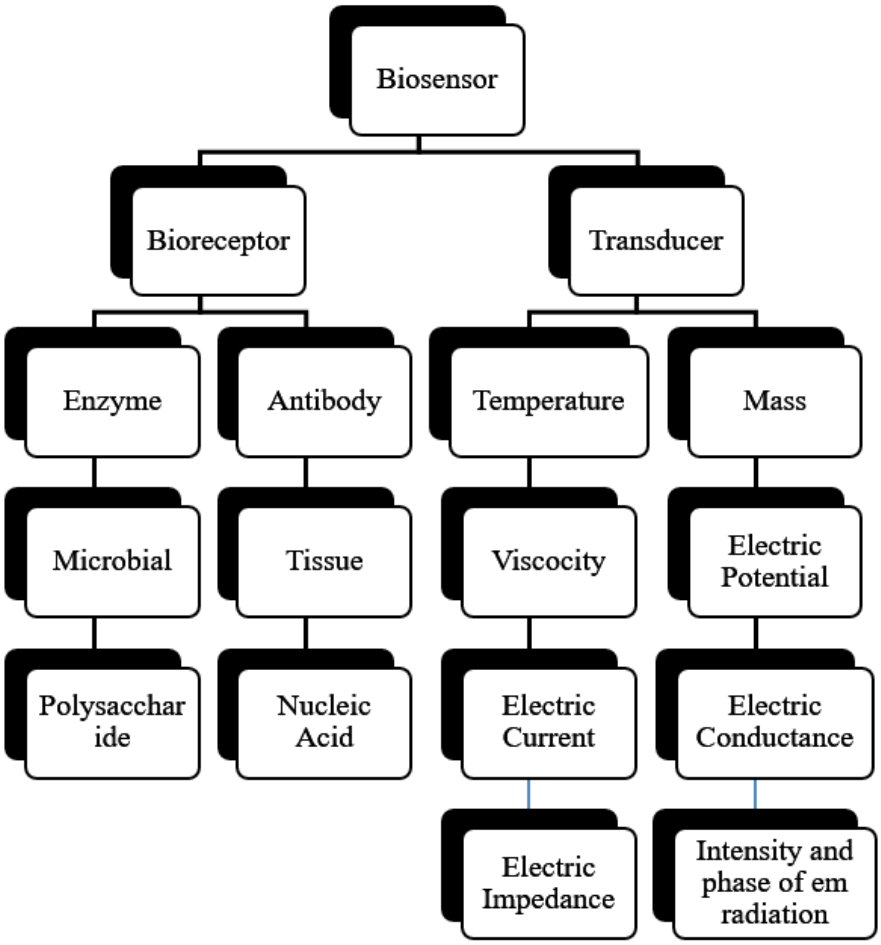

Figure 2.3.1. Elements of a Biosensor

Figure 2.3.1.1 depicts the four discrete techniques employed for coupling the "bio" and "sensor" constituents, which include barrier capture, adsorption through force, matrix trapping, and covalent bonding (11).

.

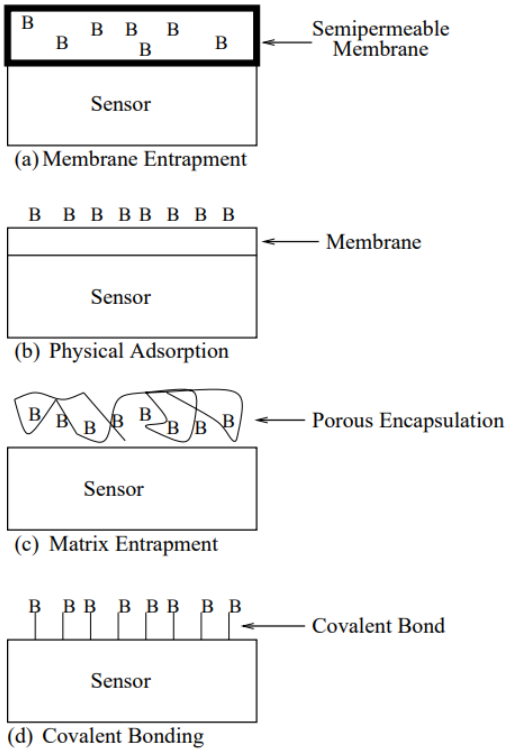

Figure 2.3.1.1. Coupling of Bio-Material with the Sensor (11).

The utilization of a semipermeable membrane to remove the sample and the bioelement characterizes the membrane entrapment approach, whereby the sensor is affixed to the bioelement. The physical adsorption mechanism relies on a synergistic interplay of van der Waals forces, hydrophobic forces, hydrogen bonds, and ionic forces to facilitate the attachment of the biomaterial onto the sensor surface. The porous entrapment methodology involves the creation of a porous encapsulation matrix that surrounds the biological material, thereby facilitating its adhesion to the sensor. Regarding covalent bonding, the reactive group of the sensor surface is utilized for binding biological materials (12).

2.3.2. Working of Biosensor

As previously mentioned, a biosensor is comprised of a biological receptor that is linked with a detector and information processing unit, allowing it to function through the process of signal transduction. The purpose of incorporating these components is to convert the physiological response into a proportional electrical response, leading to a measurable result. Biosensors are responsible for the numerical evaluation of a molecule through the establishment of a relationship between its biological activity and a detectable signal (13).

The molecule under investigation in the test sample initially engages in binding or interaction that is specific to the biological receptor, leading to a subsequent physiological alteration. . This phenomenon results in a modification of the physicochemical characteristics of the instrument, which is situated in close location to the biological receptor. Subsequently, a modification in the transducer's optical or electronic characteristics occurs, resulting in the generation of an electrical signal that can be perceived. (14).

The nature of the signal produced by the transducer is contingent upon the specific biological receptor type, and may manifest as either a voltage or a current. In the event that the transducer's output manifests as a current, it will be transformed into a commensurate voltage. Typically, the resultant voltage is of a low magnitude and is obfuscated by a high-frequency noise signal. Consequently, additional modifications, manipulations, and amplifications are necessary through diverse filters present in the signal processing module. Ultimately, it is imperative that the output produced by the signal processing unit is capable of being compared to the corresponding biological quantity that is being assessed (15).

2.3.3. Example of Biosensor

The glucometer, a widely used biosensor, serves as an apt illustration of this technology and can provide a suitable foundation for exploring the diverse classifications and utilizations of biosensors. The foremost determinant of diabetes is the level of glucose concentration in the circulatory system. Regular monitoring of blood glucose levels is crucial for individuals with diabetes. The glucose meter is a biosensor that is utilized for quantifying the concentration of glucose in blood.

Typically, the process involves employing a test strip to gather a minute blood sample for the purpose of assessing its glucose concentration. The sensor in question employs the electro-enzymatic technique, which entails the oxidation of glucose. A strip typically consists of two electrodes, namely a reference electrode and a trigger electrode. The test strip produces an electric current that quantifies the blood concentration in response to a chemical reaction.

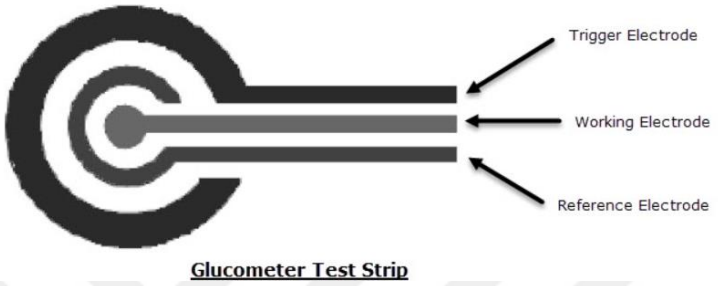

Figure 2.3.3. An instance of a biosensor

2.4. Significant characteristics of biosensors

Biosensors are subject to specific criteria or parameters that must be met, given the nature of their applications. The efficiency and usability of a biosensor are determined by these particular characteristics.

2.4.1. Sensitivity

The definition of biosensor sensitivity pertains to the correlation between the alteration in the concentration of the analyte and the magnitude of the signal produced by the transducer (16-17).

2.4.2. Selectivity

The definition of biosensor sensitivity pertains to the correlation between the alteration in the concentration of the analyte and the magnitude of the signal produced by the transducer (16-17).

2.4.3. Stability

The attribute of stability holds significant importance in biosensor applications that necessitate uninterrupted surveillance. The degree of susceptibility to environmental perturbations both internal and external to the biosensor apparatus is indicative of its stability. The stability of a system is influenced by two key factors: the degree of binding between the analyte and the bioreceptor, also known as the bioreceptor's affinity and the bioreceptor's rate of degradation over time (8).

2.4.4. Detection Limit

The term "detection limit" refers to the minimum concentration of the intended analyte that can produce a detectable signal or response. In the context of medical applications, it is desirable for a biosensor to possess a detection limit that is as low as possible, particularly when the target analyte is expected to be present at extremely low concentrations. (18).

2.4.5. Response Time

The temporal characteristic of the biosensor's signal or response generation subsequent to the interaction between the biological receptor and the target analyte is defined by this property (14,19).

2.5.6. Range or Linearity

The precision of the information obtained from a set of indicators with varying concentrations is determined by the linearity of the biosensor. The aforementioned characteristic provides valuable information regarding the biosensor's resolution, which is the smallest alteration in the concentration of the analyte of interest that can trigger a reaction from the biosensor. The ability to measure a target analyte over a wide range of levels is a crucial attribute for a biosensor, as it is a requirement for most application (8-18).

2.6. Categorization of Biosensors

Since there are several possible combinations of biorecognition molecules and transducer types, there are numerous subcategories under which biosensors can be placed. The nature of the bioreceptor molecule or the nature of the transducing element may be the most widely used method of classification.

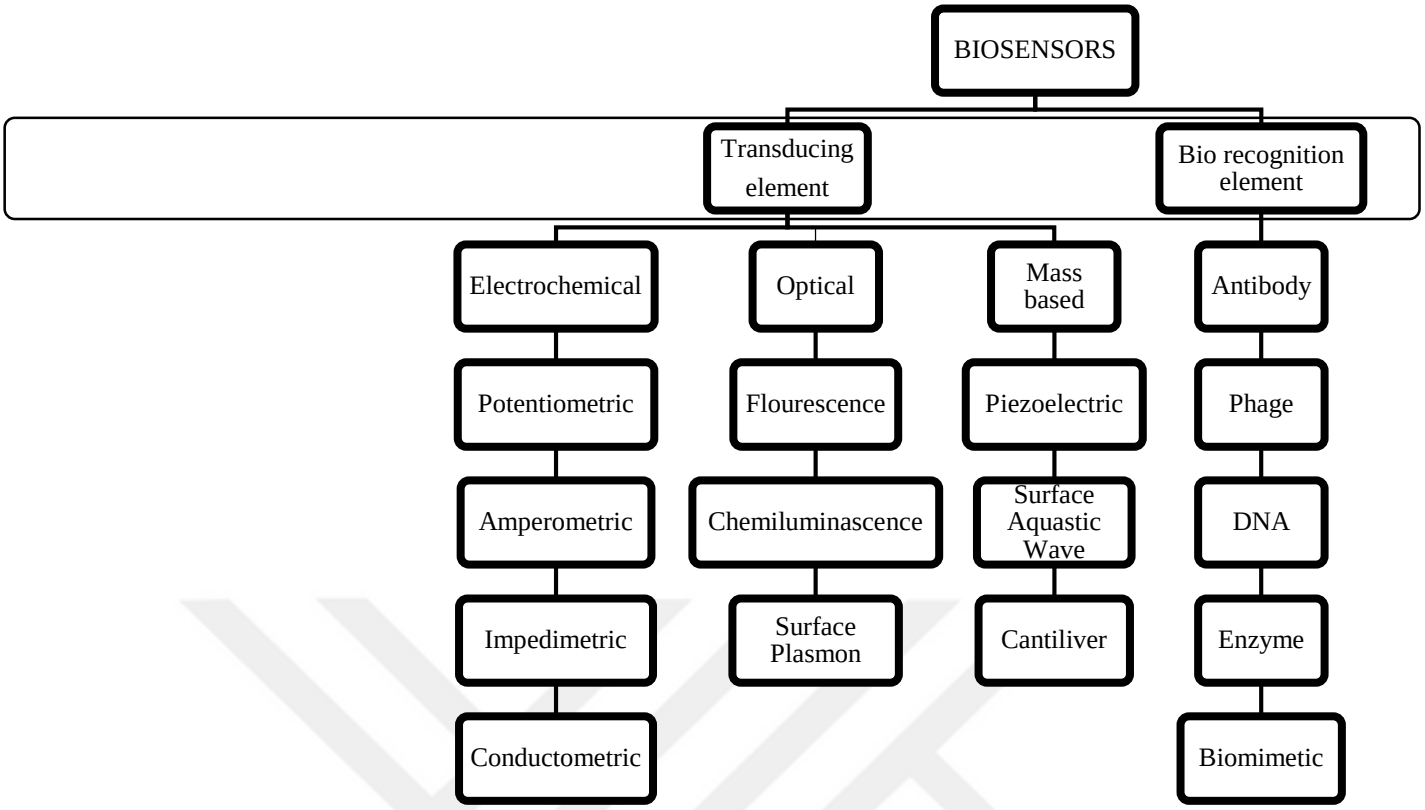

Figure 2.6. Categorization of biosensor (19).

Numerous organic molecules, including but not limited to genetic material, antibodies, enzymes, binding proteins, and oligosaccharides, have been recognized as plausible biosensory agents (20-26). Biosensory molecules are responsible for engaging with a specific target molecule and subsequently experiencing a transformation. This transformation can manifest in various ways, such as the production of heat or light, alteration in redox state, or modification in mass (27-29). The aforementioned alteration is subsequently converted into a quantifiable signal by the detector, which translates these modifications into measurable manifestations such as calorimetric, optical, potentiometric, or piezoelectric signals that are compatible with the platform. To put it differently, the transducer serves as a means of connecting the organic biosensory molecule with the electromechanical platform that is commonly used. The function of the platform is to transform the signal generated by the transducer into a quantifiable format that can be comprehended by humans. This is typically achieved by converting the transducer signal into an electronic signal, which is subsequently subjected to processing and visualization by the software.

The choice of the biosensor platform is predominantly contingent upon the particular transducer employed. Research on biosensors utilizing synthetic single-stranded nucleic acids, particularly in conjunction with electrochemical transducers, has experienced a notable surge in the past decade, despite the exploration of various recognition molecules for biosensing purposes. The term "aptamers" is frequently used to describe biorecognition nucleic acids.

2.7. An Introduction to Aptamers

Aptamers, which exhibit high affinity and specificity, are DNA or RNA molecules that are capable of binding various classes of targets (30). Due to their distinctive three-dimensional configuration, they exhibit a remarkable degree of selectivity and specificity in their binding to the intended target (31).

The capacity for binding is attributed to the three-dimensional conformation of oligonucleotides rather than the complementarity of nucleotide bases (32). The aforementioned tridimensional configuration arises from the formation of various structural motifs, such as stems, loops, bulges, hairpins, pseudoknots, triplexes, or quadruplexes, which are generated by single-stranded nucleic acids. Aptamers exhibit a high degree of specificity and affinity towards a diverse range of targets, ranging from individual molecules to complete organisms. The optimal binding observed in this context can be attributed to factors such as structural compatibility, stacking of aromatic rings, electrostatic and van der Waals interactions, hydrogen bonding, or a synergistic interplay of these phenomena (33).

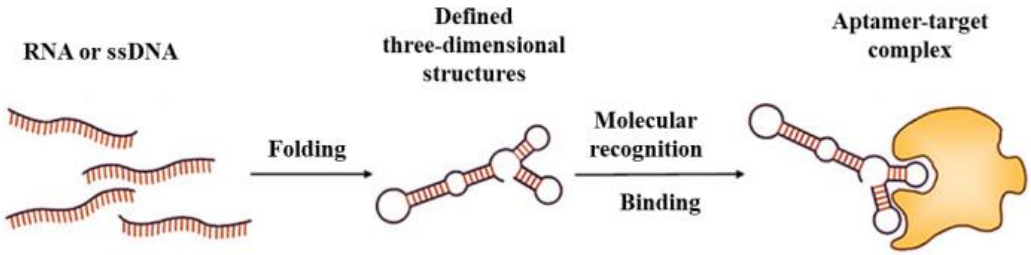

Figure 2.7. The present diagram provides a schematic representation of the recognition process between an aptamer and its target (34).

2.8. Aptamer History

For the first time in 1990, Tuerk and Gold reported the selection of RNA molecules having binding affinity to T4 DNA polymerase, gp43, and named the selection method SELEX (35). At the same time, Ellington and Szostak also described the SELEX method for identifying RNA molecules binding to the natural colors like Cibacron Blue and Reactive Blue 4. The Szostak lab termed these binding ligands as “aptamers,” referring to the Latin word “aptus”- which means fitting and the Greek word “meros,” meaning particle (36). Two years further, Ellington and Szostak demonstrated the selection of high-affinity aptamers by using the ssDNA library, DNA libraries eventually emerged as a more favored alternative to RNA libraries due to the superior inherent stability of DNA and the ease of its amplification process.Notwithstanding, owing to the increased heterogeneity in three-dimensional configurations of RNA sequences, RNA aptamers continue to be chosen (37-38). Aptamers have been increasingly sought after since their discovery in the 1990s, leading to their selection for a diverse set of targets.

2.9. Generation of Aptamers

Two main approaches can be employed to achieve the creation of ligands with high affinity and specificity, namely logical design and computational chemistry.The logical design approach utilizes chemical expertise, intuition, and a certain degree of serendipity in order to discover molecules that possess the ability to interact with the intended target (39). In the field of combinatorial chemistry, vast quantities of molecules are synthesized to generate libraries, which are subsequently screened to identify promising ligand nominees. In the year 1990, a novel combinatorial approach called in vitro selection, in vitro evolution, or SELEX (Systematic Evolution of Ligands by EXponential enrichment) was introduced as a means of generating aptamers (40).

2.9.1. Principle of SELEX Process

The SELEX technology, which was initially described in 1990, has been extensively utilized to evolve aptamers, which are nucleic acid ligands, for numerous targets. A generic SELEX process involves incubation of a random nucleic acid library, generally 10^{13} -10^{15} different sequences with a target (41). The sequences that successfully connect to the target are then partitioned, and any sequences that fail to bind or have a low-affinity are thrown out. The elution and amplification of binding sequences is commonly achieved through the utilization of the polymerase chain reaction (PCR).

This enriched pool of selected oligonucleotides is employed in the subsequent round of SELEX, and it is formed from the resultant DS-DNA, SS-DNA, or transcribed RNA. The process of repeating rounds is carried out until there is an occurrence of sequence enrichment, which subsequently enables the sequencing and characterization of aptamer candidates, as illustrated in Figure 2.9.1.

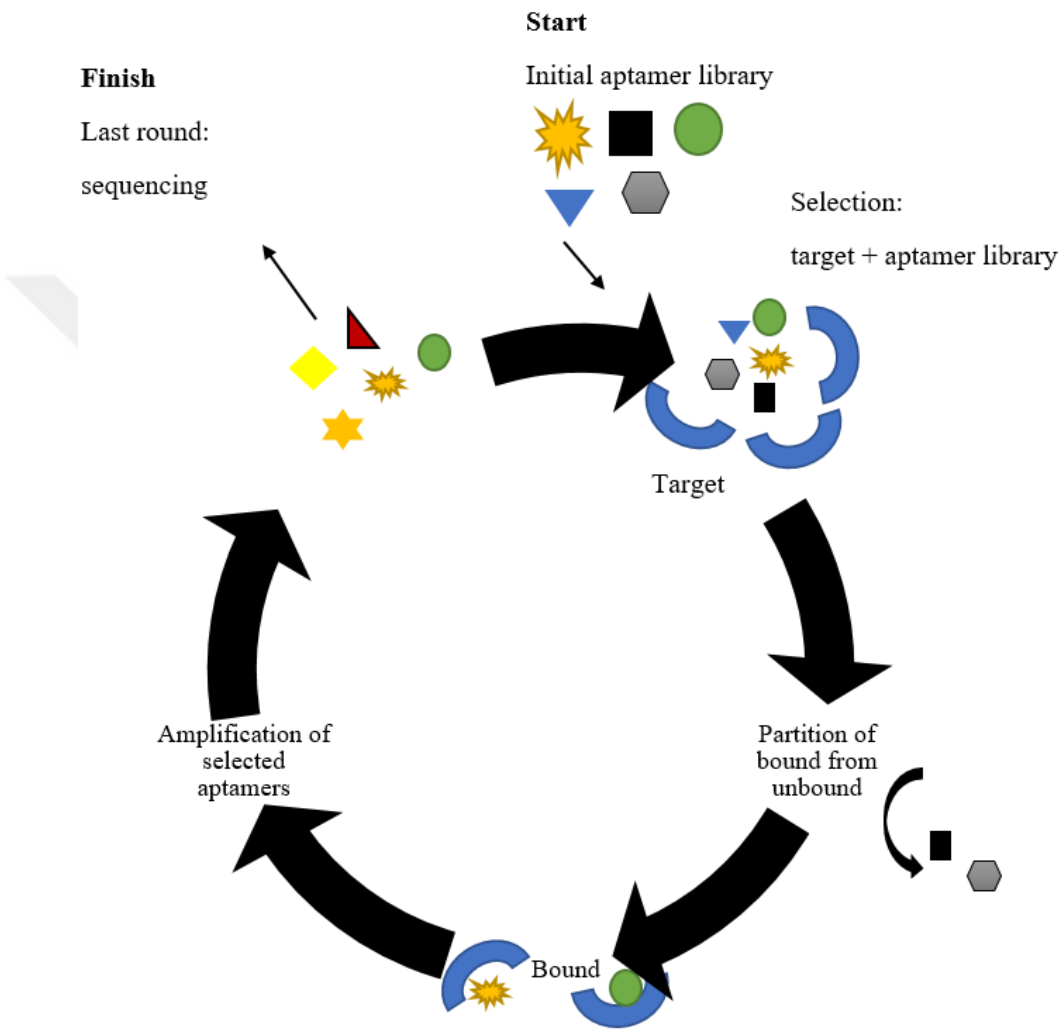

Figure 2.9.1. Overview of SELEX scheme.

2.9.2. Limitations of SELEX

Although selection strategies have undergone numerous advancements and optimizations, the SELEX process is not exempt from limitations. The overall success rate of aptamer selection has been reported to be about 50% (42).

In principle, SELEX has the potential to be applied to any target molecule. . Nonetheless, it is necessary to acknowledge that not all molecules are amenable to the in vitro selection methodology. It is imperative that the molecules of interest are obtainable in a state of utmost purity and in quantities that are adequate for the intended purpose. Aptamers may exhibit non-specific binding characteristics when generated from targets that possess slight impurities. Molecules possessing substantial hydrophobic moieties and strongly negatively charged species pose a formidable obstacle owing to the electrostatic repulsion they exhibit towards oligonucleotides. The absence of a standardized SELEX protocol is attributed to the requirement of distinct selection conditions for each target molecule. The selection of protocols is contingent upon various factors such as the characteristics of the target molecule (including its size, purity, and charge), the desired attributes of the aptamers, and the conditions of their intended application. As each targetrequires a unique approach to achieve an appropriate selection environment, it might take weeks or months to complete the aptamer selection process (43). The chemical diversity of the initial library pool represents an additional constraint of SELEX. Libraries with greater diversity are more likely to contain aptamers that exhibit high affinity and specificity. Lengthening the random region may enhance the potential for crosstalk between the flanking primer binding sites and the random region. The augmentation of structural diversity can be achieved through the alteration of library sequences. Nonetheless, it is imperative to note that only modifications that are amenable to PCR amplification are viable. Additionally, the cost attributed to the alteration is elevated, and the related examination is laborious. One further constraining element pertains to the depletion of probable binders while separating the aptamer-target complexes and eluting the sequences that have bound to the target. Moreover, Polymerase Chain Reaction (PCR) has the potential to induce mutations in the nucleotide sequences, thereby leading to the elimination of certain prospective binding agents. One additional limitation of the SELEX methodology pertains to the amplification of non-specific sequences that may occur as a result of their interaction with the tubes or solid surfaces employed during the selection process. Comprehending the constraints of the SELEX methodology holds significant importance, as certain limitations can be addressed through alterations in the SELEX parameters.

2.10. In Silico Methods for Aptamer Selection

In recent years, a novel approach has been suggested as an alternative to SELEX. This approach involves utilizing bioinformatics computational techniques such as MD and docking to develop aptamers for diverse applications. The integration of silico methodologies with SELEX and HTS can enhance the effectiveness of scientific investigations. Certain computational tools are designed specifically for the examination of high-throughput screening (HTS) experimental data. The swift proliferation and incorporation of NGS technology presents the potential for executing novel, high-capacity studies and devising fresh assessment methodologies (44-45). Computational tools offer a diverse array of techniques to a researcher. Aptamers can be designed to target both simple compounds and complex biopolymers, including proteins. Molecular modeling techniques can facilitate the discovery of novel aptamers that exhibit enhanced binding affinity towards the target molecule. Furthermore, these methodologies can aid in the identification of significant structural motifs that govern the interaction among the aptamer and its respective desire molecule. This is particularly advantageous as point mutations may be introduced to optimize aptamer binding affinity. Figure 2.10 depicts a standard modeling workflow utilized in conducting an in silico study of an aptamer/ligand.

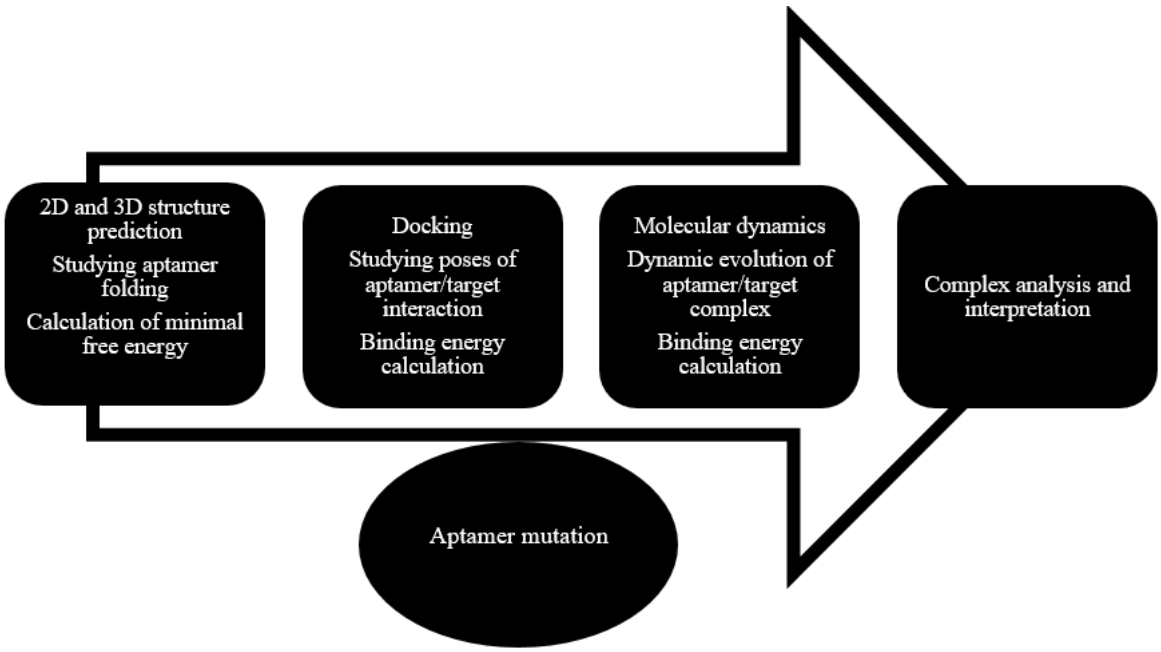

Figure 2.10. Conventional process for in silico construction and evaluation of aptamers.

2.11. Early Works and Current Works on In-Silico Aptamers Screening

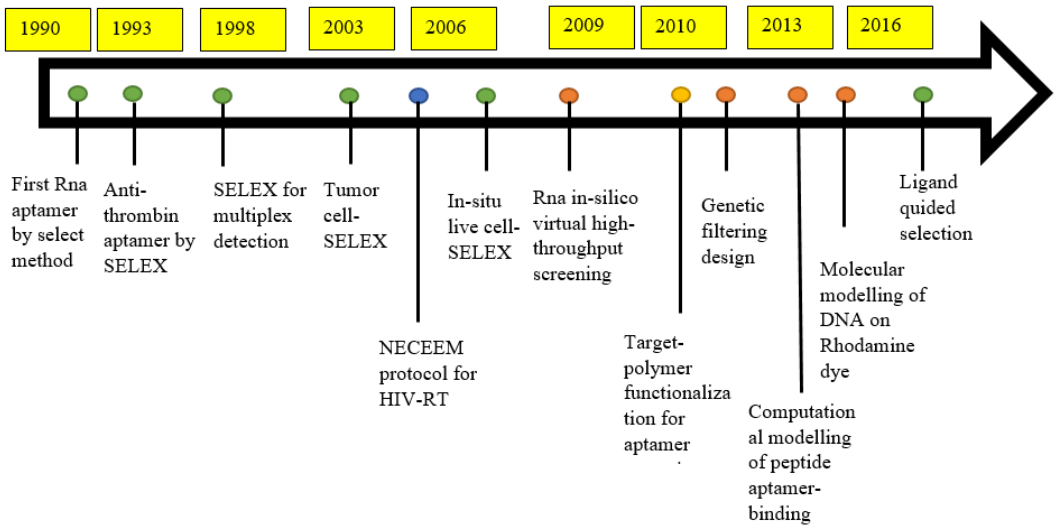

Figure 2.11. Timeline of aptamer selection procedure progress

2.12. The Utilization of In Silico Techniques for The Advancement of Aptamers

Numerous investigations have been devoted to the in silico design and modeling of aptamers, contingent upon the specific targets of said aptamers.

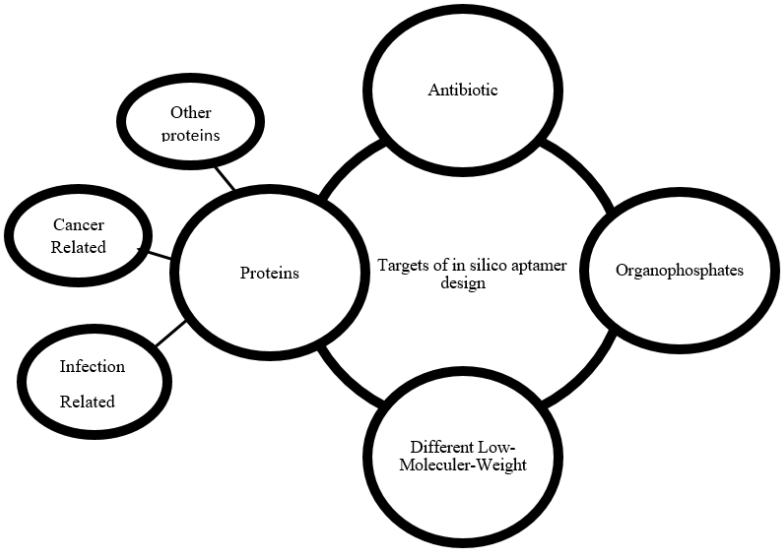

Figure 2.12. Targets of aptamers in silico applications

The binding agent molecules utilized in the creation of aptamers can be categorized into various categories, including peptides, which are particularly useful for targeting tissue due to their surface glycoproteins, as well as antimicrobial agents, chemical phosphates, and another low-molecular-weight compounds (46). The objectives and research approach of the investigation vary depending on the specific targets. The studies were categorized based on the specific aptamer target employed, as a result of this rationale.

2.12.1. Proteins As Aptamer Design Targets

Aptamer research predominantly employs proteins. The variability of aptamer structure and design is contingent upon the protein's specific structural and functional characteristics. The application of in silico design methodology has been demonstrated to enhance the binding affinity of aptamers, while simultaneously emphasizing their stability.

The utilization of in silico approach is a common practice in mathematical and mathematical principles empirical investigations to improve the binding affinity of aptamers, as demonstrated by an abundance of studies. An additional aim of the investigation is to comprehend the structural configurations that hold significance in connecting of aptamers to proteins. Thrombin has been widely utilized as a primary target for the purpose of in silico aptamer design. The blocking of thrombin is a crucial aspect of blood coagulation and therefore, it serves as a significant protein target. The significance of the HIV-1 protein lies in its involvement in the invasion process of DNA viruses. Furthermore, due to the significance of the EpCAM as an indicator for tumorigenesis, there is currently a vigorous pursuit of aptamer research aimed at elucidating the correlation among aptamers and EpCAM (47).

2.12.2. Antibiotics As Aptamer Design Targets

A significant body of in silico aptamer construction research is focused on the targeting of low-molecular-weight compounds. The aforementioned inclination is primarily linked to the potential applications of aptamers in quantitative frameworks. Superior stability, facile of regeneration, and comparatively low cost make aptamers a promising alternative to antibodies, which are mainly used for these purposes at present (48).

A prevalent challenge in the realm of in silico antibiotic aptamer creation pertains to the validation of novel methodologies and the identification of fresh sequences that exhibit enhanced affinity towards the target. Aminoglycosides are a frequently studied subject in silico aptamer modeling, particularly in the context of antibiotics (49-51).

2.12.3. Organophosphates as Aptamer Design Targets

This particular segment is devoted to the utilization of aptamer design in targeting organophosphates. Several compounds discussed in this section are considered toxic substances, including paraoxon. Free nucleotides, which are phosphorous ethers of nucleosides, play a significant role in biological systems as they serve as structural components of genetic material and catalysts. The rationale behind the aptamer design's preference for mononucleotides as targets can be accounted for by their popularity. Jokar et al. developed SS-DNA aptamers targeting the commonly used organophosphorus insecticide diazinon (52).

2.12.4. Different Low-Moleculer-Weight as Aptamer Design Targets

This section pertains to non-antibiotic and non-organophosphate low-molecular-weight compounds that are also targeted. The primary objective of the investigation conducted in this segment is to authenticate the in silico aptamer design approach and substantiate the frequent incidence of enhancing aptamer connection towards desired molecules. Frequently employed low-molecular-weight entities involve DNA bases, amino acids, amino acid derivatives, drugs, and endocrine systems. DNA aptamers targeting 17β-estradiol (E2) were created by Hilder and Hodgkiss (53). The study conducted by Zhao and colleagues involved the exploration of aptamers for N-butanoyl-L-homoserine lactone (C4-HSL) through the utilization of Systematic Evolution of Ligands by EXponential enrichment (SELEX) in conjunction with in silico prediction of tertiary structure (54). The objective of the study was to conduct a screening of DNA aptamers targeting C4-HSL in order to assess their effectiveness in inhibiting the biofilm formation of Pseudomonas aeruginosa. The results of the 3D RNA structure estimation indicate that the aptamers that were designed exhibit a Y-shaped structural unit that is highly conserved.It is probable that this particular structural entity is accountable for the attachment of C4-HSL.The outcomes of the in vitro biofilm inhibition trials suggest that the aptamers exhibited efficacy in diminishing the activity of P. aeruginosa by roughly 33% (44).

2.13. In Silico DNA Aptamer Production Restrictions

In-silico docking methodologies are subject to various constraints. The development of DNA aptamers is hindered by a scarcity of computational resources, as the majority of available software is designed for RNA aptamers (55). The capacity to forecast de novo DNA aptamer-target interactions through in silico methods is contingent upon the utilization of well-established DNA aptamers as the initial template. The feasibility of this approach is questionable in light of the restricted scope of existing DNA aptamer databases (56). Thirdly, the replication of intricate SELEX conditions, including metal ion concentrations, temperature, and the composition of diverse biofluids, may introduce complexities in the in-silico docking process, thereby posing a challenge to the dependability of in-silico selection. Furthermore, the primary limitation is attributed to the computational capability of the hardware (55).

2.14. Structure and Properties of Aptamers

2.14.1. Structure Types of Aptamers

Analyzing target interaction with secondary and tertiary structural motifs for aptamers provides precise information to create aptamers with improved affinity and specificity to a target (57). The secondary structures of aptamers are diverse and contingent upon the nucleotide sequence employed to bind specific targets. The customary three-dimensional secondary structures are depicted below and elucidated in Figures 2.14.1

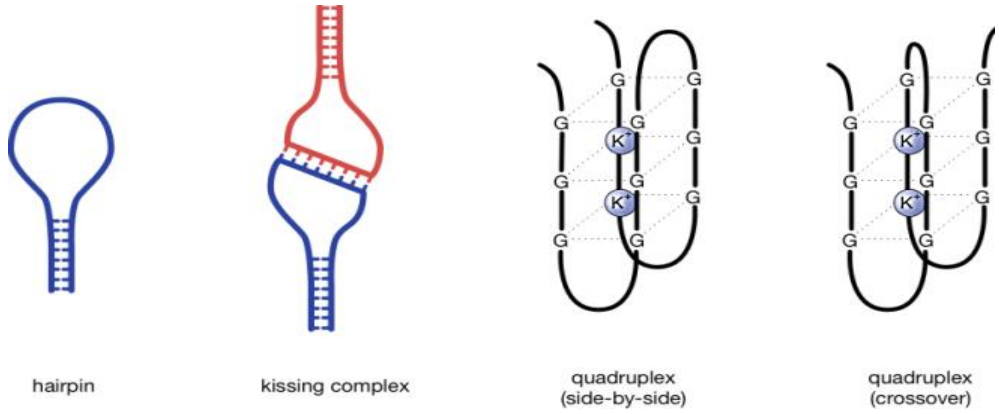

Figure 2.14.1. Aptamer secondary structures (58).

1- A hairpin, also known as a stem loop, arises from the complementary nature of two regions within a single strand, allowing for the formation of Watson-Crick base pairs.

2- A quadruplex structure manifests in guanine-rich nucleotide sequences as a result of the association of four guanine bases through hydrogen bonding.

3- The formation of the kissing complex occurs through the establishment of base pairing between the unpaired nucleotides present in one hairpin loop and those present in another hairpin loop. RNA is typically the site of its occurrence.

2.14.2. Properties of Aptamers

Aptamers are commonly composed of bases ranging from 22 to 100 in length. They consist of a variable region that is surrounded by stable parts, which facilitate amplification and recognition of the pattern.(59-60). Akin to monoclonal antibodies, aptamers possess a multitude of applications including biomarker recognition (61), therapeutics (62), diagnostics (63-66) and high throughput screening (67). Aptamers possess biophysical properties that enable them to compete with antibodies in various aspects, as stated in reference (68).

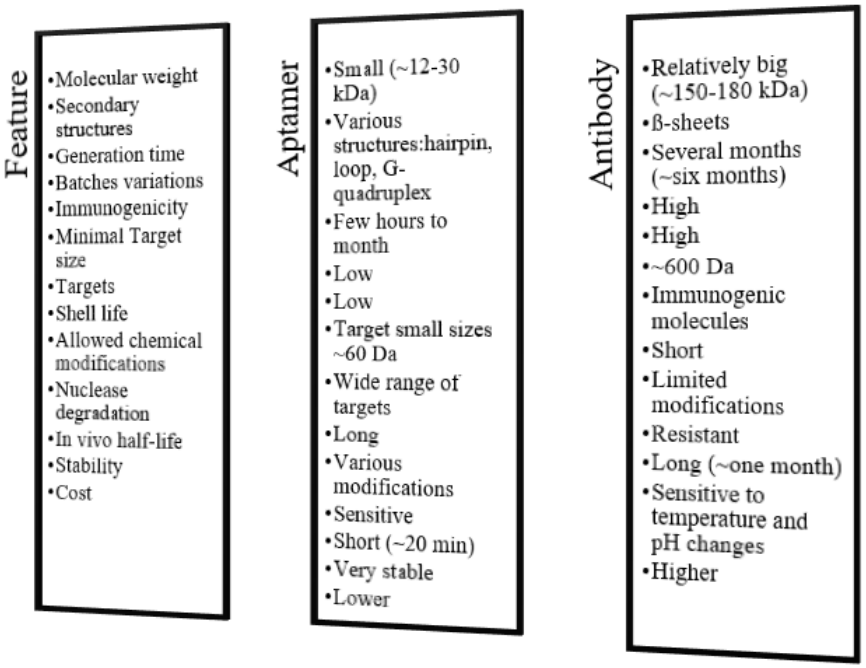

Figure 2.14.2. Comparative analysis of aptamers and antibodies.

Currently, a number of analytical designs utilizing aptamers are being developed as suitable tools for the detection and quantification of various molecules. The utilization of aptamers in chemical research is a captivating field of study due to their capacity to bind to targets with comparable affinities as antibodies. Moreover, aptamers offer various advantages. The process of aptamer regeneration can be accomplished within a matter of minutes through the desaturation and subsequent renaturation of the molecules. The optimization of bound features in Selex can be achieved through the regulation of various conditions, including but not limited to buffers, temperature, and pH. It is feasible to modify the sequence of the entity in order to regulate the selection of binding. The aptamer may be synthesized via chemical procedures in order to enhance its level of purity. This substance is generated via a laboratory-based procedure that does not necessitate the use of animal cellsIt is produced through a laboratory process that doesn't require animal cells (69). Aptamers can be a valuable and economical resource when their therapeutic properties, including stability and dynamics, are optimized and enhanced.

In addition, the utilization of aptamer techniques offers several benefits, including reduced toxicity and extended half-life (70). Aptamers possess several advantages over antibodies, such as facile synthesis, extended shelf life at ambient temperature, stability during transportation, and the utilization of diverse oligonucleotides for aptamer formation, enabling the selection of aptamer molecules for multiple targets.

Thus, aptamers are regarded as a valuable tool in the field of medicine for both diagnostic and therapeutic purposes.(71). The aptamer exhibits a specific binding affinity towards its targets, encompassing both high and low molecular weight species. Aptamers have surfaced as a potentially viable substitute for antibodies in the field of biosensing due to their capacity to function as recognition components.The K(D) value of the aptamer is comparatively higher than that of the antibody. The aptamer can be synthesized with easy strategies (72).

2.15. DNA and RNA aptamers

DNA aptamers resemble their RNA counterparts, but they are less stable and more difficult to reach. The reduced stability of the RNA aptamer can be attributed to the presence of a reactive hydroxyl group (-OH) situated within its nucleotides, specifically at the two positions of the ribose.

The hydroxyl functional group (-OH) exhibits the propensity to undergo dissociation in a solvent, particularly under basic conditions.The 2-O- group exhibits reactivity towards the phosphorous atom, thereby instigating the process of RNA hydrolysis. Eliminating the hydroxyl group leads to a rise in the nuclease resistance of the RNA molecule.

The SS-DNA aptamer exhibits greater stability in comparison to its RNA aptamer counterpart. The presence of a C-H bond within the nucleotide, specifically in the deoxyribose sugar, is a contributing factor. The dissimilarities between the SS-DNA aptamer and the RNA aptamer confer a stability advantage to the former. Chemical alteration of RNA aptamers can be employed to augment their stability. These modifications include substituting the hydroxyl group with 2′-amino or 2′-fluoro, and replacing the phosphodiester backbone with phosphorothioate or boranophosphate.

In recent times, novel chemical alterations have been discovered to enhance the stability of siRNA, involving modifications of the 2'-O-Methyl or phosphorothioate within the identical nucleotides.The utilization of RNA-based techniques in the field of biology has been expanded by the implementation of modification techniques that enhance the stability of siRNA.The locked nucleic acid technique has been utilized to generate RNA chains, resulting in a verified alteration known as spiegelmer.The aforementioned alteration induces a modification in the structural conformation of the RNA molecules.These alterations make RNA aptamers resistant to nuclease digestion, and the RNA's nucleotide activity and non-base pairing allow it to fold into a variety of complicated three-dimensional structures.In order to obtain complex molecules, libraries with vast random regions are typically used to choose SS-DNA aptamers.

One benefit of SS-DNA aptamers in comparison to RNA aptamers is their uncomplicated selection process.Reverse transcription is a necessary step in each election cycle for the selection of RNA aptamers.

The additional step is not required in the synthesis procedure of SS-DNA aptamers.In comparison to RNA aptamer production, the output of DNA aptamers is relatively more economic value (73).

2.16. Application of Aptamers

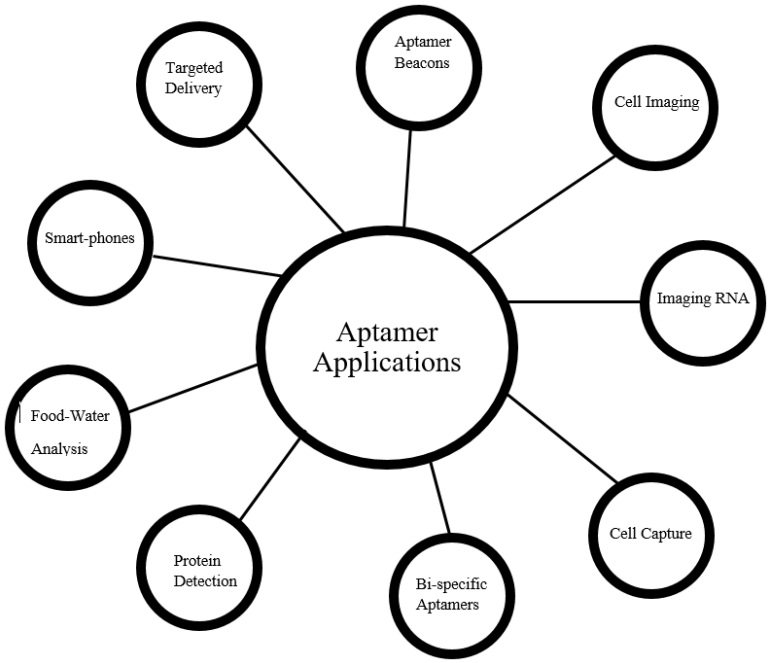

Figure 2.16. Application of aptamers.

Aptamers exhibit a broad spectrum of utility in fundamental scientific inquiry, identification of biomarkers, analysis of the environment, and medical treatment. Aptamers have the potential to be employed in fundamental research for the purpose of confirming targets and biomarker identification. Additionally, they can be put to use to investigate the functional features and mechanisms of complementary targets like enzymes and proteins (74-75). Aptamers have a variety of applications in environmental remediation, including the identification and removal of harmful chemicals for purposes such as water purification. In addition, sensors utilizing aptamers have the potential to be employed in the detection and characterization of harmful substances present in food and agricultural commodities (60). Aptamers have the potential to serve as both diagnostic detection reagents and therapeutic agents in clinical practice. In addition, the utilization of aptamers in conjunction with appropriate nanocarriers presents a promising approach for achieving targeted drug delivery (76).

2.16.1. Use of Aptamers in Diagnostics

An early and precise diagnosis is crucial for the successful management of any illness. The attainment of an early diagnosis is solely feasible through the utilization of highly responsive techniques that incorporate acute-detecting agents, such as aptamers. Aptamers have been employed in the identification of bacterial, parasitic, and viral-induced illnesses, as well as cancer and small organic molecules (as illustrated in Figure 2.16.1) The price of several current diagnostic procedures is inflated by the need for specialized equipment and trained personnel. The diagnostic procedures that are now in use could take a long time because they involve isolating infectious agents and then cultivating them in order to make a diagnosis. In certain instances, the amplification of causative agents is necessary to ensure accurate diagnosis due to their limited levels of concentration. Aptamers can be employed to streamline the process and tackle these issues (77).

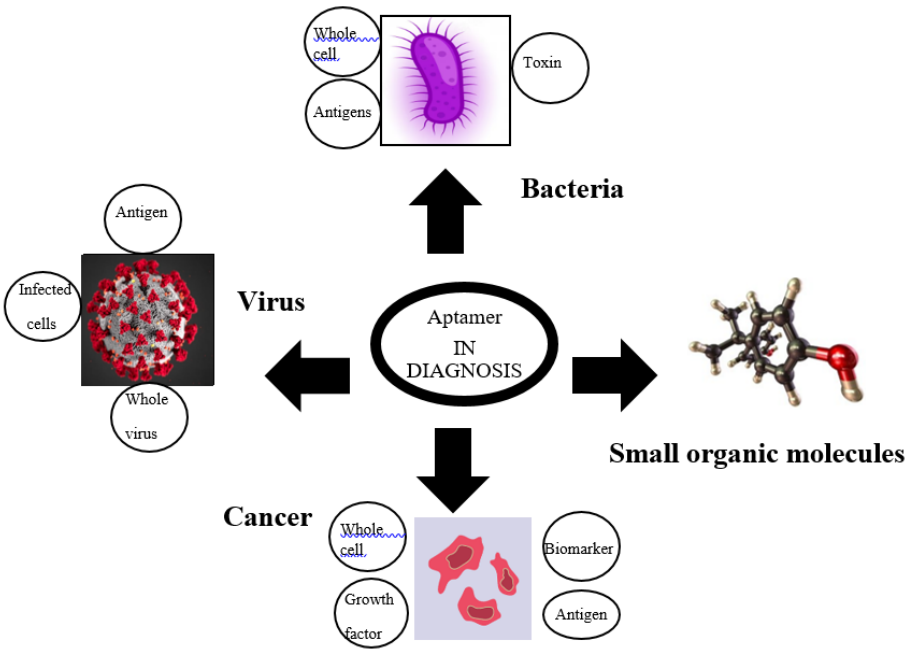

Figure 2.16.1. Application of aptamers in field of diagnosis

2.16.1.1. Aptamers in Detection of Small Molecules

Aptamers have been chosen for their specificity towards low molecular weight compounds, including but not limited to ofloxacin, ochratoxin A, bisphenol A, cocaine, bacterial endotoxins, and heavy metals such as mercury, arsenic, copper, and lead (78). These small molecules can lead to food and drinking water contamination and environmental pollutants and thus; can be toxic to humans and animals. Aptamer based-biosensor systems have been developed to detect pollution and toxins (79-80).

2.16.2. Bio-Recognition Aptamers for Endocrine-disrupting compounds (EDCs)

Commercially available products commonly used by consumers contain endocrine-disrupting chemicals (EDCs), including phthalates and bisphenols. The high persistence, toxicity, and bioaccumulation of these substances in environmental samples are a significant cause for concern. EDCs possess the capacity to interfere with the regular hormonal processes in both humans and animals, even at minimal concentrations, leading to unfavorable outcomes. (81-82). The detrimental effects of EDCs on the development and advancement of water-based organism, wildlife, and individuals have been thoroughly examined by the scientific community. There exists documented evidence of bioaccumulation and alteration of various systems, such as the endocrine and immune systems (83-84). The timely detection of pollutants is of great significance, hence the need for the advancement of biosensing tools for this purpose. Analytical methods commonly used to detect EDCs in environmental matrices include GC/MS, LCMS and LC-MS/MS (85-86). On the other hand, the analytical and pre-treatment operations are both time-consuming and difficult, and as a result, they can only be performed by trained professionals. Antibodies are widely recognized as essential biomaterials for the capture of endocrine-disrupting compounds (EDCs). The production of antibodies is a complex undertaking that entails the development of animal immune responses and monoclonal hybrid cell tumor cultures. This process is time-consuming, expensive, and lacks batch-to-batch reproducibility. These factors hinder the incorporation of antibodies as a labeling probe in applications that require rapid analysis (87). Chemical and biological sensors have the potential to serve as a viable alternative for the expeditious and localized detection of trace pollutants.

Nevertheless, the majority of these techniques are dependent on the use of antibodies.Hence, the fabrication of biosensors hinges on the biological recognition elements, which are of paramount importance. Aptamers exhibit desirable specificity, thereby enabling them to surmount the interference that may arise from diverse antigens and antibodies. Aptamers are known to exhibit significant attributes that render them crucial components in biosensors utilized for the identification of minute molecules.

2.16.2.1. Detection of Bisphenol A

Bisphenols (BPs) are a class of (EDCs) that are characterized by their dimeric structure, consisting of two phenolic moieties joined by a connecting parts.The pivotal linkageis a crucial component that serves to distinguish it from other variations. As of present, there exist approximately 20 variants of BPs. Bisphenol A, also known as BPA, is considered the most well-known member of the Bisphenol family and is also recognized as a prominent EDC. (88). Bisphenol A (BPA) has the ability to interact with the pregnane X receptor as well as various estrogen receptors, including ERα, ERβ, and estrogen related receptor γ (ERRγ). This interaction can lead to a range of endocrine disrupting effects, such as damage to the immune system, neurological toxicities, metabolic disorders, and reproductive dysfunctions within the human body. (89). In addition, Bisphenol A (BPA) has been found to display toxic effects on wildlife, particularly aquatic organisms, when its concentration reaches levels of 1-10 μg mL−1. (90). In March 2009, the United States Federal government suggested the prohibition of the utilization of BPA in "reusable food containers and other food containers." (89).

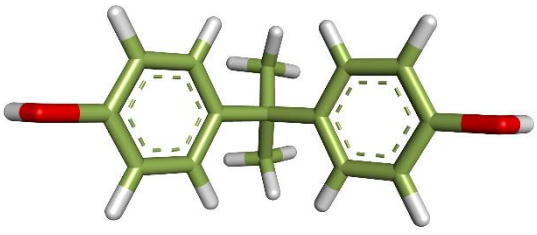

Figure 2.16.2.1. Chemical structure of BPA

2.16.2.2. Detection of 17β-estradiol

EDCs, such as 17β-estradiol, present a significant hazard as they exhibit estrogenic activity by mimicking natural hormones.

The identification of these chemical compounds in natural ecosystems is imperative in safeguarding the well-being of both the public and the environment (91). Among human beings, E2 is widely regarded as the most potent naturally occurring steroid estrogenic gender hormone (92). Exogenous estradiol (E2) is classified as an endocrine disruptor and has been shown to have deleterious impacts on male human reproductive health (93-94). The presence of E2 in ground and drinking water raises concerns, thereby necessitating the monitoring of its concentration. Moreover, E2 has been identified in the wastewater of municipal sewage treatment facilities, medical institutions, and municipal landfills (95-96). For the detection or filtration of E2, it is possible to use aptamers, as they have already used for the detection of a large number of small compounds (82).

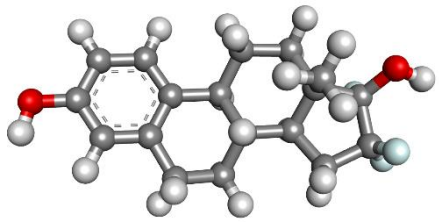

Figure 2.16.2.2. Chemical structure of 17β-estradiol

2.16.2.3 Detection of Polychlorinated biphenyls (PCBs)

PCBs have been identified as a type of (EDC) and a significant persistent organic pollutant within the class of chlorinated hydrocarbons, a group of synthetic organic chemicals (97). The presence of PCBs at trace levels in the environment persists as a significant risk to public health (98). Various sources of environmental exposure may include the consumption of food and water, inhalation of air pollutants, and occupational health hazards, among others (1).

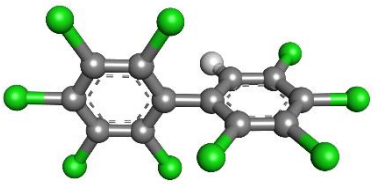

Figure 2.16.2.3. Chemical structure of PCB 72

3. MATERIALS AND METHODS

3.1. COMPUTATIONAL METHODS

The domain of molecular modeling is experiencing rapid expansion due to its versatile applications across various domains of research. Currently, it is extensively employed to investigate the molecular architecture of complex systems within the domains of physics, chemistry, and biology. Chemical and biological systems can be modeled at the molecular level using molecular simulation software. The energy of the simulated structure is determined through the utilization of molecular mechanics (MM), which relies on classical potential functions. Alternatively, quantum mechanical methods may be employed if electronic interactions are also considered. The calculations may encompass the spectroscopic characteristics and reaction pathways of the chemical systems under consideration. The field of quantum mechanics employs a range of computational techniques, including semiempirical approaches, ab initio methods, and density functional theory. Molecular modeling involves the utilization of both MM and quantum mechanical techniques. The primary objective of molecular modeling simulations is to facilitate the identification of the most optimal compound for synthesis, thereby resulting in time, labor, and cost savings.

3.1.1. Computational Chemistry Methods

Methods utilized in computational chemistry include accurate mathematical approximations and other forms of computer programming. The field of computational chemistry employs foundational principles of physics, particularly those of quantum mechanics, in order to compute and determine the characteristics of physical and chemical systems.

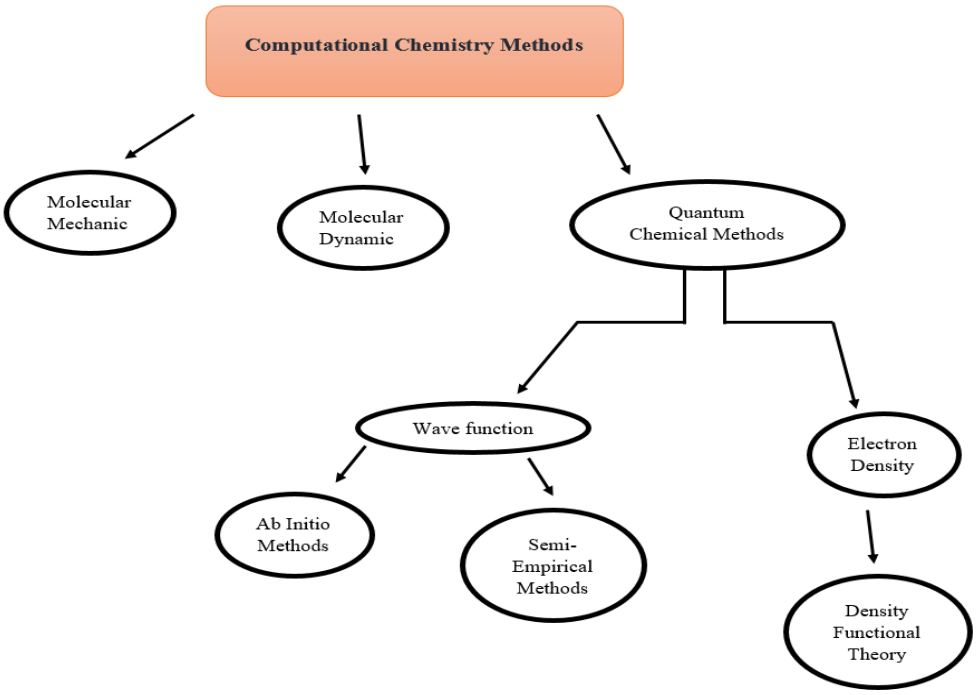

Figure 3. 1.1. Schematical computational chemistry methods

3.1.1.2. Quantum Mechanics

The utilization of QM is frequently employed in comprehending the conduct of diminutive molecules (ligands) at the atomic scale. Quantum mechanical techniques rely on utilizing an estimated wave function in order to effectively address the Schrödinger formula. The Schrödinger formula is a pivotal numerical expression that delineates the wave-like attributes of either a solitary electron or a duo of electrons situated within an atomic structure (99-100). The mathematical expression denoting the Schrödinger equation is represented by equation 3.1.

H=T + V

The aforementioned expression involves the Hamiltonian operator denoted by H, which represents the sum of kinetic energy, and T, which represents the potential energy. Additionally, the expression includes the operator V. The symbol "H" may also be denoted as formula 3.2:

$$\hat{H} = -\sum_{i=1}^{N}\frac{1}{2}\nabla_i^2 - \sum_{a=1}^{M}\frac{1}{2M_a}\nabla_a^2 - \sum_{i}^{N}\sum_{a}^{M}\frac{Z_a}{r_{ia}} + \sum_{i}^{N}\sum_{j>i}^{N}\frac{1}{r_{ij}} + \sum_{a}^{M}\sum_{b>a}^{M}\frac{Z_a Z_b}{R_{ab}}$$

The aforementioned formula comprises five distinct terms, each of which represents a specific form of energy. The initial expression pertains to the motion force of the electrons,while the subsequent term denotes the motion energy of the nucleus. The third term represents the connection energy among the nuclei and the electrons, whereas the fourth term signifies the interacting energy among the electrons. Finally, the fifth term pertains to the connection of energy among the nuclei. The nuclei are denoted by A and B, while the electrons are represented by i and j. The distance between electrons i and j is defined by rij, while the distance between nuclei A and B is defined by R_{AB}.

The resolution of this equation in multi-electron systems, specifically macromolecules, presents a considerable challenge. Consequently, various techniques have been devised to derive an estimated solution for this equation. The categorization of these techniques is typically based on three main approaches: semi-empirical, ab initio, and density functional theory (DFT) (101).

The semi-empirical approach is a computational technique that determines the electronic wave function and electron energy by disregarding the motion of nuclei and incorporating parameters derived from empirical observations. Calculating optimum values for geometric characteristics like bond length, bond angle, and dihedral angles, in addition to determining dipole moments and thermodynamic properties, is one of its many applications. Several computational methods utilized in quantum chemistry include CNDO, INDO, MINDO, ZINDO, AM1 (Austin Model), and PM3 (Parametric Method) (102-107). The ab initio method, which is a quantum mechanical technique, employs the Hartree-Fock (HF) approach to determine the average potential energy associated with electron-electron interactions (108). This approach is viable for computing molecular frequency analysis and ascertaining molecular geometry.

The employment of the DFT approach has become a prevalent practice in the study of molecular systems, with a focus on the analysis of electron structures and geometry (109). The objective of this approach is to compute the aggregate electronic energy and the distribution of electron density (110). The B3LYP/6-31g(d) model chemistry is widely regarded as a suitable general-purpose option in various settings, such as educational environments and general practice (111). The present study conducted an initial geometric optimization of the EDCs using the MM method.

The nature of the literature suggests that the B3LYP/6-31G(d) basis set is commonly utilized in studies involving small organic molecules. For this reason, the Gaussian 09W program was utilized to perform geometric optimization of said molecules employing the B3LYP/6-31G(d) basis set (112).

3.2. Process For 3D Creation From Sequence

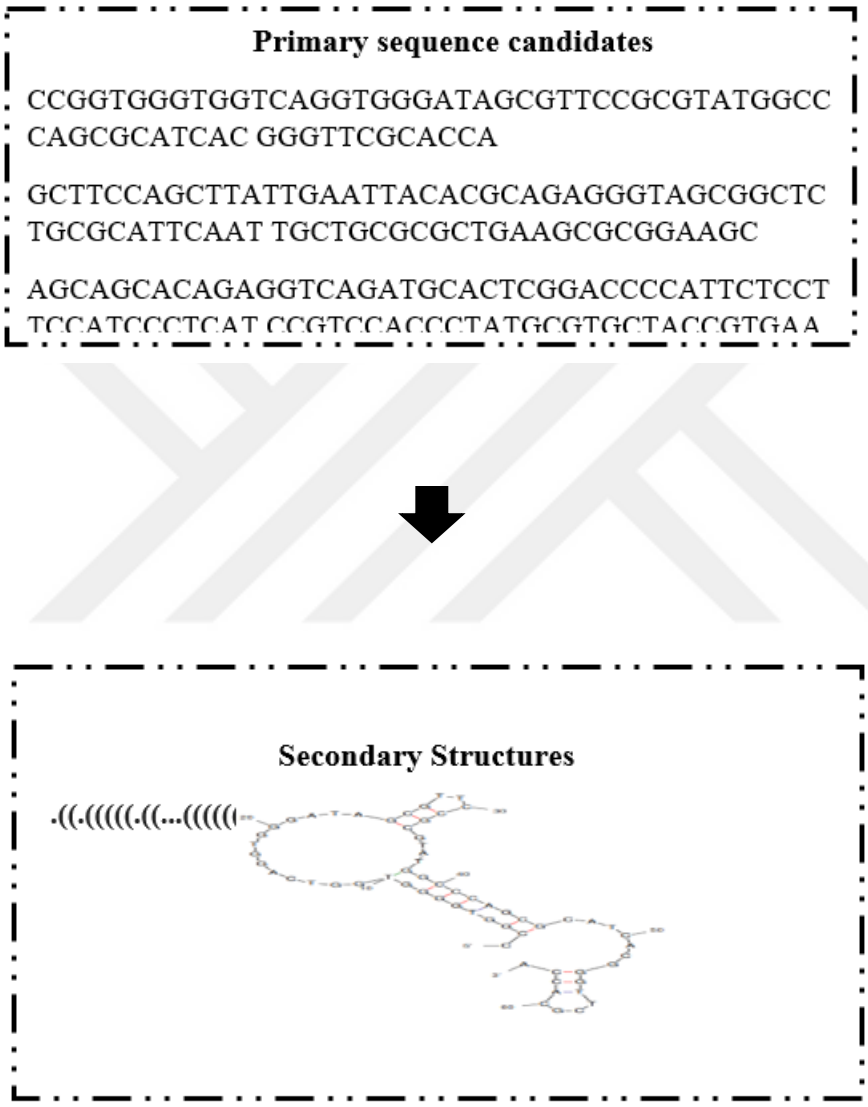

Three Dimensional Structure (3D) -RNA

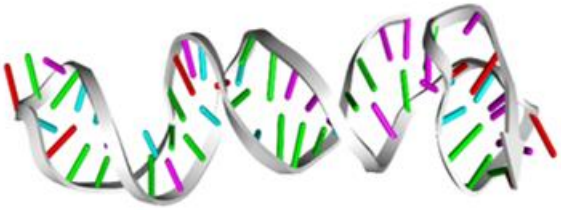

Three Dimensional Structure (3D) -DNA

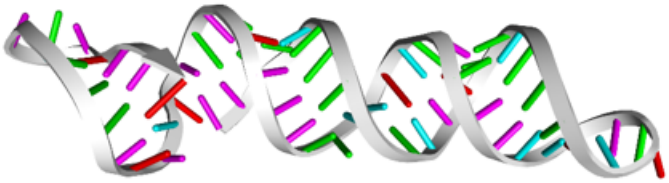

Minimized 3D DNA Three Dimensional Structure

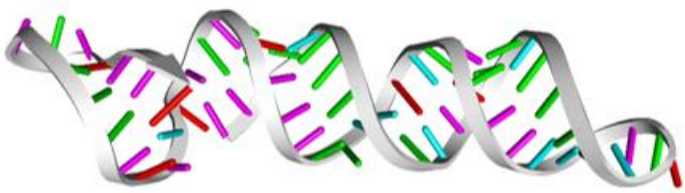

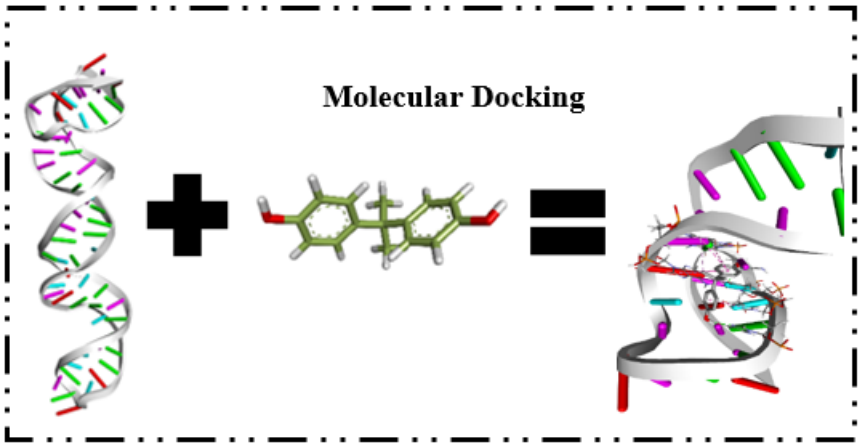
Molecular Docking

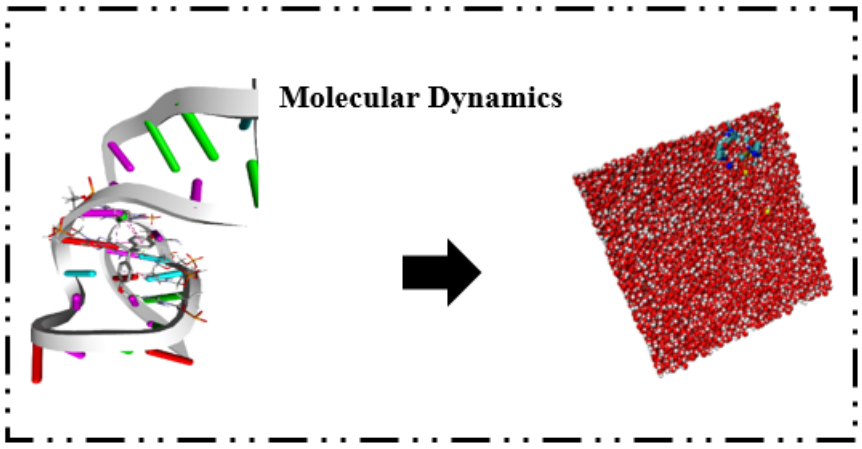
Molecular Dynamics

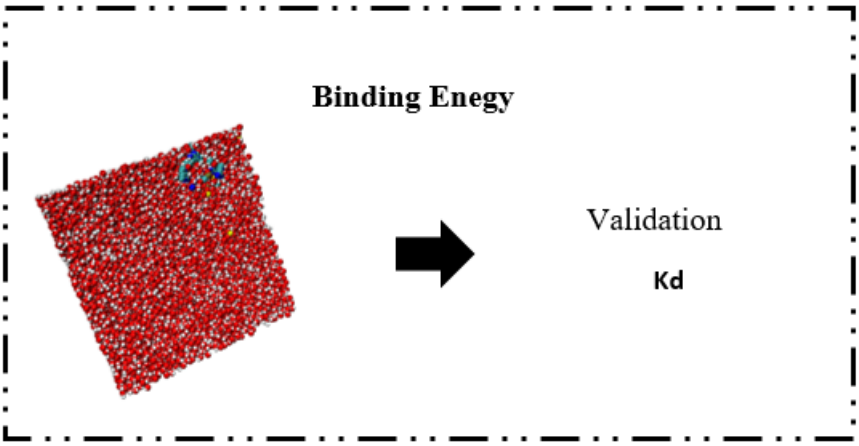

Figure 3.2. Conventional Workflow for In Silico Aptamer Creation.

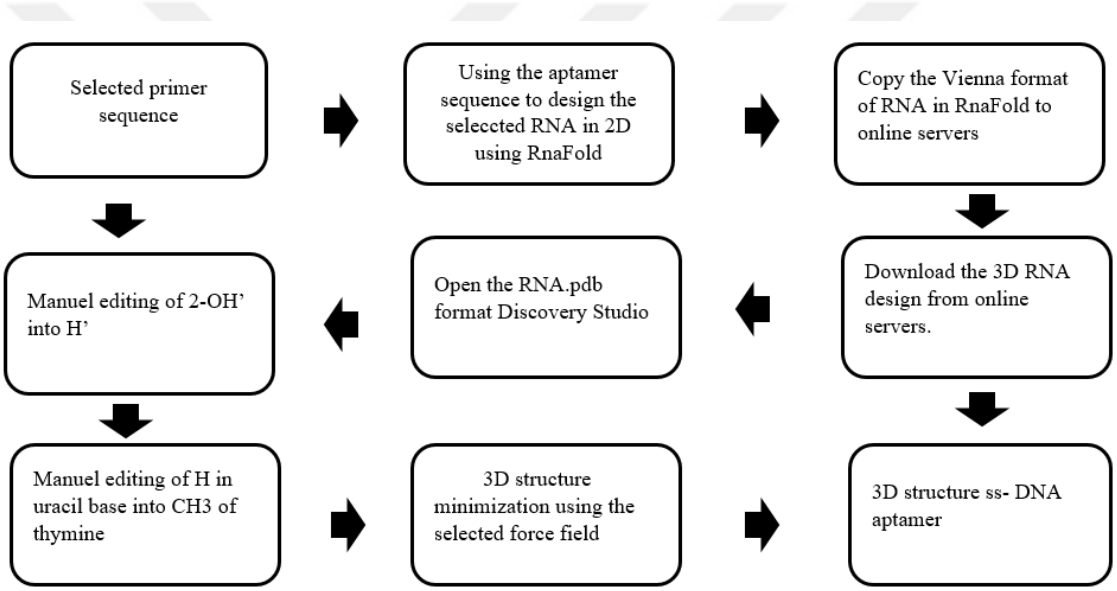

Figure 3.2.1. Methodology for modeling three-dimensional single-strand DNA aptamer structures from RNA structures.

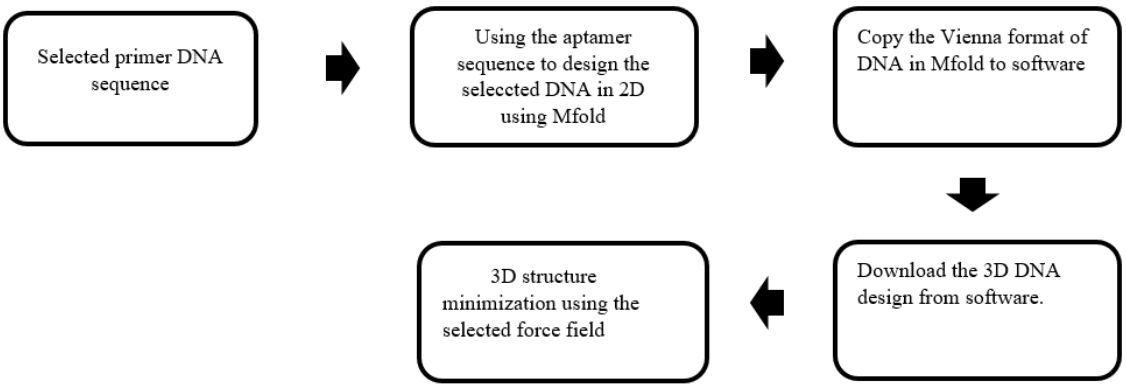

Figure 3.2.2. Process for directly modeling three-dimensional single-strand DNA

In recent times, there has been a development of computer-based techniques for the selection of aptamers via aptamer structure prediction. Additionally, there has been a study of convenient and precise methods for aptamer development. The diagram presented in Figure 3.2.1 depicts a standard process for the design of aptamers using computational methods. The process of generating 3D structures for ssDNA molecules from their nucleotide sequence involves seven primary steps, as illustrated in Figure 3.2.2.

Initially, the aptamer's secondary structure is forecasted utilizing its sequence, followed by the prediction of its tertiary structure, which is subsequently combined with the secondary structure. Following this, the process of molecular docking is executed in order to anticipate the configuration of both the aptamer and the desired substance. During this procedure, the cluster of candidates exhibiting the minimum energy is chosen.

Furthermore, molecular dynamics simulations have been conducted to evaluate the stability and attaching affinity of the aptamer-target substance complex. Following this, the assessment of the binding capacity among the aptamer and the object of interest is carried out and compared with experimental results.

3.2.1. Step 1: From The Sequence, Construct The SS-DNA Secondary Structure.

The sequences of the SS-DNA aptamers are shown in Table 1. The primer patterns targeting the BBA of SS-DNA, which are CCGGTGGGTCAGGTGGGATAGCGTTC CGCGTATGGCCCAGCGCATCACGGGTTCGCACCA, were selected from the literatür for this study, as will be described in the outcome section (113).

Aptamer	Length (nm)	Sequence (5'-3')	Number of bases
BBA	20.79	CCGGTGGGTCAGGTGGGATAGCGTTCCGCGTATGGCCCAG CGCATCACGGGTTCGCACCA	63
E_2BA	24.75	GCTTCCAGCTTATTGAATTACACGCAGAGGGTAGCGGCTCTGCGCATTCAAT TGCTGCGCGCTGAAGCGCGGAAGC	75
PBA	26.40	AGCAGCACAGAGGTCAGATGCACTCGGACCCCATTCTCCTTCCATCCCTCAT CCGTCCACCCTATGCGTGCTACCGTGAA	80

Table 3.2.1. The detailed information on the primary sequence of DNA aptamers

According to the understanding from the literature study, in order to detect and measure BPA levels in water samples utilizing the high-affinity aptamers designed, an aptamer-based bio chip testing was developed for detection BPA. Because it was believed that the aptamer-based detection technique would have a wide variety of applications in small molecule detection, the aptamer sequence that was generated against bisphenol A was selected from the literature.

The initial stage of our methodology involves the prognostication of secondary structures derived from dna and rna patterns. The primer patterns targeting the BBA of SS-DNA were selected for this study, as described in the results section.

The secondary structures of the SS-DNA and RNA molecules were forecasted through the utilization of free energy minimization techniques, utilization the mfold web server (http://mfold.rna.albany.edu/?=mfold) and RNAFold, respectively, after obtaining their nucleotide sequences (114-115).

The selection process for each aptamer involved identifying the structure with the highest thermodynamic stability, as determined by the lowest Gibbs free energy (ΔG) value. Subsequently, the equivalent Vienna output file, represented in dot-bracket notation and ct file format, was preserved.

3.2.2. Step 2: Build and Refine 3D SS-RNA Models.

The subsequent phase involves utilizing the anticipated secondary configurations as an initial reference to produce the three-dimensional structures of the corresponding single-stranded ribonucleic acid (ssRNA) and directly anticipated single-stranded deoxyribonucleic acid (ssDNA) through the utilization of online servers. The present investigation employed seven distinct online servers, namely RNAComposer, 3dRNA, Vfold3D, SimRNA, 3D-DART, iFoldRNAold, and Rosetta Farfar, for the purpose of predicting the tertiary structure of RNA aptamers (116-126). Therefore, in order to use each service, the nucleotide sequence obtained in Step 1 and its associated dot-bracket notation (Vienna file) were utilized as input.The results were written to pdb files.Five software programs, namely Avogadro, Discovery Studio Visualizer, Schrodinger, NF-ROOT, and X3DNA, have been utilized for the direct prediction of the three-dimensional configuration of DNA (116-117). In this software, only the primary sequence is used as input and saved as pdb since there is no need for secondary structures in the creation of three-dimensional structures of SS-DNA aptamers.

3.2.3. Step 3: Convert 3D SS-RNA Models into 3D SS-DNA Structures.

In the course of the subsequent phase of thr experiment, the SS-RNA 3D structures that were modeled were transferred to Discovery Studio Visualizer, where they underwent a conversion process to become SS-DNA 3D structures. The process involves the identification of individual uracil residues, followed by the substitution of the H5 particle in a methyl group, utilizing the Discovery Studio tools.

Additionally, the ribose sugar backbone is replaced with deoxyribose, through manual manipulation of the Discovery Studio tools. This is not required for the construction of three-dimensional SS-DNA models that are derived from the primer sequence.

3.2.4. Step 4: Minimized last SS-DNA 3D structures

The subsequent step in our methodology has been perform energy minimization for SS-DNA structures in which the secondary structure was generated from the primary sequence and the three-dimensional structure was generated from the secondary structure,

as well as for ss-dna three-dimensional structures generated from the primary sequences alone. The three-dimensional SS-DNA structures generated by energy minimization were refined in NAMD using the Charmm36 force field in order to eliminate geometrical inadequacies and improve structural parameters including bond length and rotations, linearly of specific sets, unbound connections, and constrained torsion rotations.

3.2.5. Step 5: Molecular Docking Between Aptamers and Their Targets

Upon determination of the tertiary structures of single-stranded DNA, the subsequent procedure involves subjecting said structures to molecular docking, as depicted in the fifth step. The utilization of molecular docking is a crucial approach in the forecasting of ideal locations for binding among substances and ligands. In the context of molecular docking, it is imperative to conduct a comprehensive search and assessment of all possible locations for binding between substances and ligands, with due consideration given to the corresponding scoring of these sites (121).

AutoDock consists of AutoDock4 and AutoDock Vina (51). AutoDock4 employs a free energy calculation method to evaluate the binding locations, while AutoDock Vina utilizes an empirical scoring function for the same purpose (122).

The experimental grading factor is a computational system developed from protein-ligand combination binding affinity data. During the training process, the connection energy is decomposed into distinct energy components, including hydrogen bonding, ionic connection, hydrophobic impact, and attaching entropy. The coefficients for each energy component are then determined and subsequently multiplied by their respective energy values. Upon completion of the modeling of DNA tertiary structures, the docking site of the aptamer-target complex can be identified. This docking site serves as the interface between the aptamer and the target.

Additionally, the utilization of molecular docking facilitates the assessment of the binding strength among the aptamer and the object through atomistic simulations (123).

The current investigation commenced by utilizing AutoGridFR to identify binding sites for all modeled aptamers. Subsequently, the SS-DNA aptamers, modeled through diverse tools, underwent docking via AutoDock Vina to obtain a more accurate determination of the bisphenol-A pose.

The SS-DNA aptamer and bisphenol-A were subjected to docking analysis, and the model with the minimal docking energy rating was determined as the optimal docking model.

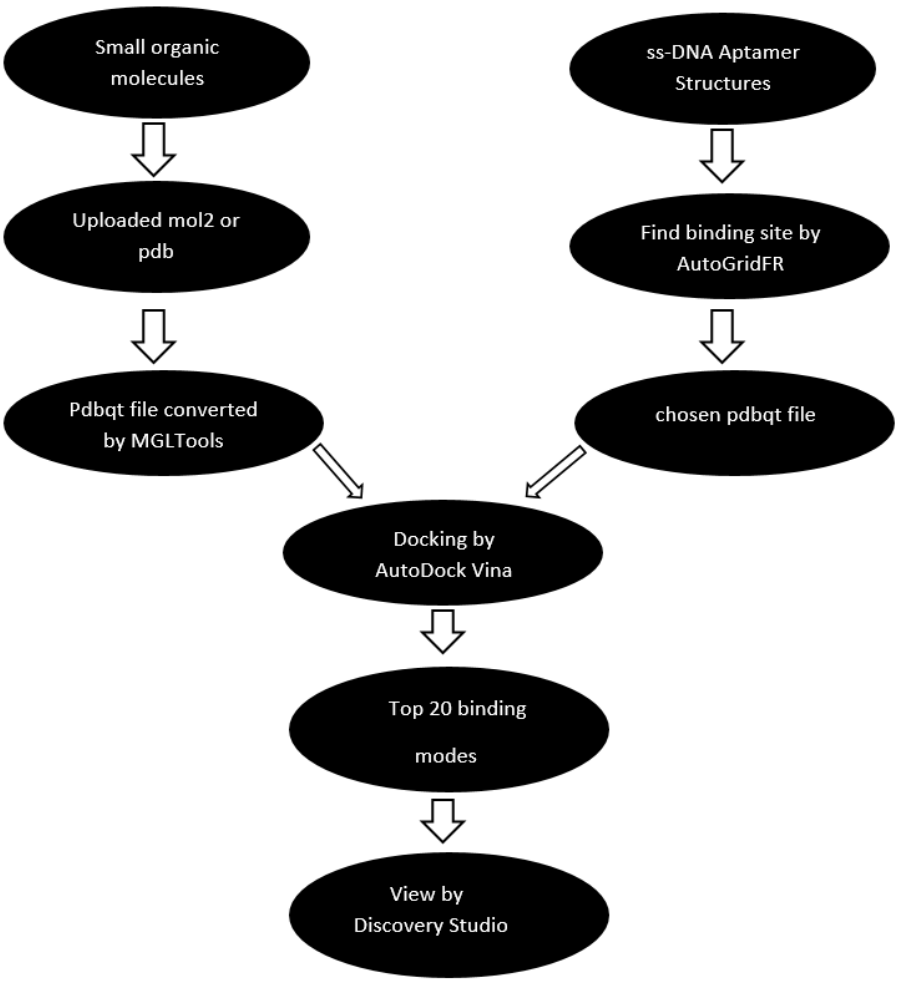

Figure 3.2.3. Molecular Docking Workflow

3.2.6. Step 6: Molecular Dynamic Simulation for Best-Docking Pose

Molecular dynamics (MD) simulation has emerged as a crucial stage in the computational exploration of drug discovery, serving as a pivotal factor in the decision-making process. The complex under investigation displays temporal variations, thereby enabling an assessment of its stability and potential for stability.

Molecular Dynamics (MD) simulation is a highly effective computational technique that enables the investigation of microscopic interactions to determine the macroscopic behavior of molecular systems.

Commonly, it is utilized to examine the dynamic interplay between the protein-ligand complex, which is a substantial system, and the influence of the aqueous environment on different protein-ligand indicates.

The approach utilized in this methodology is founded upon Newton's second law, also known as the formula of motion. Each atom in the system has a unique equation of motion, which is:

$$F_i = m_i a_i = -\nabla_i V$$

The equation mentioned above F_i as the scalar quantity of the force applied to the particle in a particular direction, mi as the mass of the particle, anda i as the velocity experienced by the object. The determination of Fi the evaluation of the adverse gradient of the particle's potential power (V) via computation.

The potential energy in question is characterized by force fields that are dependent on the atomic locations and directions. MD simulations rely on empirical potential connections present within a given system, which encompass both intramolecular and intermolecular terms, including non-bonded terms (125-126).

Currently, there exists a plethora of molecular dynamics simulation software programs. The present investigation utilized molecular dynamics (MD) simulations to scrutinize the dynamic interplay among the chosen ligand and the simulated SS-DNA aptamers. The simulations were conducted using GROMACS version 2020, NAMD, and Ambertools 23 (124-126).

The modelled Apo SS-Dna and SS-Dna aptamer-ligand complexes parametrized by using Charmm36,Charmm36m,BSC1 and OL15 force field for all atoms for 100 ns (127-129). For direct dna aptamer structures modeled from rna structures, the topology parameters for both the ligand and the SS-Dna aptamer were set up with Charmmgui and the all-atom force fields CHARMM36, Charmm36m, BSC1, and OL15 (130).

On the other hand, for directly modeled SS-DNA aptamers, topology parameters were written using Amber t-leap using OL15 and BSC1 all-atom force fields (131).

In addition, Gromacs was used to do MD simulations of RNA-based models of direct DNA aptamers, whereas NAMD was used to run MD simulations of SS-DNA aptamer models.

The three-point transferable intermolecular potential (TIP3P) water model was utilized for the water box, in order to incorporate explicit water in both modeled systems and The charge was modified through the introduction of Na+ or Cl- ions to replicate the conditions of physiological systems. The aforementioned systems underwent energy minimization through implementation of the steepest descent algorithm, utilizing a tolerance value of 1000 kJ/mol.nm.Directly modeled ss-DNA aptamers were equilibrated in two steps during NAMD simulations. The first step involved equilibrating water molecules while the second step involved constraining the DNA and ligand. In the second step, the whole system was equilibrated at three different temperatures: 200, 250, and 300 K, each for 5000 steps (i.e., 10 ps).

The NPT ensemble was utilized to conduct a production run lasting 100 nanoseconds. A shake algorithm was used to constrain hydrogen; therefore, the timestep was set to 2 fs. The 12-14 switching approach was applied to all vdw forces evaluations, with 14 serving as the cutoff. Long-range electrostatic interactions were computed using the particle mesh Ewald (PME) method, employing a maximum grid spacing of 1.5. Every time step involved PME calculations; no multi-step time stepping was used. The temperature was kept constant at 310 K. The barostat was programmed to aim for a 1 bar fluctuation in system size. There was a 2-fs time step for the integration. The appendices contain this parameter file. The DNA aptamer structures, which were modeled from RNA structures, were subjected to simulations using Gromacs. The balancing process involved 100 ps in NVT and 100 ps in NPT, after which production was carried out for 10 ns in NPT for every complex. The equilibration process involved coupling the systems with the Parrinello-Rahman barostat to regulate pressure at 1 atm, while temperature control was achieved through the use of a velocity rescaling thermostat set at 310 K.

With a Fourier grid spacing of 1.2, it was decided that the Particle Mesh Ewald (PME) would handle the extended range of Coulomb interactions. Van der Waals interactions at shorter ranges were determined using the Lennard-Jones potential with a 1.2 nm cutoff distance. Additionally, all bond lengths were constrained using the LINCS method, which is a linear constraint solver. Appendix 1 lists all of the input values that were considered.

3.2.7. Step 7: **Free energy of Binding Calculated with MM/PBSA**

The linking unrestricted energy of molecular systems plays a significant role in determining their association and reaction abilities. MMP/BSA tools, used to analyze snapshots of MD trajectories, were employed to compute the MM-PBSA binding free energy of ligand/aptamer interactions for all complexes in this work.

The current study employs the MM-PBSA method to assess the binding affinity of a complex consisting of an aptamer and ligand in order to gain a deeper comprehension of the fundamental binding system. In order to forecast the collective Gbind, an assessment was conducted on the van der Waals energy, electrostatic energy, polar solvation energy, and binding energy for each of the aptamer-ligand complexes. The aptamer-ligand binding free energy was computed using the following methodology:

Gbind = G complex - (G aptamer + Gligand) is used to determine the total binding energy of the aptamer-ligand complex, where G aptamer signifies the binding energy of the aptamer and G ligand denotes the binding energy of bisphenol-A, as investigated in this study. Estimated binding free energy and more details are presented in Appendices.

4. RESULTS

4.1. Geometry Optimization of the Endocrine-Disrupting Compounds (EDCs)

Molecular mechanics calculations in Gaussian were first performed with the ligands, which are endocrine-disrupting chemicals. Subsequently, the optimization and frequency calculations were executed utilizing the DFT B3LYP/6-31+G(d) methodology within the Gaussian 09 software package for molecular modeling Calculations were continued using these ligand structures after each optimized ligand was shown to correspond to a local minimum on the potential energy surface. As a result, the most stable ligands were found, and the optimization process was completed. Figures depicts the optimized structure of each ligand.

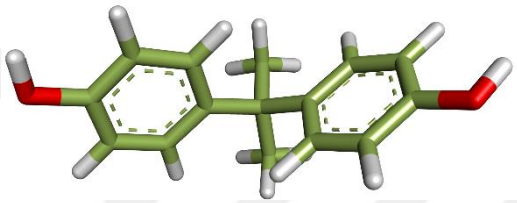

Figure 4.1a. Optimized Bisphenol A Structure

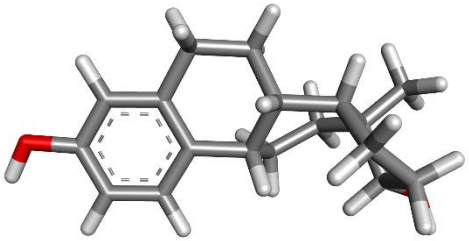

Figure 4.1.b. Optimized 17β-estradiol Structure

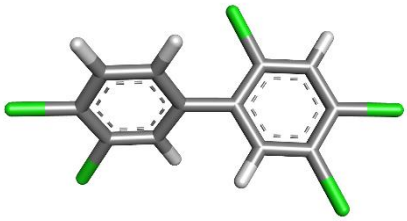

Figure 4.1.c. Optimized PCB 72 Structure

4.2. The Expectation of The Tertiary Configuration of Aptamers

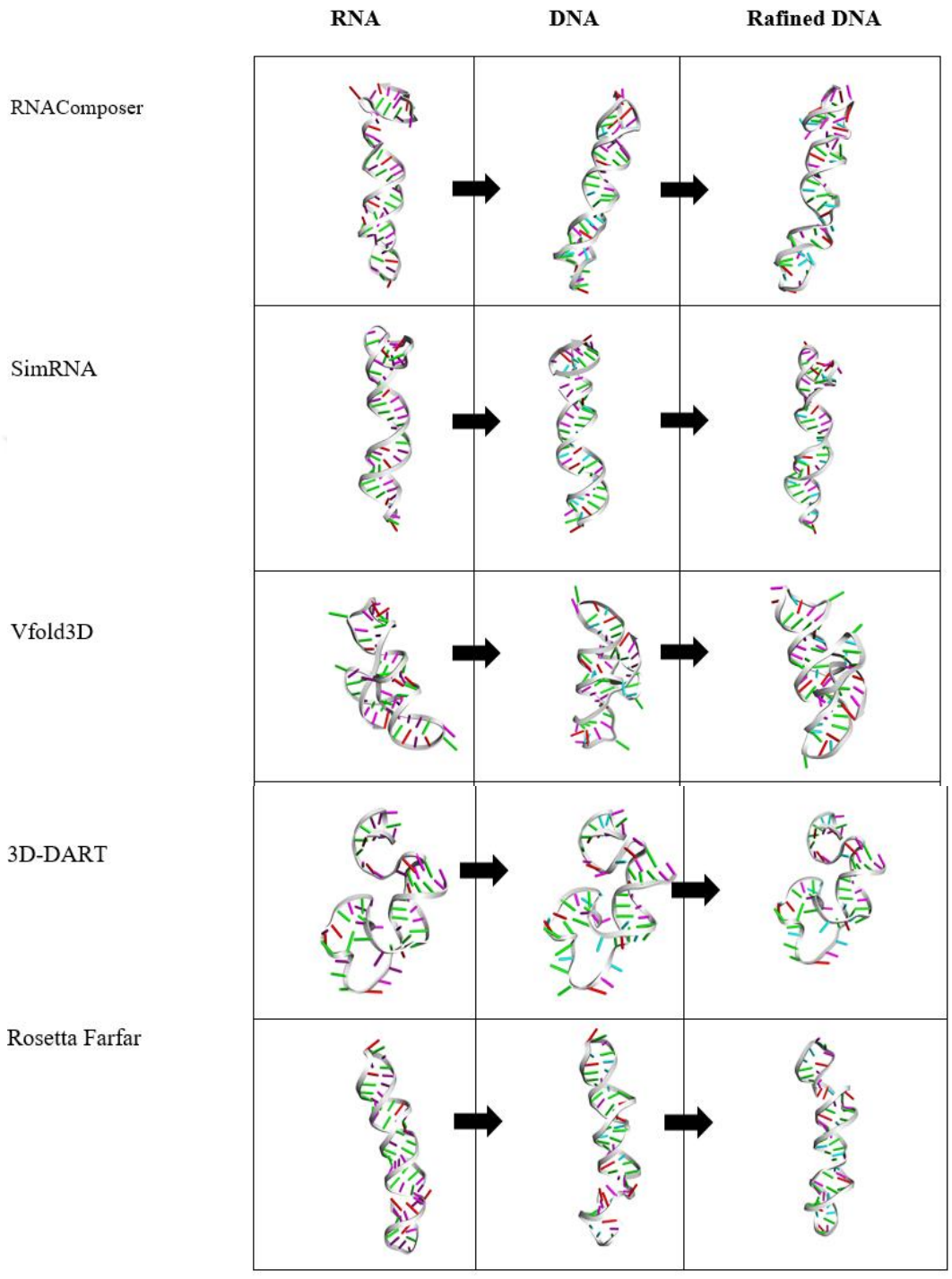

İfoldRna

3dRNA

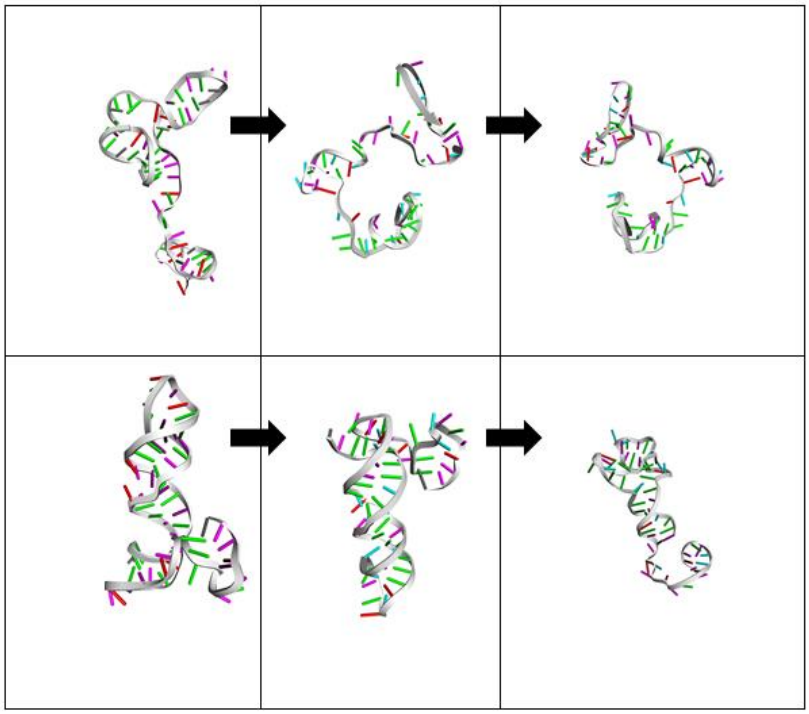

Table 4.2.a. The table displays the Rna structures modeled by each online server, the ss-Dna aptamers formed from the Rna structures, and the ss-Dna aptamer structures with energy minimization in three dimensions

	DNA	**Rafined DNA**
Avogadro	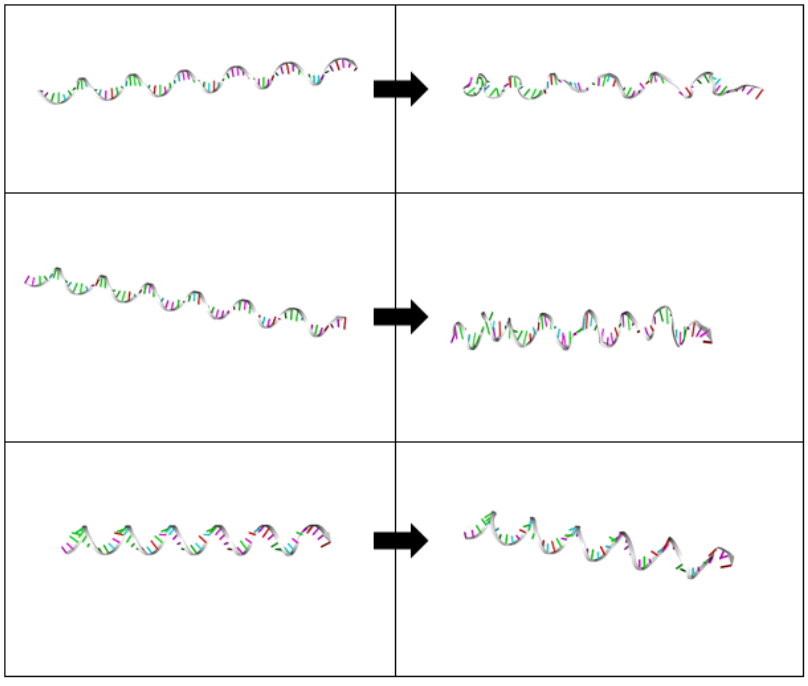	
Schrodinger		
Discovery Studio		

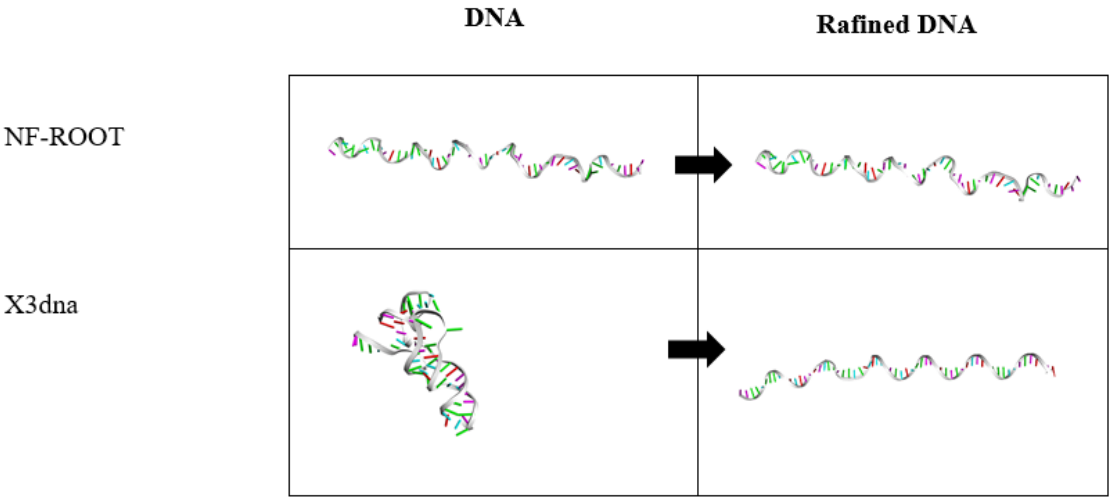

Table 4.2.b. The table displays the DNA structures modeled by each software as well as the three-dimensional energy-minimized ss-DNA aptamer structures.

4.3. Molecular Docking Results of The Modeled SS-DNA Aptamer from The SimRna Server Against Bisphenol A

The application of in silico docking involves the utilization of a biological information science methodology that systematically explores all conceivable binding sites between the aptamer and its target. Subsequently, a scoring function is employed to prioritize the compiled docking models. The target DNA sequence was bound with the ligand to determine the optimal docking position. Structure minimization of ss-DNA was performed using the CHARMM before the docking procedure. Subsequently, the Autodock Vina tool was utilized to perform the docking procedure, whereby the dimensions of the box were established as 94, 100, and 126 Angstroms along all three axes correspondingly. The number of independent runs was elevated to 80. Docking generated 20 best conformations with energy ranging from -6.9 to -5.9 kcal/mol. Two major clusters were observed in ligand binding, and a comparatively lower-energy conformation was chosen for MD simulations. Upon closer examination of Table 4.1, it can be observed that the ss-DNA/bisphenol-A complex exhibited the minimum estimated binding energy of -6.9 kcal/mol. The optimal conformation of bisphenol-A within the interface region was selected from the DLG file based on two criteria: the lowest binding energy and the smallest RMSD. Subsequently, the ss-DNA and ligand complex was subjected to analysis, wherein the various types of interactions were assessed and scrutinized using Discovery Studio. The details of hydrogen bonds are provided in Table

4.3.1. Figures 4.3.2 and 4.3.3 depict the hydrogen bond donor and acceptor regions and the charge distribution surrounding the binding site, respectively.

mode	affinity (kcal/mol)	dist from best mode rmsd 1.b. | rmsd u.b
1	-6.9	0.000 | 0.000
2	-6.9	0.154 | 5.551
3	-6.7	0.444 | 5.470
4	-6.6	3.759 | 7.754
5	-6.6	1.294 | 5.645
6	-6.6	1.283 | 2.053
7	-6.5	3.756 | 7.770
8	-6.4	4.306 | 6.653
9	-6.4	2.656 | 5.620
10	-6.4	2.681 | 4.214
11	-6.2	2.877 | 4.327
12	-6.1	3.147 | 7.274
13	-6.0	4.711 | 7.320
14	-6.0	30.199 | 32.735
15	-6.0	30.185 | 32.290
16	-6.0	19.268 | 21.529
17	-6.0	7.007 | 9.233
18	-6.0	2.987 | 4.648
19	-6.0	7.010 | 9.113
20	-5.9	19.227 | 21.807

Table 4.3.1. Molecular docking scores of ss-DNA, which are modeled from the SimRna server, against bisphenol-A

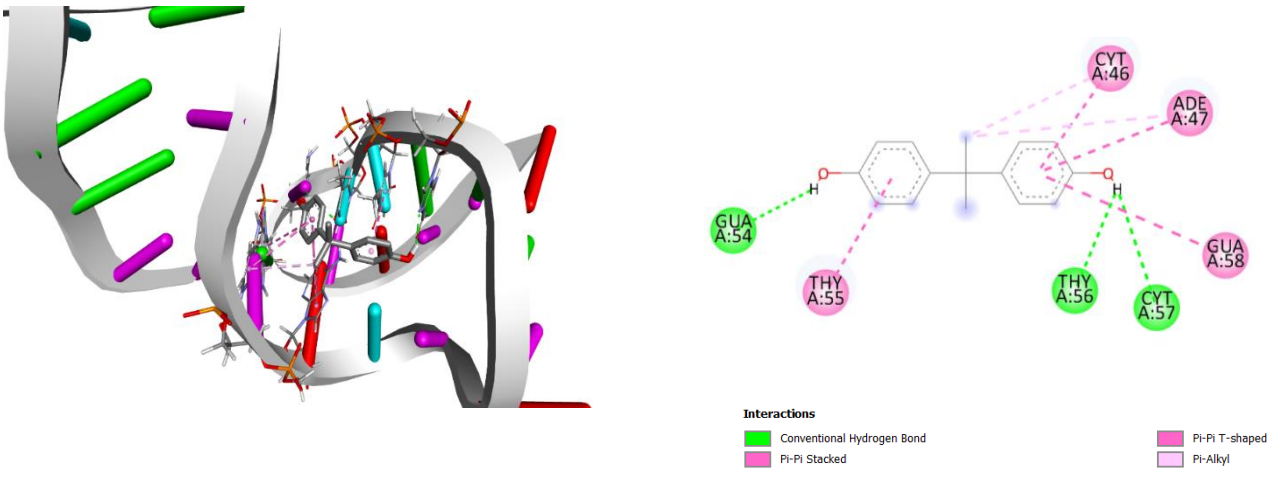

Figure 4.3.1. (a) Docked Pose of the Bisphenol-A with ss-DNA and (b) 2D representation of the interaction between them

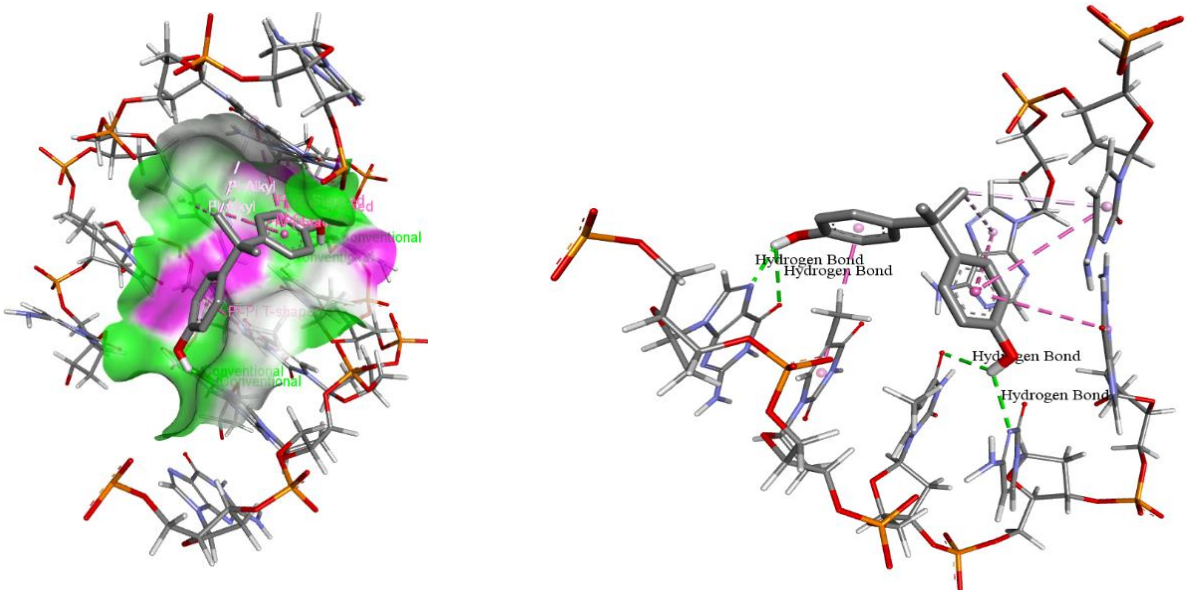

Figure 4.3.2. (a) donor and acceptor h-bond sites surrounding the ligand; (b) h-bond between bisphenol A and ss-DNA aptamer

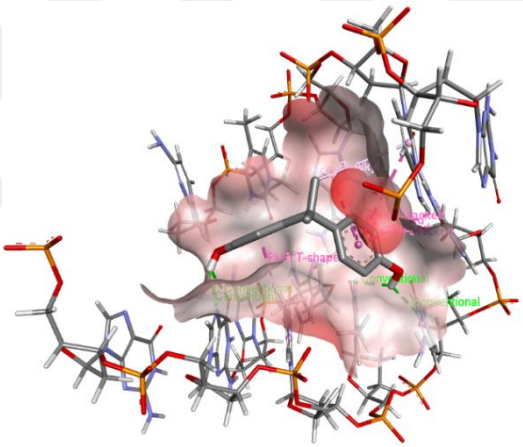

Figure 4.3.3. Distribution of charges at the interaction site

Name	Distance	Category	Types	From	Chemistry	To
A:B0:H-A:GUA54:06	3,00421	Hydrogen Bond	Conventional	A:B0:H	H-Donor	A:GUA54:06
A:B0:H-A:GUA54:N7	2,17454	Hydrogen Bond	Conventional	A:B0:H	H-Donor	A:GUA54:N7
A:B0:H-A:THY56:O4	2,44079	Hydrogen Bond	Conventional	A:B0:H	H-Donor	A:THY56:04
A:B0:H-A:CYT57:N3	2,69638	Hydrogen Bond	Conventional	A:B0:H	H-Donor	A:CYT57:N3

Table 4.3.2. Details of Hydrogen Bonds between DNA and Ligand.

4.4. Molecular Docking Results of The Modeled SS-DNA Aptamer from The Rosetta Farfar Server Against Bisphenol A

The optimal docking position of the target DNA sequence was determined through its binding with the ligand. Structure reduction of ss-DNA was accomplished using the CHARMM before the docking method. Subsequently, the Autodock Vina tool was utilized to perform the docking procedure, whereby the dimensions of the box were established as 94, 100, and 126 Angstroms along all three axes correspondingly. The number of independent runs was elevated to 80. Docking generated 20 optimal conformations with energy ranging from -6.5 to -6.2 kcal/mol. The docking results suggest a greater negative binding energy for ss DNA/bisphenol-A of -6.5 kcal/mol. The best conformation of bisphenol-A within the interface region was selected from the DLG file based on two criteria: the lowest binding energy and the shortest RMSD. Afterwards, the ss-DNA and ligand complex was subjected to analysis, wherein the various sorts of interactions were examined and analyzed utilizing Discovery Studio. The details of hydrogen bonds are provided in Table 4.4.1 Figures 4 and 5 depict the hydrogen bond donor and acceptor regions and the charge distribution surrounding the binding site.

mode	**affinity (kcal/mol)**	**dist from best mode** **rmsd 1.b. | rmsd u.b**
1	-6.5	0.000 | 0.000
2	-6.5	0.042 | 5.480
3	-6.4	0.070 | 5.618
4	-6.4	17.164 | 18.754
5	-6.3	14.165 | 16.126
6	-6.3	3.225 | 5.657
7	-6.3	9.942 | 12.717
8	-6.3	9.923 | 12.247
9	-6.3	20.689 | 22.018
10	-6.3	14.367 | 15.828
11	-6.3	1.389 | 2.043
12	-6.3	18.233 | 20.220
13	-6.3	18.237 | 19.458
14	-6.3	10.581 | 12.441
15	-6.3	10.593 | 12.511
16	-6.2	3.302 | 6.268
17	-6.2	17.435 | 19.042
18	-6.2	3.287 | 4.362
19	-6.2	17.098 | 18.747
20	-6.2	3.365 | 4.764

Table 4.4.1. Molecular docking scores of ss-DNA, which are modeled from the Rossie Farfar server, against bisphenol-A

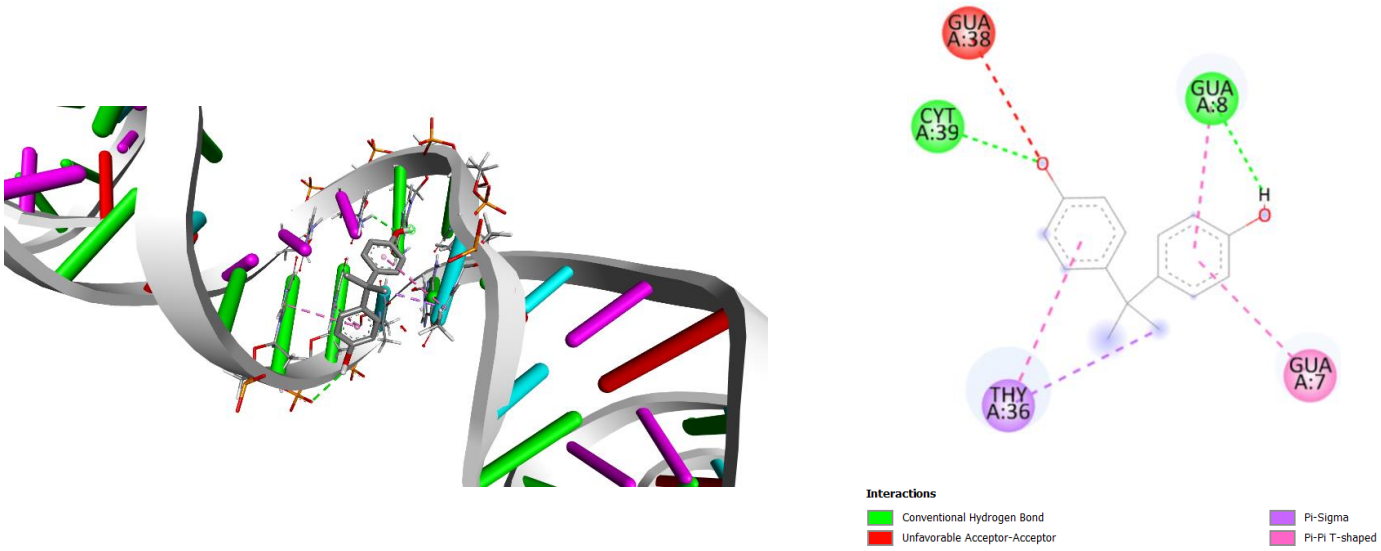

Figure 4.4.1 (a) Docked Pose of the Bisphenol-A with ss-DNA and (b) 2D representation of the interaction between them

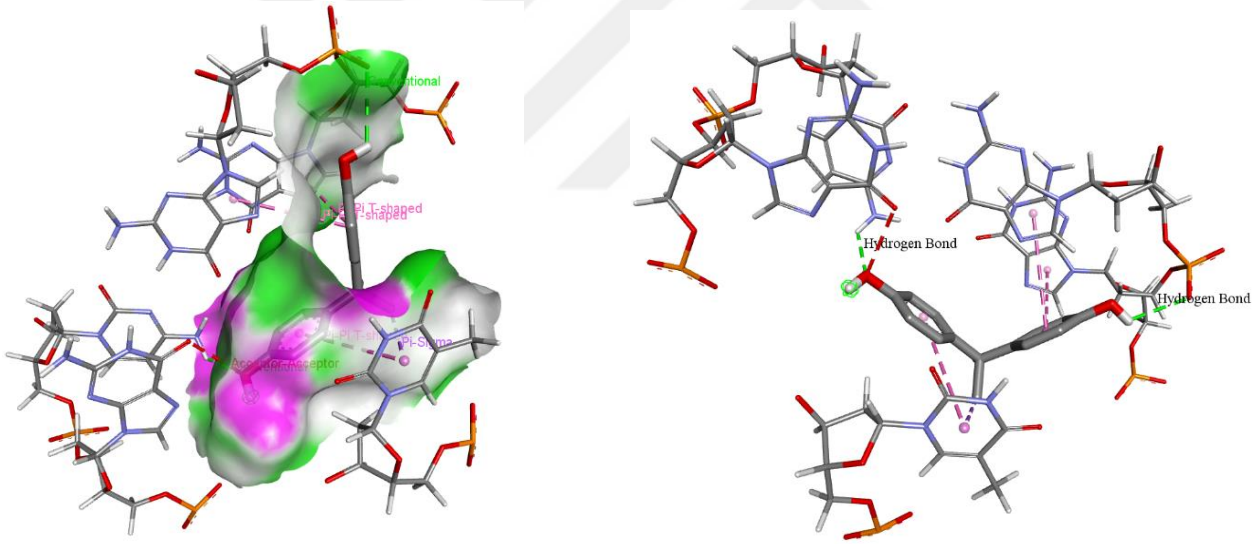

Figure 4.4.2 (a) donor and acceptor h-bond sites surrounding the ligand; (b) h-bond between bisphenol A and ss-DNA aptamer

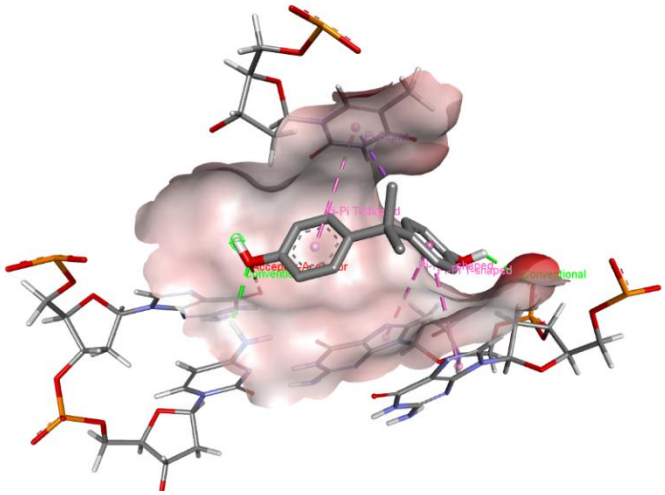

Figure 4.4.3. Distribution of charges at the interaction site

Name	Distance	Category	Types	From	Chemistry	To
A:CYT39:H42-:UNK:O	2,47415	Hydrogen Bond	Conventional	A:CYT39:H42	H-Donor	:UNK:O
:UNK:H-A:GUA8:O2P	2,99583	Hydrogen Bond	Conventional	:UNK0:H	H-Donor	A:GUA8:O2P

Table 4.4.2 Details of Hydrogen Bonds between DNA and Ligand.

4.5. Molecular Docking Results of The Modeled SS-DNA Aptamer from The Rna Composer Server Against Bisphenol A

The appropriate docking site of the target DNA sequence was discovered through its interaction with the ligand. Structure reduction of ss-DNA was performed using the CHARMM forcefield before the docking procedure. Subsequently, the Autodock Vina tool was utilized to perform the docking procedure, whereby the dimensions of the box were established as 94, 100, and 126 Angstroms along all three axes correspondingly. The number of independent runs was elevated to 80.

Docking generated 20 optimal conformations with energy ranging from -6.3 to -5.7 kcal/mol. The docking data show a larger negative binding energy for ssDNA/bisphenol-A of -6.3 kcal/mol. The optimal conformation of bisphenol-A within the interface region was picked from the DLG file based on two criteria: the lowest binding energy and the shortest RMSD. Afterward, the ss-DNA and ligand complex was exposed to investigation, wherein the various forms of interactions were studied and assessed utilizing Discovery Studio. The details of hydrogen bonds are provided in Table 4.5.1 Figures 4.5.2 and 4.5.3 depict the hydrogen bond donor and acceptor regions and the charge distribution surrounding the binding site.

mode	affinity (kcal/mol)	dist from best mode rmsd 1.b. | rmsd u.b
1	-6.3	0.000 | 0.000
2	-6.3	1.612 | 2.316
3	-6.2	1.531 | 5.899
4	-6.2	31.116 | 33.099
5	-6.2	1.221 | 5.657
6	-6.2	31.121 | 33.265
7	-6.1	14.189 | 16.140
8	-6.1	14.186 | 16.581
9	-6.1	2.779 | 4.518
10	-6.1	11.473 | 13.495
11	-6.1	18.255 | 20.001
12	-6.1	18.254 | 20.737
13	-6.0	11.526 | 13.662
14	-5.9	2.509 | 6.049
15	-5.9	4.551 | 7.051
16	-5.8	3.438 | 6.534
17	-5.8	4.803 | 8.462
18	-5.8	12.890 | 14.482
19	-5.8	12.945 | 14.311
20	-5.7	12.670 | 14.661

Table 4.5.1. Molecular docking scores of ss-DNA, which are modeled from the Rna Composer server, against bisphenol-A

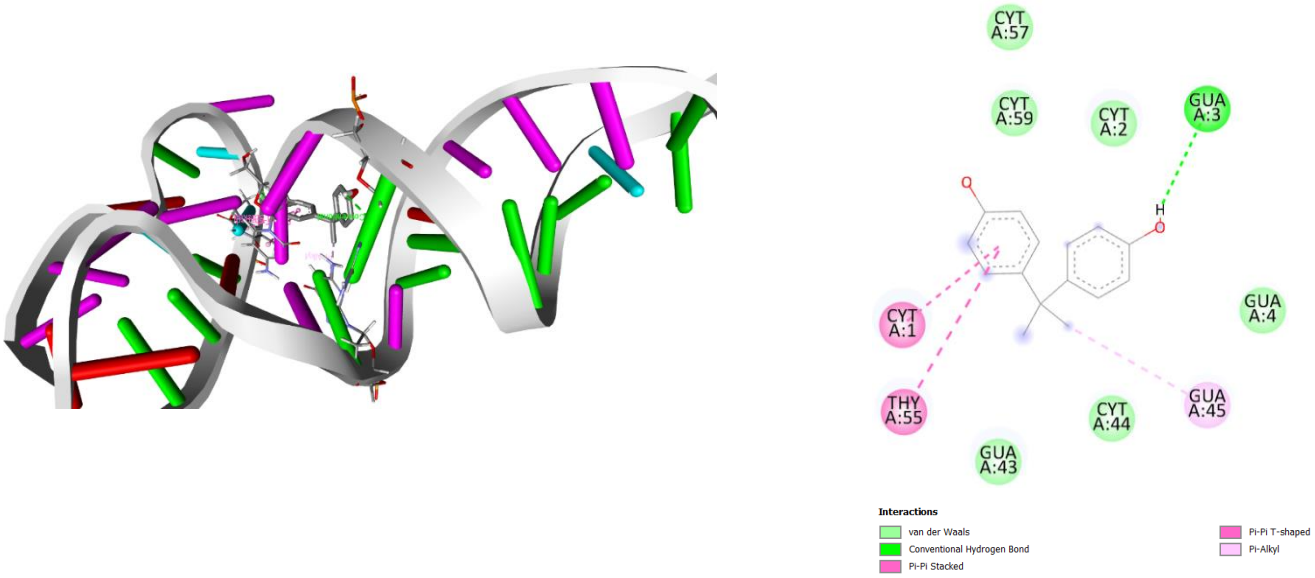

Figure 4.5.1. (a) Docked Pose of the Bisphenol-A with ss-DNA and (b) 2D representation of the interaction between them

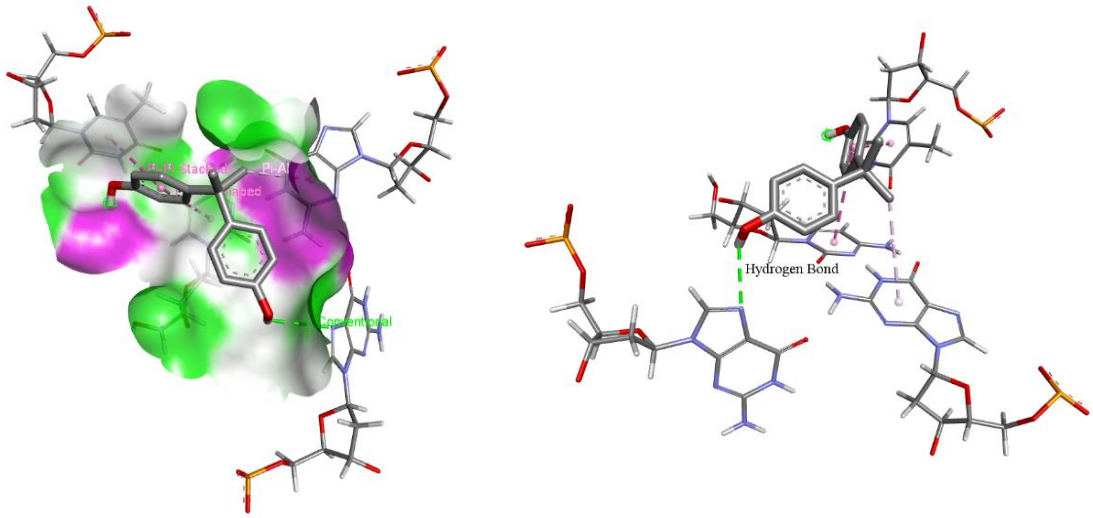

Figure 4.5.2 (a) donor and acceptor h-bond sites surrounding the ligand; (b) h-bond between bisphenol A and ss-DNA aptamer

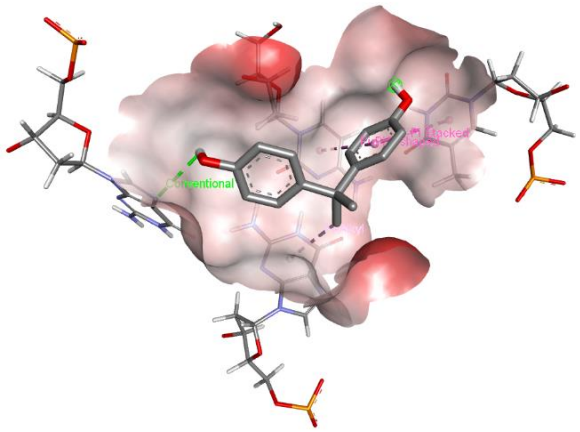

Figure 4.5.3. Distribution of charges at the interaction site

Name	Distance	Category	Types	From	Chemistry	To
A:B0:H-A:GUA3:N7	2,90499	Hydrogen Bond	Conventional	A:B0:H	H-Donor	A:GUA3:N7

Table 4.5.2. Details of Hydrogen Bonds between DNA and Ligand.

4.6. Molecular Docking Results of The Modeled SS-DNA Aptamer from The Vfold3D Server Against Bisphenol A

The proper docking site of the target DNA sequence was determined through its interaction with the ligand. Structure reduction of ss-DNA was conducted using the CHARMM before the docking method. Subsequently, the Autodock Vina tool was utilized to perform the docking procedure, whereby the dimensions of the box were established as 94, 100, and 126 Angstroms along all three axes correspondingly. The number of independent runs was elevated to 80. Docking generated 20 optimal conformations with energies ranging from -6.7 to -5.7 kcal/mol. The docking data show a larger negative binding energy for ssDNA/bisphenol-A of -6.7 kcal/mol. The best conformation of bisphenol-A within the interface region was determined from the DLG file based on two criteria: the lowest binding energy and the shortest RMSD. Following that, the ss-DNA and ligand complex was exposed to the inquiry, wherein the various types of interactions were explored and assessed utilizing Discovery Studio. The details of hydrogen bonds are provided in Table 4.6.1 Figures 4.6.2 and 4.6.3 depict the hydrogen bond donor and acceptor regions and the charge distribution surrounding the binding site

mode	**affinity (kcal/mol)**	**dist from best mode** **rmsd 1.b. | rmsd u.b**
1	-6.7	0.000 | 0.000
2	-6.7	0.053 | 5.732
3	-6.6	0.416 | 5.602
4	-6.4	1.684 | 5.565
5	-6.4	1.702 | 5.585
6	-6.3	1.684 | 2.409
7	-6.3	1.779 | 2.780
8	-6.2	16.649 | 19.783
9	-6.2	16.626 | 19.859
10	-6.2	13.850 | 15.402
11	-6.0	1.898 | 2.406
12	-5.9	21.611 | 24.607
13	-5.9	21.238 | 24.118
14	-5.9	2.873 | 6.128
15	-5.9	2.779 | 3.763
16	-5.8	24.866 | 26.250
17	-5.8	16.441 | 18.520
18	-5.7	24.826 | 26.679
19	-5.7	12.456 | 16.004
20	-5.7	25.517 | 27.212

Table 4.6.1. Molecular docking scores of ss-DNA, which are modeled from the Vfold3D server, against bisphenol-A

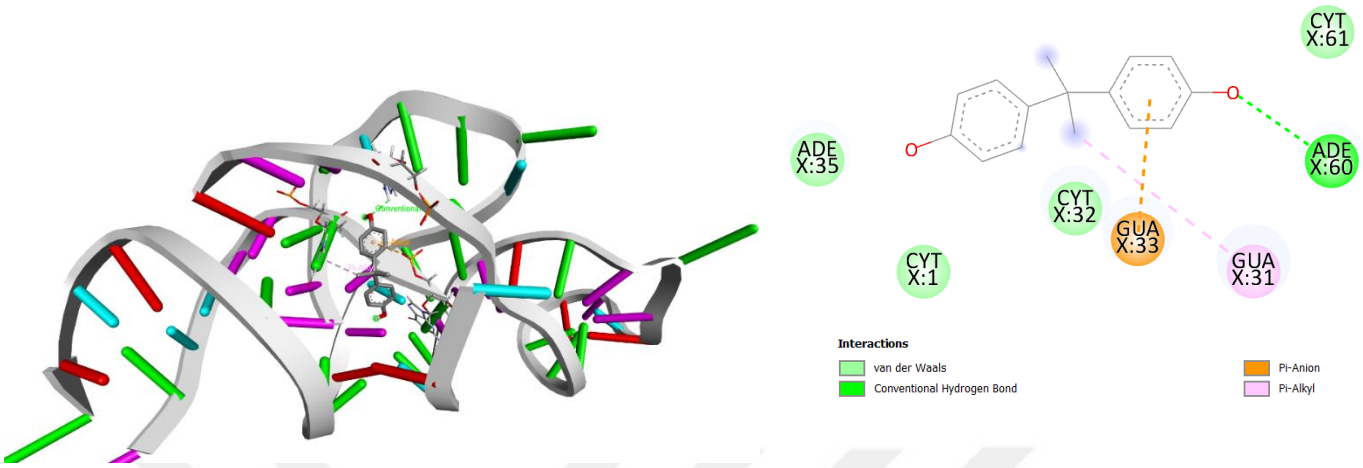

Figure 4.6.1 (a) Docked Pose of the Bisphenol-A with ss-DNA and (b) 2D representation of the interaction between them

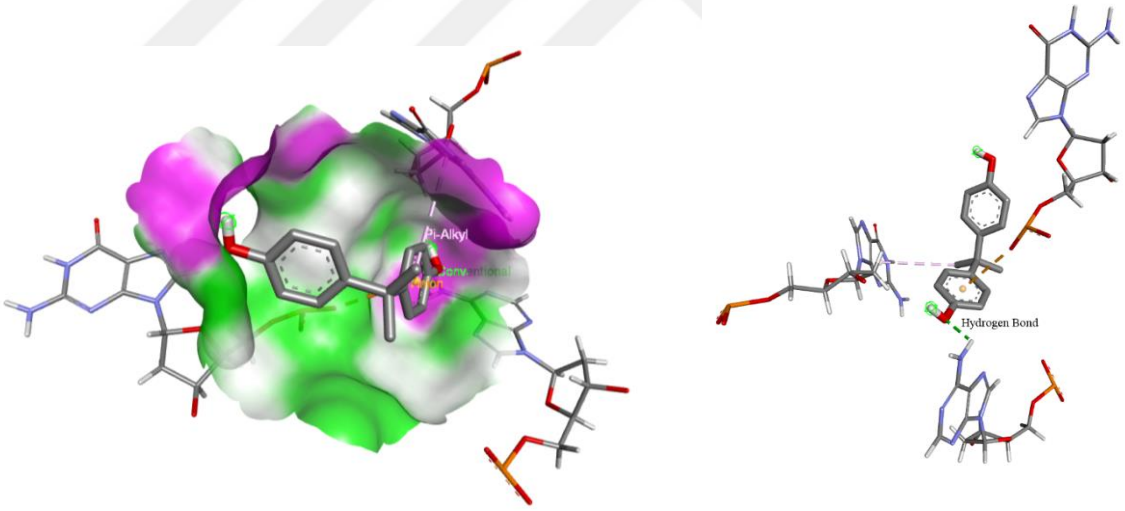

Figure 4.6.2. (a) donor and acceptor h-bond sites surrounding the ligand; (b) h-bond between bisphenol A and ss-DNA aptamer

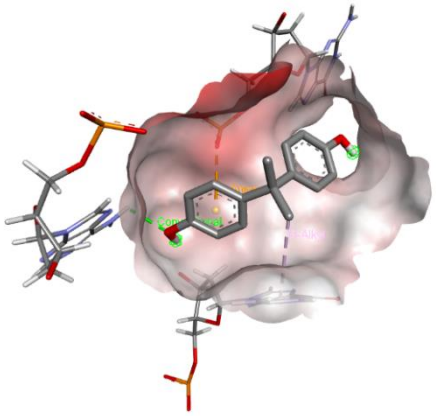

Figure 4.6.3. Distribution of charges at the interaction site

Name	Distance	Category	Types	From	Chemistry	To
X:ADE60:H62-A:B0:O	2,43333	Hydrogen Bond	Conventional	X:ADE 60:H62	H-Donor	A:B0:O

Table 4.6.2. Details of Hydrogen Bonds between DNA and Ligand.

4.7. Molecular Docking Results of The Modeled SS-DNA Aptamer from The 3dRNA Server Against Bisphenol A

The correct docking site of the target DNA sequence was established through its interaction with the ligand. Structure reduction of ss-DNA was accomplished using the CHARMM before the docking procedure. Subsequently, the Autodock Vina tool was utilized to perform the docking procedure, whereby the dimensions of the box were established as 94, 100, and 126 Angstroms along all three axes correspondingly. The number of independent runs was elevated to 80.

Docking generated 20 optimal conformations with energies ranging from -7.0 to -6.0 kcal/mol. The docking data show a larger negative binding energy for ssDNA/bisphenol-A of -7.0 kcal/mol. The best conformation of bisphenol-A within the interface region was determined from the DLG file based on two criteria: the lowest binding energy and the shortest RMSD. With that, the ss-DNA and ligand complex was exposed to the inquiry, wherein the many forms of interactions were investigated and assessed employing Discovery Studio. The details of hydrogen bonds are provided in Table 4.7.1. Figures 4.7.2 and 4.7.3 depict the hydrogen bond donor and acceptor regions and the charge distribution surrounding the binding site.

mode	affinity (kcal/mol)	dist from best mode rmsd 1.b. | rmsd u.b
1	-7.0	0.000 | 0.000
2	-6.9	0.079 | 5.593
3	-6.8	0.155 | 5.587
4	-6.8	0.523 | 33.099
5	-6.5	1.703 | 5.650
6	-6.5	1.664 | 2.689
7	-6.4	2.132 | 3.328
8	-6.4	2.112 | 5.628
9	-6.3	1.688 | 2.135
10	-6.3	1.669 | 5.874
11	-6.2	24.179 | 25.766
12	-6.2	2.555 | 5.963
13	-6.1	25.614 | 26.762
14	-6.1	25.809 | 27.300
15	-6.1	1.879 | 2.415
16	-6.1	1.991 | 5.925
17	-6.1	5.047 | 6.260
18	-6.1	5.489 | 8.578
19	-6.0	6.075 | 7.653
20	-6.0	6.115 | 9.281

Table 4.7.1. Molecular docking scores of ss-DNA, which are modeled from the 3dRNA server, against bisphenol-A

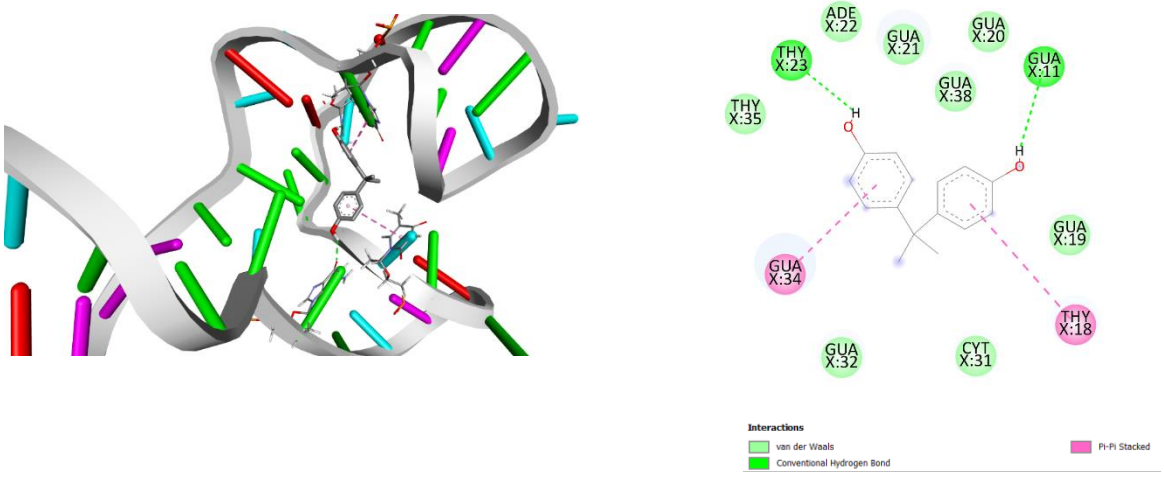

Figure 4.7.1. (a) Docked Pose of the Bisphenol-A with ss-DNA and (b) 2D representation of the interaction between them

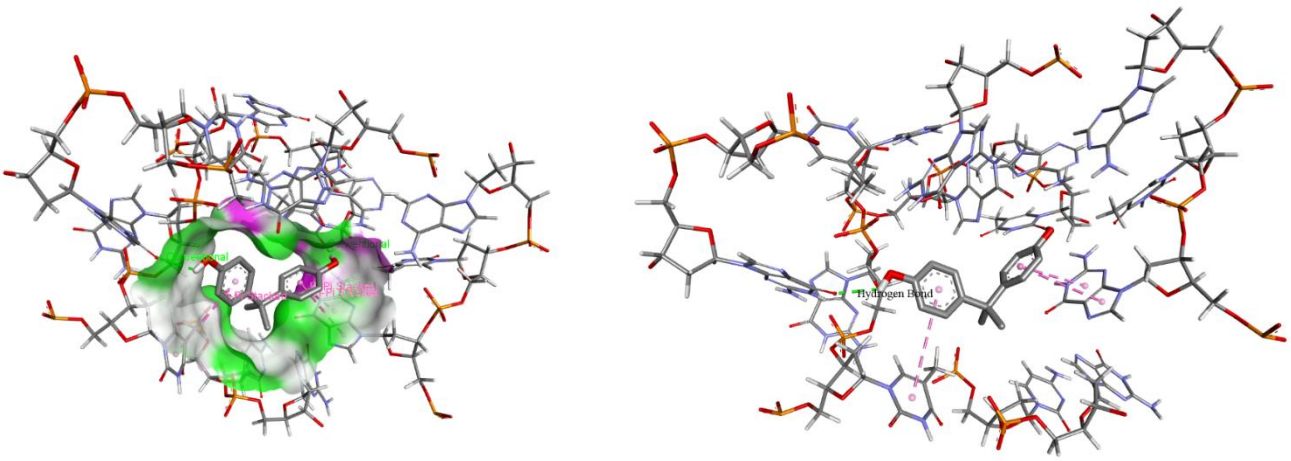

Figure 4.7.2. (a) donor and acceptor h-bond sites surrounding the ligand; (b) h-bond between bisphenol A and ss-DNA aptamer

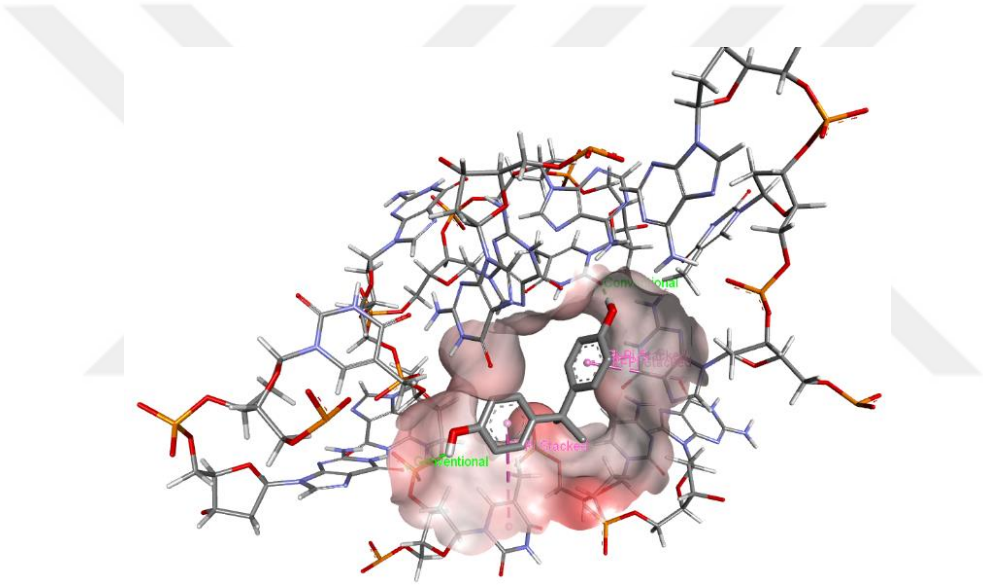

Figure 4.7.3. Distribution of charges at the interaction site

Name	Distance	Category	Types	From	Chemistry	To
X:B0:H-X:GUA11:O6	2,34901	Hydrogen Bond	Conventional	X:B0:H	H-Donor	X:GUA11:O6
X:B0:H-X:THY23:O2	2,0791	Hydrogen Bond	Conventional	X:B0:H	H-Donor	X:THY23:O2

Table 4.7.2. Details of Hydrogen Bonds between DNA and Ligand.

4.8. Molecular Docking Results of The Modeled SS-DNA Aptamer from The 3D-DART Server Against Bisphenol A

The target DNA sequence was coupled with the ligand to establish the best docking point. Structure reduction of ss-DNA was accomplished using the CHARMM forcefield before the docking method. Later, the docking was conducted using the Autodock Vina tool, where the box dimension was set to 120, 90, and 98 Angstroms for the x, y, and z axes, respectively. The exhaustiveness was increased to 80. Docking generated 20 best conformations with energy ranging from -6.0 to -5.4 kcal/mol. The docking results suggest a greater negative binding energy for ss DNA/bisphenol-A of -6.0 kcal/mol. The best conformation of bisphenol-A within the interface region was selected from the DLG file based on two criteria: the lowest binding energy and the shortest RMSD. Then the ss-DNA and ligand complex was exposed to analysis, wherein the various forms of interactions were evaluated and studied employing Discovery Studio. The details of hydrogen bonds are provided in Table 4.8.1. Figures 4.8.2 and 4.8.3 depict the hydrogen bond donor and acceptor regions and the charge distribution surrounding the binding site.

mode	**affinity (kcal/mol)**	**dist from best mode**	
		rmsd 1.b.	**rmsd u.b**
1	-6.0	0.000	0.000
2	-6.0	0.076	5.484
3	-5.9	14.952	18.521
4	-5.9	2.206	5.780
5	-5.9	1.764	2.549
6	-5.8	20.655	23.419
7	-5.8	20.645	24.042
8	-5.8	1.423	5.674
9	-5.7	1.395	2.054
10	-5.7	2.748	5.719
11	-5.7	16.241	18.166
12	-5.6	15.370	18.615
13	-5.6	3.746	6.813
14	-5.6	15.275	19.073
15	-5.6	2.576	3.936
16	-5.6	1.161	5.520
17	-5.5	14.638	18.367
18	-5.5	21.085	23.195
19	-5.5	21.051	23.650
20	-5.4	21.244	22.905

Table 4.8.1. Molecular docking scores of ss-DNA, which are modeled from the 3d-dart server, against bisphenol-A

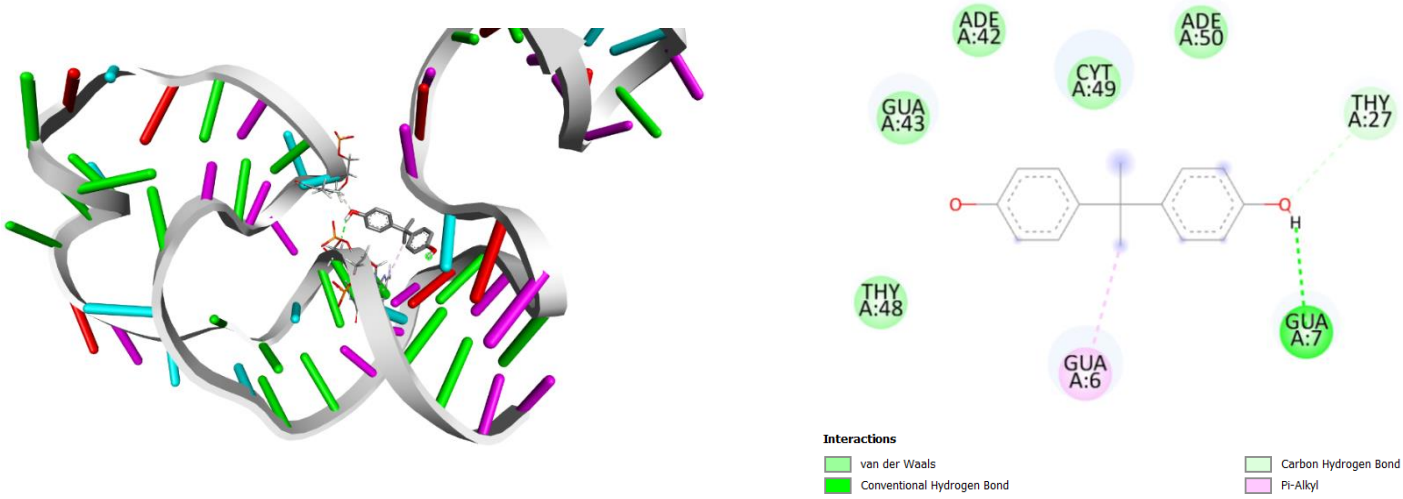

Figure 4.8.1. (a) Docked Pose of the Bisphenol-A with ss-DNA and (b) 2D representation of the interaction between them

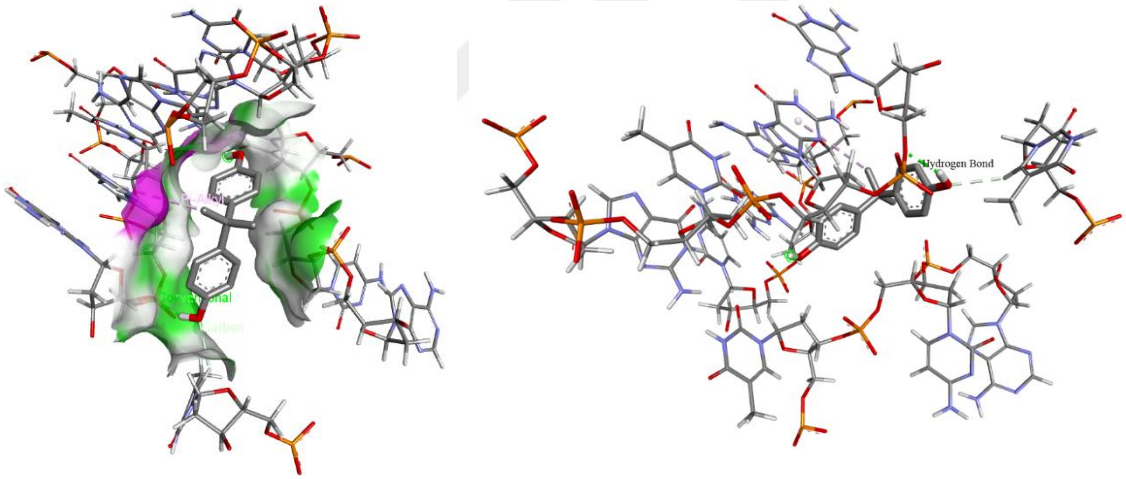

Figure 4.8.2. (a) donor and acceptor h-bond sites surrounding the ligand; (b) h-bond between bisphenol A and ss-DNA aptamer

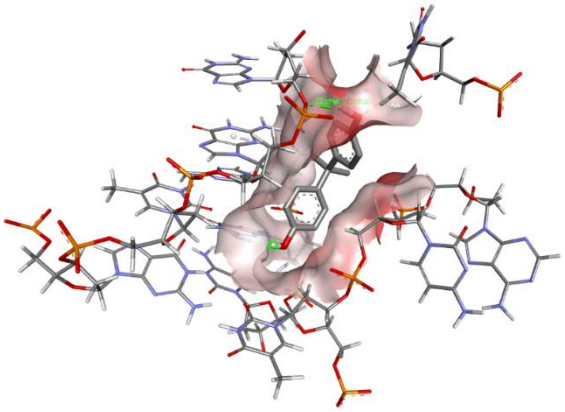

Figure 4.8.3. Distribution of charges at the interaction site.

Name	Distance	Category	Types	From	Chemistry	To
A:B0:H-A:GUA7:O5’	2,16832	Hydrogen Bond	Conventional	A:B0:H	H-Donor	A:GUA7:O5’
A:THY27:H6-A:B0:O	2,76065	Hydrogen Bond	Conventional	A:THY 27:H6	H-Donor	A:B0:O

Table 4.8.2. Details of Hydrogen Bonds between DNA and Ligand.

4.9. Molecular Docking Results of The Modeled SS-DNA Aptamer from The İFoldRna Server Against Bisphenol A

The target DNA sequence was coupled with the ligand to establish the best docking point. Structure reduction of ss-DNA was accomplished using the CHARMM before the docking method. Subsequently, the Autodock Vina tool was utilized to perform the docking procedure, whereby the dimensions of the box were established as 94, 100, and 126 Angstroms along all three axes correspondingly. The number of independent runs was elevated to 80. Docking generated 20 best conformations with energy ranging from -6.9 to -5.9 kcal/mol. The docking results suggest a greater negative binding energy for ss DNA/bisphenol-A of -6.9 kcal/mol. The best conformation of bisphenol-A within the interface region was selected from the DLG file based on two criteria: the lowest binding energy and the shortest RMSD. Then the ss-DNA and ligand complex was exposed to analysis, wherein the various forms of interactions were evaluated and studied employing Discovery Studio. The details of hydrogen bonds are provided in Table 4.9 Figures 4.9.3 and 4.9.4 depict the hydrogen bond donor and acceptor regions and the charge distribution surrounding the binding site.

mode	affinity (kcal/mol)	dist from best mode rmsd 1.b. | rmsd u.b
1	-6.9	0.000 | 0.000
2	-6.9	0.102 | 5.708
3	-6.5	2.392 | 3.693
4	-6.5	2.411 | 5.639
5	-6.4	3.297 | 5.985
6	-6.3	2.622 | 4.173
7	-6.3	3.284 | 5.424
8	-6.3	6.859 | 9.515
9	-6.2	3.116 | 6.531
10	-6.2	7.178 | 8.464
11	-6.2	3.051 | 4.464
12	-6.2	6.599 | 9.202
13	-6.2	3.056 | 4.466
14	-6.2	3.053 | 6.431
15	-6.1	3.004 | 4.350
16	-6.1	3.328 | 5.549
17	-6.1	6.235 | 8.058
18	-6.1	2.095 | 3.179
19	-6.0	6.408 | 8.885
20	-5.9	6.824 | 8.788

Table 4.9.1. Molecular docking scores of ss-DNA, which are modeled from the ifoldRna server, against bisphenol-A

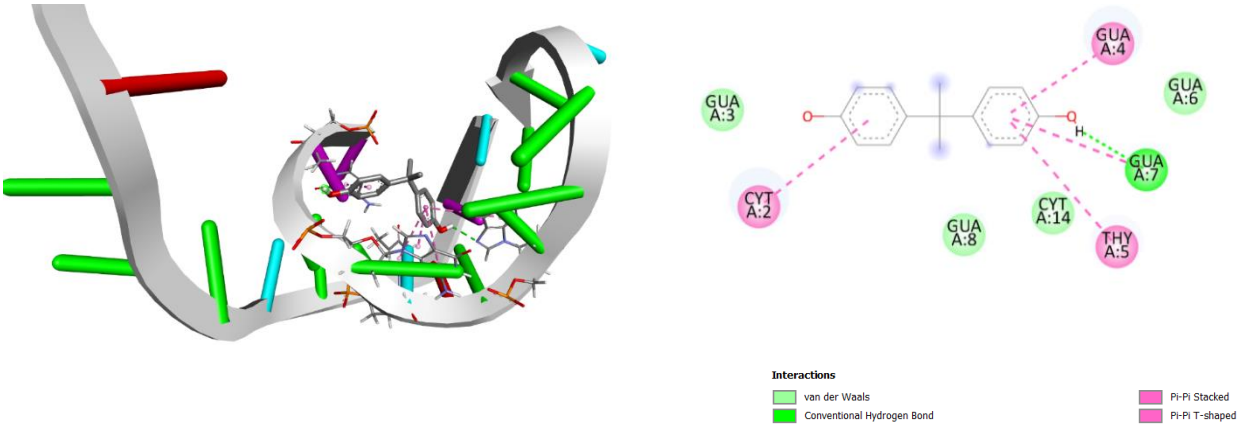

Figure 4.9.1. (a) Docked Pose of the Bisphenol-A with ss-DNA and (b) 2D representation of the interaction between them

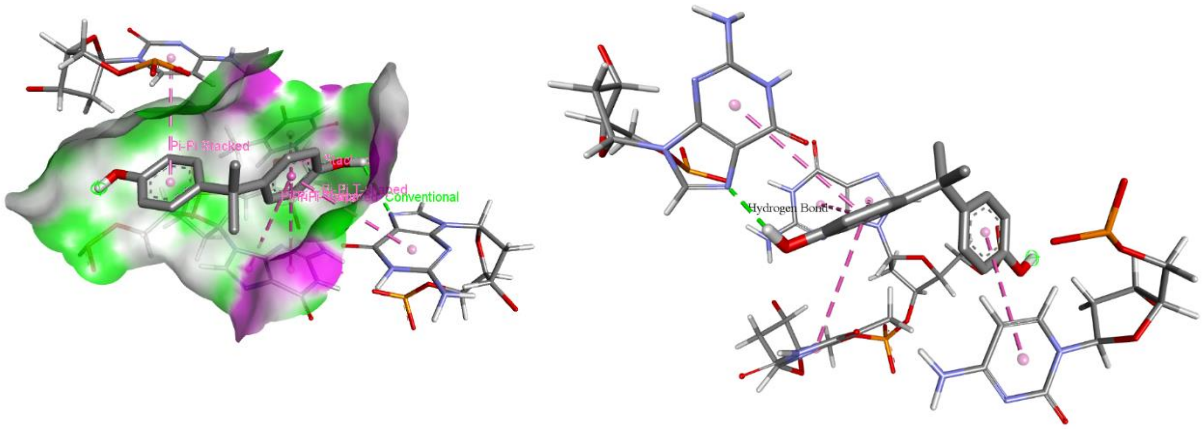

Figure 4.9.2. (a) donor and acceptor h-bond sites surrounding the ligand; (b) h-bond between bisphenol A and ss-DNA aptamer

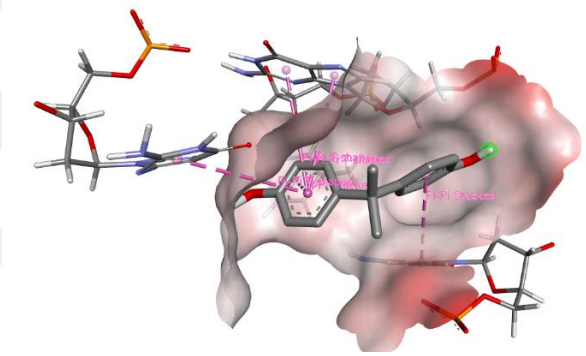

Figure 4.9.3. Distribution of charges at the interaction site

Name	Distance	Category	Types	From	Chemistry	To
A:B0:H-A:GUA7:N7	2,56651	Hydrogen Bond	Conventional	A:B0:H	H-Donor	A:GUA7:N7

Table 4.9.2. Details of Hydrogen Bonds between DNA and Ligand.

4.10. Molecular Docking Results of The Modeled SS-DNA Aptamer from The Schrodinger Software Against Bisphenol A

The appropriate docking site of the target DNA sequence was discovered through its interaction with the ligand.Structure reduction of SS-DNA was accomplished using the CHARMM before the docking method.

Subsequently, the Autodock Vina tool was utilized to perform the docking procedure, whereby the dimensions of the box were established as 94, 100, and 126 Angstroms along all three axes correspondingly. The number of independent runs was elevated to 80.Docking generated 20 optimal conformations with energies ranging from -5.7 to –4.8 kcal/mol. The docking data show a larger negative binding energy for ss DNA/bisphenol-A of -5.7 kcal/mol. The optimal conformation of bisphenol-A within the interface region was picked from the DLG file based on two criteria: the lowest binding energy and the shortest RMSD. Afterward, the ss-DNA and ligand complex was exposed to investigation, wherein the various forms of interactions were studied and assessed utilizing Discovery Studio. The details of hydrogen bonds are provided in Table 4.10.1. Figures 4.10.1 and 4.10.2 depict the hydrogen bond donor and acceptor regions and the charge distribution surrounding the binding site.

mode	**affinity (kcal/mol)**	**dist from best mode** **rmsd 1.b. | rmsd u.b**
1	-5.7	0.000 | 0.000
2	-5.7	0.085 | 5.576
3	-5.4	11.006 | 12.902
4	-5.4	10.798 | 12.401
5	-5.3	10.994 | 11.862
6	-5.3	10.800 | 13.379
7	-5.3	11.808 | 14.613
8	-5.3	11.818 | 13.884
9	-5.3	11.189 | 13.629
10	-5.1	1.440 | 5.475
11	-5.1	3.482 | 7.032
12	-5.1	5.561 | 8.920
13	-5.1	1.470 | 2.124
14	-5.0	11.213 | 13.187
15	-5.0	11.190 | 13.771
16	-5.0	3.731 | 6.621
17	-4.9	1.526 | 2.410
18	-4.9	1.479 | 5.472
19	-4.9	1.511 | 2.242
20	-4.8	11.207 | 13.340

Table 4.10.1. Molecular docking scores of SS-DNA, which are modeled from the Schrodinger server, against bisphenol-A

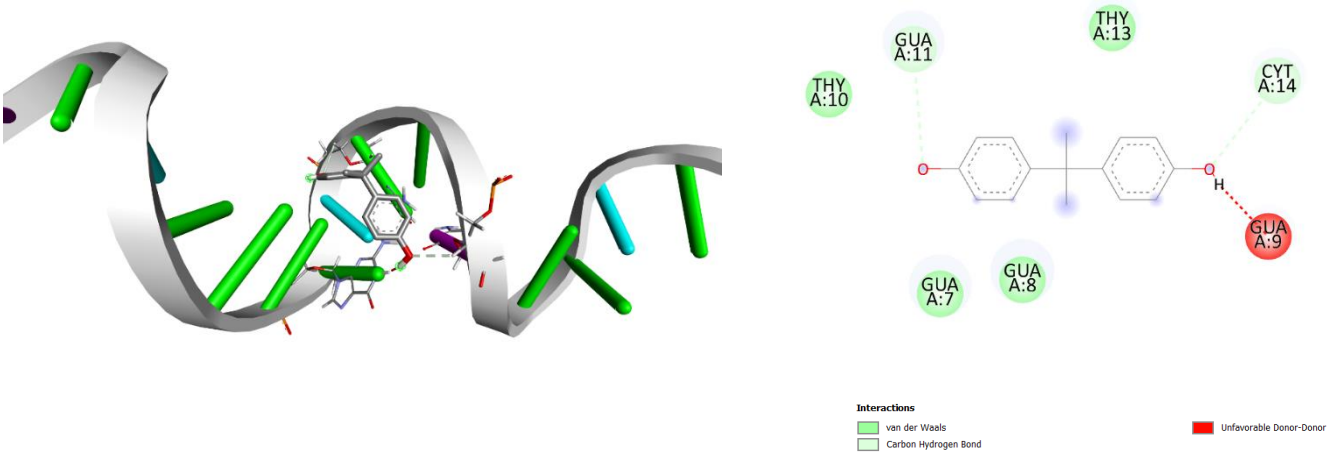

Figure 4.10.1. (a) Docked Pose of the Bisphenol-A with ss-DNA and (b) 2D representation of the interaction between them

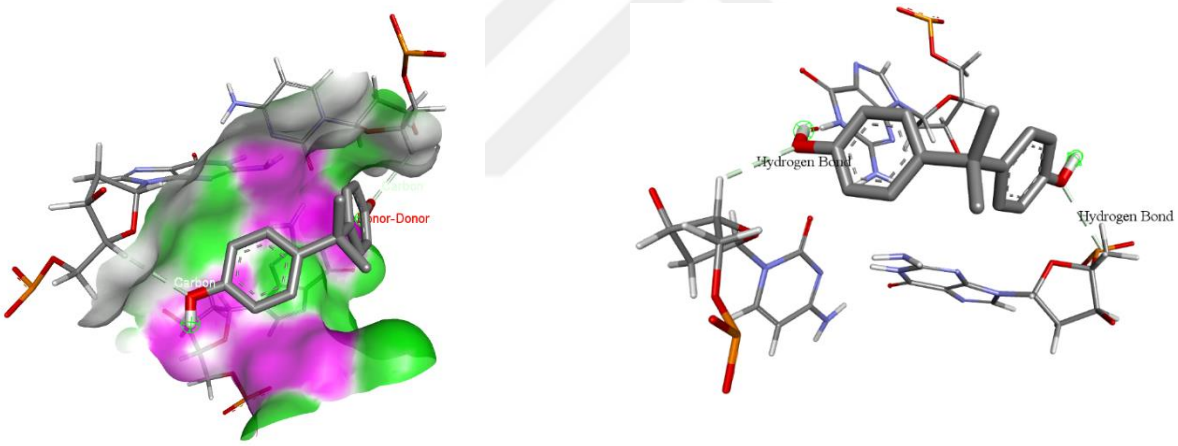

Figure 4.10.2. (a) donor and acceptor h-bond sites surrounding the ligand; (b) h-bond between bisphenol A and ss-DNA aptamer

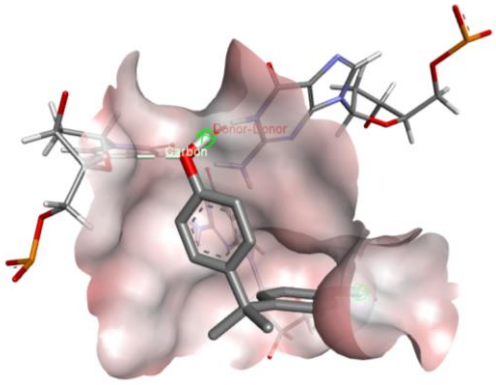

Figure 4.10.3. Distribution of charges at the interaction site.

Name	Distance	Category	Types	From	Chemistry	To
A:GUA11:H4'-A:B0:O	3,0222	Hydrogen Bond	Carbon Hydrogen Bond	A:GUA 11:H4'	H-Donor	A:B0: O
A:CYT14:H4'-A:B0:O	2,7953 7	Hydrogen Bond	Carbon Hydrogen Bond	A:CYT1 4:H4'	H-Donor	A:B0: O

Table 4.10.2. Details of Hydrogen Bonds between DNA and Ligand

4.11. Molecular Docking Results of The Modeled SS-DNA Aptamer from The Nflex-Root Software Against Bisphenol A

The proper docking site of the target DNA sequence was determined through its interaction with the ligand. Structure reduction of ss-DNA was performed using the CHARMM before the docking procedure. Subsequently, the Autodock Vina tool was utilized to perform the docking procedure, whereby the dimensions of the box were established as 94, 100, and 126 Angstroms along all three axes correspondingly. The number of independent runs was elevated to 80. Docking generated 20 optimal conformations with energies ranging from -4.7 to -4.3 kcal/mol. The docking data reveal a larger negative binding energy for ssDNA/bisphenol-A of -4.7 kcal/mol. The optimal conformation of bisphenol-A within the interface region was picked from the DLG file based on two criteria: the lowest binding energy and the shortest RMSD. Afterward, the ss-DNA and ligand complex was exposed to investigation, wherein the various forms of interactions were studied and assessed utilizing Discovery Studio. The details of hydrogen bonds are provided in Table 4.11. Figures 4.11.2 and 4.11.3 depict the hydrogen bond donor and acceptor regions and the charge distribution surrounding the binding site.

mode	affinity (kcal/mol)	dist from best mode rmsd 1.b. | rmsd u.b
1	-4.7	0.000 | 0.000
2	-4.6	0.256 | 5.491
3	-4.6	80.881 | 82.783
4	-4.6	0.189 | 5.618
5	-4.6	98.166 | 100.069
6	-4.6	80.927 | 82.790
7	-4.5	49.737 | 51.971
8	-4.5	46.795 | 48.932
9	-4.5	1.475 | 1.916
10	-4.5	49.679 | 51.686
11	-4.4	1.320 | 5.527
12	-4.4	86.443 | 88.315
13	-4.4	42.560 | 44.752
14	-4.4	65.971 | 68.158
15	-4.4	66.038 | 68.224
16	-4.3	15.250 | 16.639
17	-4.3	42.541 | 44.585
18	-4.3	3.551 | 6.084
19	-4.3	86.552 | 88.389
20	-4.3	64.916 | 67.064

Table 4.11.1. Molecular docking scores of ss-DNA, which are modeled from the Nflex-Root server, against bisphenol-A

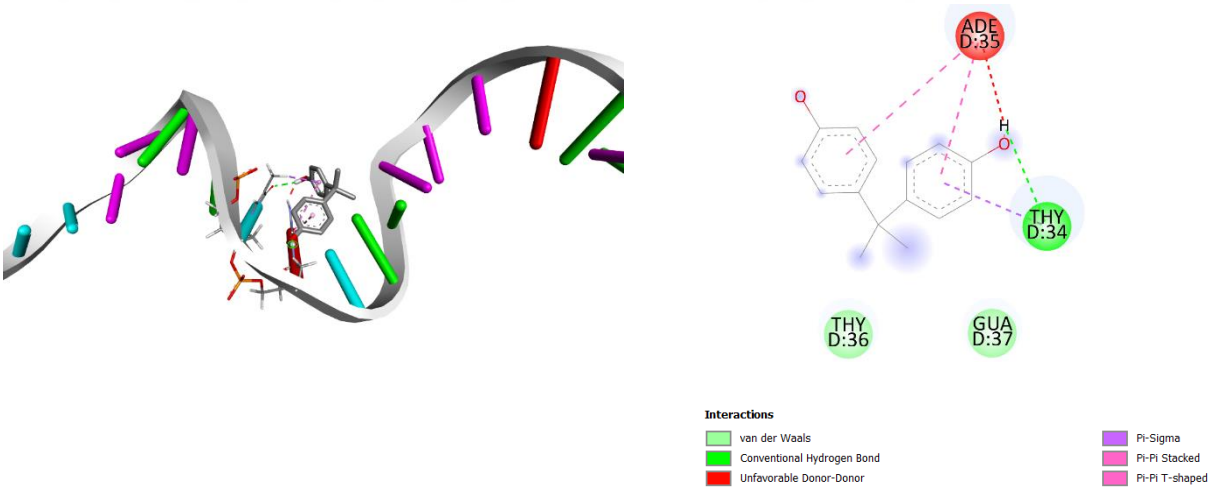

Figure 4.11.1. (a) Docked Pose of the Bisphenol-A with ss-DNA and (b) 2D representation of the interaction between them

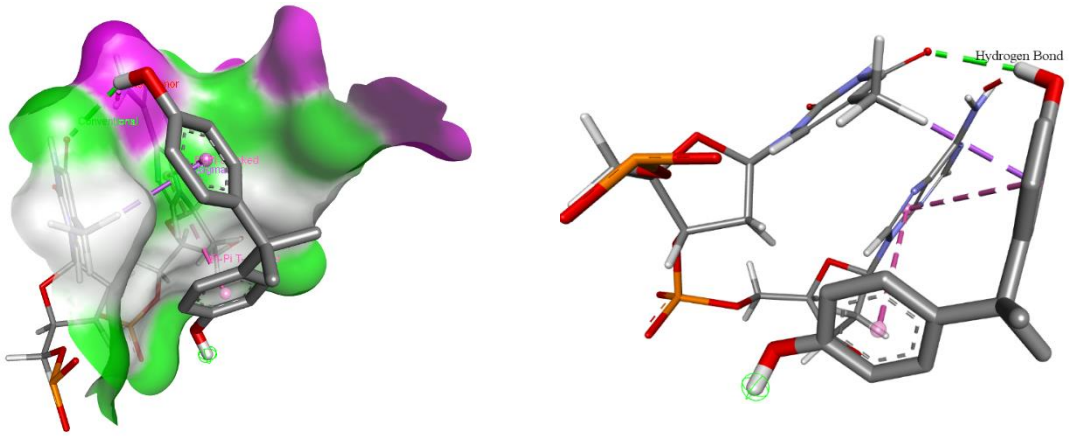

Figure 4.11.2. (a) donor and acceptor h-bond sites surrounding the ligand; (b) h-bond between bisphenol A and ss-DNA aptamer

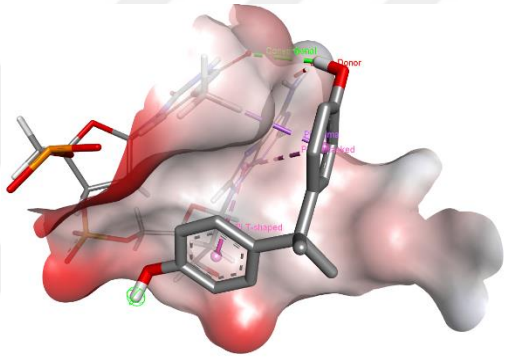

Figure 4.11.3. Distribution of charges at the interaction site

Name	Distance	Category	Types	From	Chemistry	To
D:B0:H-D:THY34:O4	2,3667	Hydrogen Bond	Conventional	D:B0:H	H-Donor	D:THY34:O4

Table 4.11.2. Details of Hydrogen Bonds between DNA and Ligand.

4.12. Molecular Docking Results of The Modeled SS-DNA Aptamer from The Avogadro Software Against Bisphenol A

The proper docking site of the target DNA sequence was determined through its interaction with the ligand. Structure reduction of ss-DNA was performed using the CHARMM before the docking procedure.

Subsequently, the Autodock Vina tool was utilized to perform the docking procedure, whereby the dimensions of the box were established as 94, 100, and 126 Angstroms along all three axes correspondingly. The number of independent runs was elevated to 80. Docking generated 20 optimal conformations with energies ranging from -5.6 to -4.7 kcal/mol. The docking data reveal a larger negative binding energy for ssDNA/bisphenol-A of -5.6 kcal/mol. The optimal conformation of bisphenol-A within the interface region was picked from the DLG file based on two criteria: the lowest binding energy and the shortest RMSD. Afterward, the ss-DNA and ligand complex was exposed to investigation, wherein the various forms of interactions were studied and assessed utilizing Discovery Studio. The details of hydrogen bonds are provided in Table 4.12.1 Figures 4.12.2 and 4.12.3 depict the hydrogen bond donor and acceptor regions and the charge distribution surrounding the binding site.

mode	**affinity (kcal/mol)**	**dist from best mode**	
		rmsd 1.b.	**rmsd u.b**
1	-5.6	0.000	0.000
2	-5.5	0.430	1.688
3	-5.5	0.473	5.491
4	-5.3	4.475	6.904
5	-5.3	4.482	8.166
6	-5.3	4.378	6.888
7	-5.2	5.835	8.831
8	-5.2	6.045	9.076
9	-5.2	6.040	8.589
10	-5.0	5.402	7.934
11	-5.0	2.528	4.021
12	-5.0	1.641	5.633
13	-5.0	1.422	2.391
14	-4.9	2.502	5.951
15	-4.9	1.753	2.430
16	-4.9	6.921	9.286
17	-4.9	3.099	5.421
18	-4.9	3.035	5.351
19	-4.8	2.767	6.235
20	-4.7	1.985	5.855

Table 4.12.1. Molecular docking scores of ss-DNA, which are modeled from the Avogadro server, against bisphenol-A

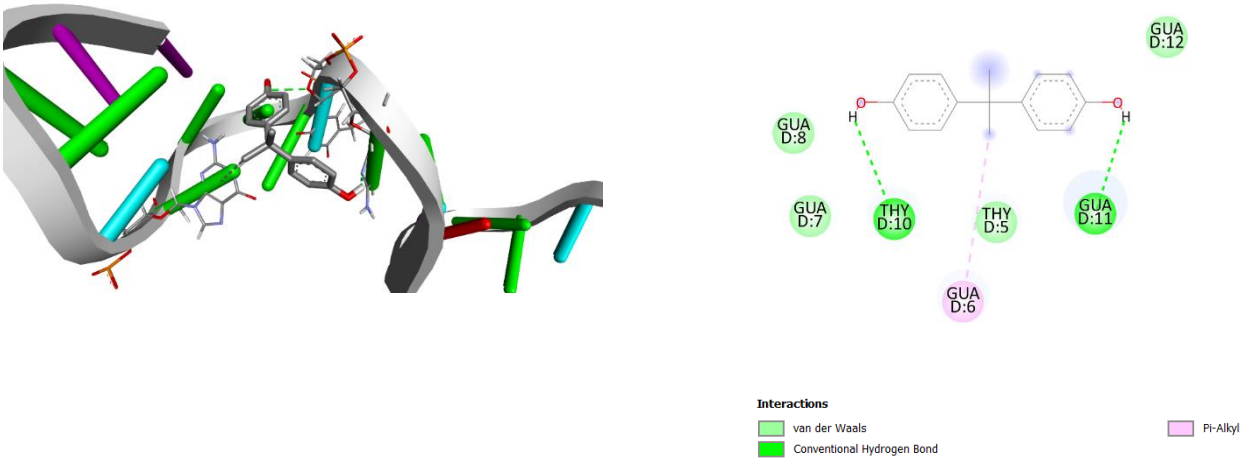

Figure 4.12.1. (a) Docked Pose of the Bisphenol-A with ss-DNA and (b) 2D representation of the interaction between them

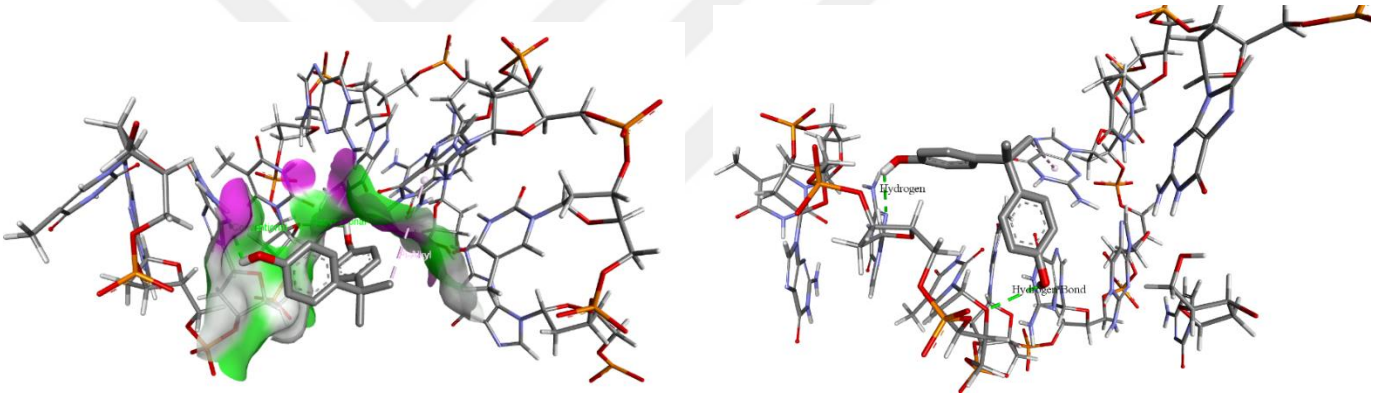

Figure 4.12.2. (a) donor and acceptor h-bond sites surrounding the ligand; (b) h-bond between bisphenol A and ss-DNA aptamer

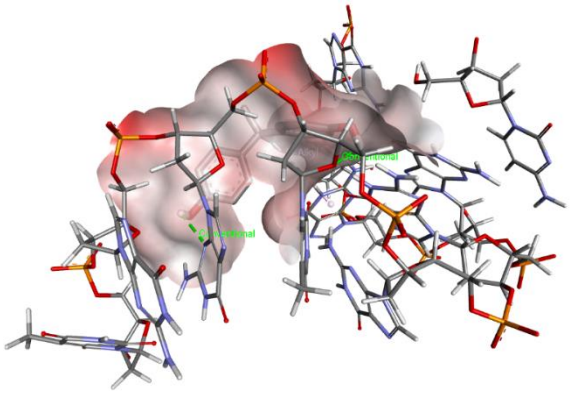

Figure 4.12.3. Distribution of charges at the interaction site

Name	Distance	Category	Types	From	Chemistry	To
D:B0:H-D:THY10:O4’	2,77023	Hydrogen Bond	Conventional	D:B0:H	H-Donor	D:THY10:O4’
D:B0:H-D:GUA11:N3	2,47408	Hydrogen Bond	Conventional	D:B0:H	H-Donor	D:GUA11:N3

Table 4.12.2. Details of Hydrogen Bonds between DNA and Ligand

4.13. Molecular Docking Results of The Modeled SS-DNA Aptamer from The Discovery Studio Visualizer Against Bisphenol A

The correct docking site of the target DNA sequence was established through its interaction with the ligand. Structure reduction of ss-DNA was conducted using the CHARMM before the docking method. Subsequently, the Autodock Vina tool was utilized to perform the docking procedure, whereby the dimensions of the box were established as 94, 100, and 126 Angstroms along all three axes correspondingly. The number of independent runs was elevated to 80. Docking generated 20 optimal conformations with energies ranging from -4.8 to -4.3 kcal/mol. The docking data reveal a larger negative binding energy for ssDNA/bisphenol-A of -4.8 kcal/mol. The optimal conformation of bisphenol-A within the interface region was picked from the DLG file based on two criteria: the lowest binding energy and the shortest RMSD. Afterward, the ss-DNA and ligand complex was exposed to the investigation, wherein the various forms of interactions were studied and assessed utilizing Discovery Studio.

The details of hydrogen bonds are provided in Table 4.13.1. Figures 4.13.2 and 4.13.3 depict the hydrogen bond donor and acceptor regions and the charge distribution surrounding the binding site.

mode	affinity (kcal/mol)	dist from best mode rmsd 1.b. | rmsd u.b
1	-4.8	0.000 | 0.000
2	-4.8	0.069 | 5.612
3	-4.7	31.316 | 32.858
4	-4.5	31.311 | 33.333
5	-4.5	43.558 | 45.393
6	-4.5	43.569 | 45.537
7	-4.5	43.146 | 45.182
8	-4.5	12.854 | 15.526
9	-4.5	43.114 | 45.300
10	-4.5	12.828 | 15.673
11	-4.4	41.970 | 44.637
12	-4.4	1.422 | 2.107
13	-4.4	29.154 | 31.029
14	-4.4	4.129 | 5.698
15	-4.4	42.202 | 45.161
16	-4.4	63.127 | 65.151
17	-4.4	1.454 | 5.525
18	-4.3	4.152 | 7.195
19	-4.3	45.520 | 47.029
20	-4.3	29.508 | 31.667

Table 4.13.1. Molecular docking scores of ss-DNA, which are modeled from the Disscovery studio server, software against bisphenol-A

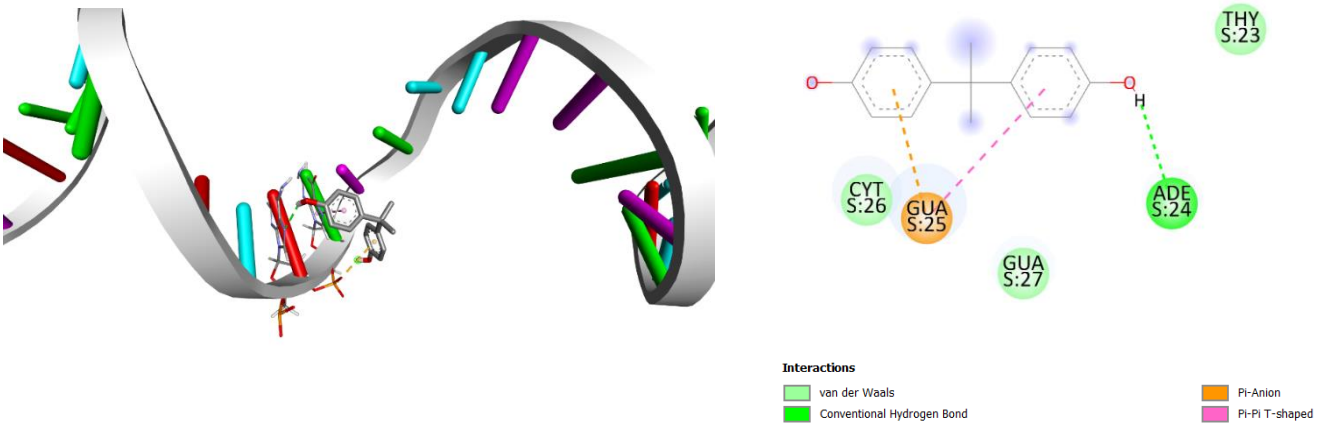

Figure 4.13.1. (a) Docked Pose of the Bisphenol-A with ss-DNA and (b) 2D representation of the interaction between them

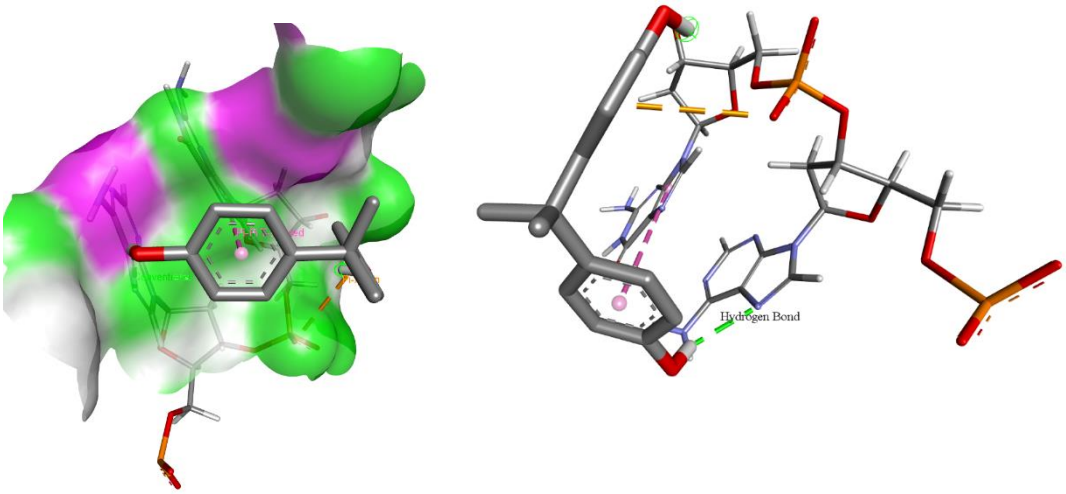

Figure 4.13.2. (a) donor and acceptor h-bond sites surrounding the ligand; (b) h-bond between bisphenol A and ss-DNA aptamer

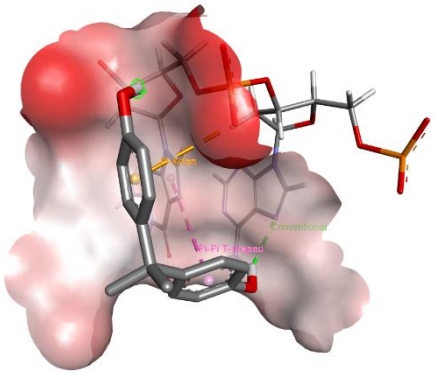

Figure 4.13.3. Distribution of charges at the interaction site

Name	Distance	Category	Types	From	Chemistry	To
S:B0:H-S:ADE24:N7	2,29307	Hydrogen Bond	Conventional	S:B0:H	H-Donor	S:ADE24:N7

Table 4.13.2. Details of Hydrogen Bonds between DNA and Ligand

4.14. Molecular Docking Results of The Modeled SS-DNA Aptamer from The X3DNA Software Against Bisphenol A

The precise docking site of the target DNA sequence was established through its interaction with the ligand.

Structure reduction of ss-DNA was conducted using the CHARMM before the docking procedure. Subsequently, the Autodock Vina tool was utilized to perform the docking procedure, whereby the dimensions of the box were established as 94, 100, and 126 Angstroms along all three axes correspondingly. The number of independent runs was elevated to 80. Docking generated 20 optimal conformations with energies ranging from -5.1 to -4.3 kcal/mol. The docking data reveal a larger negative binding energy for ssDNA/bisphenol-A of -5.1 kcal/mol. The optimal conformation of bisphenol-A within the interface region was selected from the DLG file based on two criteria: the lowest binding energy and the shortest RMSD. Afterward, the ss-DNA and ligand complex was exposed to the inquiry, wherein the various forms of interactions were studied and assessed utilizing Discovery Studio. The details of hydrogen bonds are provided in Table 4.14.1 Figures 4.14.2 and 4.14.3 depict the hydrogen bond donor and acceptor regions and the charge distribution surrounding the binding site.

mode	**affinity (kcal/mol)**	**dist from best mode** **rmsd 1.b. | rmsd u.b**
1	-5.1	0.000 | 0.000
2	-5.1	0.157 | 5.526
3	-4.9	0.681 | 1.776
4	-4.8	1.100 | 5.528
5	-4.8	2.501 | 5.614
6	-4.8	2.467 | 3.858
7	-4.7	1.833 | 5.298
8	-4.7	2.423 | 3.551
9	-4.7	21.194 | 23.721
10	-4.6	2.068 | 2.845
11	-4.5	21.307 | 22.644
12	-4.5	21.356 | 22.772
13	-4.5	2.474 | 5.206
14	-4.5	5.204 | 8.764
15	-4.4	2.419 | 3.190
16	-4.4	11.671 | 13.436
17	-4.4	11.644 | 13.805
18	-4.4	11.580 | 13.353
19	-4.3	11.036 | 13.411
20	-4.3	11.500 | 13.162

Table 4.14.1. Details of Hydrogen Bonds between DNA and Ligand

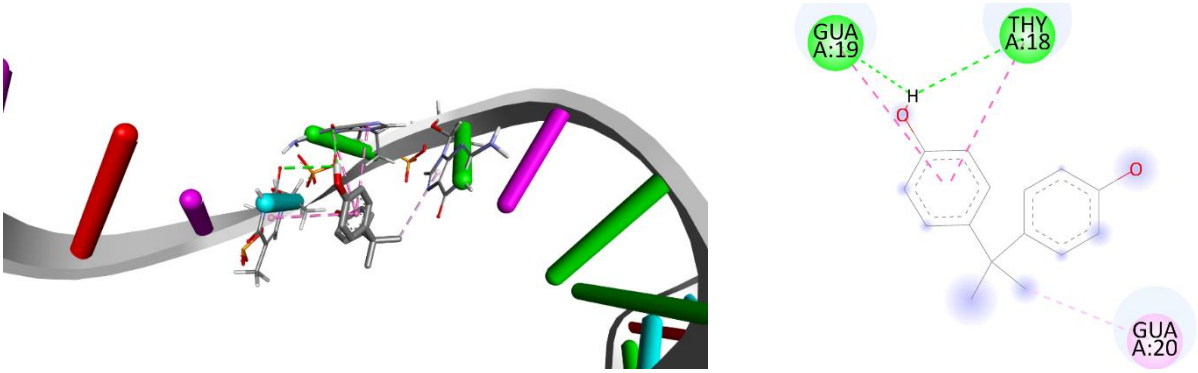

Figure 4.14.2. (a) Docked Pose of the Bisphenol-A with ss-DNA and (b) 2D representation of the interaction between them

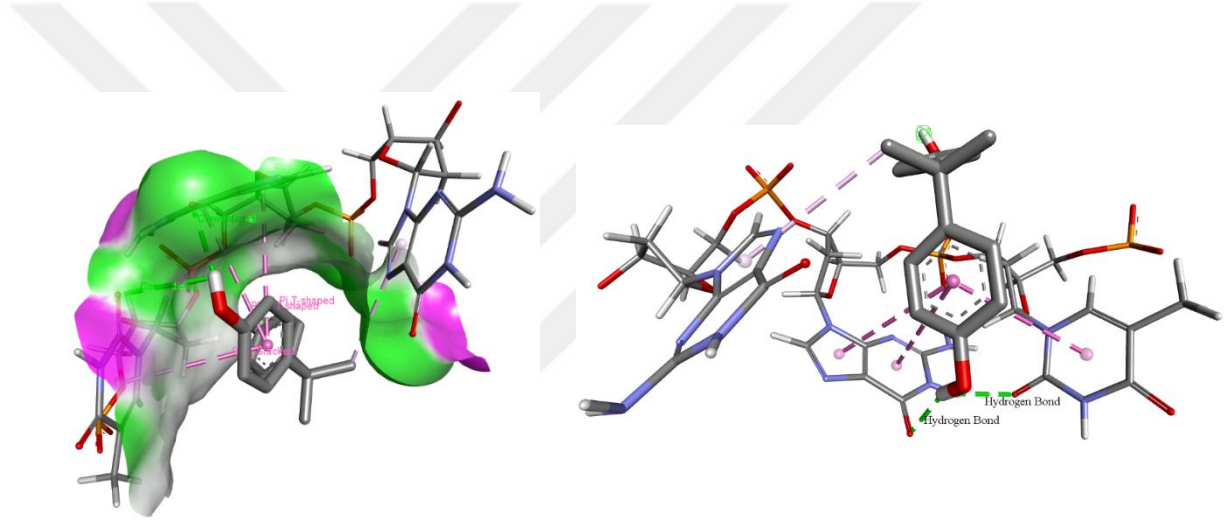

Figure 4.14.3. (a) donor and acceptor h-bond sites surrounding the ligand; (b) h-bond between bisphenol A and ss-DNA aptamer

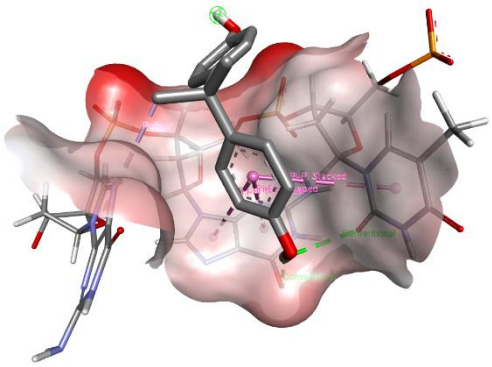

Figure 4.14.4. Distribution of charges at the interaction site

Name	Distance	Category	Types	From	Chemistry	To
A:B0:H-A:THY18:O2	3,06662	Hydrogen Bond	Conventional	A:B0:H	H-Donor	A:THY18:O2
A:B0:H-A:GUA19:O6	2,019118	Hydrogen Bond	Conventional	A:B0:H	H-Donor	A:GUA19:O6

Table 4.14.2. Details of Hydrogen Bonds between DNA and Ligand

4.15. SS-Dna Aptamer Structures Modeled from RNA Structures Comparison of Their Stability with Molecular Dynamics (MD) Simulations

The results of the MD simulation were investigated by evaluating the stability of the ss-DNA for 100 ns. Various metrics like the radius of gyration, rmsd, rmsf, and h-bond were investigated. The graphs of these parameters using the four force fields specified are compared.

4.16. Molecular Dynamics Results of the Modeled Apo SsS-DNA Aptamer from The SimRna

Apo ss-DNA, which is modeled on the SimRna server, was subjected to MD simulation to investigate stability for four force fields, which are Charmm36, Charmm36m, BSC1, and OL15, during 100 ns using Gromacs software.

4.16.1. Analysis of the Root Mean Square Deviation (RMSD)

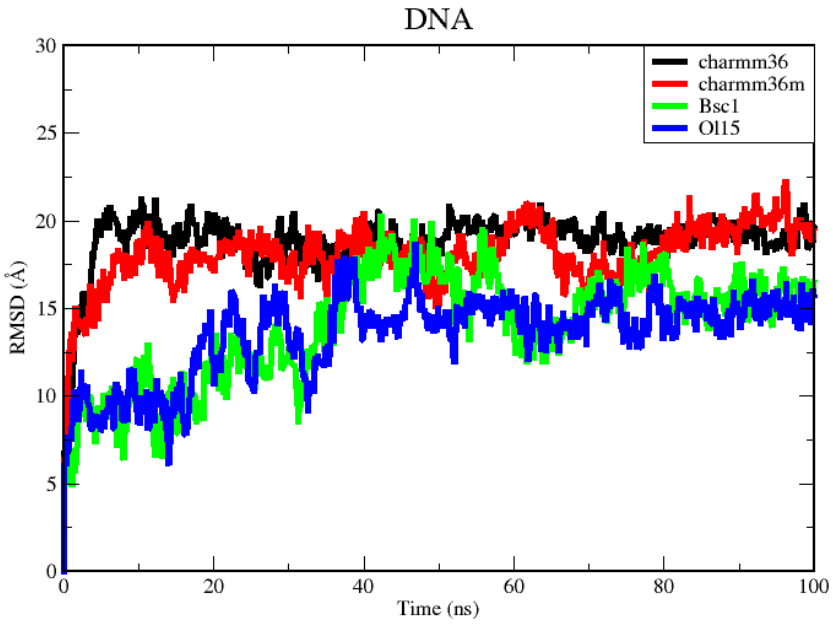

Figure 4.16.1 The evaluation root means square deviations (RMSDs) of Apo ss-DNA atoms versus 100 ns of MD simulation

Upon examination of the RMSD graph, it is evident that the application of the charmm36 and charmm36m force fields to the modeled apo DNA structures results in significantly larger RMSD values compared to the bsc1 and ol15 force fields. Furthermore, a notable disparity exists between the RMSD values of the DNA structures modeled using the charmm36 and charmm36m force fields and those modeled using the bsc1 and ol15 force fields.

RMSD	**Charmm36**	**Charmm36m**	**BSC1**	**OL15**
DNA	18.72	18.65	13.90	13.39

Table 4.16.1. DNA RMSD values by force field

In the first 10 ns of the graph for charmm36 and charmm36m, the rmsd value increased substantially. After the first 10 ns, the structure of charmm36 exhibited minimal fluctuations between 20 and 40 ns and remained stable with fewer fluctuations from 40 ns until the end of the simulation.

Regarding charmm36m, it was observed that minimal fluctuations were present between 20 and 50 ns after the initial 10 ns, albeit at a higher magnitude than those observed in charmm36.

Furthermore, it was observed that charmm36m exhibited a notable augmentation at approximately 60 ns subsequent to 40 ns, whereas charmm36 did not manifest such an escalation at 60 ns. Subsequent to a period of stability lasting until 80 nanoseconds, the observed phenomenon exhibited a marked increase surpassing that of charmm36, persisting until the conclusion of the simulation.

Upon application of Bsc1 and Ol15, both exhibited a rise in DNA structures subsequent to the initiation time, which then reached a state of stability until 20 ns. However, beyond the 20 ns, a notable escalation was observed in both Bsc1 and Ol15. Notably, the increase in Ol15 was found to be more pronounced than that of Bsc1.

A notable escalation was noted during the time frame of 40 ns to 50 ns, however, the magnitude of the escalation in bsc1 surpasses that of ol15. Following a 50 ns interval, the root-mean-square deviation (RMSD) metric for ol15 exhibited a decrease and subsequently stabilized with minimal fluctuations until the conclusion of the simulation.

Conversely, bsc1 demonstrated a continued increase in RMSD after 50 ns and only achieved equilibrium within the final 10 ns of the simulation. Notably, bsc1 reached equilibrium with a larger RMSD value than ol15.

Based on an analysis of both the RMSD values and the structural equilibrium, it can be concluded that the DNA aptamer containing OL15 exhibits a greater degree of structural stability.Based on an analysis of both the RMSD values and the structural equilibrium, it can be concluded that the DNA aptamer containing OL15 exhibits a greater degree of structural stability.

4.16.2. Assessment of RMSF

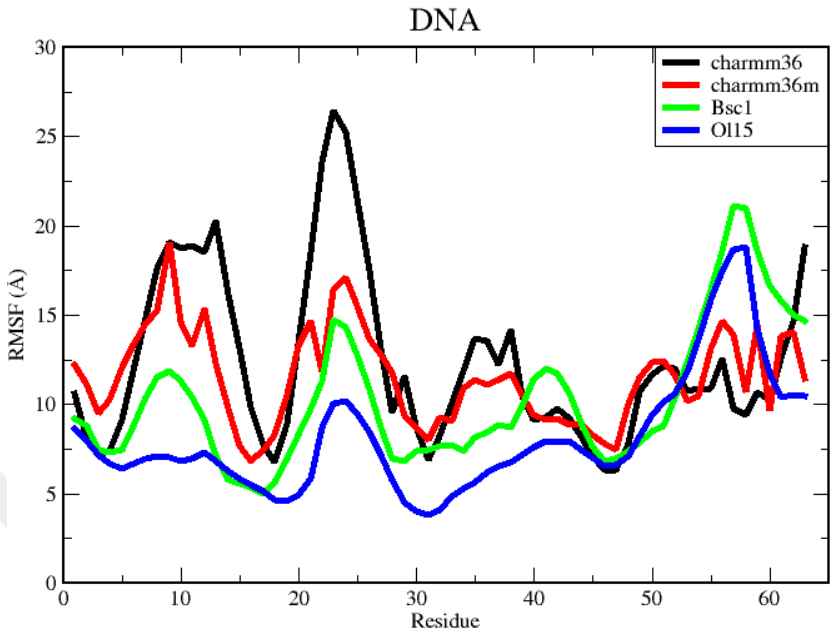

Figure 4.16.2. Residual fluctuations (RMSF) of ss-DNA atoms during 100 ns MD simulations

Upon examination of the RMSF graph, it is evident that the charmm36 model exhibits the most elevated RMSF value, whereas the OL15 model displays the most minimal RMSF value. The observed rmsf peaks for the charmm36 simulation are located at 8-15, 21-25, 35-38, 51-52, and 62-63. Meanwhile, the charmm36m simulation exhibits rmsf peaks at 8-13, 20-28, 35-38, 50-52, 55-57, 59, and 61-62. The specified intervals for BSC1 are 8-10, 22-25, 40-42, 53-56, 57-58, and 59-60, while for OL15, the intervals are 23-24 and 55-58. The root means square fluctuation (rmsf) peaks detected in Charmm36 exhibit a greater degree of broadness in comparison to those observed in Charmm36m, bsc1, and Ol15. In particular, with regards to charmm36, the most significant rise in RMSF is noted within the range of 22 to 25. This interval encompasses the nucleotide bases T, A, G, and C, which exhibit the most substantial degree of fluctuation. The nucleotide sequence comprising G, T, G, G, G, T, C, A, and G exhibits the second most substantial augmentation within the range of 8 to 15. The Charmm36m model exhibits notable fluctuations primarily in the adenine (A) and guanine (G) nucleobases, particularly within the range of 21 to 25.

The base pairs located in the region between 55 and 60 exhibit a peak in root mean square fluctuation (RMSF) for both BSC1 and OL15. Additionally, it should be noted that there are differences between the charmm36 and charmm36m models.

4.16.3. Analysis of Radius of gyration (RG)

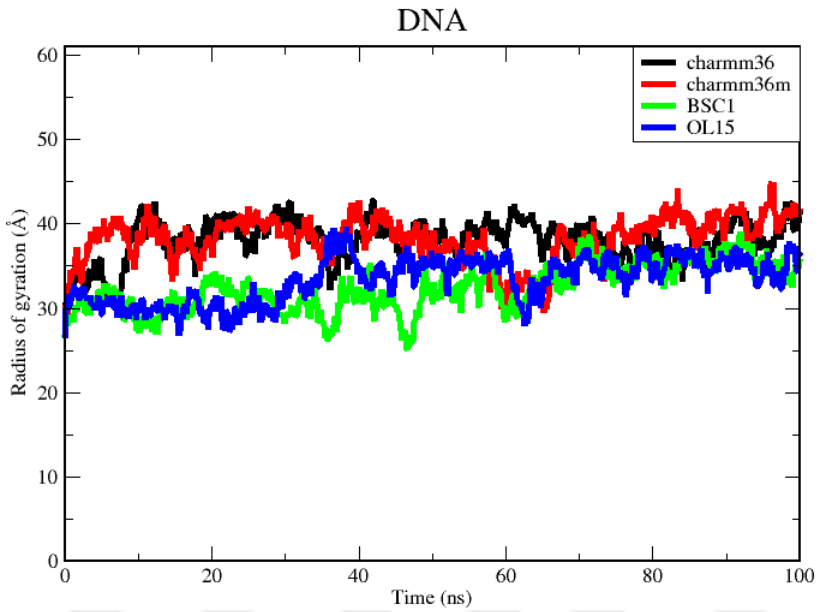

Figure 4.16.3. Represents the ROG values of the Apo ss-DNA for 100 ns.

The parameter Rg plays a crucial role in determining the level of compactness exhibited by a given structure throughout the simulation. Elevated Rg values are indicative of a reduction in the density of DNA structures, which implies a heightened level of pliability and a diminished level of stability. In contrast to the CHARMM36 and CHARMM36m force fields, the DNA structures in the BSC1 and OL15 states exhibit a reduced radius of gyration. The graph illustrates that the DNA constructs of charmm36 and charmm36m exhibited a greater number of conformational changes, whereas BSC1 and OL15 DNA constructs demonstrated a higher level of stability throughout the simulation.

4.16.4. Hydrogen Bond Analysis

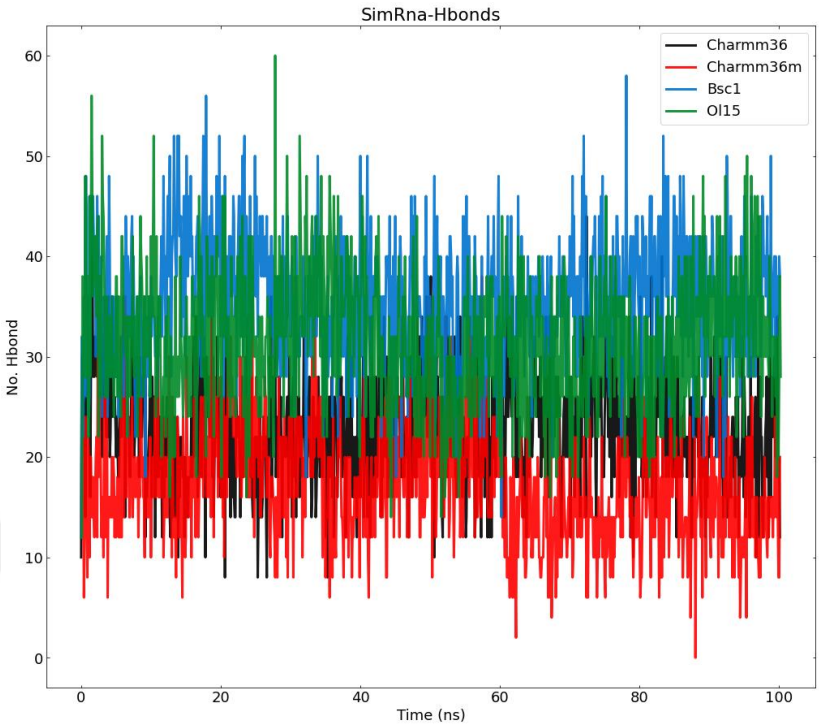

Figure 4.16.4. Represents the quantity of hydrogen bonds responsible for the 100 ns sustainability of the ss-DNA.

During the simulation, alongside the analyses of RMSD and RMSF, the stability of hydrogen bonds (H-bonds) in Apo ss-DNA was also scrutinized. In order to gain an understanding of the stability exhibited by biomolecules, it is crucial to undertake a geometric analysis of hydrogen bonding. The stability of a system can be attributed to the existence of hydrogen bonds. The maintenance of structural integrity in biomolecules is reliant on the crucial interaction of hydrogen bonds. In the context of molecular dynamics (MD) modeling, the formation of hydrogen bonds serves a crucial function in preserving the structural stability of the system. During the complete duration of the MD simulation, it was observed that the quantity of hydrogen bonds present in the single-stranded DNA without ligand states exhibited a dynamic behavior, as depicted in Figure 9. The graph illustrates that ss-DNA structures exhibit a greater number of hydrogen bonds in the bsc1 and ol15 situations while displaying a lower quantity of hydrogen bonds in the charmm36 and charmm36m simulations throughout the course of the simulation. An elevation in the stability of the created structures is associated with a greater number of hydrogen bonds.

4.17. Molecular Dynamics Results of the Modeled Apo SS-DNA Aptamer from The Rosetta-Farfar

Apo ss-DNA, which is modeled on the Rosetta-Farfar server, was subjected to Gromacs-based MD simulation for 100 ns to investigate the stability of four force fields, namely Charmm36, Charmm36m, BSC1, and OL15.

4.17.1. Analysis of RMSD

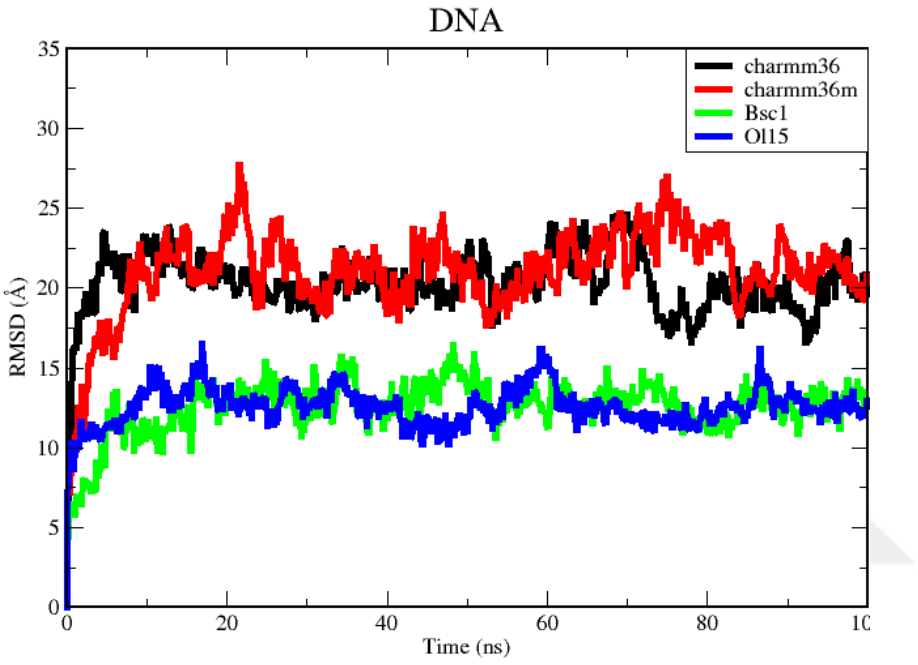

Figure 4.17.1. The Assessment RMSDs of Apo ss-DNA atoms versus 100 ns of MD simulation.

When we look at the RMSD graph, the RMSD value of the DNA structures of apo DNA structures, charmm36, and charmm36m, when a force field is applied, has a larger RMSD value than bsc1 and ol15, and there is a notable distinction among the RMSD outcomes of the DNA structures in the case of charmm36, charmm36m, and bsc1, ol15 DNA structures. Upon examination of the charmm36 and charmm36 m graphs, it was observed that the RMSD value exhibited a notable increase within the initial 10 ns from the outset. Regarding charmm36, the structure exhibits negligible fluctuations subsequent to the initial 10 ns, succeeded by a reduction in the root-mean-square deviation (rmsd) value at approximately 20 ns. Conversely, in the case of charmm36m, a noteworthy escalation in the rmsd value is observed around the 20 ns mark, subsequent to the initial increase.

In both diagrams, fluctuations persist throughout the simulation, and the rmsd fluctuations are greater in charmm36m than in charmm36, with a significant increase in 36m at 75 ns and a decrease in charmm36 at 70 ns. When Bsc1 and Ol15 were applied, both DNA structures increased after the start time, but ol15 increased less after the initial position. Significant fluctuations were observed in both cases around 20 ns, but the increase in ol15 was greater. Following these significant fluctuations, minimal fluctuations were observed for both structures from 20 ns to 40 ns, and at 50 ns, there was an increase in bsc1 and a decrease in ol15. Between 60 and 80 ns, there was a drop in the value of ol15, whereas an increase in the value of bsc1 was detected. In spite of the fact that there was a noticeable increase in both cases at 85 ns, we can see that the structures for each cases eventually reached a state of equilibrium in the final 10 ns of the simulation.

In comparison to the cases observed in charmm36 and charmm36m, it has been observed that Dna aptamers utilized in ol15 and bsc1 exhibit a higher degree of structural stability, as evidenced by the attainment of equilibrium in both rmsd values and structures.

RMSD	**Charmm36**	**Charmm36m**	**BSC1**	**OL15**
DNA	17.89	21.02	10.005	11.07

Table 4.17.1. DNA RMSD values by force field.

4.17.2. Assessment of RMSF

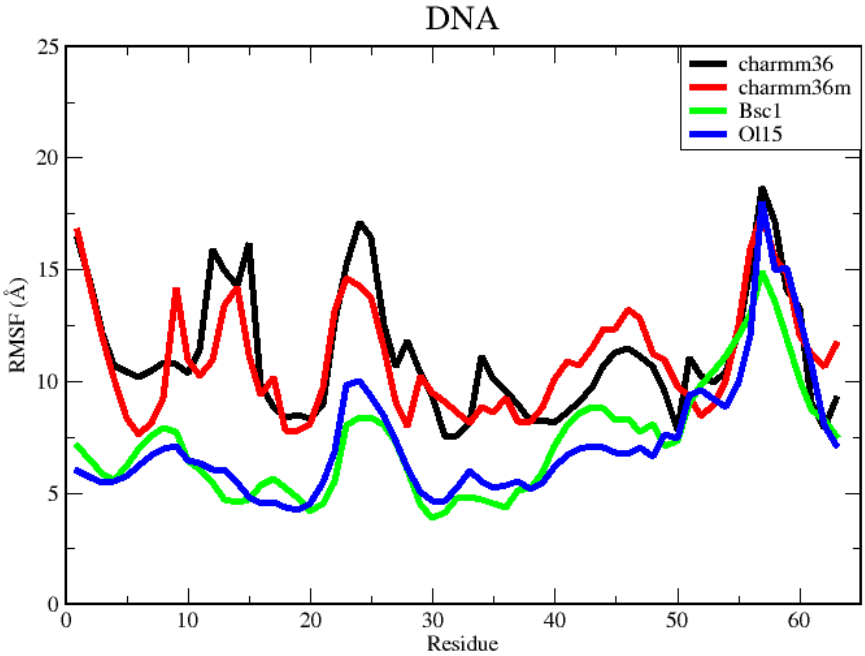

Figure 4.17.2. Residual fluctuations (RMSF) of ss-DNA atoms during 100 ns MD simulations

Upon examination of the RMSF graphs, it can be observed that the charmm36 model exhibits the greatest RMSF value, whereas the BSC1 model displays the lowest RMSF value. In the context of charmm36, it was observed that three distinct peaks exhibited significant root mean square fluctuation (RMSF) values, specifically within the ranges of 12-15, 23-25, and 56-58. Conversely, for charmm36m, the corresponding ranges were 9, 13-14, 23-25, 44-47, and 56-59. The BSC1 exhibits significant peaks at 23-25, 40-42, and 55-58, whereas the OL15 displays prominent peaks at 23-25 and 57-59. The Charmm36 model exhibited a notable rise in root-mean-square fluctuation (RMSF) particularly between nucleotide positions 56 and 58. Notably, the bases within this range, namely T, C, and G, displayed the most significant increase of fluctuation. Furthermore, it was observed that charmm36m, bsc1, and ol15 exhibited significant root mean square fluctuation (rmsf) values within the same region, which corresponds to the hairpin segment of the aptamer DNA structure. These nucleotide bases are believed to be responsible for the observed increase in the rmsf value.

4.17.3. Analysis of Radius of gyration (RG)

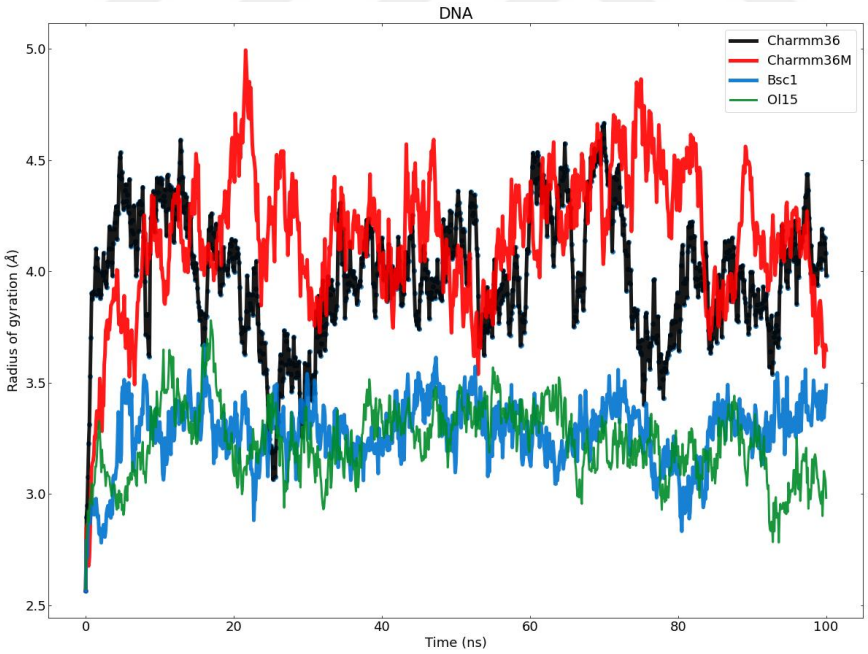

Figure 4.17.3. Represents the ROG values of the Apo ss-DNA for 100 ns

The degree of compactness of a structure is determined by the parameter Rg. Elevated RG values are indicative of a reduction in the density of DNA configurations, which implies heightened pliability and diminished steadiness.

In comparison to the charmm36 and charmm36m models, the BSC1 and OL15 DNA constructs exhibit reduced radii of gyration. As a result, the DNA structures of charmm36 and charmm36m have undergone a greater degree of conformational alterations. The graph depicts that DNA structures subjected to BSC1 and OL15 treatments exhibited a comparatively greater level of stability throughout the simulation.

4.17.4. Hydrogen bond analysis

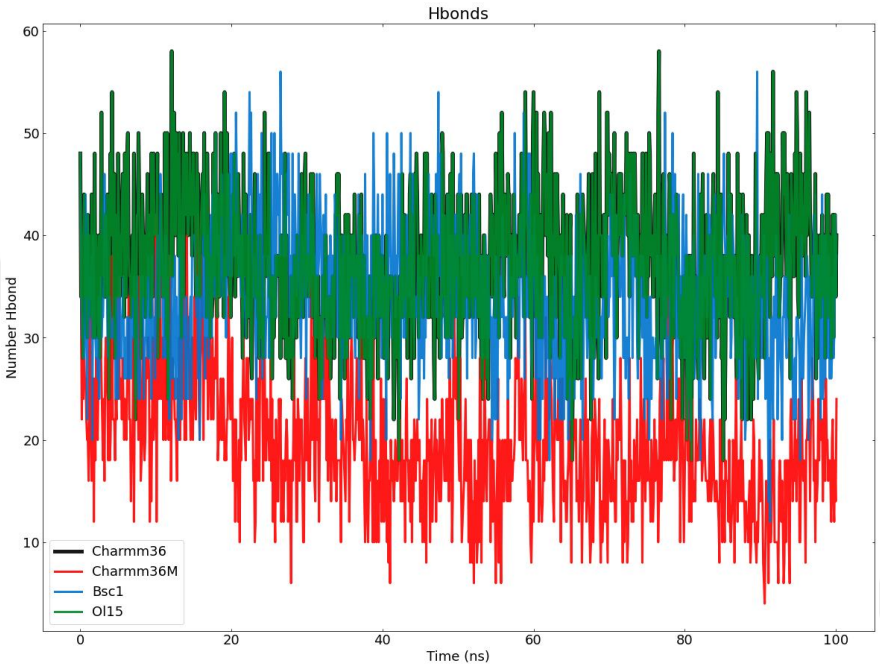

Figure 4.17.4. Represents the amount of hydrogen bonds responsible for the stability of the ss-DNA throughout the 100 ns.

The number of H-bonds that were formed by Apo ss-DNA was calculated throughout the 100 ns simulation period and plotted on a graph, and the results have been shown in Figure 10. The graph shows that over the course of the simulation, total amount of hydrogen bonds in ss-DNA structures is highest in the bsc1 and ol15 cases, and lowest in the charmm36 and charmm36m simulations. Since the increased stability of the formed structures is associated with more hydrogen bonds, the ss-DNA structure in the OL15 state is more stable.

4.18. Molecular dynamics results of the modeled Apo ss-DNA aptamer from the Rna Composer

Apo ss-DNA, which is modeled on the Rna composer server, was subjected to MD simulation to investigate stability for four force fields, which are Charmm36, Charmm36m, BSC1, and OL15, during 100 ns using Gromacs software.

4.18.1. Analysis of RMSD

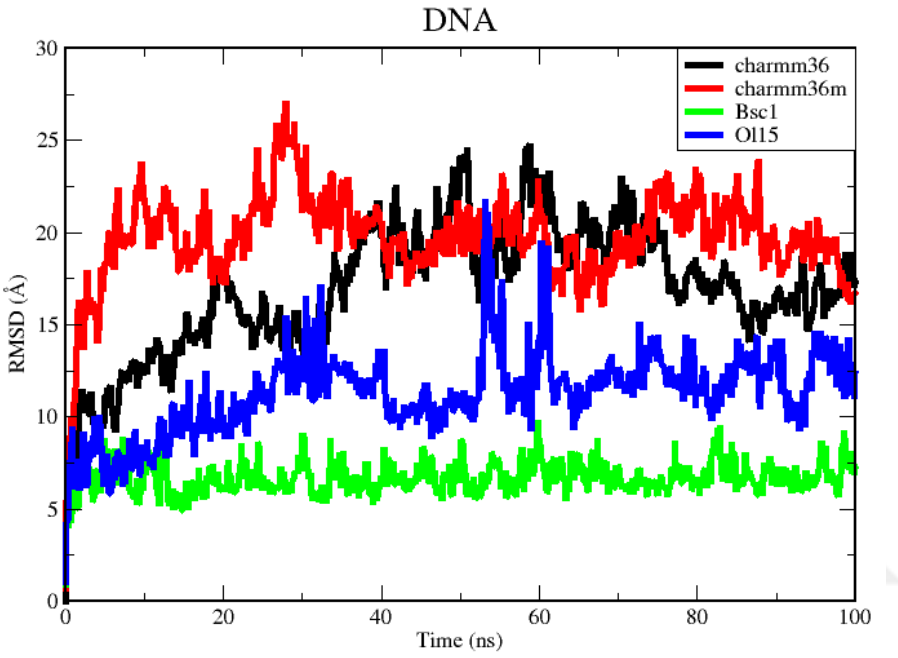

Figure 4.18.1. The assessment RMSDs of Apo ss-DNA atoms versus 100 ns of MD simulation.

RMSD	Charmm36	Charmm36m	BSC1	OL15
DNA	17.89	19.716	6.648	10.005

Table: 4.18.1. DNA RMSD values by a force field.

The graphical representation of Charmm36 indicates a notable elevation in the root-mean-square deviation (rmsd) indicator during the first 20 ns coming from the baseline position. The root mean square deviation (RMSD) exhibited a transient decrease subsequent to 20 ns, but subsequently resumed an upward trend, culminating in its maximum value between 40 and 60 ns.Following the 70 nanoseconds, there was a decrease in the RMSD, which eventually led to the achievement of the minimum RMSD value at around 80 nanoseconds.

The simulation demonstrated a consistent value during the final 10 ns; however, significant fluctuations were observed throughout the simulation. It is not possible to conclude that the DNA structure remained stable, as it exhibited a pattern of continuous increase and decrease.

The simulation results obtained using the charmm36m force field exhibit a substantial rise in the initial position during the first 20 ns, surpassing the corresponding increase observed in the charmm36 graph.

Following a period of 20 ns, the escalation persists with heightened fluctuations and culminates in the utmost Root Mean Square Deviation value. Subsequent to the initial 40 ns, a notable reduction was observed, which persisted with minimal variability until the 70 ns. Despite the passage of time, the structure has not yet attained equilibrium; however, it exhibits greater stability during the final 10 ns of the simulation.

Upon application of Bsc1 and Ol15, a significant rise in the initial positions is observed in contrast to the cases in charmm36 and charmm36m. Furthermore, the extent of this increase is even lower in the case of bsc1. The BSC1 graph displays a high degree of stability in the aptamer DNA structure, which is maintained consistently throughout the simulation.

Conversely, the OL15 graph exhibits comparatively lower stability in the aptamer DNA structure when compared to the BSC1 case. The OL15 graph exhibits a notable surge in rmsd values within the 50–60 ns timeframe. Subsequently, it displays a comparatively lower degree of stability than the BSC1 graph. However, the OL15 graph maintains a consistent value with minimal fluctuations until the conclusion of the simulation.

4.18.2. Assessment of RMSF

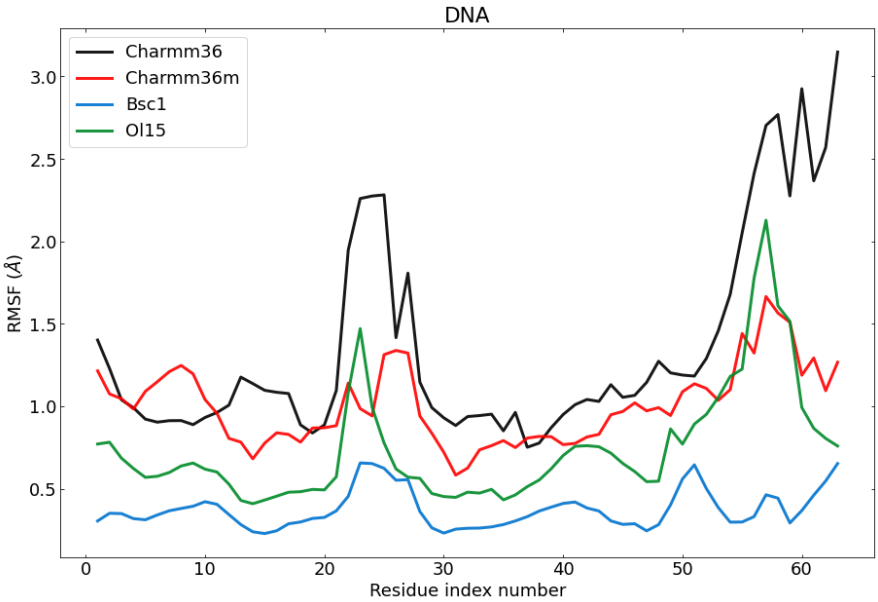

Figure 4.18.2. Residual fluctuations (RMSF) of ss-DNA atoms during 100 ns MD simulations

The RMSF metric is utilized to evaluate the significance of specific nucleotide pairs in preserving the inherent conformation of DNA structures. A higher RMSF value corresponds to increased flexibility, whereas a lower RMSF value indicates a more stable region. After analyzing the RMSF graph, it can be noted that the charmm36 model displays the highest RMSF value, while the BSC1 model exhibits the lowest RMSF value.

The regions exhibiting the most prominent maxima for Charmm36 are the nucleotide bases located at the termini of the ss-DNA aptamer 5' 3' sequence within the -A- and hairpin loop regions. The hairpin stem and loop regions of the aptamer structure, specifically the bases ranging from 22 to 26, exhibit a notable surge in their levels. This increase is indicative of a reduction in the stability of the aptamer-DNA structure. The charmm36m model exhibits dissimilarities from charmm36 in terms of the regions that display significant RMSF peaks. Notably, the rmsf peak pertaining to the base sequence in the end region is markedly low in charmm36m.

The DNA aptamer structure exhibits regions with the most elevated root-mean-square fluctuation (RMSF) values, which are situated within the hairpin loop region and range from 57 to 59. The subsequent observation pertains to the area exhibiting the most elevated point, which is situated within the loop and spans from 25 to 27 bases.

Upon examination of BSC1 and OL15, it can be observed that the root mean square fluctuation (rmsf) peaks exhibited by these structures are comparatively lower than those of charmm36 and charmm36m. The RMSF peaks, which are indicative of increased structural flexibility, are notably low in the context of BSC1. This observation suggests that the aptamer-DNA structure exhibits greater stability under these conditions, particularly in the context of BSC1.

4.18.3. Analysis of Radius of gyration (RG)

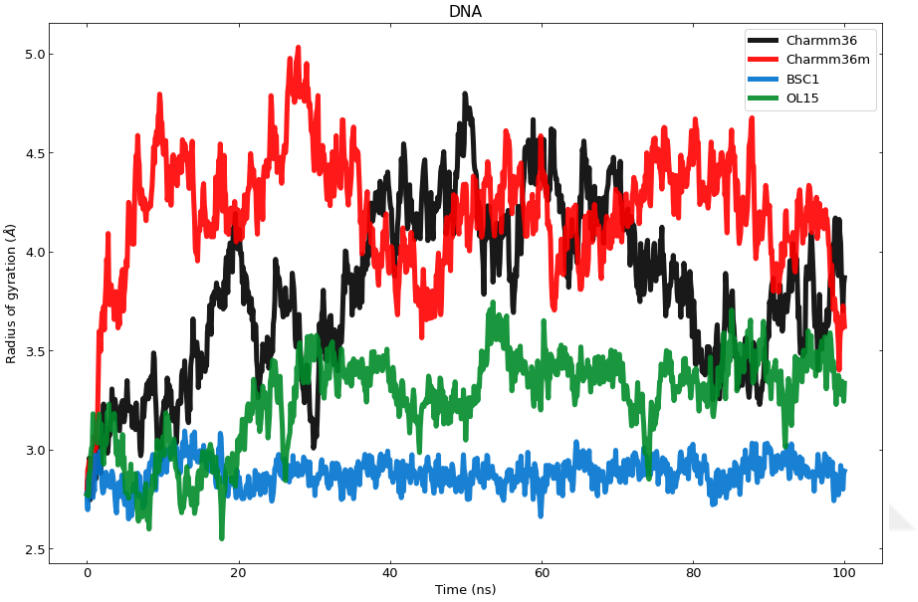

Figure 4.18.3. Represents the ROG values of the Apo ss-DNA for 100 ns.

The parameter Rg determines a structure's compactness. A boost in RG levels denotes a reduction in the compactness of DNA structures, signifying an increase in flexibility and a decrease in stability. When examining the graph, it is evident that the DNA structure in case bsc1 is the most stable structure among four distinct force fields, as it maintained a constant value throughout the simulation, attained equilibrium, and maintained its stability. The stability of the DNA structure was observed to be comparatively higher in the OL15 case as compared to the charmm36 and charmm36m cases.

4.18.4. Hydrogen bond analysis

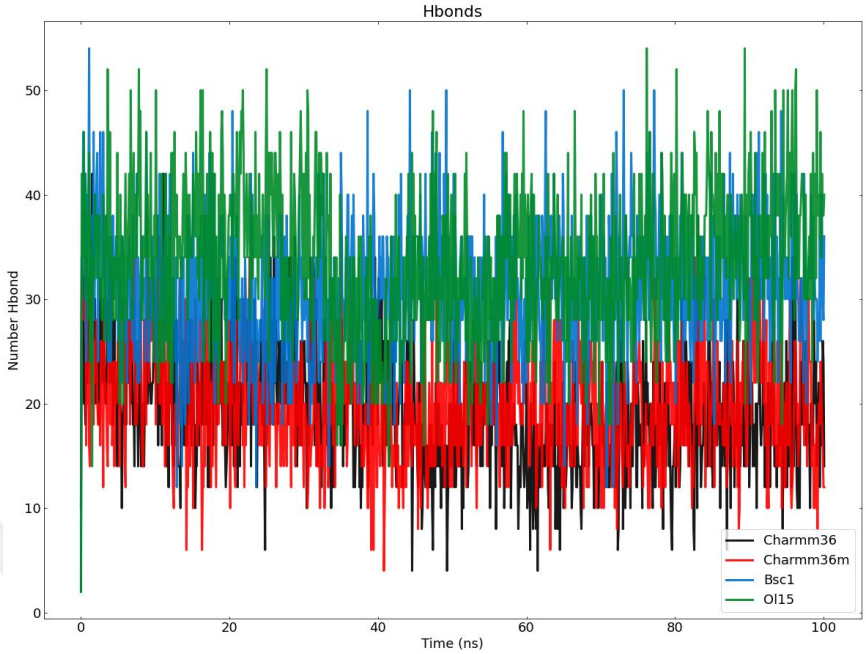

Figure 4.18.4. Represents the quantity of hydrogen bonds responsible for the 100 ns sustainability of the ss-DNA.

The quantification of hydrogen bonds formed by Apo ss-DNA was computed over the course of a 100 ns simulation duration and visually represented through a graph, as depicted in Figure 10. The graph depicts that over the course of the simulation, the quantity of hydrogen bonds present in ss-DNA structures is maximal in the bsc1 and ol15 scenarios, while it is minimal in the charmm36 and charmm36m simulations. The heightened stability of the structures that are formed is correlated with an increase in the quantity of hydrogen bonds. As a result, the ss-DNA structure in the OL15 and BSC1 states exhibits greater stability.

4.19. Molecular dynamics results of the modeled Apo ss-DNA aptamer from the Vfold3D Analysis of the Root Mean Square Deviation (RMSD)

Apo ss-DNA, which is modeled on the Vfold3d server, was subjected to MD simulation to examine stability for four force fields, namely Charmm36, Charmm36m, BSC1, and OL15, for 100 ns using Gromacs software.

4.19.1. Analysis of the Root Mean Square Deviation (RMSD)

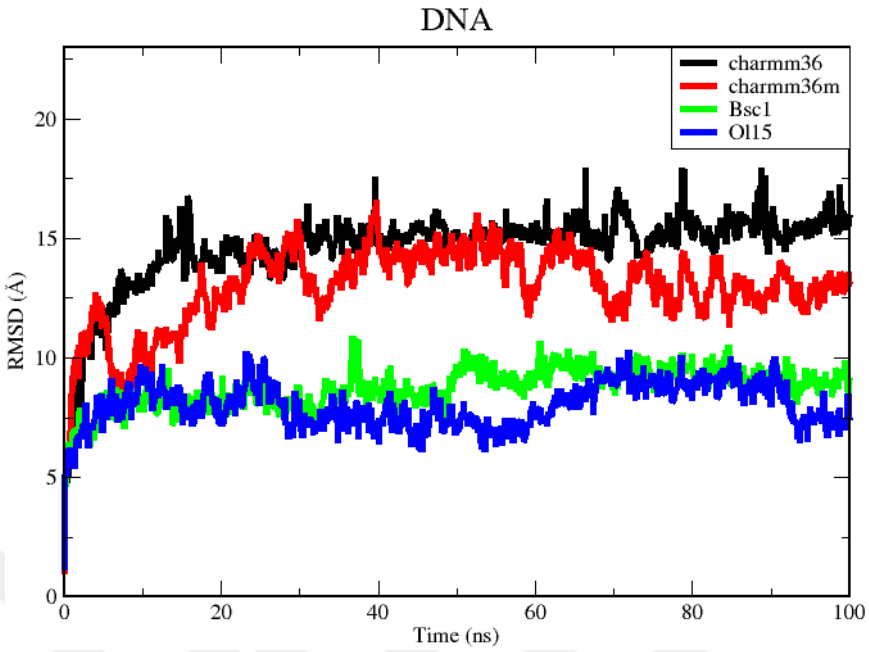

Figure 4.19.1. The evaluation root means square deviations (RMSDs) of Apo ss-DNA atoms versus 100 ns of MD simulation.

When examining the RMSD graph, the RMSD value for charmm36 and charmm36m force fields from apo ss-DNA structures is greater than bsc1 and ol15, and the RMSD value for the Ol15 state DNA structure is the lowest.

RMSD	**Charmm36**	**Charmm36m**	**BSC1**	**OL15**
DNA	14.48	12.80	8.674	7.946

Table 4.19.1. DNA RMSD values by force field.

When examining the Charmm36 graph, there is a significant increase in the rmsd value during the first 20 ns from the start of the simulation. After 20 ns, the structure is stable because it does not exhibit large fluctuations until the end of the simulation, but between 40 and 60 ns, the structure has stabilized completely. The Charmm36m model exhibits an initial rise in the root-mean-square deviation (rmsd) value within the first 10 ns through starting point, followed by a brief decrease. Subsequently, the rmsd value experiences an upward trend until the 30 ns, culminating in its peak value at the 40 ns.

Subsequently, an equilibrium state is attained within the time interval of 40-60 nanoseconds, followed by a decline and fluctuation, ultimately stabilizing during the final 10 ns of the simulation.

The graph reveals that the DNA structures of Bsc1 and Ol15 exhibited an increase subsequent to the start time. However, Ol15 demonstrated a slightly greater increase beyond the initial position. Both cases reached equilibrium at approximately 20 ns. Notably, the aptamer DNA structure in Ol15 exhibited a high degree of stability from 30 ns to 60 ns, despite an increase in the root-mean-square deviation (rmsd) value up to 70 ns. The system returned to equilibrium at 90 ns, with a particularly stable structure observed during the final 5 ns of the simulation.

The Bsc1 case exhibited fluctuations whereby the root mean square deviation (rmsd) value increased for a duration of 70 ns subsequent to 30 ns, indicating the extent to which the structure deviated from its initial position. However, the structure attained stability after 70 ns and remained stable throughout the simulation.

4.19.2. Assessment of RMSF

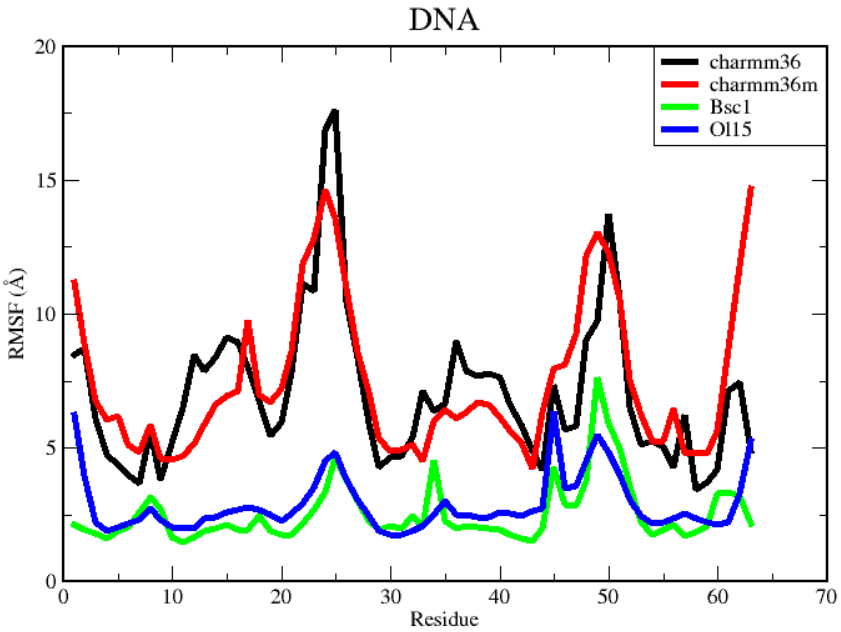

Figure 4.19.2. The evaluation root means square deviations (RMSDs) of Apo ss-DNA atoms versus 100 ns of MD simulation.

Upon examination of the RMSF graphs, it is evident that the charmm36 model exhibits the most elevated RMSF value, whereas the BSC1 model displays the least RMSF value. The nucleotide sequence with the highest peak for charmm36 is -G-C- within the 24–25 range. Furthermore, the peak value of the RMSF is observed to be -A at 50. The charmm36m model exhibits peak values of -G-C- in the 24-25 range, consistent with those observed in charmm36.

Additionally, a high rmsf value is observed in the -A- region at the end of the 5' 3' sequence, as well as in the -C- region at the head of the 5' 3' sequence.

The Root Mean Square Fluctuation (RMSF) values exhibited by bsc1 and OL15 are comparatively lower than those of charmm36 and charmm36m. In each instance, there were notable spikes in the 24-25 range, and while both also exhibited elevated rmsf values at 45, bsc1 demonstrated comparatively lower values than OL15. The OL15 structure exhibits elevated root mean square fluctuation (rmsf) values in both its head and tip regions, whereas BSC1 did not display a corresponding rise in rmsf.

4.19.3. Analysis of Radius of gyration (RG)

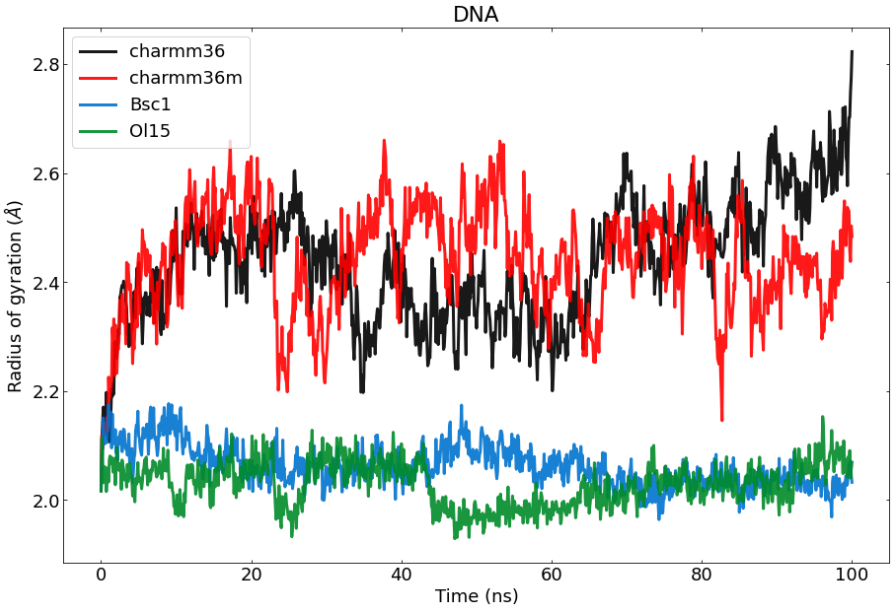

Figure 4.19.3. Represents the ROG values of the Apo ss-DNA for 100 ns.

In comparison to BSC1 and OL15, the DNA constructs of charmm36 and charmm36m exhibit a reduced radius of gyration, indicating a higher degree of conformational changes. Upon comparing BSC1 and OL15, it is observed that there exist no significant disparities between the RG structures.

During the initial 10 nanoseconds, BSC1 exhibited a lower level of stability compared to OL15. Between 20 and 40 ns, both structures demonstrated a consistent increase in compactness. Subsequently, a noteworthy decline in the Rg value was observed in OL15 until 60 nanoseconds, whereas BSC1 exhibited a significant increase after 65 ns. Despite this, both structures resumed a constant value. Ultimately, BSC1's DNA structure stabilized, while OL15 was unable to maintain its stability.

Upon examination of the graphs for charmm36 and charmm36m, it can be observed that both exhibit an initial increase in RG value up to the first 20 ns. In particular, the increase in RG value is more pronounced in charmm36m. However, while a decrease in RG value is observed in charmm36m after a 20 ns signal, a decrease in RG value is observed in charmm36 after 30 ns. Significant fluctuations have been observed, particularly in periods ranging from 40 to 60 nanoseconds, specifically in the Charmm36 model. However, it can be stated that the Charmm36 model reached an equilibrium state within the aforementioned time period. Following a 65-nanosecond signal, the OL15 and BSC1 models exhibited distinct behavioral patterns. Within 20 nanoseconds, a significant decrease in the stability of the structure was observed in the charmm36 model, whereas an increase in the stability of the structure was observed in the charmm36m model.

4.19.4. Hydrogen bond analysis

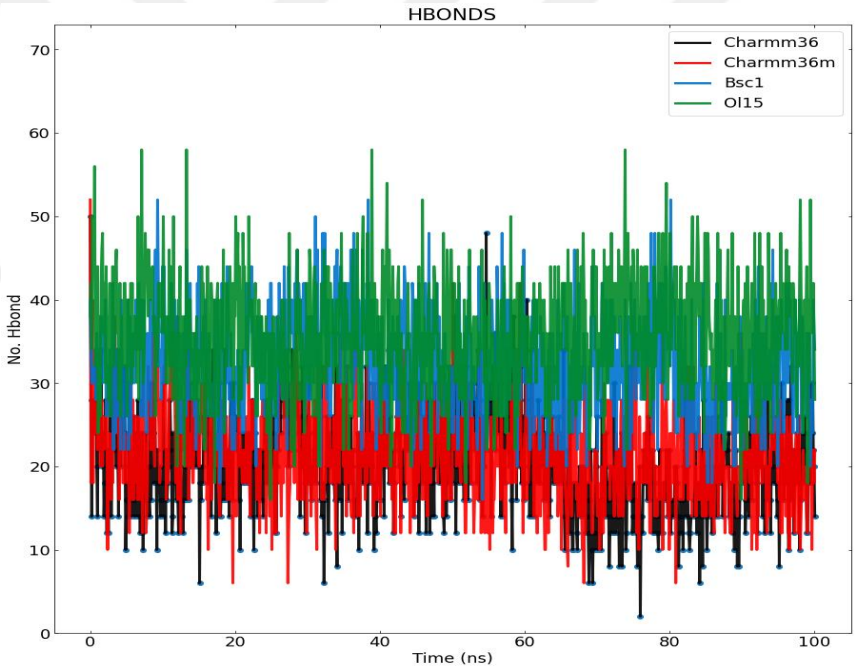

Figure 4.19.4. Represents the quantity of hydrogen bonds responsible for the 100 ns sustainability of the ss-DNA.

4.20. Molecular dynamics results of the modeled Apo ss-DNA aptamer from the 3dRNA Analysis of the Root Mean Square Deviation (RMSD)

Using Gromacs software, Apo ss-DNA, which is modeled on the 3dRNA server, was subjected to MD simulation to assess stability for four force fields, Charmm36, Charmm36m, BSC1, and OL15, over 100 ns.

4.20.1. Analysis of the Root Mean Square Deviation (RMSD)

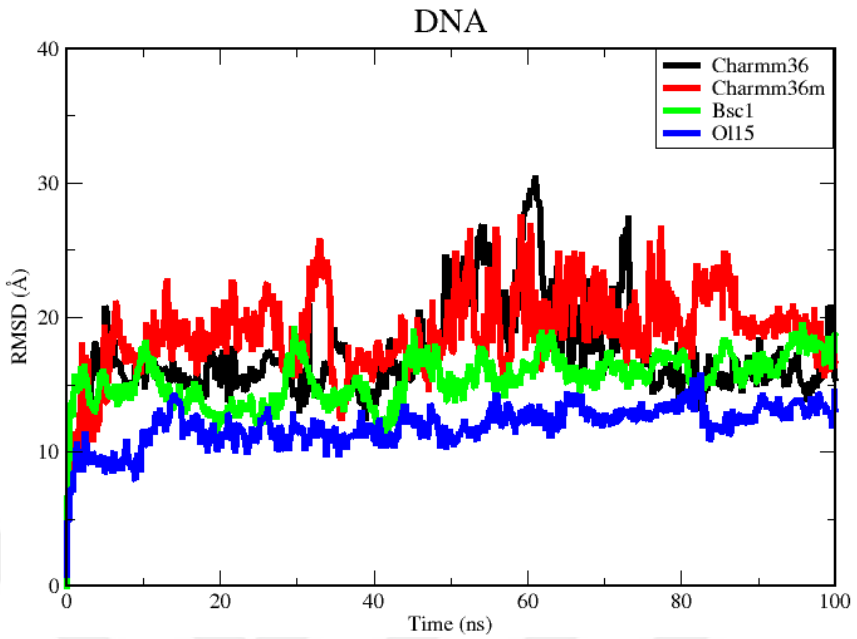

Figure 4.20.1. The evaluation root means square deviations (RMSDs) of Apo ss-DNA atoms versus 100 ns of MD simulation.

Upon examination of the RMSD plot, it is evident that the RMSD values of the DNA structures in the charmm36 and charmm36m states exhibit greater values in comparison to the apo DNA structures of bsc1 and ol15. Notably, the DNA structure in the OL15 state displays the lowest RMSD value, while charmm36m exhibits the highest RMSD value.

RMSD	**Charmm36**	**Charmm36m**	**BSC1**	**OL15**
DNA	17.89	21.02	10.005	11.07

Table 4.20.1. DNA RMSD values by force field

In the first 5 ns, the RMSD value of the Charmm36 model increased, resulting in 40 ns of constant values. Subsequently, the rmsd value displayed a continuous increase from 40 ns to 80 ns, culminating in its maximum value at approximately 60 ns. Following the 80 nanosecond mark, a notable reduction in the root-mean-square deviation (RMSD) value was observed, which subsequently stabilized for the duration of the simulation.

The Charmm36m simulation exhibited a substantial rise during the initial 10 ns, followed by a period of equilibrium from 10 ns to 30 ns. A sudden decrease in the RMSD value was observed at the 30 nanosecond mark, followed by a brief stabilization period.

However, from 50 nanoseconds onwards, the system exhibited continuous fluctuations until approximately 85 nanoseconds, after which it stabilized briefly towards the end of the simulation. Overall, the system's stability was found to be comparatively lower than that of Charmm36. Upon examination of the DNA aptamer structures in the BSC1 and OL15 cases, it can be posited that the DNA aptamer structure in the OL15 case exhibits greater stability in comparison to the bsc1, charmm36, and charmm36m structures. This assertion is supported by both the smaller root-mean-square deviation (RMSD) value and the observation that it displays fewer fluctuations throughout the simulation, ultimately stabilizing at the conclusion of the simulation.

4.20.2. Assessment of RMSF

Upon examination of the RMSF graphs, it has been seen that the charmm36 model exhibits the greatest RMSF worth, whereas the OL15 model displays the lowest RMSF value. According to Charmm36, the regions with the highest peaks are located at the bases situated at the end of the ss-DNA aptamer 5' 3' sequence in the -A-, hairpin loop, and internal loop regions.

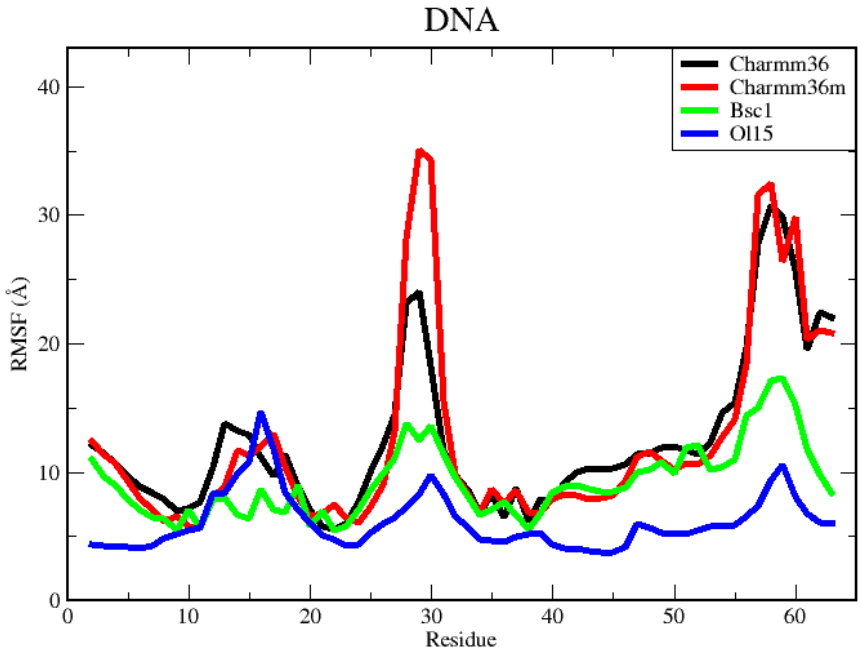

Figure 4.20.2. Residual fluctuations (RMSF) of ss-DNA atoms during 100 ns MD simulations

These regions contribute to the destabilization of the aptamer-dna structure. The Charmm36m model exhibits a prominent peak in the 29-30 region, which is situated within the internal loop. Additionally, another peak of notable magnitude is observed between 56-60, also located within the internal loop.

The comparative analysis of the RMSF values of OL15 and BSC1 with those of charmm36 and charmm36 indicates that the DNA structures in the former exhibit greater stability. The BSC1 region exhibits a peak of notable magnitude in the 55-60 range within the internal loop, thereby conferring greater flexibility to the aptamer DNA structure. Conversely, the OL15 region displays a peak of significant magnitude in the 13-17 range, which distinguishes it from the remaining three cases.

4.20.3. Analysis of Radius of gyration (RG)

The compactness of a structure is determined by the parameter Rg. Elevated RoG values are indicative of a reduction in the density of DNA structures, which implies an augmentation in pliability and a decline in steadiness.

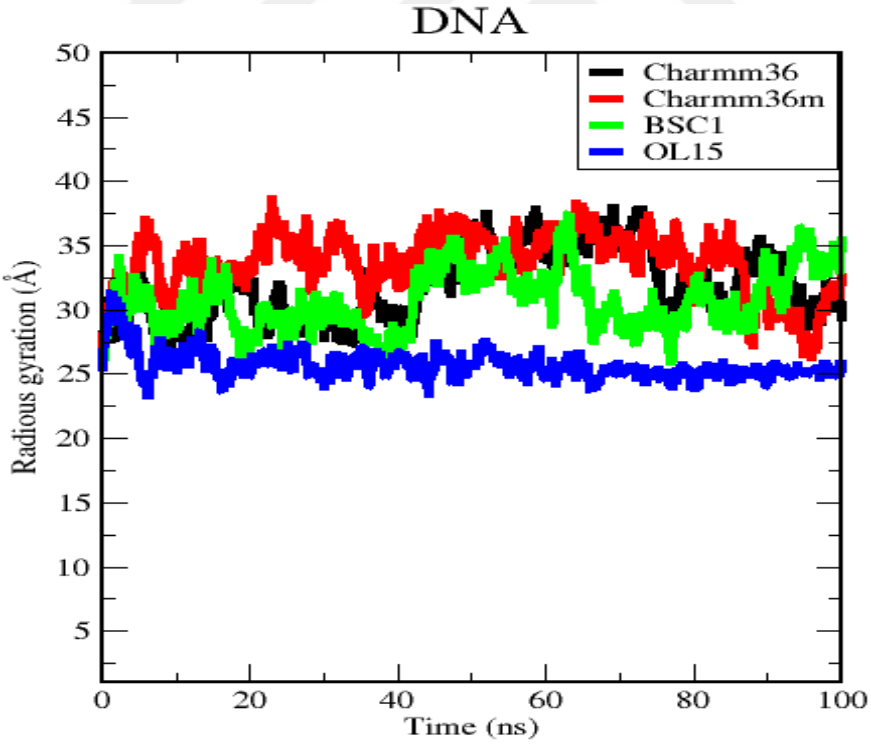

Figure 4.20.3. Represents the ROG values of the Apo ss-DNA for 100 ns.

Upon examination of the graph, it is evident that the DNA structure in the OL15 state exhibits remarkable stability across four distinct force fields.

Specifically, this structure maintains a consistent value throughout the simulation, achieves equilibrium, and sustains its stabilization over time.

4.20.4. Hydrogen bond analysis

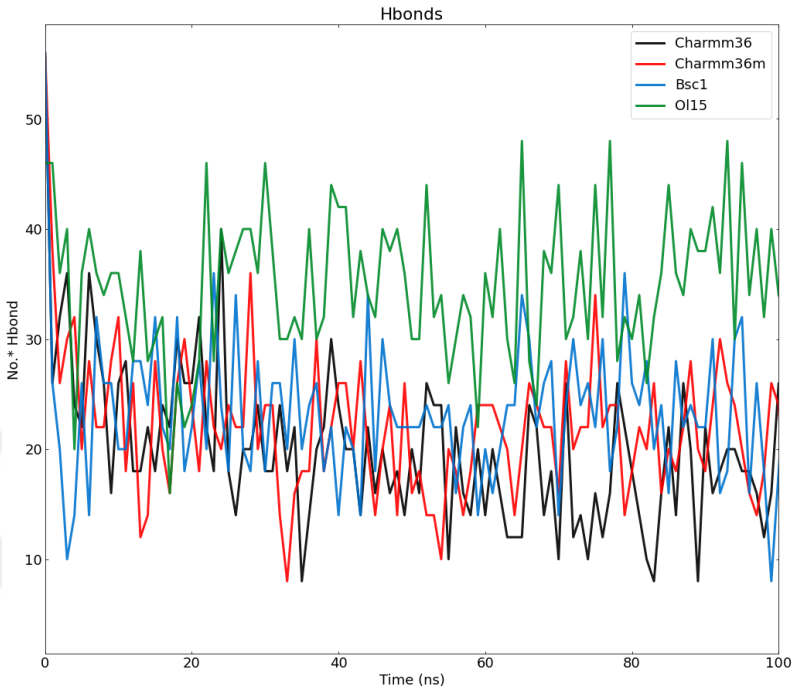

Figure 4.20.4. Represents the quantity of hydrogen bonds responsible for the 100 ns sustainability of the ss-DNA.

Within the simulation, ss-DNA structures exhibit a greater number of hydrogen bonds under OL15 conditions, but a reduced number under charmm36, charmmm36m, and bsc1 conditions. There exists a positive correlation between the quantity of hydrogen bonds and the stability of the structures that are formed.

Throughout the simulation, ss-DNA structures exhibit a greater number of hydrogen bonds under the OL15 case, but a reduced number under the charmm36, charmmm36m, and bsc1 cases.

4.21. Molecular dynamics results of the modeled Apo ss-DNA aptamer from the 3D-DART

Apo ss-DNA, which is modeled on the 3D-DART server, was subjected to MD simulation for 100 ns using Gromacs software to investigate stability for four force fields, namely Charmm36, Charmm36m, BSC1, and OL15.

4.21.1. Analysis of RMSD

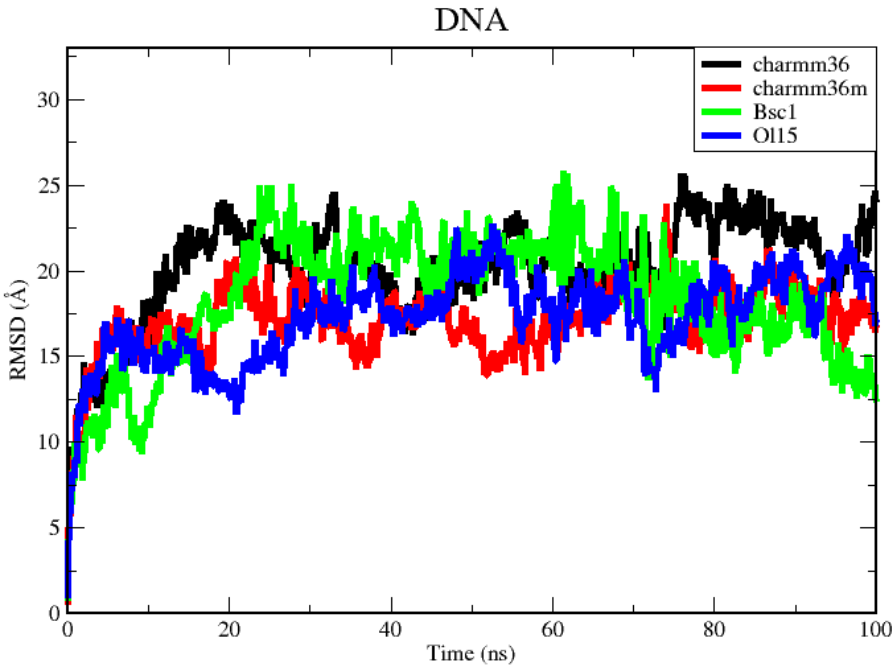

Figure 4.21.1. The evaluation root means square deviations (RMSDs) of Apo ss-DNA atoms versus 100 ns of MD simulation.

When examining the RMSD graph, the charmm36 structure has the highest RMSD value among the apo DNA structures, whereas the OL15 structure has the lowest RMSD value.

RMSD	**Charmm36**	**Charmm36m**	**BSC1**	**OL15**
DNA	20.04	17.08	18.01	16.99

Table 4.21.1. DNA RMSD values by force field

The Charmm36 simulation exhibited a notable motion of the aptamer DNA structure from its initial position, with a significant augmentation observed after 10 ns. The observed trend demonstrated a steady rise over a period of 20 ns, followed by persistent fluctuations, indicating a fluctuating state. The root mean square deviation (RMSD value attained its maximum after 80 ns, and the structure failed to attain equilibrium by the conclusion of the simulation, suggesting inadequate folding of the aptamer DNA structure.In the case of Charmm36m, the graph depicts the displacement of the DNA structure from its initial position during the simulation.

The structure remained in a state of equilibrium until the 20 ns, after which the root-mean-square deviation (rmsd) value increased and continued to fluctuate until the 60 ns. This fluctuation ultimately resulted in a conformational change of the DNA aptamer.

The simulation exhibited a peak in rmsd at 75 ns, surpassing all other time points, but it can be inferred that the system achieved equilibrium during the final 10 ns of the simulation. Furthermore, the stability of the system was found to exceed that of the DNA aptamer structure in the Charmm36 state.

Regarding BSC1, the DNA aptamer structure experienced a rise in rmsd value at the onset of the simulation, followed by a sustained increase until the 30 ns mark. During this period, the aptamer structure underwent a significant conformational alteration.However, from 30 ns to 60 ns, it reached an equilibrium state. Following the 60 ns, a decrease in the root-mean-square deviation (RMSD) value was observed, indicating that the simulation had returned to a state of equilibrium during the final 5 ns. In terms of, despite exhibiting the lowest RMSD value, it persisted in fluctuating throughout the simulation and failed to attain equilibrium by the conclusion of said simulation.

4.21.2 Assessment of RMSF

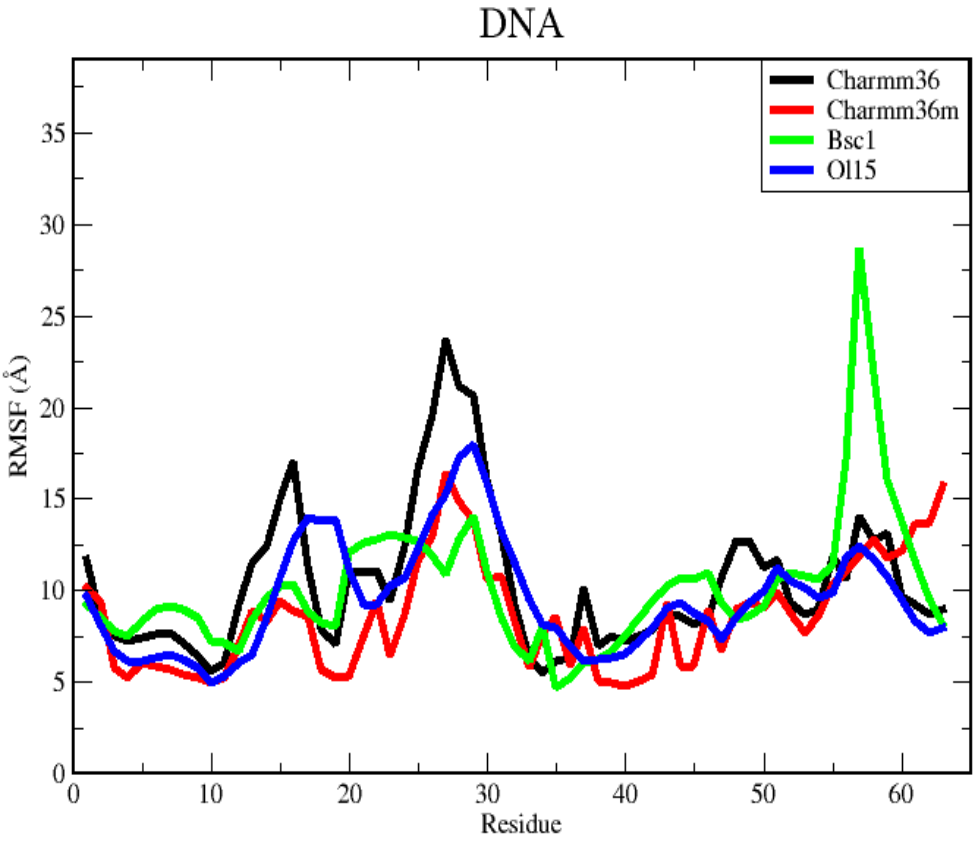

Figure 4.21.2. Residual fluctuations (RMSF) of ss-DNA atoms during 100 ns MD simulations

When we look at the RMSF graph, charmm36 shows the highest rmsf value, while Charmm36m has the lowest rmsf value. The regions that give the highest peak for Charmm36 are the bases 26-30 and 15-16 in the ss-DNA aptamer, which are located in the internal loop of the ssDNA aptamer structure and cause high flexibility.In the case of charmm36m, the regions giving the highest flexibility are similar to charmm36 but lower than charmm36.The ssDNA-aptamer structure in the BSC1 state exhibits adistinct peak in comparison to other states, with the highest intensity observed at the terminal end of the DNA molecule.In the ssDNA aptamer structure in the OL15 state, the regions showing the highest flexibility are similar to Charmm36 and charmm36m.

4.21.3 Analysis of Radius of gyration (RG)

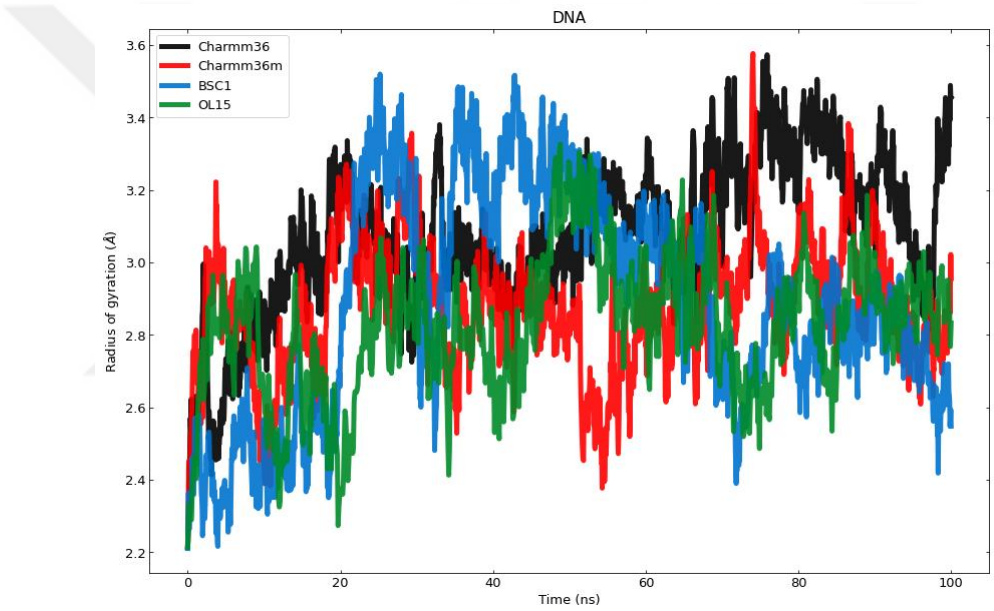

Figure 4.21.3. Represents the ROG values of the Apo ss-DNA for 100 ns.

In the case of four distinct force fields, the most stable structure is the DNA structure in the OL15 state, which remained at a constant value throughout the simulation, reached equilibrium and maintained its stability. BSC1 exhibited the highest RG value among four distinct force fields, particularly between 20 and 40 ns.

The structure's RG value attained its maximum, indicating that the aptamer is unfolded. Although the RG value decreases after 40 ns until the end of the simulation, the compactness of the DNA structure is extremely low.In the case of Charmm36, the DNA structure exhibited a fluctuating behavior from the beginning to the end of the simulation and a significant increase at the end of the simulation, indicating that the compactness of the DNA aptamer is exceedingly low.

The DNA-aptamer structures in the cases of OL15 and charmm36m exhibited similar behavior throughout the simulation, but both reached equilibrium at the conclusion of the simulation, with the case of OL15 reaching equilibrium in the last 5 ns.

4.21.4. Hydrogen bond analysis

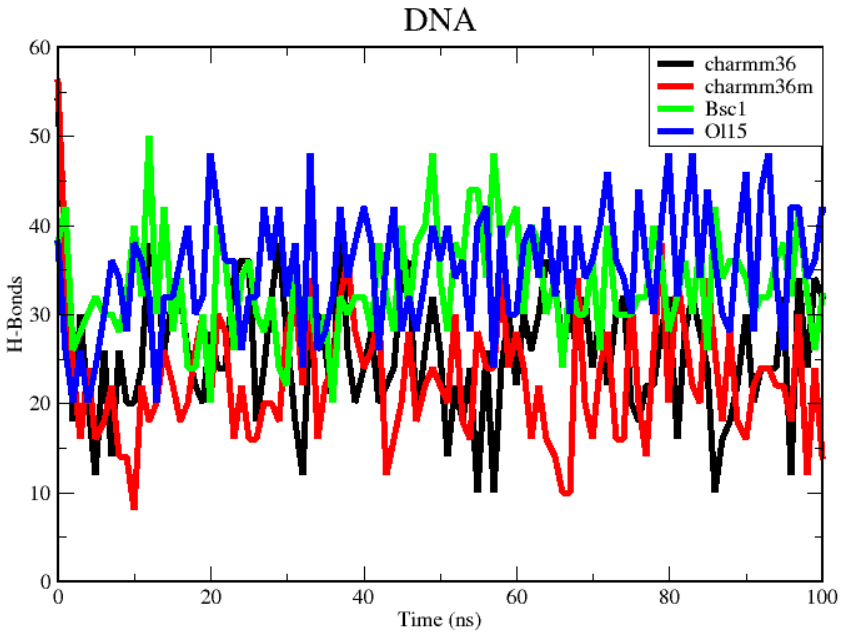

Figure 4.21.4. Represents the quantity of hydrogen bonds responsible for the 100 ns sustainability of the ss-DNA.

The graphical representation illustrates that the ss-DNA structures' maximum hydrogen bonding observed during the simulation is higher in bsc1 and ol15 cases. This indicates that the structure's stabilization is positively correlated with the increase in hydrogen bonding and is comparatively more stable than charmm36 and charmm36m.

4.22. Molecular dynamics results of the modeled Apo ss-DNA aptamer from the İfoldRNA

Gromacs software was used to conduct an MD simulation on Apo ss-DNA, which was modeled on the ifoldRNA server. This simulation lasted for one hundred nanoseconds and investigated the stability of Apo ss-DNA under the influence of four different force fields: Charmm36, Charmm36m, BSC1, and OL15.

4.22.1. Analysis of the Root Mean Square Deviation (RMSD)

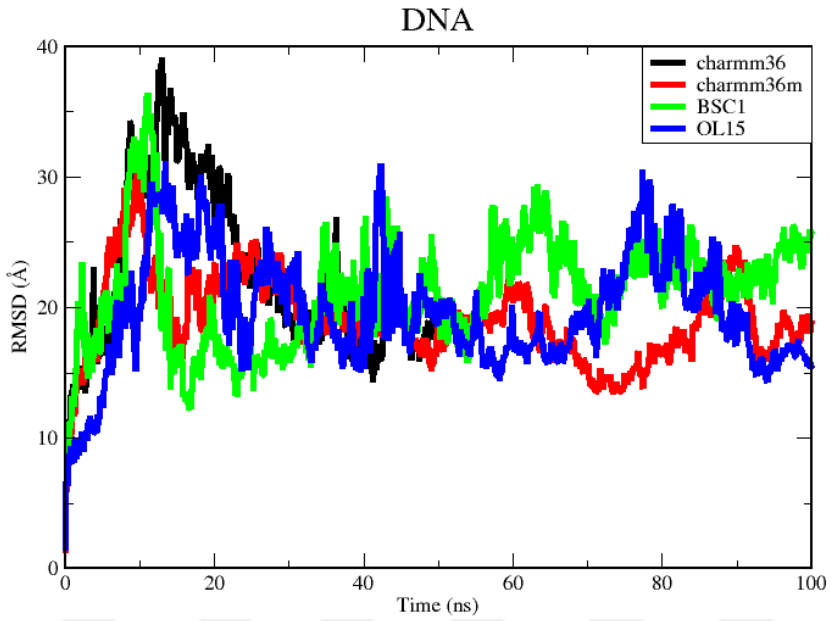

Figure 4.22.1. The evaluation root means square deviations (RMSDs) of Apo ss-DNA atoms versus 100 ns of MD simulation.

Upon examination of the RMSD plot, it is evident that the apo DNA structures exhibit varying RMSD values. Specifically, the charmm36 model displays the highest RMSD value, whereas the DNA structure in the BSC1 state exhibits the lowest RMSD value.

During the initial 10 ns of the simulation, it was observed that the root mean square deviation (RMSD) value significantly increased in four cases. This observation suggests that the structure of the single-stranded DNA aptamer did not undergo proper folding. Despite observing a notable decline in the root-mean-square deviation (RMSD) values following 10 ns, there were fluctuations evident in each cases over the course of the simulation. In the case of BSC1, the molecular configuration achieved stabilization during the final 5 ns of the simulation.

4.22.2. Assessment of RMSF

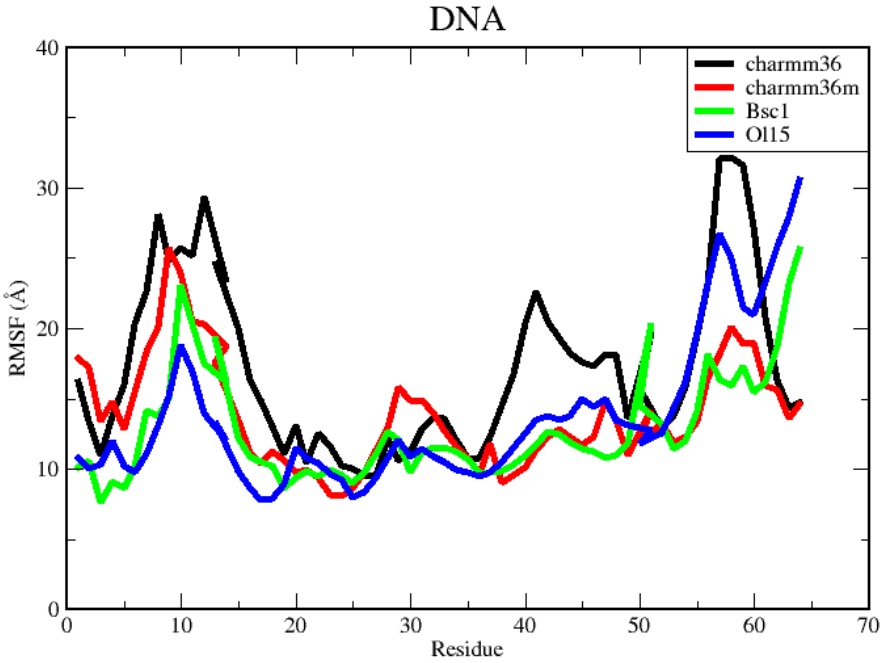

Figure 4.22.2. Residual fluctuations (RMSF) of ss-DNA atoms during 100 ns MD simulations

Upon analysis of the RMSF plots, it is evident that the charmm36 model demonstrates the greatest RMSF magnitude, while the BSC1 model exhibits the lowest RMSF magnitude. The regions that exhibit the most significant elevation are situated in the hairpin stem and loop regions of the aptamer configuration, leading to a reduction in the stability of the aptamer-DNA structure.

4.22.3. Analysis of Radius of gyration (RG)

Upon examination of the graph, it is evident that the RG values for both charmm36 and charmm36m exhibit a notable increase, particularly at the 80 and 90 ns marks of the simulation, where the Rg value reaches its maximum level. Regarding Bsc1 and Ol15, it can be observed that despite a lower Rg value, the structures exhibit instability throughout the simulation. However, they are comparatively more stable than Charmm36 and Charmm36m.

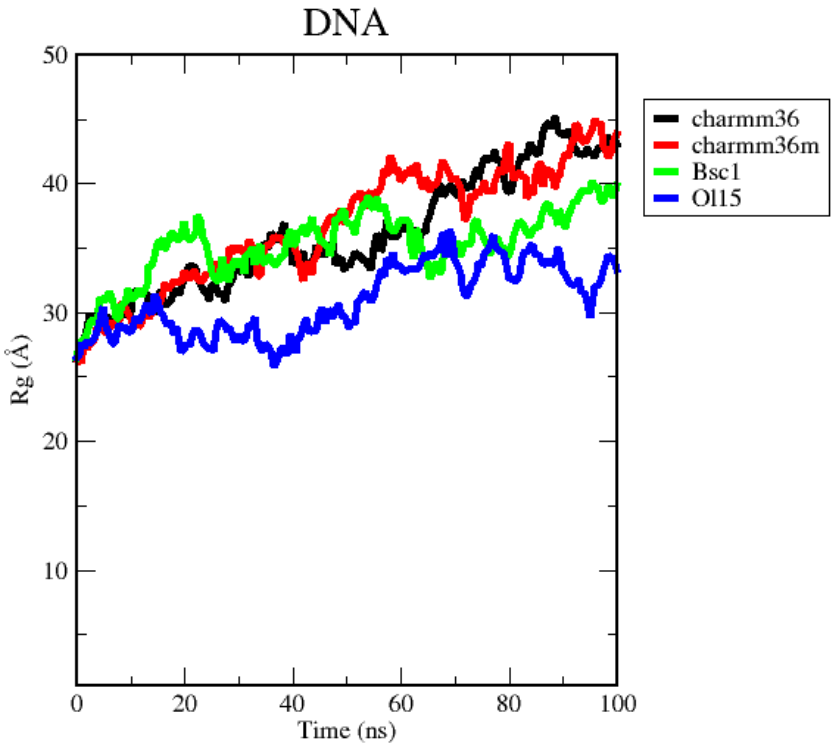

Figure 4.22.3. Represents the ROG values of the Apo ss-DNA for 100 ns.

4.22.4. Hydrogen bond analysis

The evaluation of hydrogen bonds established by Apo ss-DNA was computed throughout a simulation duration of 100 ns and graphically illustrated in Figure 10. The graphical depiction demonstrates that the highest level of hydrogen bonding observed during the simulation of ss-DNA structures is greater in the bsc1 and ol15 cases.

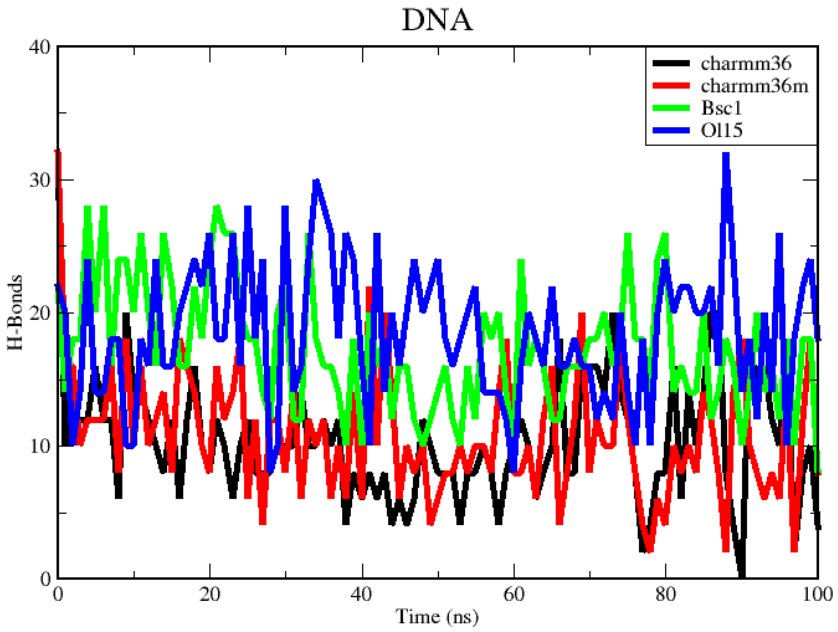

Figure 4.22.4. Represents the quantity of hydrogen bonds responsible for the 100 ns sustainability of the ss-DNA.

4.23. Molecular Dynamics Results of The Modeled Apo SS-DNA Aptamer from The Avogadro

The stability of ss-DNA was assessed over a period of 100 ns through the utilization of Gromacs and Namd in the evaluation of the results obtained from the MD simulation. Several metrics, including the radius of gyration, RMSD, RMSF, and hydrogen bonding, were examined. A comparison is made between the graphs of said parameters utilizing the four designated force fields.

4.23.1. Analysis of RMSD

Upon examination of the RMSD plot, it is evident that the apo DNA structures in the charmm36 and charmm36m states exhibit a greater RMSD value compared to bsc1 and ol15. Specifically, the charmm36 state displays the highest RMSD value, whereas bsc1 demonstrates the lowest RMSD value.

RMSD	Charmm36	Charmm36m	BSC1	OL15
DNA	17.89	21.02	10.005	11.07

Table 4.23.1. DNA RMSD values by force field

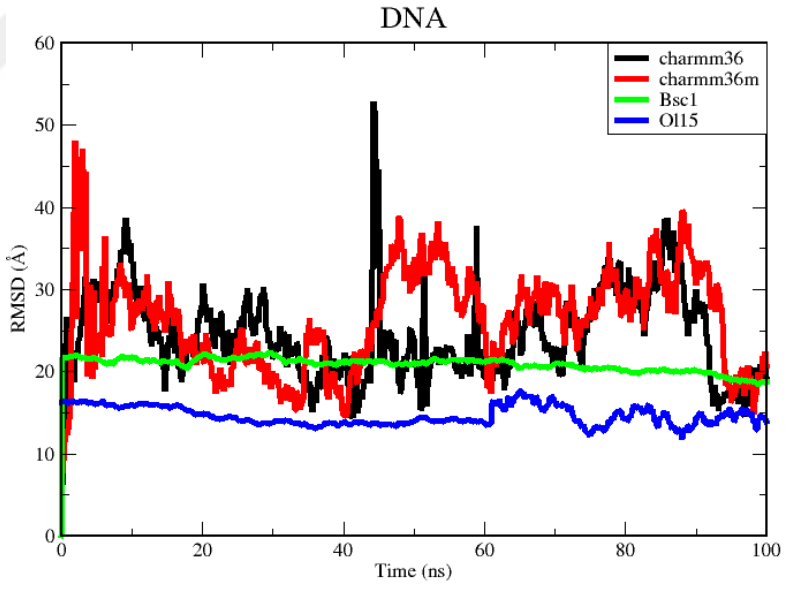

Figure 4.23.1. The evaluation root means square deviations (RMSDs) of Apo ss-DNA atoms versus 100 ns of MD simulation.

In the case of charmm36 and charmm36m, an increase in the rmsd value is observed from the starting position of the simulation and the structures exhibited similar behaviour until 45 ns, but charmm36 reached the highest rmsd value at 45 ns.

Throughout the simulation, the DNA structures in both the bsc1 and ol15 cases remained constant. Notably, the bsc1 case exhibited greater stability than ol15, despite having a higher root-mean-square deviation value.

4.23.2. Assessment of RMSF

Upon examination of the RMSF graphs, it is observed that the charmm36 and charmm36m models exhibit the most elevated RMSF values, whereas the Bsc1 model demonstrates the least RMSF value. The regions exhibiting the highest degree of peak concentration in the context of charmm36 and charmm36m are the bases located within the hairpin loop, as well as the internal loop region situated towards the terminus of the ss-DNA aptamer 5' 3' sequence. The aforementioned regions are known to induce a reduction in stability of the aptamer-DNA structure. The region with the highest peak in BSC1 is the 60–63 range of the internal loop, which makes the aptamer DNA structure more flexible, whereas in OL15, similar to BSC1, the internal loop bases render the structure unstable.

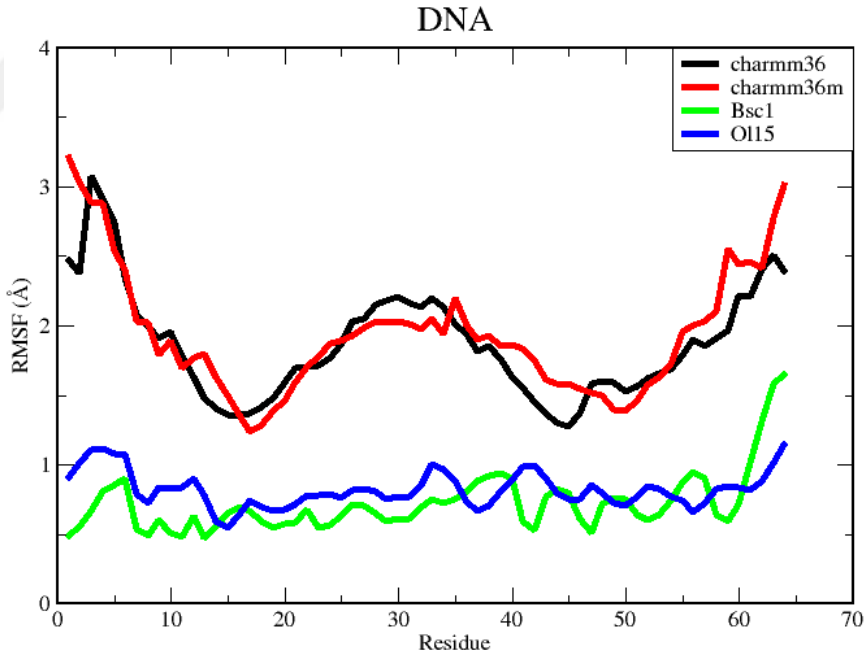

Figure 4.23.2. Residual fluctuations (RMSF) of ss-DNA atoms during 100 ns MD simulations

4.23.3. Analysis of Radius of gyration (RG)

The graph indicates that the DNA structures in the BSC1 and Charmm36 cases demonstrated similar behavior throughout the simulation. Furthermore, the compactness of the structure remained relatively stable, as evidenced by the lack of significant fluctuations in Rg values for both cases during the simulation.

The Charmm36m and OL15 simulations exhibited a notable disparity in the Rg value, particularly beyond the 60 ns. Specifically, the Charmm36m Rg value demonstrated a decline, whereas the OL15 Rg value displayed an increase. The degree of compactness that the aptamer structure displayed depended on the magnitude of the aforementioned changes.

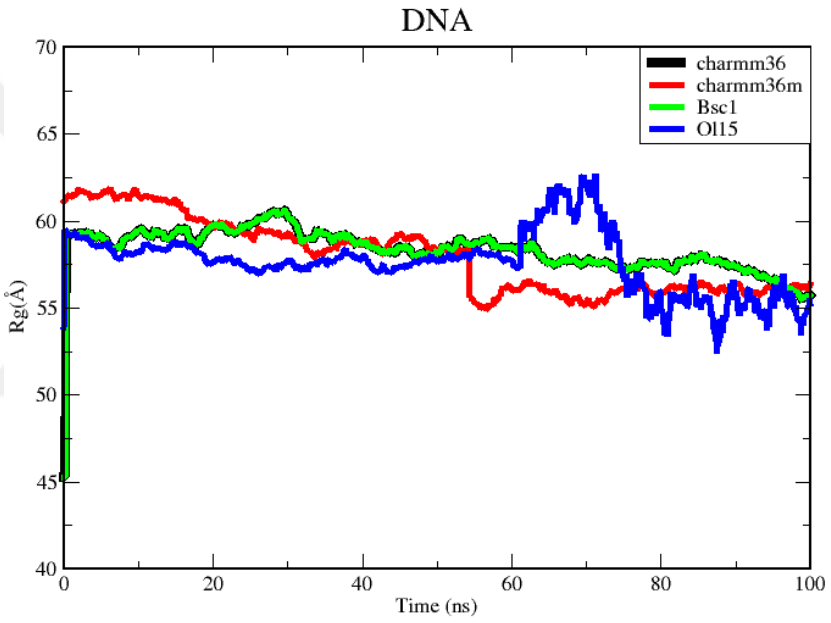

Figure 4.23.3. Represents the ROG values of the Apo ss-DNA for 100 ns.

4.23.4. Hydrogen bond analysis

In addition to analyzing RMSD and RMSF)of Apo ss-DNA during the simulation, the stability of hydrogen bonds (H-bonds) was also analyzed. During the complete 100 nanosecond molecular dynamics simulation, dynamic behavior of the amount of hydrogen bonds were observed in the single-stranded DNA without a ligand, as depicted in Figure 9.

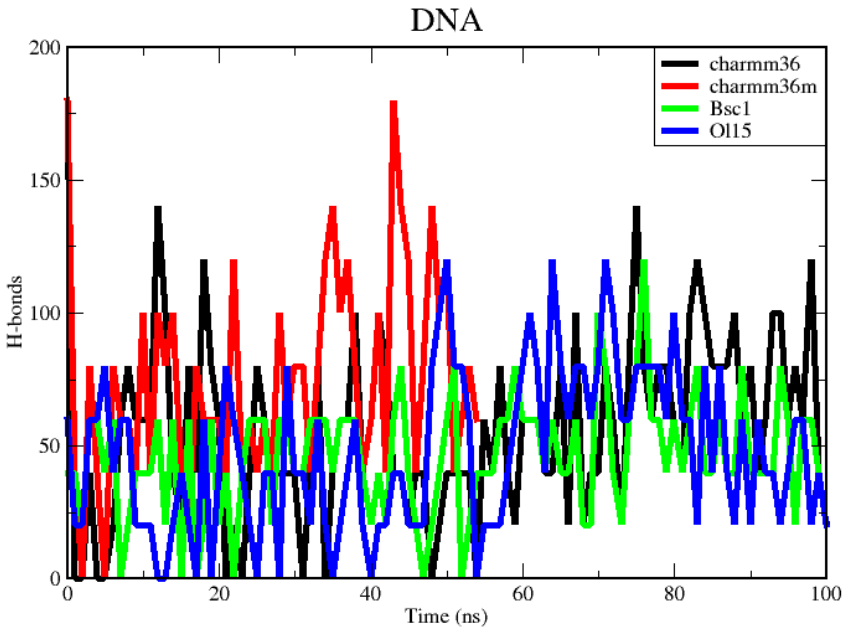

Figure 4.23.4. Represents the quantity of hydrogen bonds responsible for the 100 ns sustainability of the ss-DNA

The present study reveals that ss-DNA structures exhibit hydrogen bonding up to the initial 50 ns in the charmm36 and charmm36m cases, whereas in the bsc1 and ol15 cases, hydrogen bonding is observed throughout the simulation.

4.24. Molecular dynamics results of the modeled Apo ss-DNA aptamer from the Schrodinger

Apo ss-DNA, modeled from Schrodinger's software, has been submitted to the MD simulation to study stability for the four force fields utilizing Gromacs software for 100 ns, Charmm36, Charmm36m strength fields, and Namd software for BSC1 and OL15.

4.24.1. Analysis of RMSD

When we look at the RMSD graph, the rmsd values of the apo DNA structures bsc1, and ol15 force field DNA structures, charmm36 and charmm36m force field have a greater RMSD value, and OL15 has the greatest rmsd value, while the DNA structure in the charmm36m state has the lowest rmsd structure.

RMSD	Charmm36	Charmm36m	BSC1	OL15
DNA	17.89	21.02	10.005	11.07

Table 4.24.1. DNA RMSD values by force field

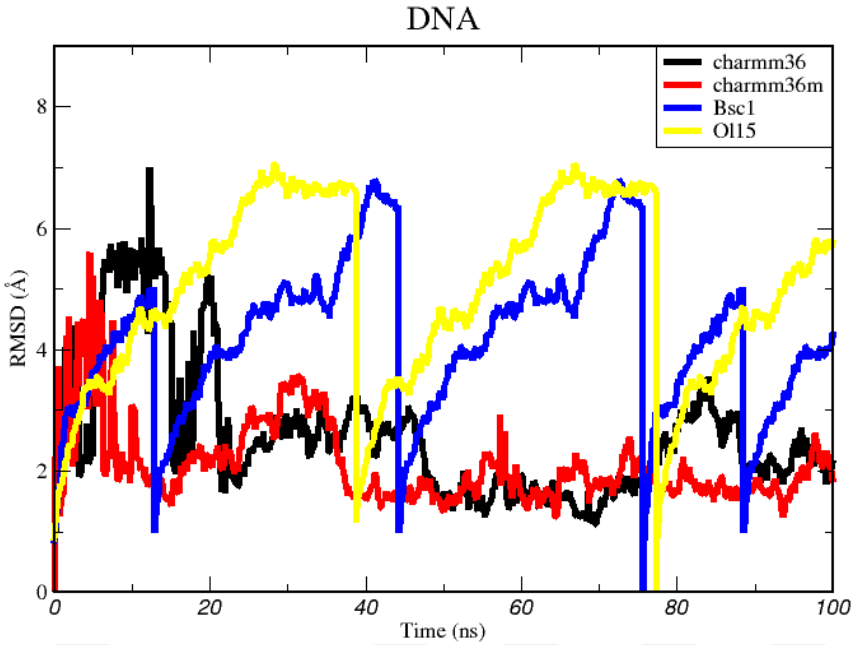

Figure 4.24.1. The evaluation root means square deviations (RMSDs) of Apo ss-DNA atoms versus 100 ns of MD simulation.

When we look at the graph, in the instance of charmm36, the RMSD value raised in the first 5 ns from the initial position, and then a sudden decrease was observed and continued with fluctuations throughout the simulation, while in the case of charmm36m, a high rmsd value was observed in the first 20 ns, and then the rmsd values decreased, but it exhibited an up and down situation throughout the simulation. The dna aptamer structures in the BSC1 and OL15 cases exhibited similar behaviour, both in terms of high rmsd values and high fluctuations and these structures were extremely unstable and did not demonstrate good folding.

4.24.2. Assessment of RMSF

When we look at the RMSF graphs, charmm36 displays the highest RMSF value, while OL15 has the lowest RMSF value. The highest peak regions for charmm36 and charmm36m are the bases in the hairpin loop region at the head end of the ss-DNA aptamer 5' 3' sequence. The RMSF values for Bsc1 and Ol15 are substantially lower compared to charmm36 and charmm36m. The region yielding the highest peak for Bsc1 is the base located in the hairpin loop region at the end of the ss-DNA aptamer 5' 3' sequence.

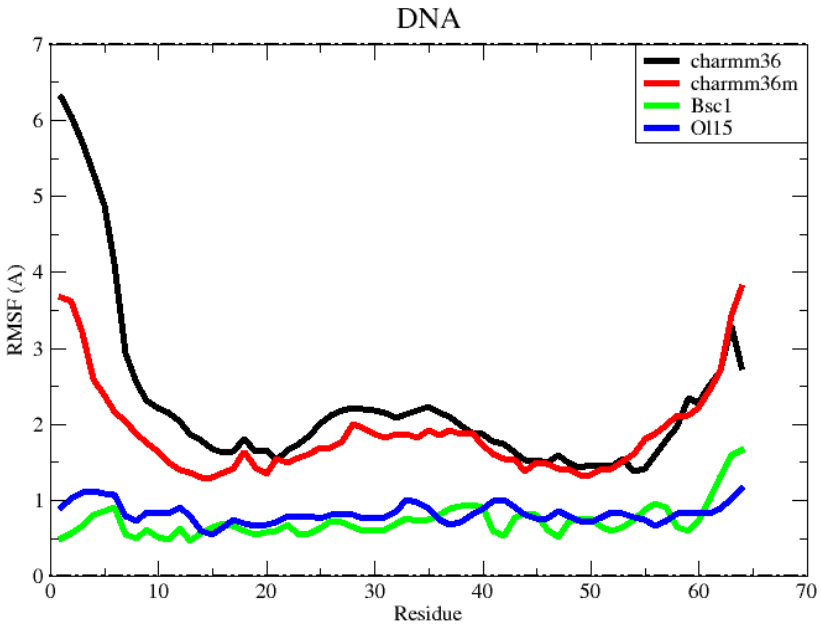

Figure 4.24.2. Residual fluctuations (RMSF) of ss-DNA atoms during 100 ns MD simulations

4.24.3. Analysis of Radius of gyration (RG)

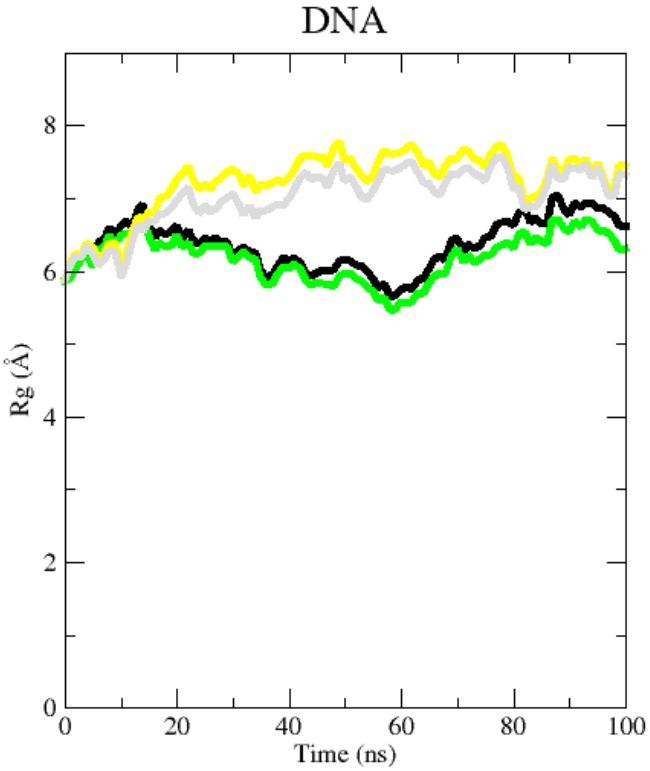

Figure 4.24.3. Represents the ROG values of the Apo ss-DNA for 100 ns.

The parameter Rg defines how compact a structure is. An rise in RoG values suggests a decrease in the compactness of DNA structures, indicating increased flexibility and decrease.When we look at the graph, charmm36 and charmm36m RG values are lower than bsc1 and ol15 in four different force fields, however Rg values are not stable for all four cases.

4.24.4. Hydrogen bond analysis

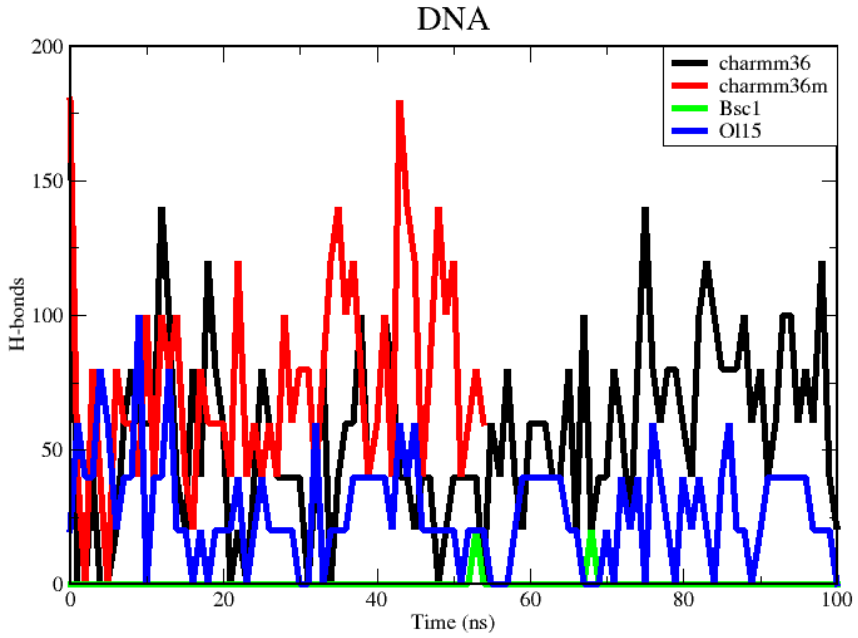

Figure 4.24.4. Represents the quantity of hydrogen bonds responsible for the 100 ns sustainability of the ss-DNA.

From the graph, it can be seen that in the case of charmm36m, ss-DNA structures exhibit hydrogen bonding up to the first 50 ns, while in the case of bsc1, very little hydrogen bonding was detected, and the strongest hydrogen bonding was recorded in charmm36.

4.25. Molecular dynamics results of the modeled Apo ss-DNA aptamer from the Discovery Studio Visualizer

Apo ss-DNA, modeled using Discovery Studio's program, has been assessed to the MD simulation to evaluate stability for the four force fields using Gromacs software for 100 ns, Charmm36 and Charmm36m strength fields, and Namd software for BSC1 and OL15.

4.25.1. Analysis of RMSD

When we look at the RMSD graph, the RMSD value of the apo DNA structures, charmm36, and charmm36m force field DNA structures has a bigger RMSD value than the bsc1 and ol15 force fields. In the case of Charmm36, a considerable increase in the rmsd value was noticed in the first 20 ns from the beginning point, and after 20 ns, it continued with ups and downs and reached the greatest rmsd value of roughly 40 ns.

RMSD	**Charmm36**	**Charmm36m**	**BSC1**	**OL15**
DNA	17.89	21.02	10.005	11.07

Table 4.25.1. DNA RMSD values by force field

After 40 ns, although the rmsd value reduced, the fluctuations in the rmsd values led to a shift in the stability of the structure. In the case of charmm36m, the structure did not continue in a constant range throughout the simulation and exhibited similar behavior to charmm36. In the cases of BSC1 and OL15, aptamers are more stable than charmm36 and charmm36m. Particularly in the case of OL15, the aptamer did not endure significant conformational changes during simulation, indicating that it is more stable than the other cases

4.25.2. Assessment of RMSF

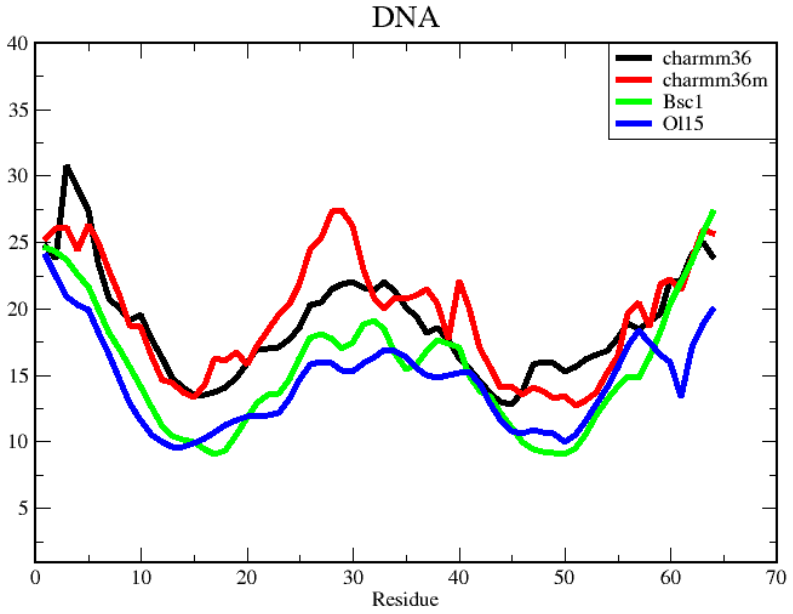

Figure 4.25.2. Residual fluctuations (RMSF) of ss-DNA atoms during 100 ns MD simulations

In the RMSF graphs, charmm36 has the highest value, while OL15 has the lowest. The bases at the end and head of the ss-DNA aptamer 5' 3' sequence, the hairpin loop, and the internal loop region are the most prominent regions for charmm36 and charmm36m.

The aforementioned regions have been observed to induce a reduction in stability of the aptamer-DNA structure. Furthermore, it was observed that the DNAs in both the bsc1 and ol15 cases exhibited significant root mean square fluctuation (rmsf) values within a similar range of regions. Notably, these bases are situated within the hairpin segment of the aptamer DNA structure and are believed to be responsible for the observed increase in the rmsf value.

4.25.3. Analysis of Radius of gyration (RG)

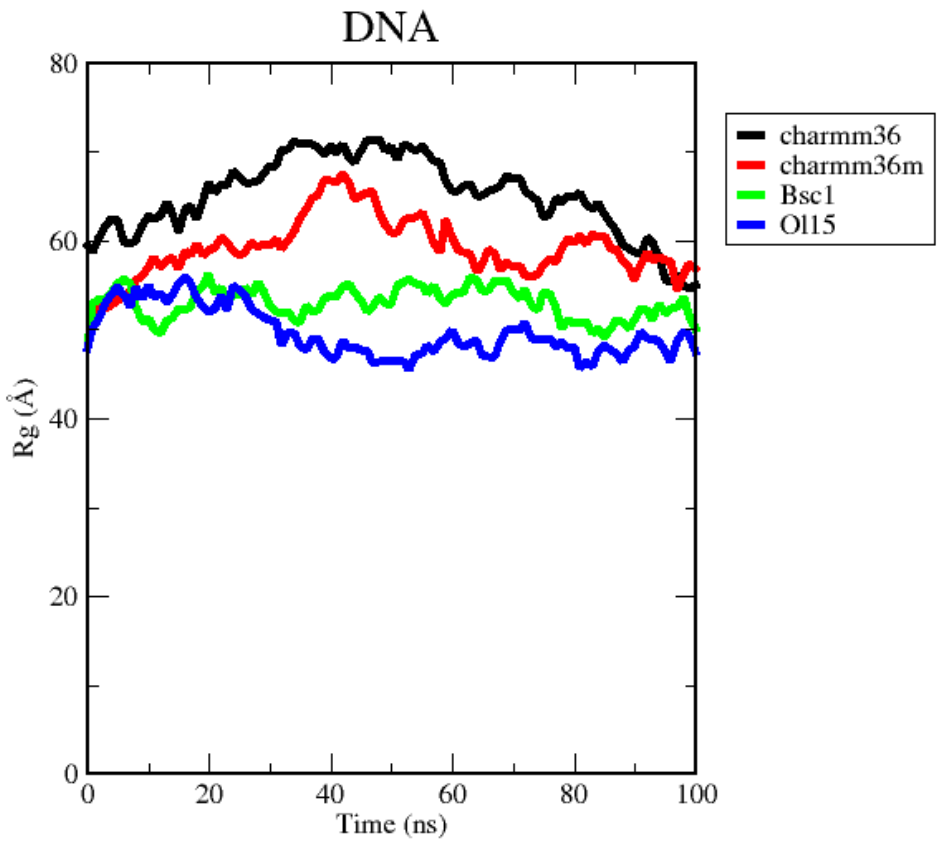

Figure 4.25.3. Represents the ROG values of the Apo ss-DNA for 100 ns.

The compactness of a structure is determined by the RG parameter. Upon examination of the graphical representation, it can be observed that the Rg values exhibit variability across four distinct force fields.

Specifically, the Rg values obtained from the charmm36 and charmm36m force fields are comparatively greater than those derived from the BSC1 and OL15 force fields. The structures in charmm36 and charmm36m have experienced a greater degree of conformational alterations and exhibit reduced levels of folding.

4.25.4. Hydrogen bond analysis

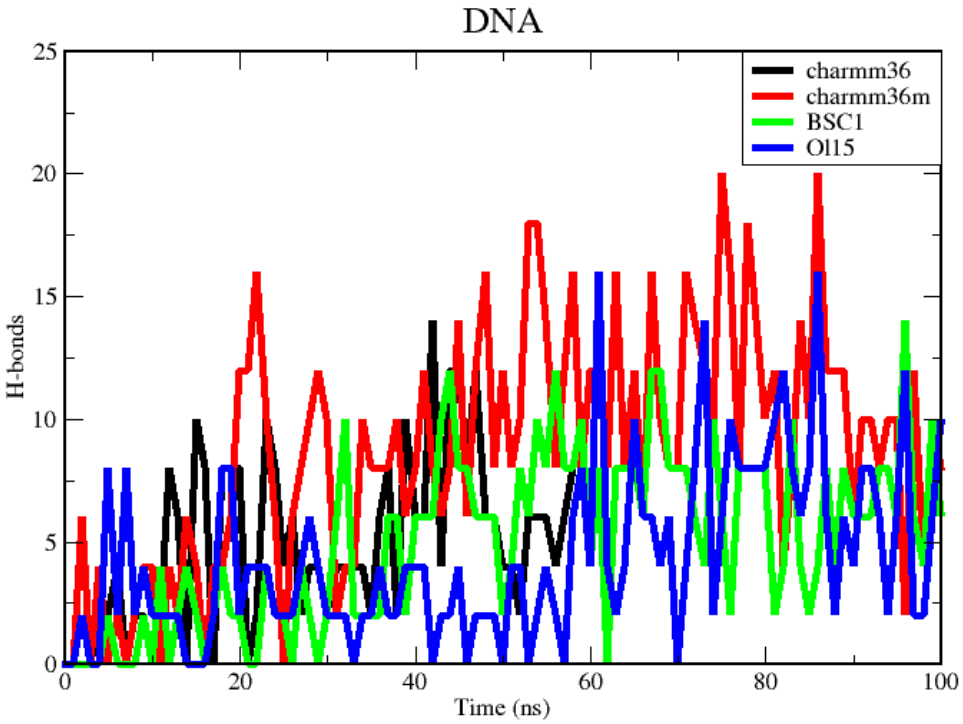

Figure 4.25.4. Represents the count of hydrogen bonds responsible for the stability of the ss-DNA throughout the 100 ns.

The graphical representation indicates that the charmm36m model demonstrates the superior level of hydrogen bonding throughout the simulation, whereas the charmm36 model displays hydrogen bonding numbers only up to 60 ns. In the BSc1 and Ol15 cases, hydrogen bonding is also seen throughout the simulation, but it is weaker than charmm36m.

4.26. Molecular dynamics results of the modeled Apo ss-DNA aptamer from the Nflex-Root

Four different force fields (Gromacs for 100 ns, Charmm36 and Charmm36m strength fields, and Namd for BSC1 and OL15) have been used to a model of Apo ss-DNA created in Nflex Root and subjected to MD simulation to assess stability.

4.26.1. Analysis of RMSD

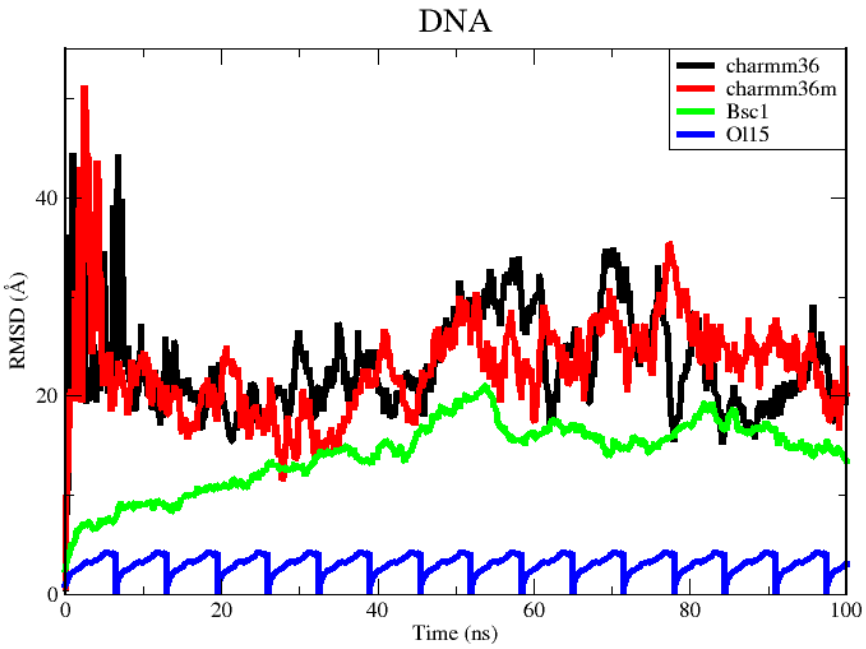

Figure 4.26.1. The evaluation root means square deviations (RMSDs) of Apo ss-DNA atoms versus 100 ns of MD simulation.

When examining the RMSD graph, the RMSD values for the apo DNA structures, charmm36, and charmm36m force field DNA structures are greater than those for bsc1 and ol15. When comparing the graphs of charmm36 and charmm36m, the rmsd value increased substantially within the first 10 nanoseconds. Despite a substantial decrease in rmsd values afterward, the simulation revealed a great deal of fluctuation, indicating that the structures do not fold. Although the Bsc1 structure endures conformational changes throughout the simulation, it is more stable than those of charmm36 and charmm36m, whereas the ol15 structure is outside the periodic boundary conditions and is extremely unstable.

4.26.2. Assessment of RMSF

The RMSF graphs indicate that the charmm36 model exhibits the greatest value, whereas the OL15 model displays the least value.

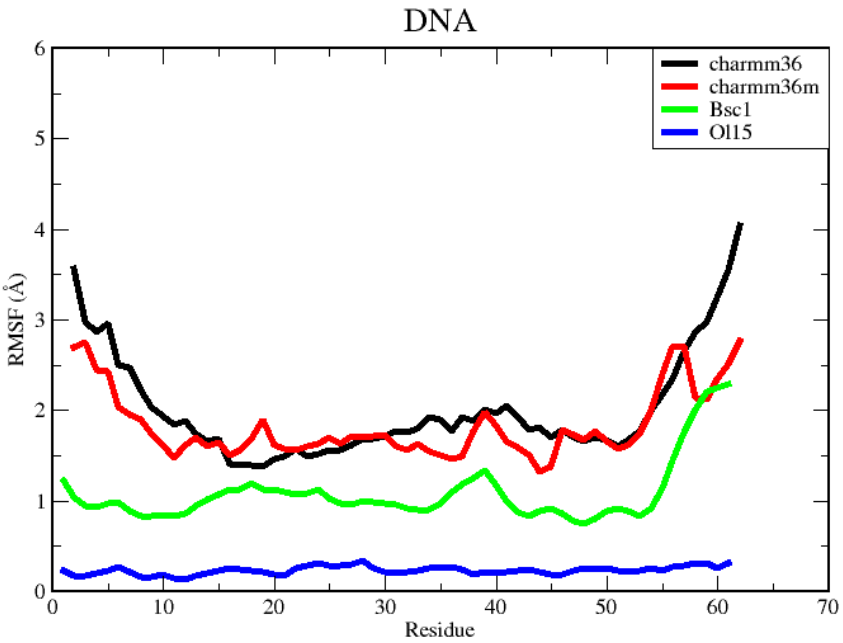

Figure 4.26.2. Residual fluctuations (RMSF) of ss-DNA atoms during 100 ns MD simulations

The most notable regions for charmm36 and bsc1 are the bases at the end and beginning of the Ss-DNA aptamer 5' 3' sequence, the hairpin loop, and the inner loop region. In contrast to the other three instances, the bases between 20 and 30 are the most prominent regions in Ol15.

4.26.3. Analysis of Radius of gyration (RG)

Compared to charmm36 and charmm36m, BSC1 and OL15 DNA structures have lesser radii of gyration. Therefore, the DNA structures of charmm36 and charmm36m have endured more conformational changes. During simulation, DNA constructs treated with BSC1 and OL15 were able to maintain a greater degree of stability, according to the findings.

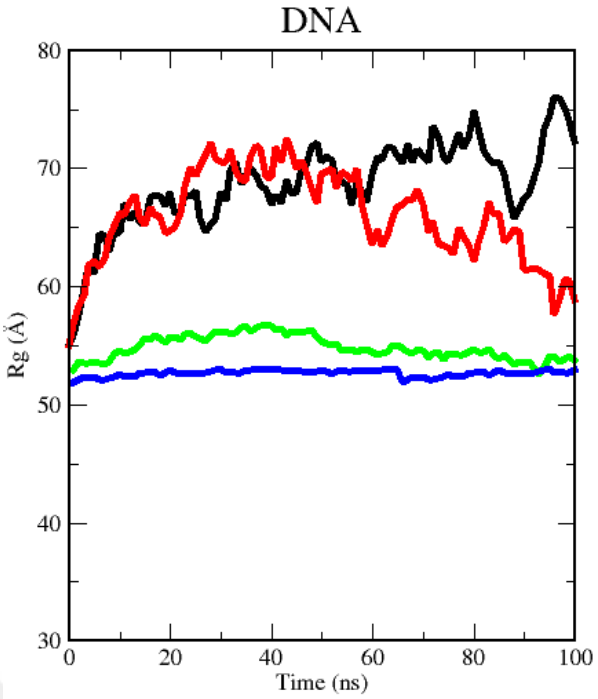

Figure 4.26.3. Represents the ROG values of the Apo ss-DNA for 100 ns.

4.26.4. Hydrogen bond analysis

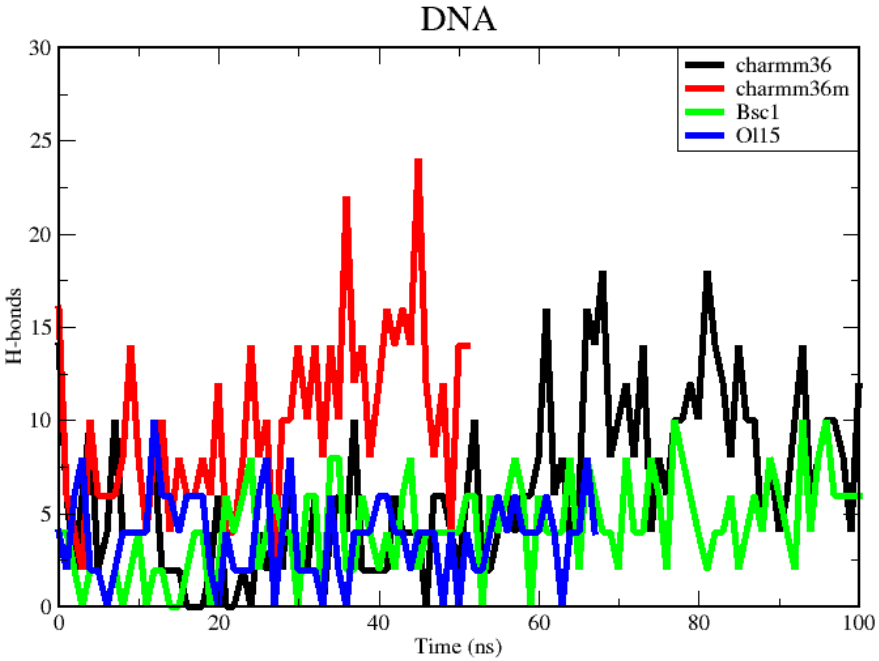

Figure 4.26.4. Represents the count of hydrogen bonds responsible for the stability of the ss-DNA throughout the 100 ns.

4.27. Molecular dynamics results of the modeled Apo ss-DNA aptamer from the X3DNA

A model of Apo ss-DNA was built in X3dna and subjected to MD simulation to evaluate stability using four distinct force fields (Gromacs for 100 ns, Charmm36 and Charmm36m strength fields, and Namd for BSC1 and OL15).

4.27.1. Analysis of the RMSD

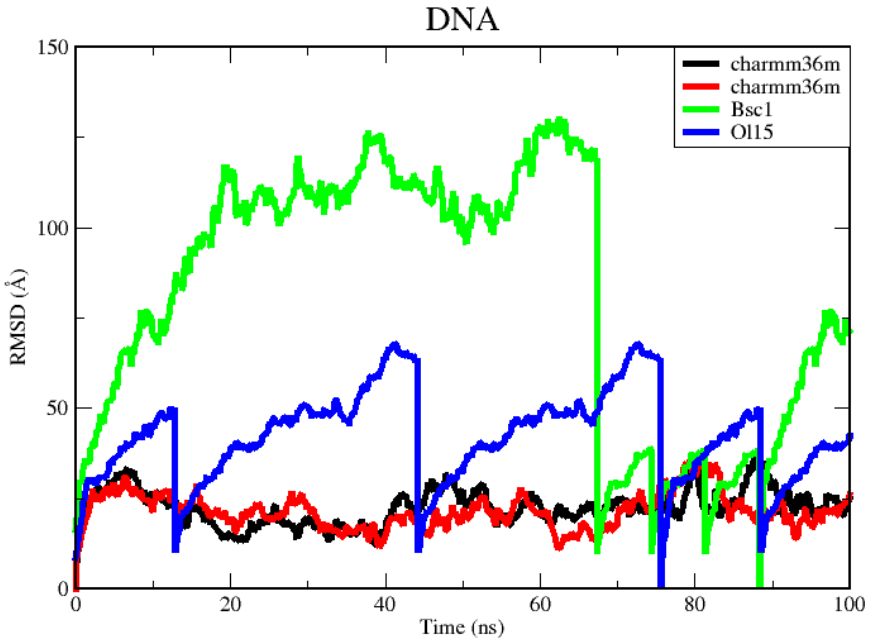

Figure 4.27.1. The evaluation root means square deviations (RMSDs) of Apo ss-DNA atoms versus 100 ns of MD simulation.

When examining the graph, the case with the highest RMSD value is BSC1, while the case with the lowest RMSD value is Charmm36m. Throughout the simulation, the ss-dna structures of charmm36 and charmm36m are more stable than those of ol15 and bsc1 due to lower rmsd values and fewer fluctuations.

4.27.2. Assessment of RMSF

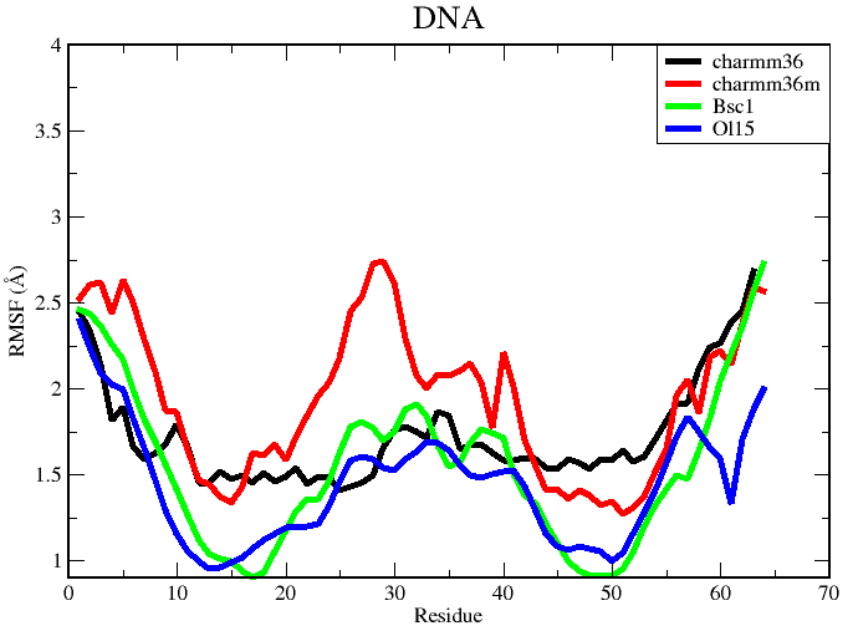

Figure 4.27.2. Residual fluctuations (RMSF) of ss-DNA atoms during 100 ns MD simulations

Ol15 displays the lowest RMSF peak, while charmm36m displays the maximum RMSF peak. In the case of charmm36m, the regions exhibiting high peaks are 25–30, and the bases are located at the sequence's end. In the case of Charmm36, Bsc1, and Ol15, the most flexible regions of ss-dna structures are the bases at the head and end of the sequence; these bases are located in the hairpin loop and internal region of the aptamer structure and make the structure less stable.

4.27.3. Analysis of Radius of gyration (RG)

The DNA structures of BSC1 and OL15 have reduced radii of gyration compared to those of charmm36 and charmm36m. However, considerable fluctuations are shown during the simulation, and the Rg values for all four examples are not constant, indicating that the ss-DNA aptamers for each case are exceedingly unstable and do not display good folding.

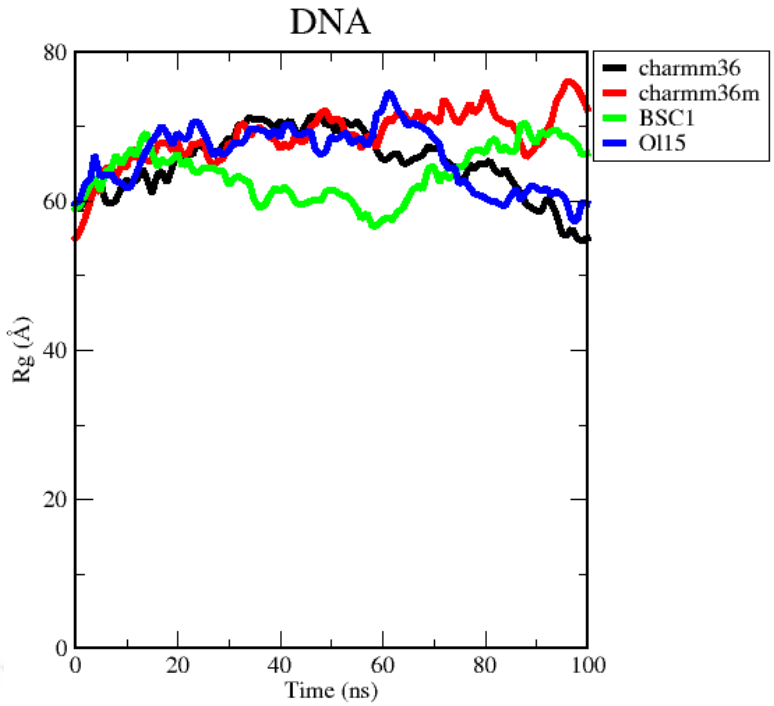

Figure 4.27.3. Represents the ROG values of the Apo ss-DNA for 100 ns.

4.27.4. Hydrogen bond analysis

The Bsc1 model exhibits the highest degree of hydrogen bonding throughout the simulation, whereas the charmm36m model exhibits the highest degree of hydrogen bonding only up to 40 ns. The charmm36 and Ol15 cases also exhibit the highest degree of hydrogen bond formation throughout the simulation, but to a lesser extent than Bsc1.

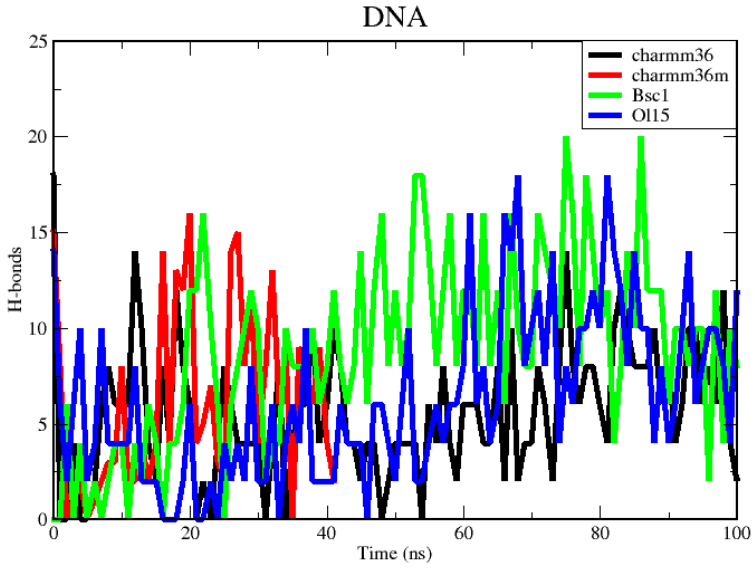

Figure 27.4.4. Represents the number of hydrogen bonds responsible for the stability of the ss-DNA throughout the 100 ns.

4.28. Molecular dynamic simulation analysis of the modeled SS-DNA aptamer from the Sim-RNA server against bisphenol A

The ss-dna-ligand complex formed through molecular docking was selected for molecular dynamics simulation with a 100 ns time scale utilizing the two versions of the AMBER force field and the two versions of Charmm force fields. Multiple variables like the radius of gyration, rmsd, rmsf, and h-bond were investigated. The graphs of these parameters using the four force fields specified are compared.

4.28.1. Analysis of RMSD

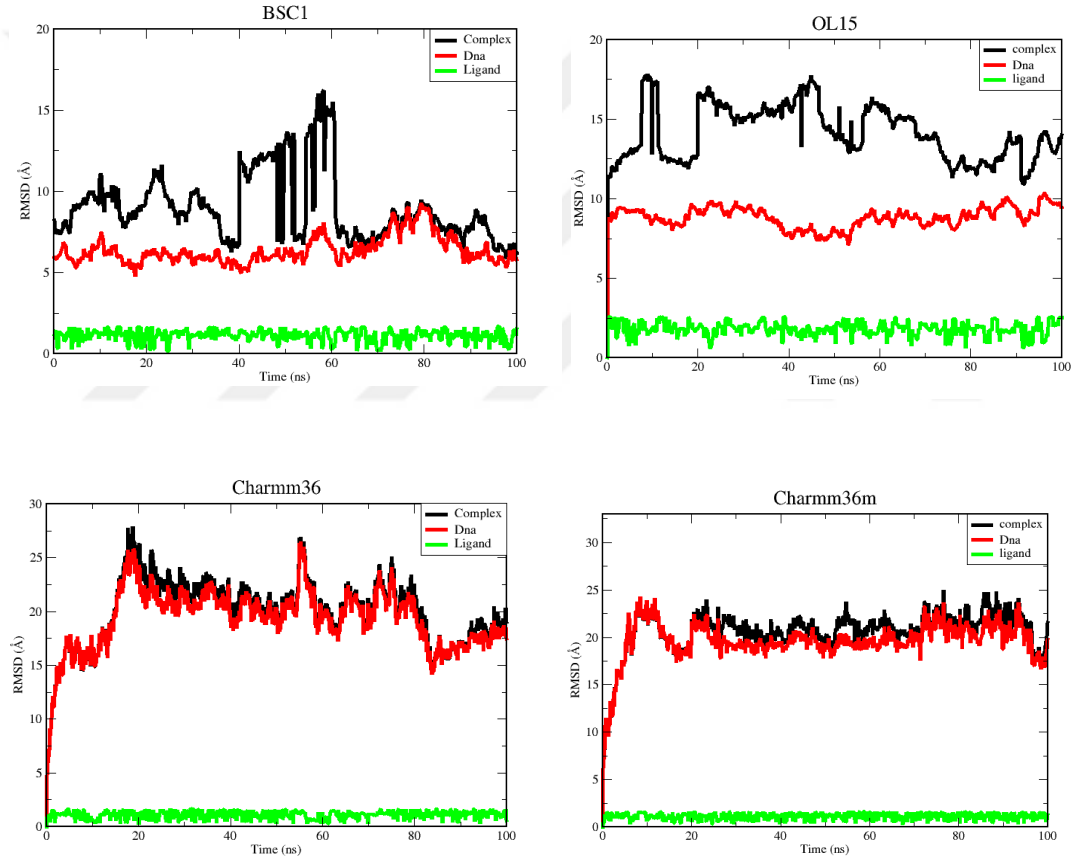

Figure 4.28.1. RMSDs of the SS-DNA-ligand complex versus 100 ns of MD simulation for each force field

charmm36m has the highest RMSD value of the four complex structures, while bsc1 has the lowest. The comparative analysis of figures charmm36 and charmm36m reveals that the aptamer structure of the DNA-ligand complex exhibits a reduced RMSD value in comparison to charmm36m.

The RMSD values for the complexes in the charmm36 and charmm36m models are 20.20 Å and 20.94 Å, respectively. Increased RMSD values resulted in a notable alteration in the conformation of the DNA-ligand complex, leading to decreased stability.

RMSD	Ligand	Dna	Complex
Charmm36	1.718	19.25	20.20
Charmm36m	1.757	19.55	20.94
BSC1	1.761	6.329	9.009
OL15	2.01	8.904	14.08

Table 4.28.1. RMSD values by force field

The ligand bisphenol-A exhibits a lower root-mean-square deviation value in binding with charmm36. However, it displays substantial fluctuations throughout the simulation. Conversely, in the case of the complex structure charmm36m with the identical ligand, notable fluctuations were observed only during the initial 20 ns of the simulation and remained relatively stable thereafter. While exhibiting the lowest root-mean-square deviation RMSD value in the bsc1 state, the DNA-ligand complex demonstrated the greatest RMSD value during the timeframe of 40 to 60 ns. Subsequent to this temporal interval, the RMSD exhibited a decrease to a certain degree, albeit with notable oscillations, and ultimately stabilized during the final 5 ns of the simulation.

Upon examination of ol15, it is observed that its root-mean-square deviation (RMSD) value is greater than that of bsc1, yet less than that of charmm36 and charmm36m. However, ol15 exhibits significant fluctuations during the simulation, particularly within the initial 10 ns and between 20 and 40 ns, where it displays the highest RMSD values. Subsequent to this temporal point, despite a drop in the RMSD measure fluctuations persist throughout the simulation, thereby indicating that an equilibrium state is not attained.

Upon examination of the ligands, it was observed that in the context of charmm36, the ligand displayed a diminished root-mean-square deviation (RMSD) in comparison to charmm36m, bsc1, and ol15. Specifically, the mean RMSD value of the ligand was recorded as 1.718 Å, 1.757 Å, 1.761 Å, and 2.01 Å, correspondingly. While the RMSD value for the binding of the bisphenol ligand in charmm36 is low, it exhibits greater fluctuations during the simulation in comparison to charmm36m. The ligand exhibited reduced root-mean-square deviation (RMSD) and lower fluctuations in BSC1 as compared to O15. Regarding O15, it can be inferred that the ligand is outside of its domain due to its high rmsd and increased fluctuations.

This suggests a change in the binding direction of the ligand in the case of O15. Furthermore, the trajectories were examined, and the findings indicated that the ligands exhibited movement away from the DNA domain and the binding site at specific intervals.

4.28.2. Analysis of RMSF

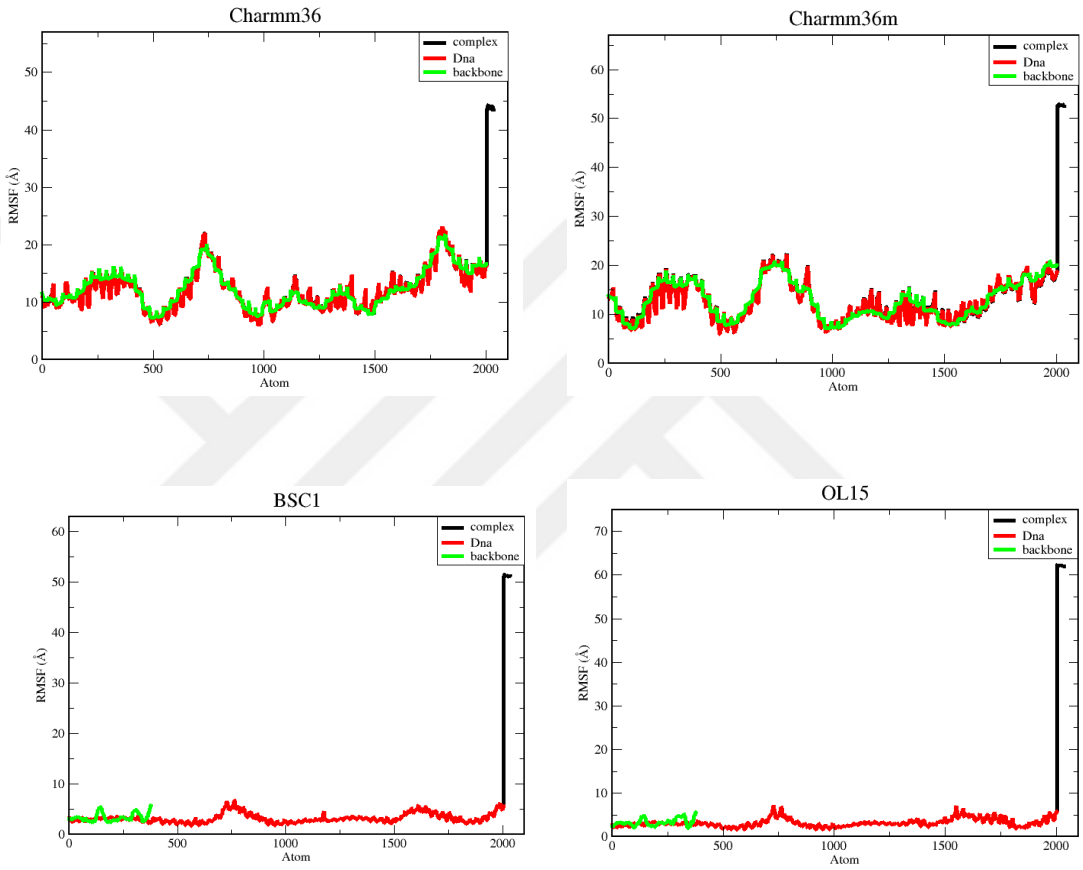

Figure 4.28.2. RMSFs of the SS-DNA-ligand complex versus 100 ns of MD simulation for each force field

The Charmm36 graph displays noteworthy fluctuations in the base indices of 56–58 and 23–25, with the corresponding base pairs being T–C–G and A–G–C, respectively. The DNA aptamer structure exhibits high RMSF values for three bases (A-G-C) that are situated in the duplex region and outside the binding site. Additionally, the base pairs located in the hairpin loop region (56–58) display higher RMSF values despite being located within the binding site.

The Charmm36m graph exhibits notable peaks that surpass those of Charmm36, and the root mean square fluctuation (RMSF) values are also higher in Charmm36m compared to Charmm36. Conversely, upon examining the BSC1 and OL15 graphs, it is observed that the notable peaks are commensurate with those of Charmm36. However, the RMSF peaks for both DNAs exhibit a lower magnitude compared to charmm36 and charmm36m.

Upon examination of the complex systems, it is observed that the OL15 complex exhibits the greatest root-mean-square fluctuation (RMSF) value, whereas the Charmm36 complex displays the lowest value. This suggests that the OL15 complex possesses a more unconstrained terminal loop. Furthermore, it is noteworthy that the prominent peaks observed in both DNA and complex structures exhibit identical base pairs within corresponding regions for charmm36m, bsc1, and ol15. These regions are situated in the hairpin loop of the DNA aptamer structure, which is known to decrease its stability.

4.28.2. Gyration Radius Variation

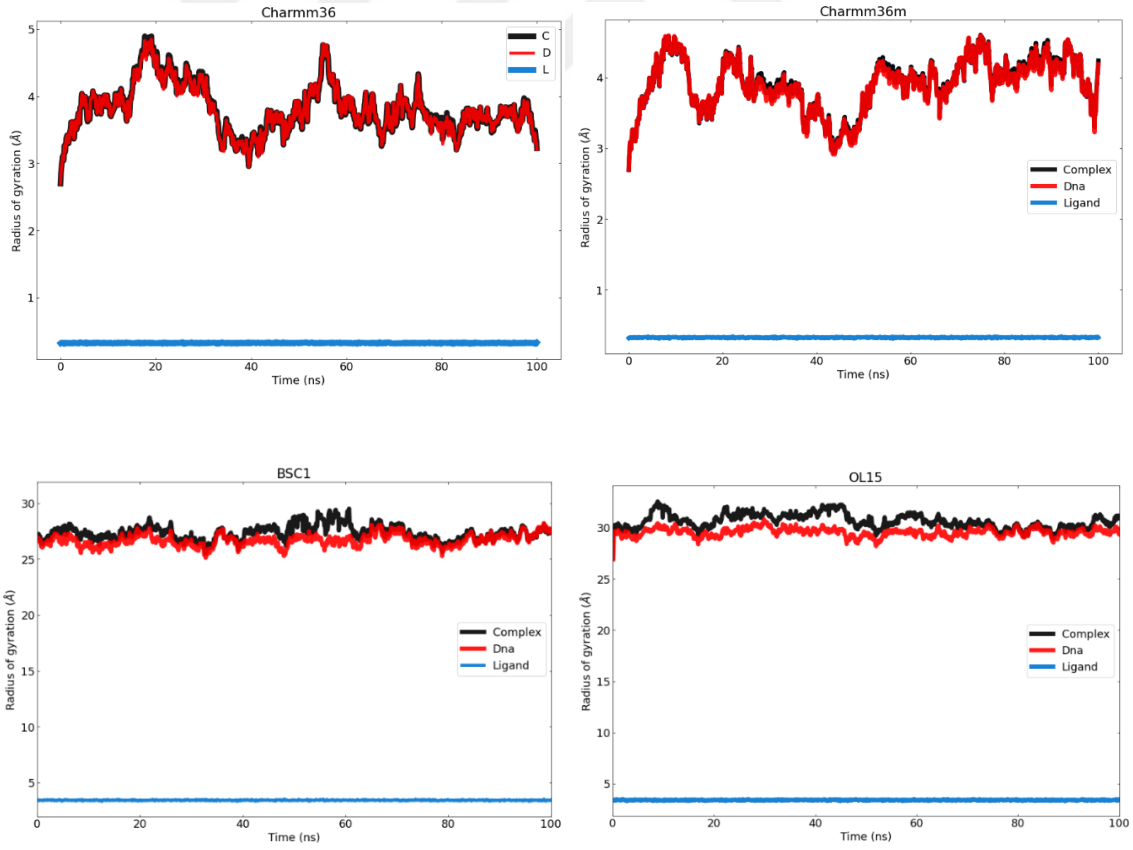

Figure 4.28.3. RGs of the SS-DNA-ligand complex versus 100 ns of MD simulation for each force field

The Charmm36 graph indicates that the DNA-ligand complex exhibited an average RG value exceeding 4.5 Å and displayed the greatest deviation, particularly following the initial 10 ns. However, a notable reduction was observed at 40 ns. The compactness of the structure exhibited an upward trend at 50 ns, while the average radius of gyration (Rg) remained stable with minor fluctuations from that point until the conclusion of the simulation.

The complex system in charmm36m exhibited a notable RG value, particularly during the initial stages of the simulation. Subsequently, the RG value decreased, but it experienced a subsequent increase after 50 ns. In contrast to the charmm36 model, the level of compactness exhibits a higher degree throughout the entirety of the simulation, while the stability of the system is comparatively reduced.

In contrast, the compactness exhibited by the BSC1 and OL15 systems differs significantly from that of the charmm36 and charmm36m systems. Despite the elevated RG values observed in BSC1 and OL15, it is noteworthy that the complexes exhibit a notable degree of stability and compactness, as evidenced by their lack of significant alteration.

In comparison to BSC1 and OL15, the DNA-ligand complex exhibited a smaller radius of gyration in BSC1 and demonstrated a greater degree of stability throughout the simulation. Therefore, it can be inferred that the complex displays a stronger binding affinity with the ligand in BSC1 as opposed to OL15.

The observed decrease in compactness in the CHARMM36 and CHARMM36m models could potentially be attributed to an alteration in the interaction profile between the DNA and ligand species. In general, the results of the RG analysis indicated that the interaction of the aforementioned four molecules led to alterations in the molecular structure.

4.28.4. Hydrogen bond

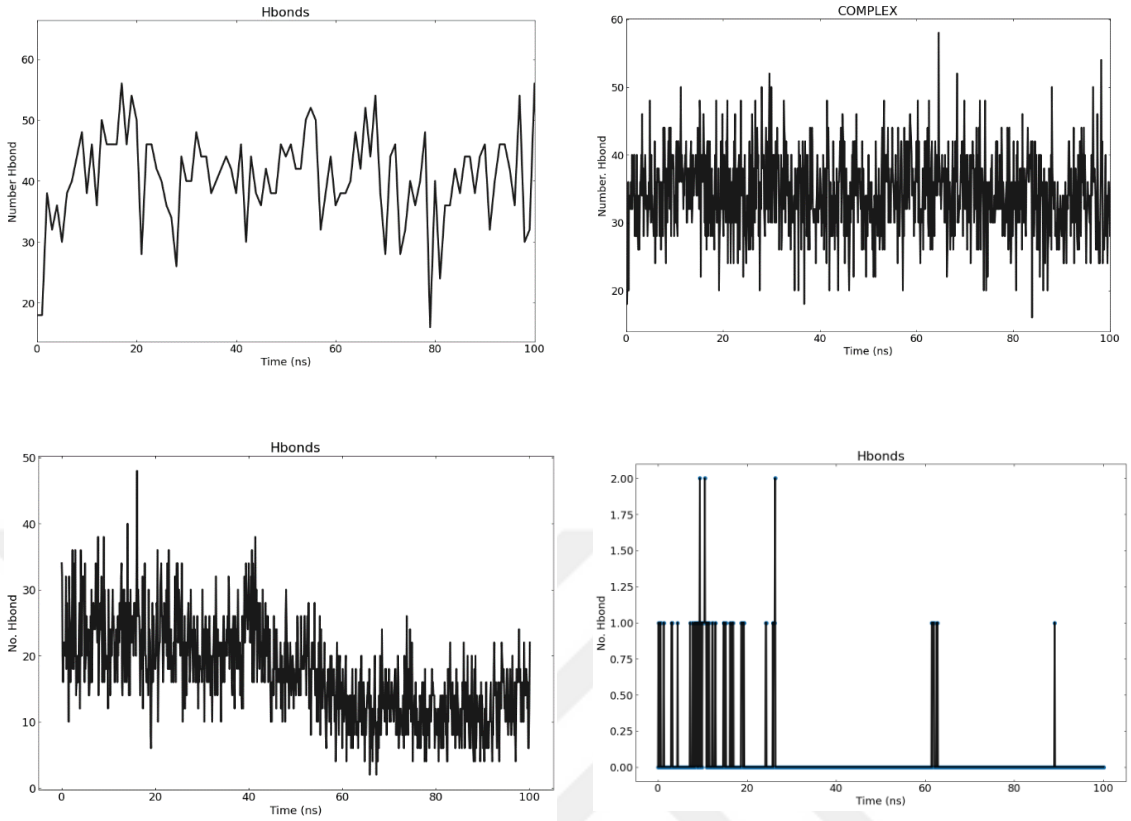

Figure 4.28.4. Hbonds of the SS-DNA-ligand complex versus 100 ns of MD simulation for each force field

Throughout the entirety of the MD simulation, it was turned out that the number of hydrogen bonds within the single-stranded DNA with ligand state displayed dynamic tendencies, as illustrated in Figure 4.28.4. The graphical representation illustrates that the OL15 state displayed the highest count of hydrogen bonds among the complex structures, whereas the BSC1 state exhibited the lowest count of hydrogen bonds. The enhanced stability of the structures that are formed is correlated with an increased quantity of hydrogen bonds.

4.28.5. Analysis of PCA and DCCM

PCA is a valuable methodology for extracting significant insights from Molecular Dynamics (MD) trajectories through the segregation of global slow motions from local fast motions.The utilization of Principal Component Analysis (PCA) has facilitated the detection of conformational changes in DNA structures, as well as the identification and comprehension of significant coherent motions in diverse regions.

Furthermore, this technique can be employed to investigate the impact of diverse parameters on collective movement and simplify the intricacy of motion, which is associated with the steadiness of the system and the functions of DNA. Figures depicting PCA plots for the Charmm36, Charmm36m, BSC1, and Ol15 DNA structures within each respective system have been presented. It is useful to predict important movements in orbit. Principal Component Analysis (PCA) was conducted utilizing the software tools RStudio and Bio3D.

In the case of Charmm36 DNA, the first three eigenvectors account for 31.65%, 31.65%, and 11.12%, whereas in the case of Charmm36m DNA, they account for 41.79%, 41.79%, and 9.1%. In the case of BSC1 DNA, the first three eigenvectors account for 30.37 percent, 30.37 percent, and 16.76 percent, whereas in the case of OL15 DNA, they account for 38.81 percent, 38.81 percent, and 7.32 percent. Charmm36m DNA exhibited the highest PC1 (41.79%), indicating that it endures greater conformational changes. In contrast, OL15 DNA showed the lowest PC1 (7.32%), indicating that it has undergone fewer conformational alterations.

charmm36

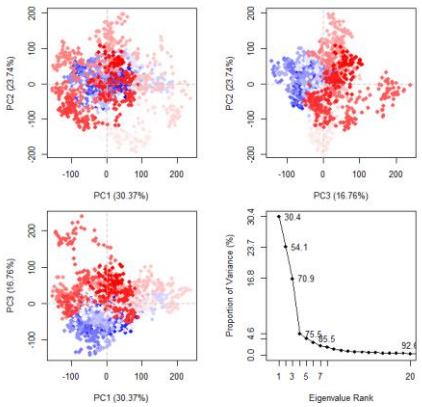

charmm36m

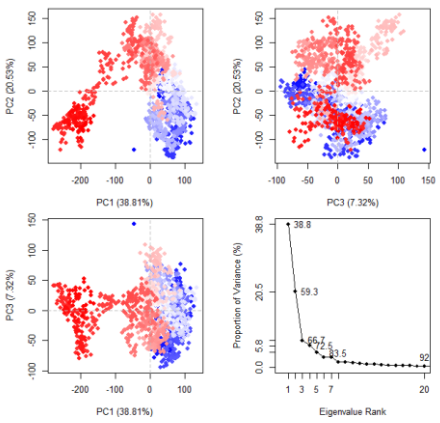

BSC1

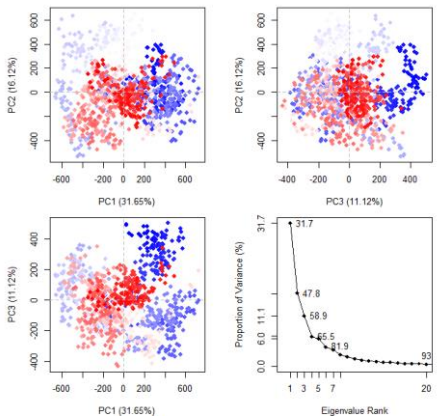

OL15

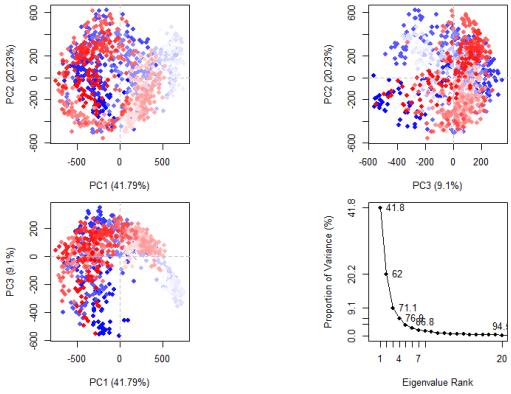

Figure 4.28.5. PCA of the SS-DNA-ligand complex versus 100 ns of MD simulation for each force field

Charmm36- Complex

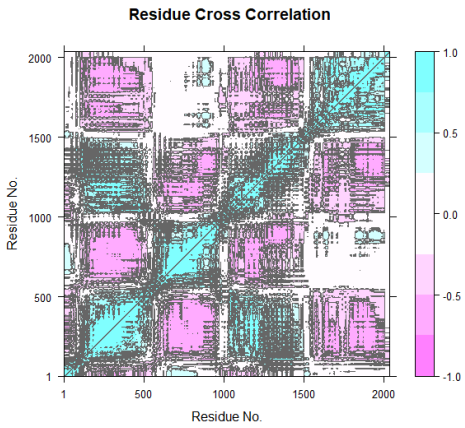

DNA

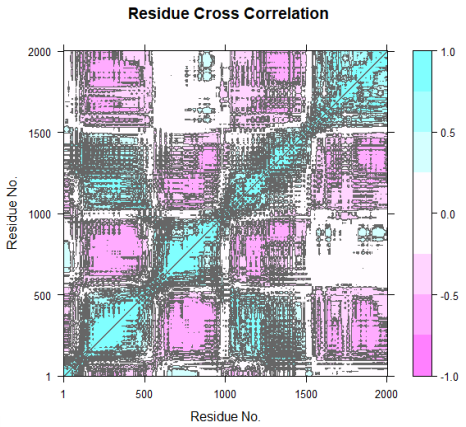

Charmm36m-Complex

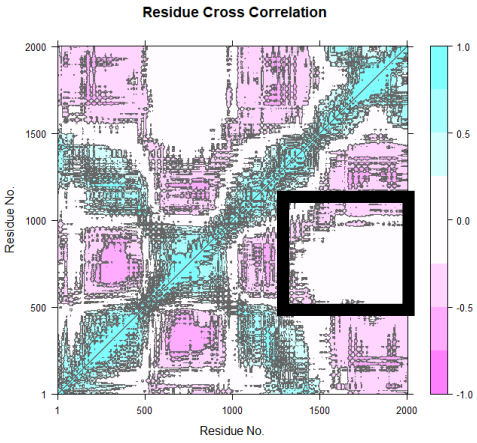

DNA

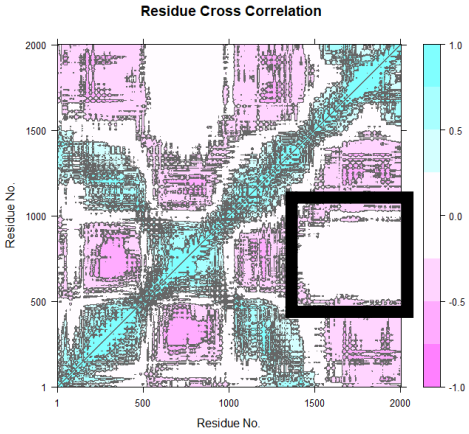

BSC1-Complex

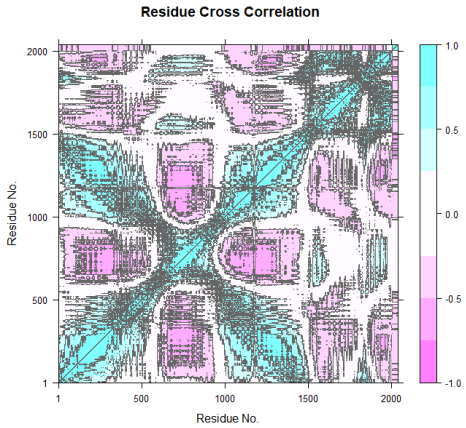

DNA

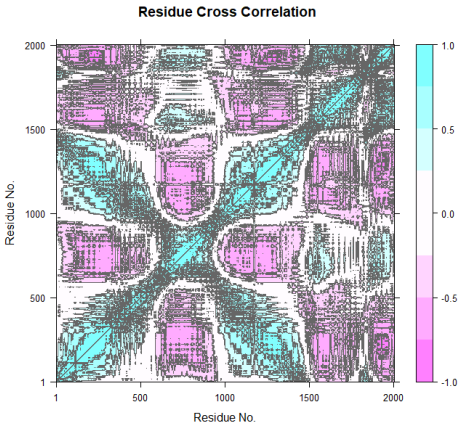

OL15-Complex DNA

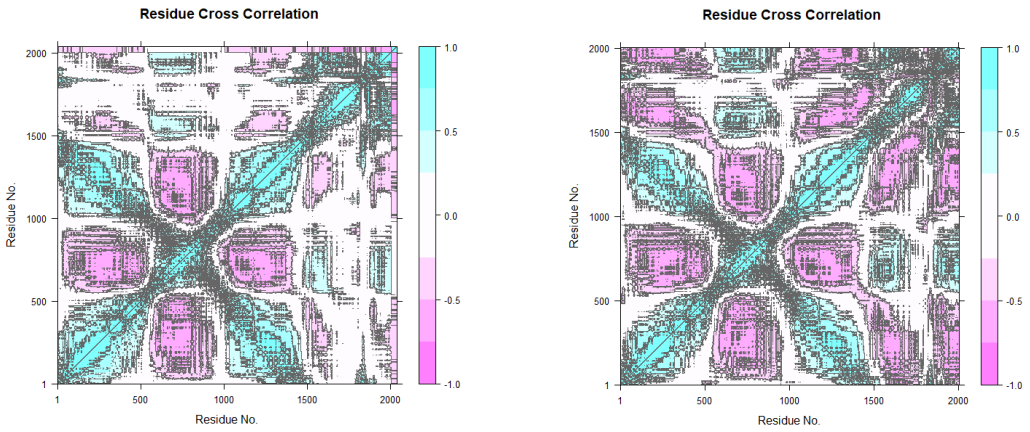

Figure 4.28.6. DCCM of the SS-DNA-ligand complex versus 100 ns of MD simulation for each force field

Upon analyzing the DCCM schematics of the four systems, it was noted that the associated movements displayed by each system were markedly distinct. The Charmm36m system displayed a relatively higher degree of collective movements that demonstrated a positive correlation compared to the DNA system in Charmm36. Conversely, the movements that exhibited a negative correlation did not exhibit a significant variance. The interrelated movements within the systems are discernible, particularly in the indicating regions demarcated by black dashed boxes. However, upon inspecting the bsc1 and OL15 systems, conspicuous distinctions between the two systems are not readily apparent.

4.29. Molecular dynamic simulation analysis of the modeled SS-DNA aptamer from the Rosetta-Farfar server against bisphenol A

The molecular docking process resulted in the formation of an ss-DNA-ligand complex, which was subsequently subjected to an MD simulation spanning a time scale of 100 ns. Two different versions of the AMBER and Charmm force fields were employed in the simulation. Various parameters such as the radius of gyration, RMSD, RMSF, and hydrogen bonding were analyzed. A comparison is made between the graphs of said parameters utilizing the four designated force fields.

4.29.1. Root Mean Square Deviation (RMSD)

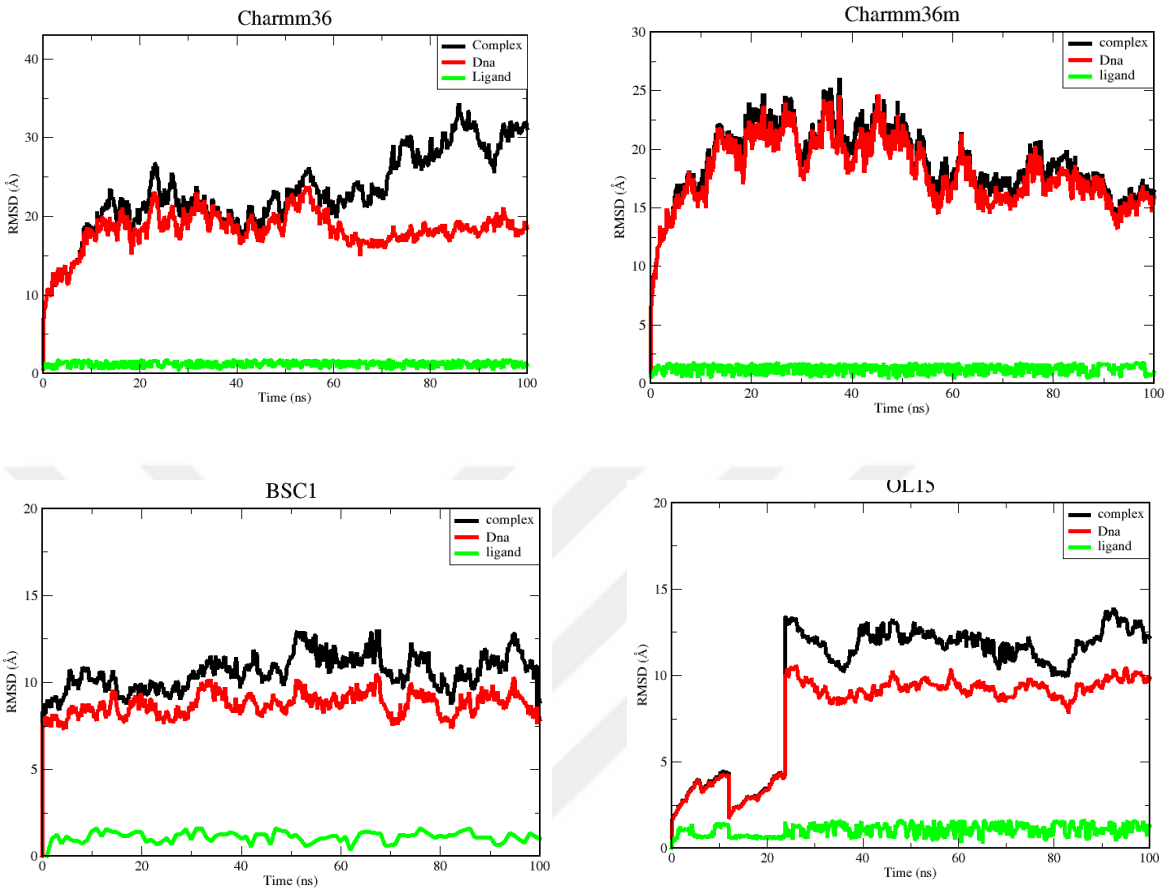

Figure 4.29.1. RMSDs of the SS-DNA-ligand complex versus 100 ns of MD simulation for each force field

Among the four complex structures, it can be revealed that charmm36 exhibits the highest RMSD value, whereas bsc1 demonstrates the lowest. Elevated RMSD values result in a notable alteration in the conformation of the DNA-ligand complex, indicating reduced stability..The comparative analysis of the DNA-ligand complex aptamer structure in charmm36 and charmm36m, as depicted in their respective graphs, indicates that the RMSD value is comparatively higher in charmm36. The RMSD levels for the complexes in charmm36 and charmm36m are 24.47 Å and 19.11 Å, correspondingly.

The complex structure of the Bba ligand in charmm36 displayed fluctuations in binding throughout the simulation, but these fluctuations were not statistically significant until 60 ns. The value of root mean square deviation (RMSD) increased significantly after 60 ns and culminated at 85 ns, indicating that the binding of the ligand caused a substantial conformational change in the structure of the complex.

RMSD	Ligand	Dna	Complex
Charmm36	1.526	18.12	24.47
Charmm36m	1.615	17.98	19.11
BSC1	1.013	8.071	10.550
OL15	1.073	8.893	10.605

Table 4.29.1. RMSD values by force field

In contrast, the charmm36m simulation exhibited a notable initial rise in the RMSD value. However, unlike the charmm36 complex, the RMSD values subsequently decreased after 50 ns and remained within a specific range until the conclusion of the simulation, indicating that the system had achieved a state of equilibrium. Despite the fact that the DNA-ligand complex exhibits the lowest Root Mean Square Deviation (RMSD) value in the BSC1 instance, there is a negligible disparity between it and OL15 with regard to RMSD value. Upon examination of the graphs, it is evident that the two complex structures displayed distinct behaviors over the course of the simulation. Upon examining the BSC1 graph, it is evident that the complex configuration exhibited a marginal increment from its initial placement at the onset of the simulation. A decrease was observed at 20 nanoseconds, followed by an increase in the root-mean-square deviation (RMSD) value at 30 nanoseconds, which reached its maximum level at 65 nanoseconds. Subsequent to this point, the phenomenon persisted until the termination of the simulation, exhibiting some degree of variability.

Upon examining the graph of OL15, it can be observed that there was a slight increase at the beginning of the simulation, followed by a subsequent increase, reaching its highest peak at 20 ns. After 20 ns, the simulation exhibited periodic fluctuations, with some intervals showing an increase and others a decrease, ultimately resulting in minimal waves at the simulation's end . Although the RMSD complex values of OL15 and BSC1 are similar, it can be concluded that the complex structure in BSC1 is more stable than in OL15 and exhibits better ligand binding.

Compared to charmm36, charmm36m, and ol15, ligand bsc1 exhibited a lower RMSD than charmm36, charmm36m, and ol15, with average RMSD values of 1.526, 1.615, 1.013, and 1.073, respectively.

In charmm36m, the RMSD value for ligand binding is a bit greater than in charmm36; compared to charmm36, the simulation has moved outside of the binding site in the last 10ns. Despite the RMSD value of the ligand in BSC1 compared to Ol15, it is evident that the ligand binding affinity is comparatively weaker in Ol15 during the initial 20 nanoseconds of the simulation. Specifically, the ligand breaks down from the binding site in Ol15 but subsequently rebinds after 20 nanoseconds, and this behavior persists throughout the simulation. In addition, the trajectories were analyzed, and the findings revealed that the ligands were occasionally outside of the DNA region and the binding region.

4.29.2. Root Mean Square Fluctuation

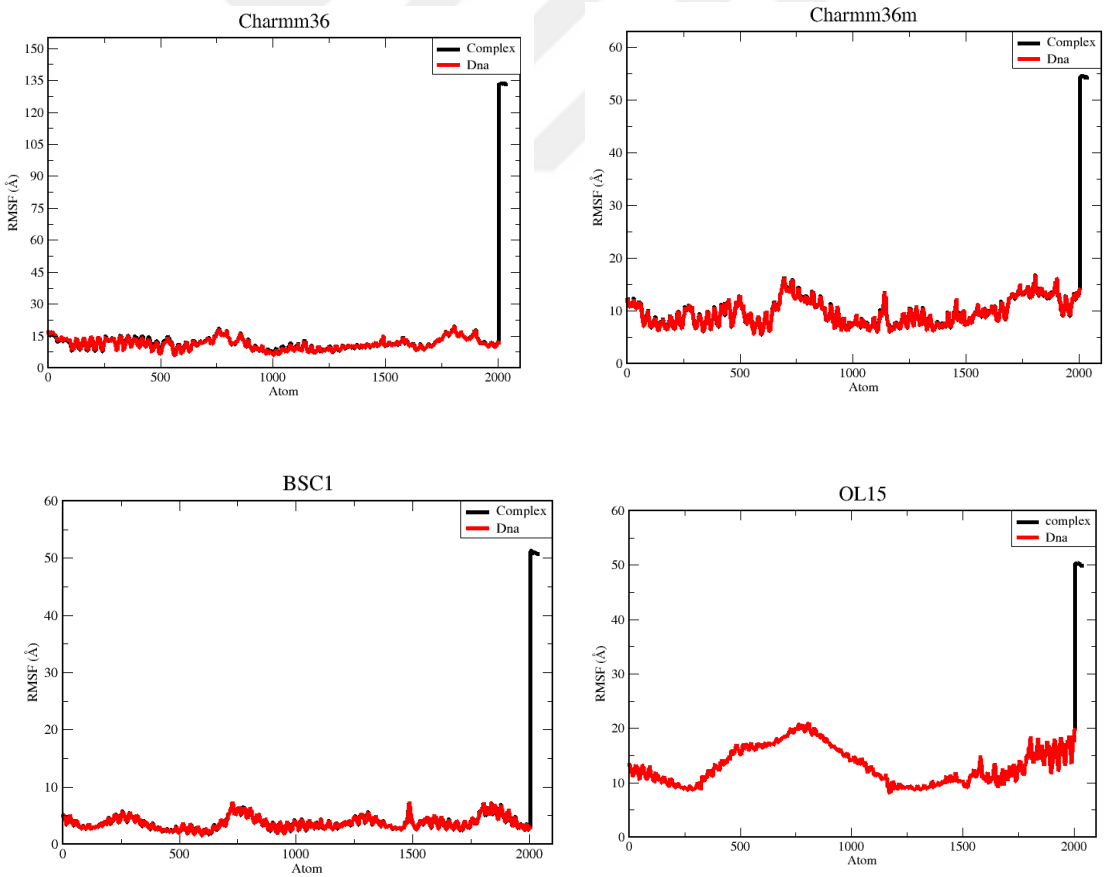

Figure 4.29.2. RMSFs of the SS-DNA-ligand complex versus 100 ns of MD simulation for each force field

The RMSF quantifies the extent of displacement of atomic positions relative to their initial positions, thereby depicting the dynamic characteristics of the interaction between DNA and ligand. To put it differently, RMSF functions as an illustration of the dynamic nature of the interplay between DNA and ligand. The RMSF data pertaining to DNA-ligand complexes is graphically represented to depict the mean fluctuation of each base residue. The figures presented in this context pertain to a 100-nanosecond molecular dynamics trajectory. Upon examining the RMSF Charmm36 graph, notable fluctuations were detected in the base indices 56–61 and 23–25. The base pairs in these regions were identified as T-C-G-C-A-C and A-G-C, respectively.

Three bases, specifically those in the 23–25 regions, exhibit high RMSF values. These bases are situated within the internal loop segment of the DNA aptamer structure and do not extend beyond the DNA binding site. Meanwhile, the base pairs in the 56–61 regions, which are located within the hairpin loop segment of the structure, also display elevated rmsf values despite being situated within the binding site. Conversely, upon examining the BSC1 and OL15 charts, it is evident that the significant peaks, specifically the RMSF values, exhibit a lower magnitude. The significant RMSF peaks in BSC1 are situated in the 23–24, 47, and 58–60 regions. The nucleobases present in these regions are A-G, A, and G-C-A, respectively. These bases are located in the hairpin loop region, which exhibits high peaks and is situated outside the binding site. The OL15 exhibits a notable RMSF peak, primarily located in the stem and internal loop regions, specifically in the 23–26 region, with the highest magnitude observed in the A–G–C-G sequence.

4.29.3. Gyration Radius Variation

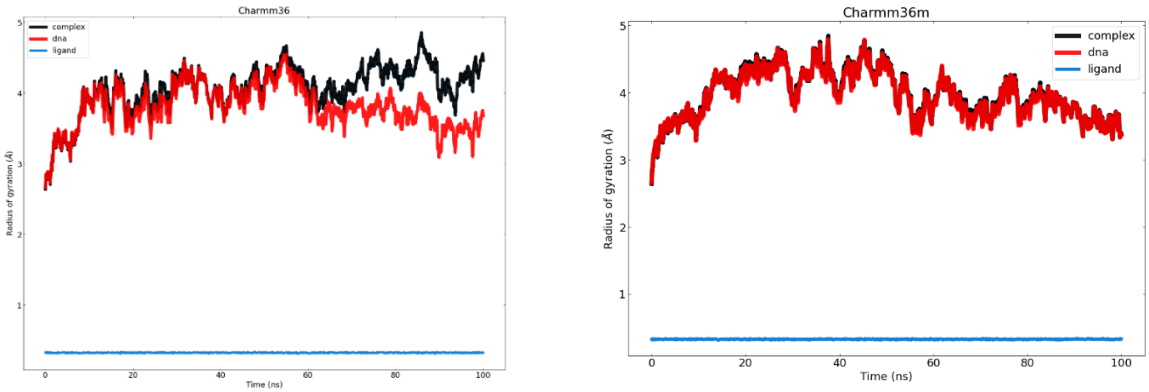

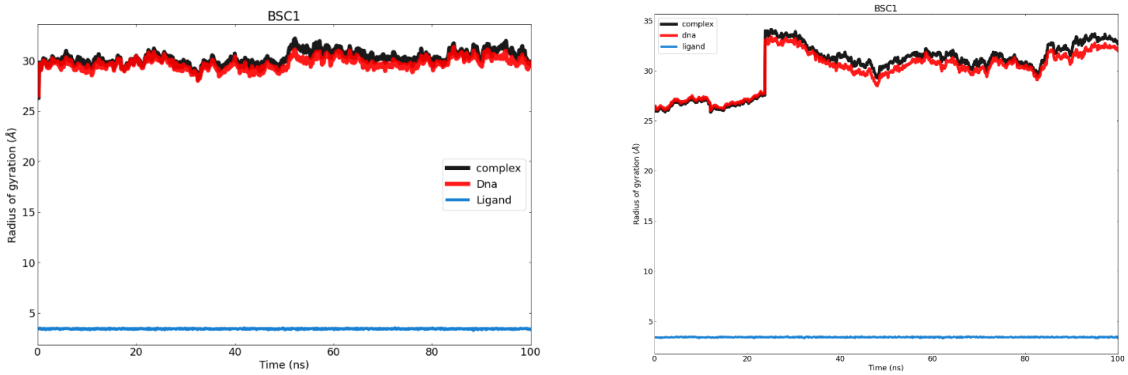

Figure 4.29.3. RGs of the SS-DNA-ligand complex versus 100 ns of MD simulation for each force field

The Charmm36 diagram illustrates that the DNA-ligand complex exhibited an RG value exceeding 4 on average. The complex formed between DNA and ligand exhibited an RG value exceeding 4.5 Å on average. Notably, the Rg values of both the DNA and complex systems displayed an upward trend throughout the simulation, with a particularly significant increase observed at the 50 ns mark. The compactness of both the complex and the DNA exhibited a decrease over time.

However, it was observed that the radius of gyration (Rg) of DNA decreased steadily throughout the simulation, whereas the complex structure displayed an increase in Rg, particularly at 85 ns, ultimately reaching its maximum value. The observed augmentation in the complex configuration denotes a significant alteration in the structure, resulting in the densification of the aptamer.

The Charmm36m simulation demonstrated elevated radius of gyration (RG) measurements, particularly during the initial stages, for the complex system. The RG values reached their peak between the time intervals of 20 and 40 nanoseconds, following which a decline in the RG values was observed. The aforementioned observation implies a rise in the compactness of the aptamer structure. Furthermore, the persistent decline in RG values throughout the simulation period signifies a surge in the stability of the complex system. The RG values of the systems located in BSC1 and OL15 exhibit a notable increase in comparison to those of charmm36 and charmm36m.

Despite the elevated RG value observed in the BSC1 graph, the general trend of the RG curve remains consistent with notable fluctuations throughout the simulation duration, indicating that the aptamer experiences certain conformational alterations.

Nonetheless, the aptamer's overall compactness experiences a slight impact. Conversely, with respect to OL15, the RG value exhibits a notable elevation, and a marked conformational shift is observed throughout the simulation. Specifically, subsequent to the 20 nanosecond mark, the Rg value experiences a substantial surge, and notable fluctuations persist until the conclusion of the simulation, with the structure failing to attain a state of stability. The observed noteworthy augmentations and variations in the Rg value suggest the presence of a substantial conformational alteration. Overall, the research group's findings indicated that the interaction of these four compounds resulted in alterations to the molecular structure.

4.29.4. Hydrogen bond

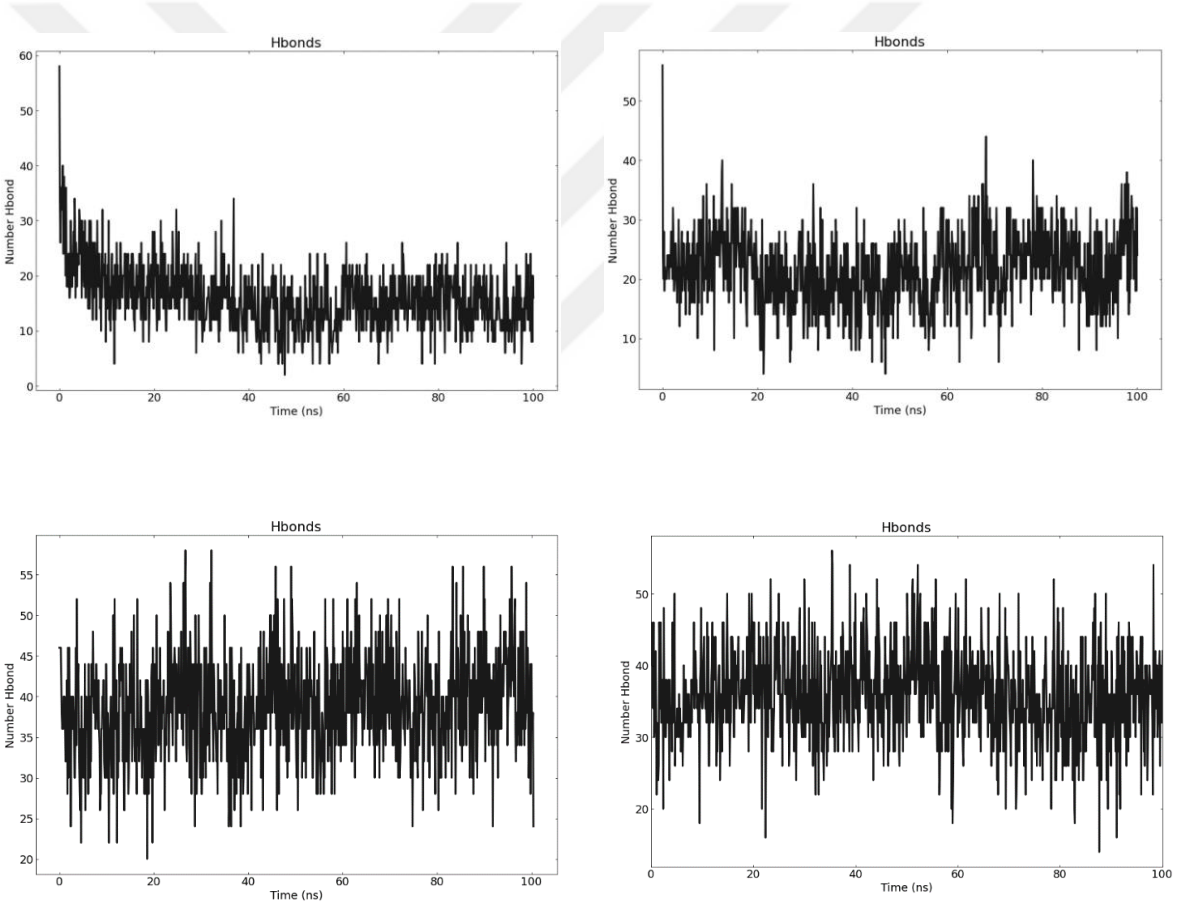

Figure 4.29.4. Hbonds of the SS-DNA-ligand complex versus 100 ns of MD simulation for each force field

To comprehend the interrelationships among biomolecules, it is necessary to conduct a geometric examination of hydrogen bonding. The maintenance of structural integrity in biomolecules is reliant on the crucial interaction of hydrogen bonds. The establishment of hydrogen bonds is a critical factor in maintanining the stability of complexes in the realm of MD modeling.

During the entirety of the molecular dynamics simulation, it was observed that the amount of hydrogen bonds present in states where the ligand is bound exhibited a dynamic pattern, as depicted in Figure 9. In the course of the molecular dynamics simulation, it was demonstrated that the amount of hydrogen bonds created between the DNA and ligand was comparatively lower in the charmm36 model as opposed to the charmm36m model. The graphical representations illustrate that the complex in the OL15 case exhibits the greatest quantity of hydrogen bonds alongside the simulation. An enhancement in the quantity and duration of hydrogen bonds formed is linked to an enhanced binding affinity.

4.29.5. Analysis of PCA and DCCM

Charmm36-DNA

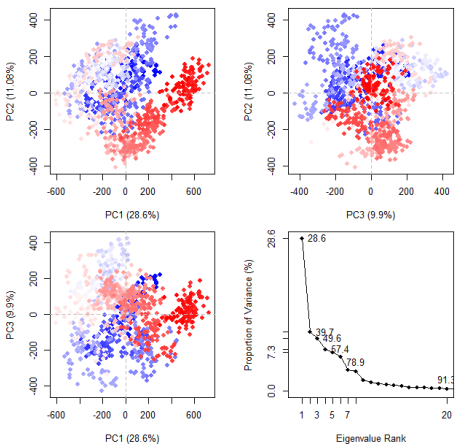

Complex

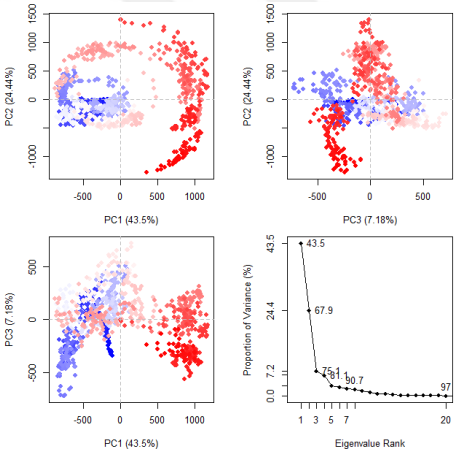

Charmm36m-DNA

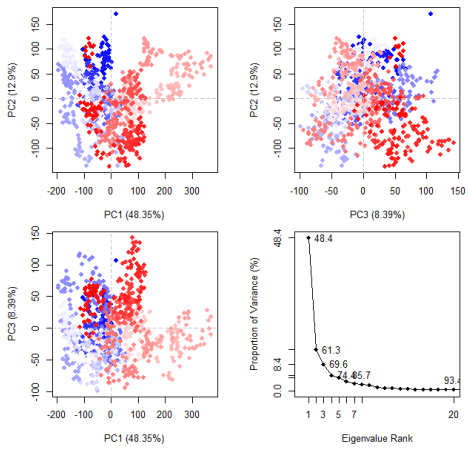

Complex

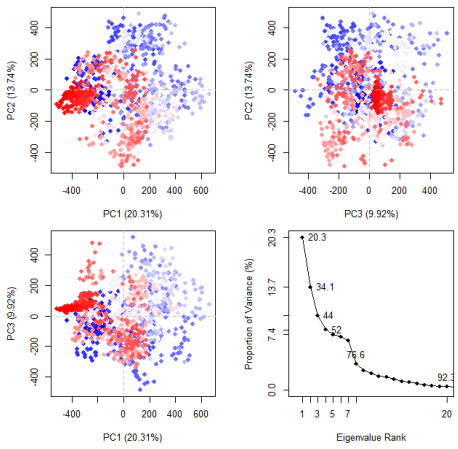

BSC1-DNA

Complex

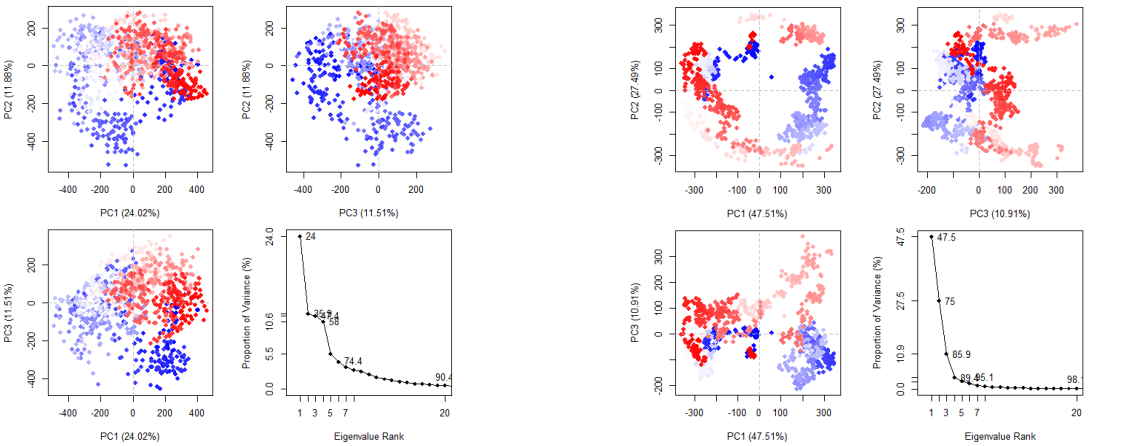

OL15-DNA

Complex

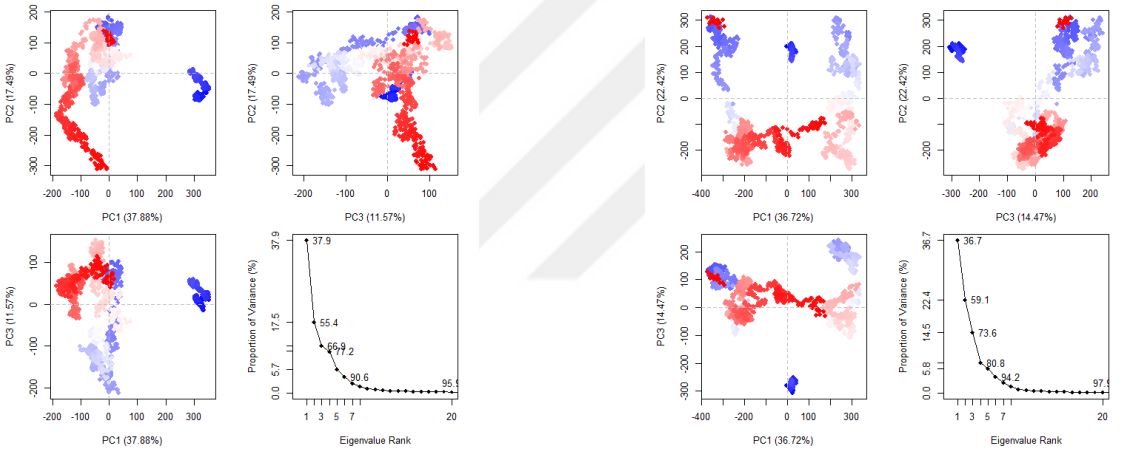

Figure 4.29.5. PCA of the SS-DNA-ligand complex versus 100 ns of MD simulation for each force field

The results of the PCA analysis indicate that for Charmm36 DNA, the first three eigenvectors explain 28.6%, 28.6%, and 9.9% of the variance, while for Charmm36m DNA, the first three eigenvectors account for 24.02%, 24.02%, and 11.51% of the variance. Regarding BSC1 DNA, the results of PCA analysis indicate that the initial three eigenvectors explain 48.35%, 48.35%, and 8.39% of the variance. Conversely, for OL15 DNA, the first three eigenvectors account for 37.88%, 37.88%, and 11.57% of the variance. The BSC1 DNA exhibited the highest PC1 value (48.35%), suggesting that it undergoes more significant conformational alterations.

The examination of conformational changes in aptamer-ligand complexes in the Charmm36 system reveals that the first three eigenvectors contribute to 43.5%, 43.5%, and 7.18% of the variance, respectively. Similarly, in the Charmm36m system, the first three eigenvectors account for 20.31%, 20.31%, and 9.92% of the variance, as determined by PCA analysis. PCA analysis reveals that in the instance of BSC1, the first three eigenvectors are composed of 47.51%, 47.51%, and 10.91% DNA, respectively. Similarly, in the case of OL15, DNA accounts for 36.72%, 36.72%, and 14.47% of the first three eigenvectors. The BSC1 aptamer-ligand system exhibited the highest PC1 value of 47.51%, suggesting that the aptamer-ligand complex experiences significant conformational alterations.

Complex-Charmm36

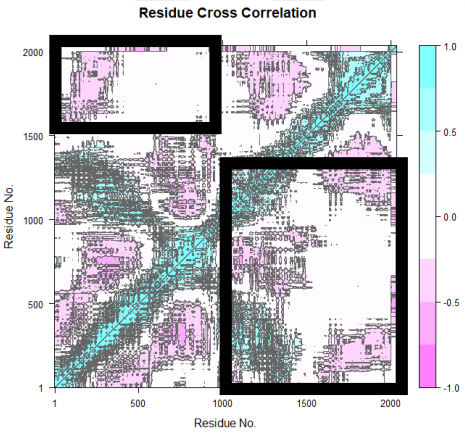

DNA

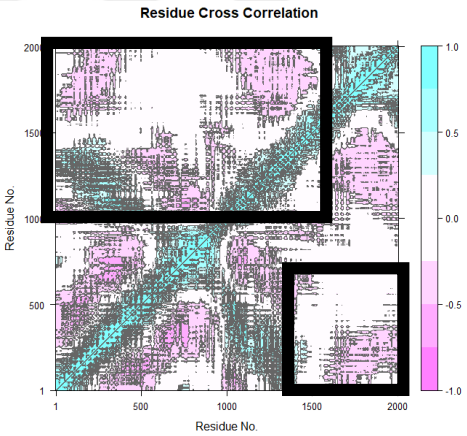

Complex-Charmm36m

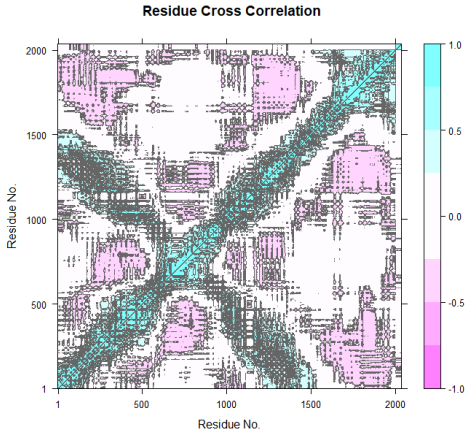

DNA

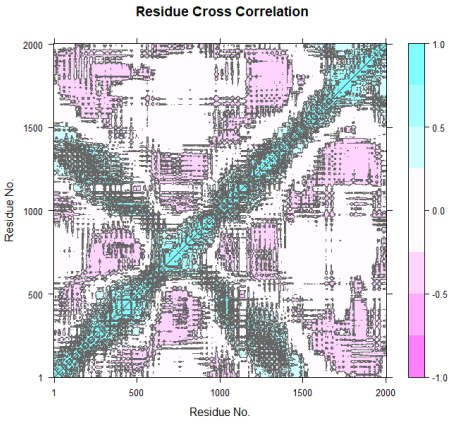

Complex-BSC1 DNA

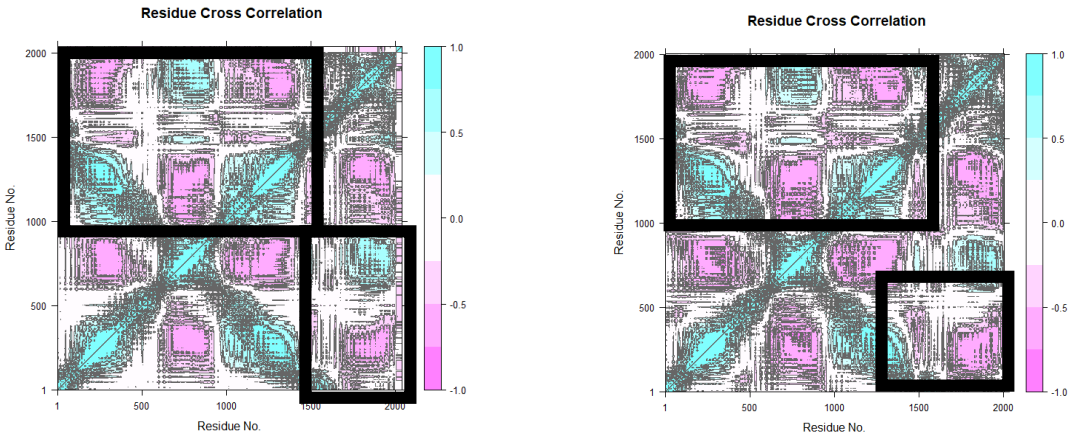

Complex-OL15 DNA

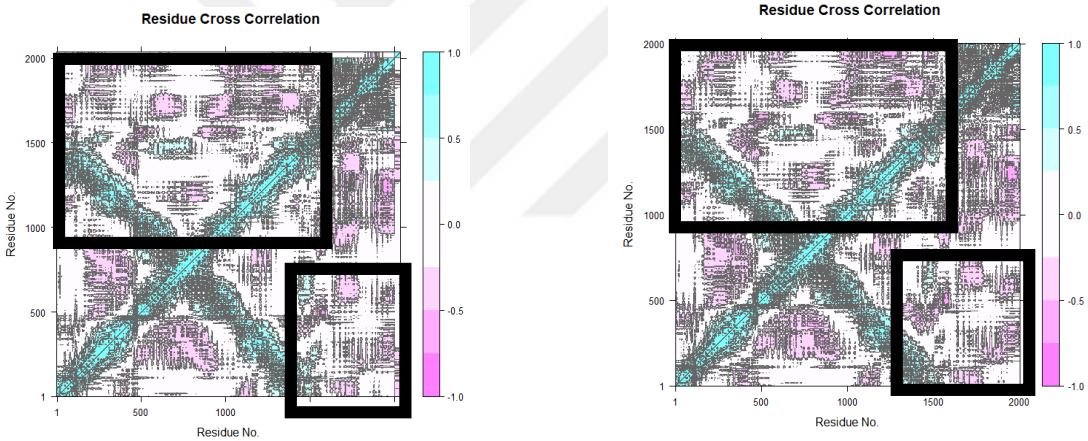

Figure 4.29.6. DCCM of the SS-DNA-ligand complex versus 100 ns of MD simulation for each force field

After conducting a comparative analysis of the aptamer-ligand structures in charmm36 and charmm36m, it was noted that specific areas of the system demonstrated an augmentation in positive correlation in charmm36m. Conversely, negative correlation decreased in certain regions while increasing in others in charmm36m. Upon examining the intricate systems present in BSC1 and OL15, it is observed that there is a notable reduction in the negative correlation within OL15 as compared to BSC1. Additionally, there is a marked decrease in the positive correlation between both systems.

4.30. Molecular dynamic simulation analysis of the modeled ss-DNA aptamer from the Rna-Composer server against bisphenol A

The outcome of the molecular docking procedure yielded a complex of ss-DNA and ligand, which was subsequently subjected to a molecular dynamics simulation that spanned a time scale of 100 nanoseconds. The simulation utilized two distinct iterations of the AMBER and Charmm force fields. The study involved an analysis of several parameters, including the radius of gyration, RMSD, RMSF, and hydrogen bonding. A comparative analysis is conducted on the graphical representations of the aforementioned parameters, utilizing the four specified force fields.

4.30.1. Root Mean Square Deviation (RMSD)

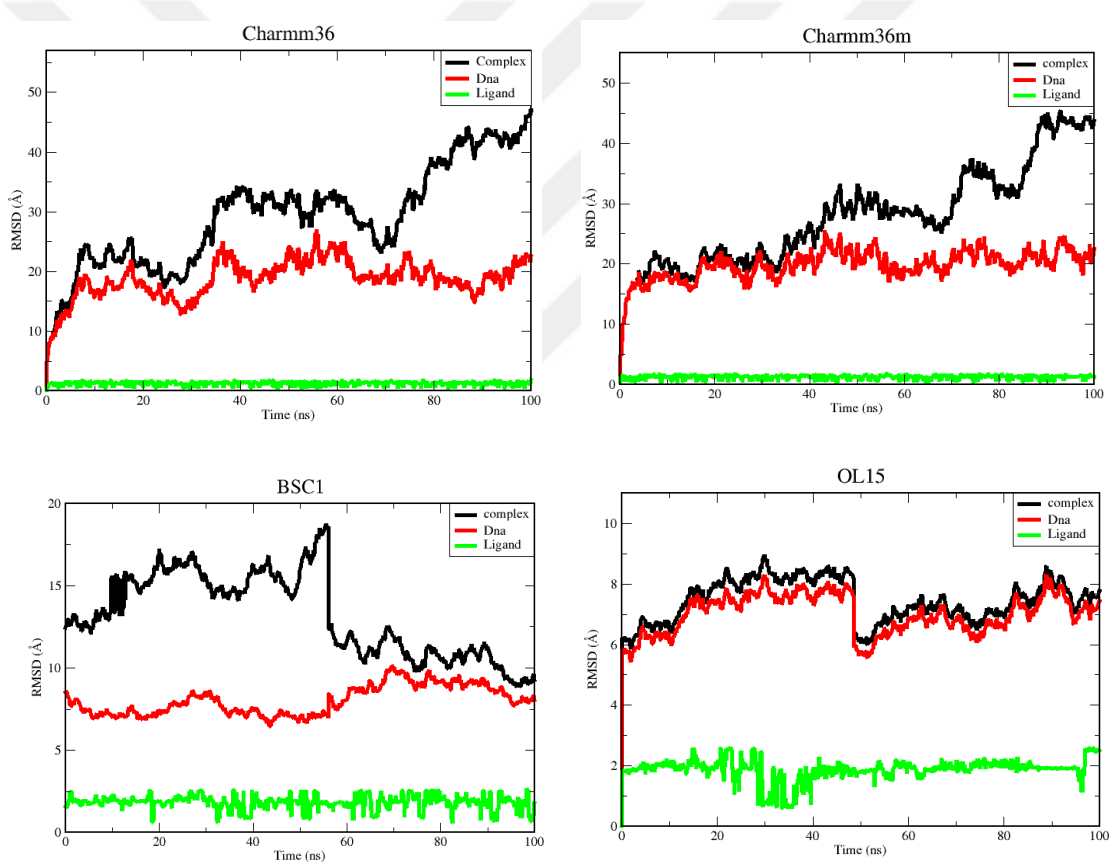

Figure 4.30.1. RMSDs of the SS-DNA-ligand complex versus 100 ns of MD simulation for each force field

Among the four complex configurations, it can be observed that the charmm36 complex exhibits the greatest RMSD value, whereas the aptamer-ligand complex situated at OL15 manifests the lowest RMSD value. Elevated RMSD values result in notable alterations in the conformation of the DNA-ligand complex, indicating reduced stability.

RMSD	**Ligand**	**Dna**	**Complex**
Charmm36	1.758	18.67	32.35
Charmm36m	1.761	19.71	30.26
BSC1	1.790	7.823	13.600
OL15	1.890	7.056	7.488

Table 4.30.1. RMSD values by force field

Upon examining Figures charmm36 and charmm36m, it can be observed that the DNA-ligand complex aptamer structure in charmm36 exhibits a higher RMSD value in comparison to charmm36m. Additionally, the former structure displays significant fluctuations throughout the simulation and fails to reach equilibrium by the end of the simulation. Subsequent to the 70 ns, a boost in the RMSD value was observed, persisting until the conclusion of the simulation. In both cases, the structural stability of the aptamer-ligand complexes is affected. However, it is noteworthy that the Charmm36m complex structure exhibits greater stability compared to Charmm36.

The behavior of DNA-ligand complexes in the BSC1 and OL15 states exhibits notable dissimilarities in comparison to that of charmm36 and charmm36m. Upon examination of solely the RMSD magnitude, it is apparent that the RMSD values exhibited by the DNA-ligand complexes in the bsc1 and ol15 states are notably diminished. From this observation, it can be inferred that the DNA aptamer-ligand complexes possess greater stability in comparison to charmm36 and charmm36m, as they undergo significantly less conformational alteration.

Upon examining the BSC1 graph, it is evident that there is a noteworthy surge in the initial 10 ns of the simulation. This surge persists until 30 ns and culminates in its maximum value, particularly around 50 ns. The observed escalation in the RMSD values is indicative of a persistent alteration in the aptamer conformations, plausibly attributable to the aptamer's opening. At 50 ns, an abrupt reduction was detected, which persisted with minor declines until the conclusion of the simulation.

The ol15 plot exhibits a comparable rise within the initial 50 nanoseconds to that of the bsc1 case. However, the magnitude of this increase is comparatively lower than that observed in bsc1, thus suggesting a greater degree of aptamer folding. Following a time interval of 50 nanoseconds, it demonstrated analogous characteristics to those detected in BSC1.

Upon examination of the ligands in the context of charmm36m, it was observed that the ligand exhibited displacement from the binding site in certain areas. During the simulation in Charmm36, the ligand exhibited persistent motion within its orbit. The Bsc1 graphic depicts that the ligand remained stable throughout the simulation, maintaining its position within the binding region without any deviation until 20 ns. However, subsequent to this point, RMSD value exhibited a slight increase and remained constant thereafter.

In contrast, the OL15 graph depicts the ligand's stability throughout the simulation. Specifically, the ligand remained stable from the onset of the simulation until 20 ns, at which point there was an increase in the RMSD value. Subsequently, a sudden drop was observed between 20 and 40 ns, indicating that the ligand dissociated from the binding site during this interval. However, between 40 and 80 ns, the ligand exhibited fluctuations with both increases and decreases. Notably, between 80 and 90 ns, the ligand demonstrated exceptional stability, which is attributed to its strong binding affinity with the aptamer during this period.

4.30.2. Root Mean Square Fluctuation

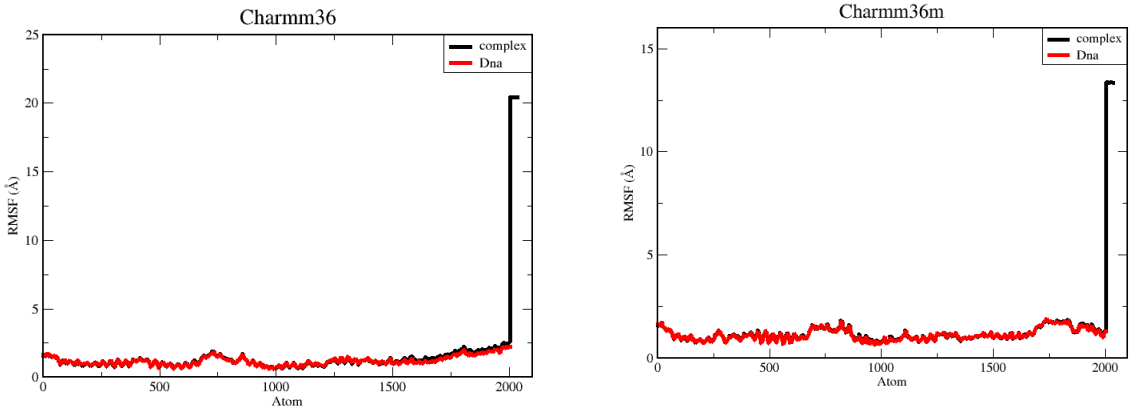

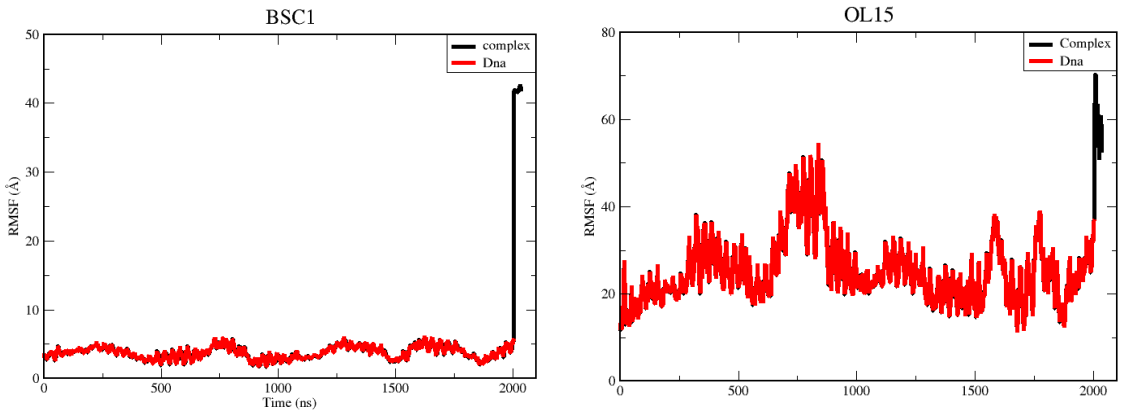

Figure 4.30.2. RMSFs of the SS-DNA-ligand complex versus 100 ns of MD simulation for each force field

The assessment of the RMSF Charmm36 graph reveals notable fluctuations in specific areas, namely the base indices 60–63, 57–59, and 23–24. These regions correspond to the base pairs A-C-C-A, C-G-C, and A-G, respectively. The base pairs located within the 60–63 region exhibit the greatest root-mean-square fluctuation value among the analyzed bases.

The bases exhibiting high root-mean-square fluctuation (RMSF) values are situated in the internal loop and hairpin regions of the DNA aptamer structure and are positioned outside the binding site. Notably, in Charmm36m, the RMSF peak of the terminal bases displayed comparatively lower flexibility than in Charmm36.

Upon examination of the BSC1 and OL15 graphs, it can be showed that the BSC1 graph exhibits a higher proportion of regions with high flexibility in comparison to the OL15 graph. The nucleotide bases situated between 22 and 26 exhibit the greatest degree of flexibility in OL15. It was observed that the identical region exhibited a notable degree of flexibility, with the terminal bases also displaying a significant level of flexibility. Upon examination of the complex configurations, it was observed that ol15 exhibited the most elevated root-mean-square fluctuation (RMSF) value, whereas charmm36m displayed the lowest. This finding suggests that the complex structure in OL15 possesses a more unconstrained terminal loop.

4.30.3. Gyration Radius Variation

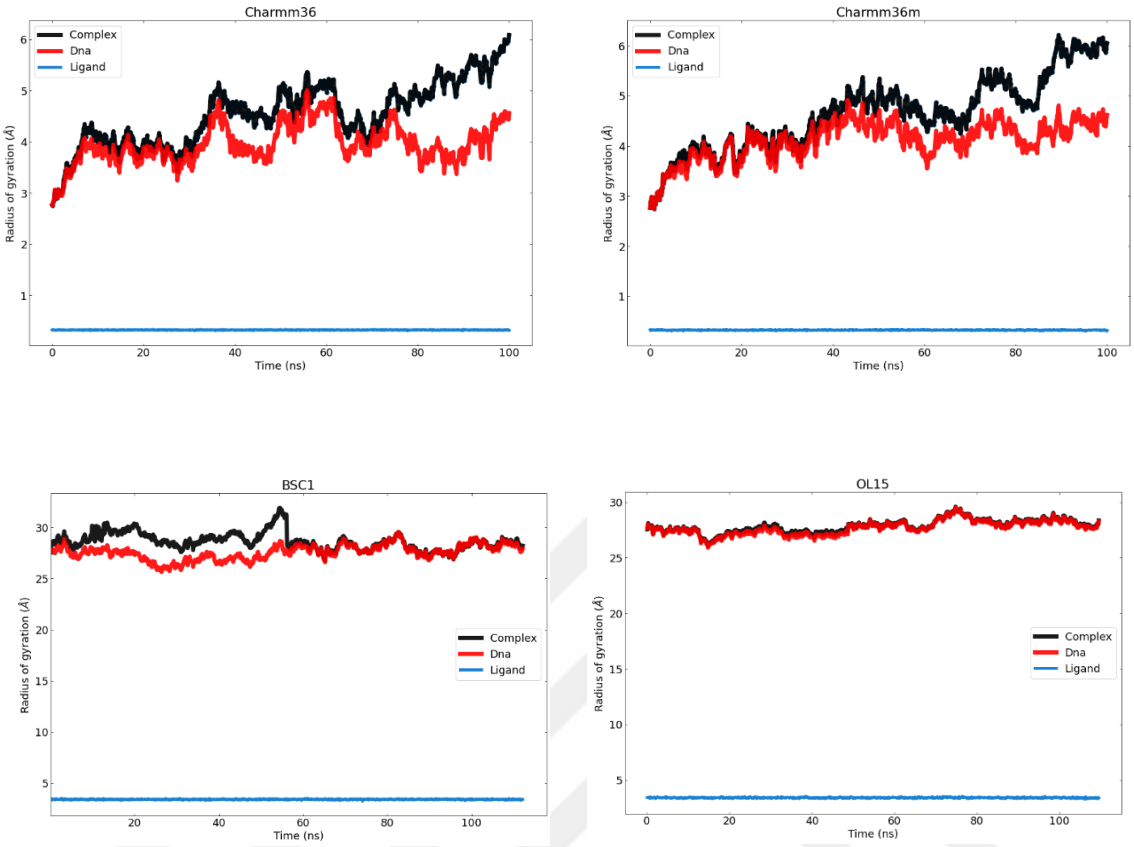

Figure 4.30.3. RGs of the SS-DNA-ligand complex versus 100 ns of MD simulation for each force field

The Charmm36 graph indicates that the DNA-ligand complex exhibited an average radius of gyration (RG) exceeding 5 Å. While the RG value displayed negligible fluctuations during the initial 30 ns of the simulation, it subsequently escalated beyond this point. The complex structure exhibited a transient decline within the 60–70 ns timeframe, followed by a consistent rise thereafter. The observed elevation in the RG value is indicative of the unfolding of the aptamer. The Charmm36m aptamer complex demonstrated similar behavior to Charmm36, particularly at 70 ns, where the RG value displayed a significant rise and persisted until the conclusion of the simulation, suggesting that the aptamer remained unfolded.

4.30.4. Hydrogen bond

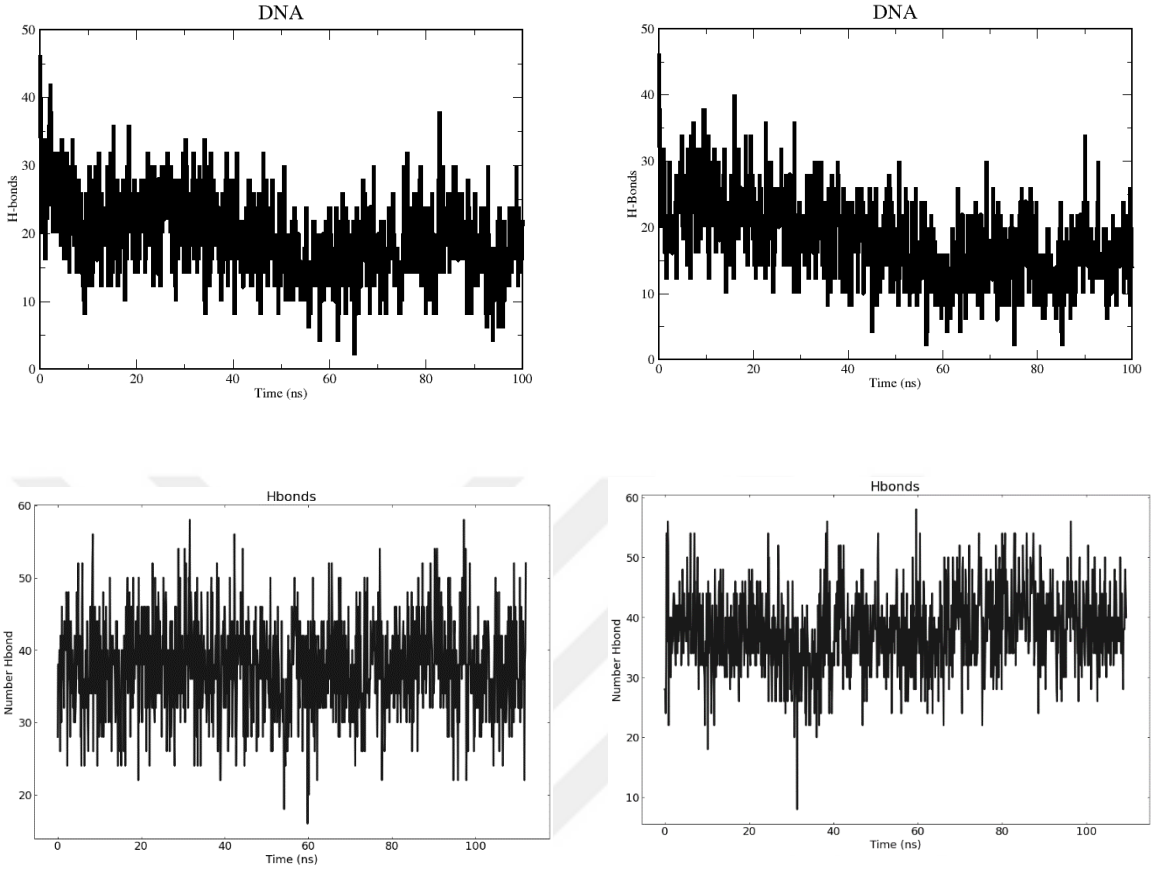

Figure 4.30.4. Hbonds of the SS-DNA-ligand complex versus 100 ns of MD simulation for each force field

Throughout the entirety of the MD simulation, a dynamic pattern was observed in the quantity of hydrogen bonds present in the ligand-bound states, as depicted in Figure 9. The outcomes of the MD indicates that the BSC1 and OL15 states exhibited the highest number of hydrogen bonds formed between DNA and ligand. Conversely, the charmm36 and charmm36m states demonstrated a decrease in hydrogen bond formation over a 50 ns period, which was comparatively less than that observed in the BSC1 and OL15 states.

4.30.5. Analysis of PCA and DCCM

When the DCCM schematics of the four systems are analyzed, it can be seen that related motions of the four systems differ considerably.

Positive correlation motions and negative correlation motions of the complex system in BSC1 have changed considerably and are greatly amplified in comparison to the motions of the other complex systems. DCCM (Dynamic Cross Correlation Matrix) analysis of the complex system at charmm36 revealed a significant increase in positive correlation motions compared to charmm36m upon ligand binding, whereas DCCM analysis of the complex system at charmm36m revealed an increase in negative correlation motions and a slight decrease in positive correlation motions after ligand binding. Compared to BSC1, the negative correlation motions of the complex system in the OL15 state decreased significantly after ligand binding.

Charmm36-complex DNA

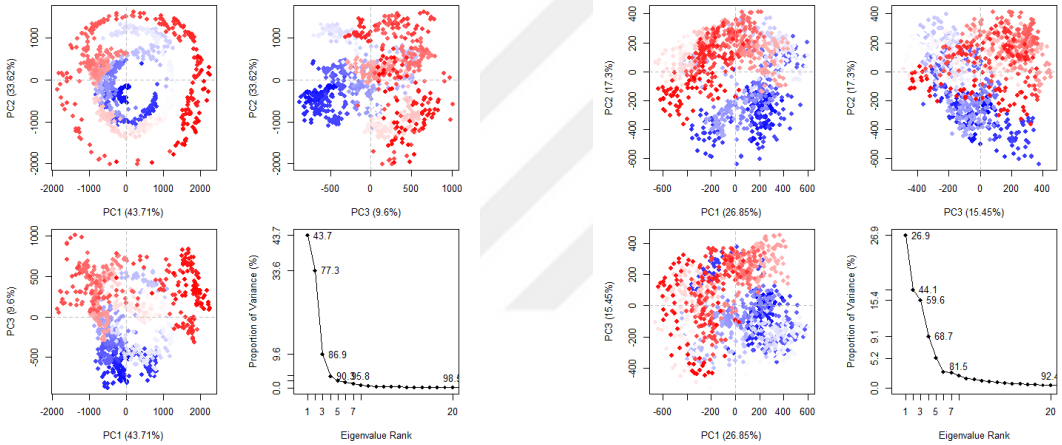

Charmm36m-complex DNA

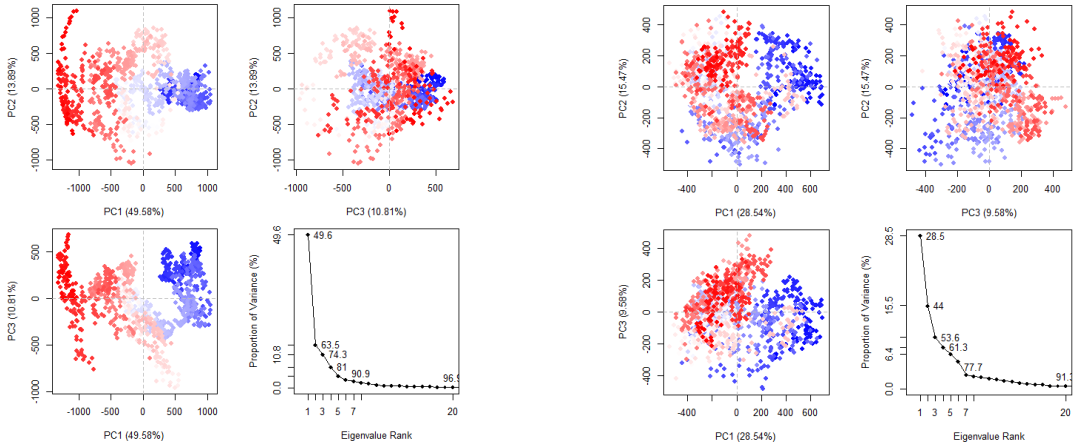

BSC1-complex DNA

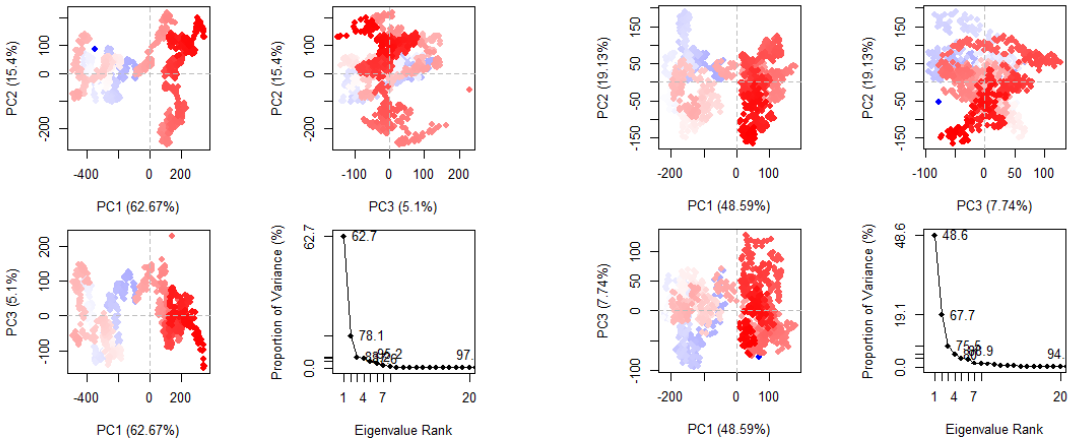

OL15-complex DNA

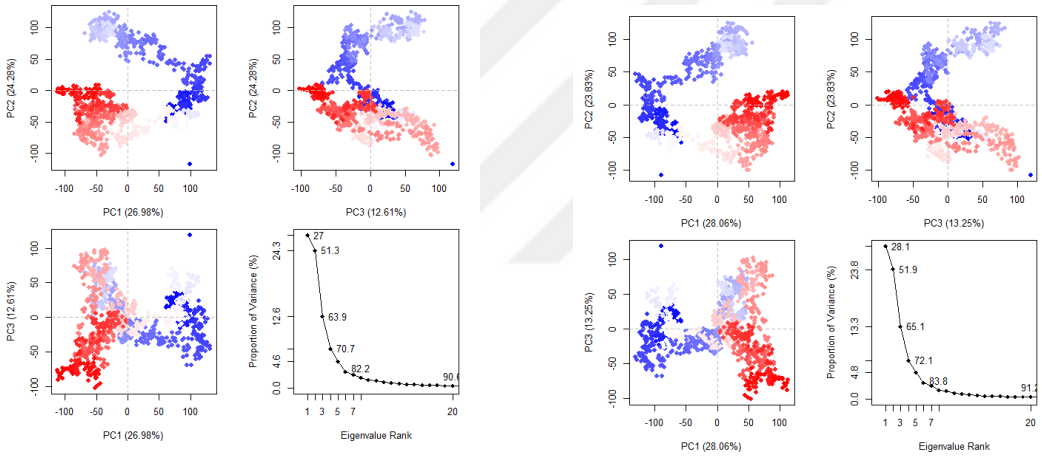

Figure 4.30.5. PCA of the SS-DNA-ligand complex versus 100 ns of MD simulation for each force field

Charmm36-complex DNA

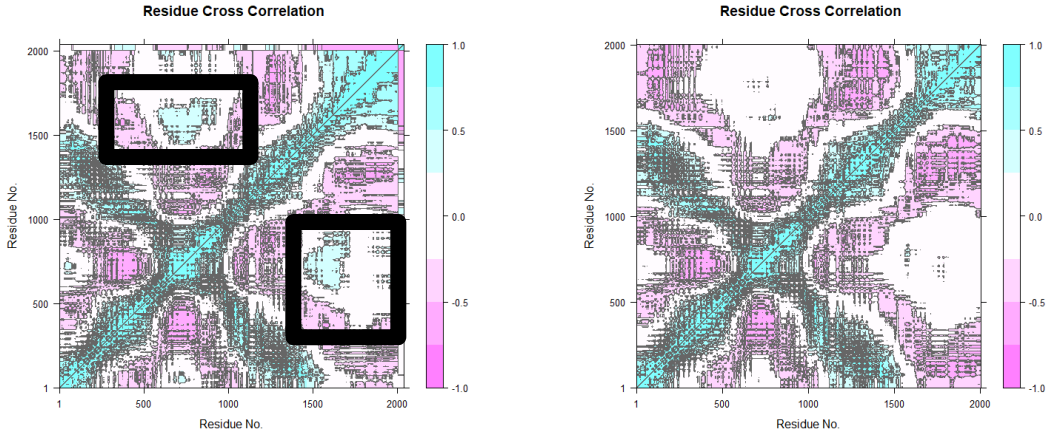

Charmm36m-complex DNA

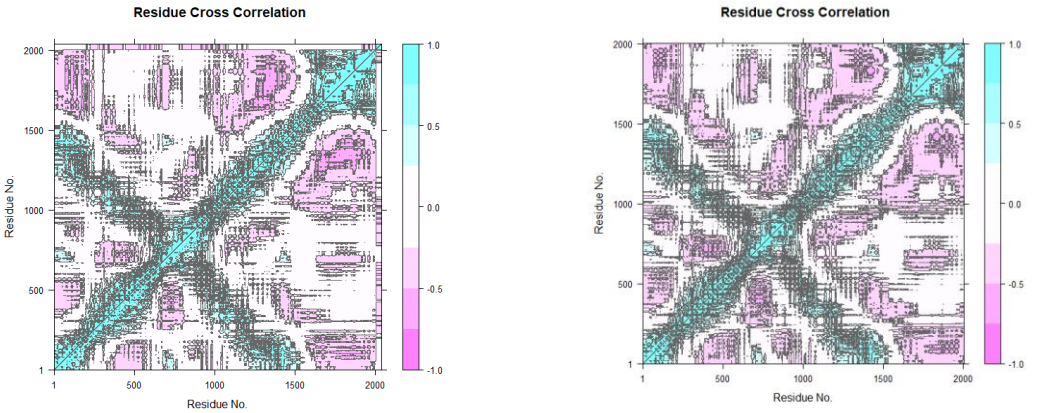

BSC1-complex DNA

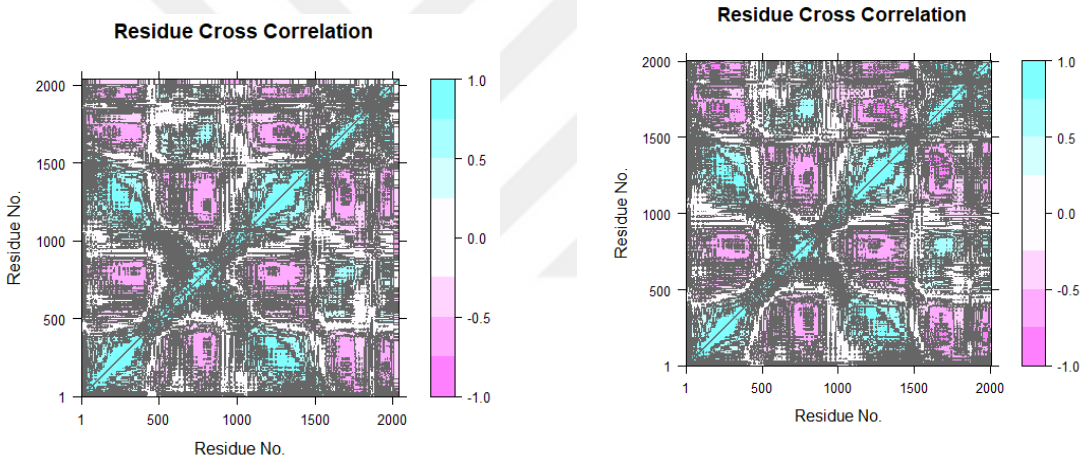

OL15-Complex DNA

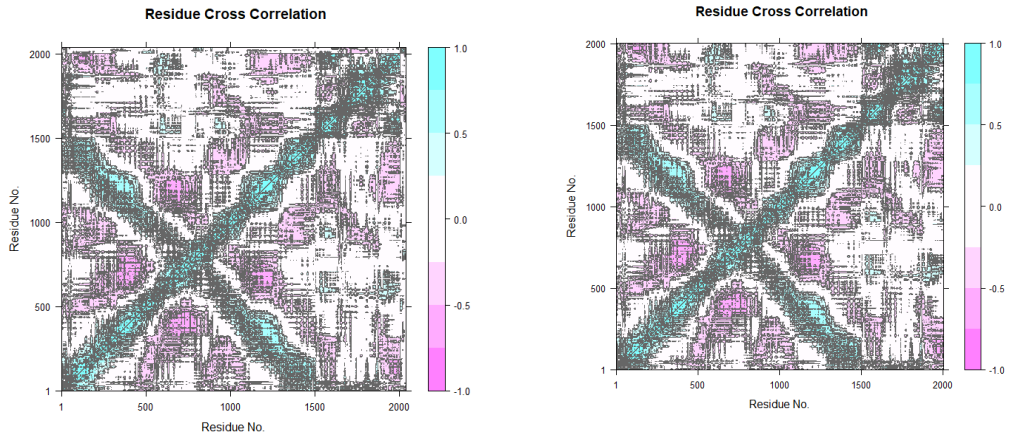

Figure 4.30.6. DCCM of the SS-DNA-ligand complex versus 100 ns of MD simulation for each force field

4.31. Molecular dynamic simulation analysis of the modeled ss-DNA aptamer from the Vfold3D server against bisphenol A

The molecular docking process resulted in the formation of a complex between ss-DNA and the ligand. This complex was then subjected to a molecular dynamics simulation that lasted for 100 nanoseconds. Two versions of the AMBER and Charmm force fields were used in the simulation. Hydrogen bonding, as well as the radius of gyration, RMSD, and RMSF, were analyzed. The four stated force fields are used to analyze the graphical representations of the forementioned data and draw conclusions.

4.31.1 Root Mean Square Deviation (RMSD)

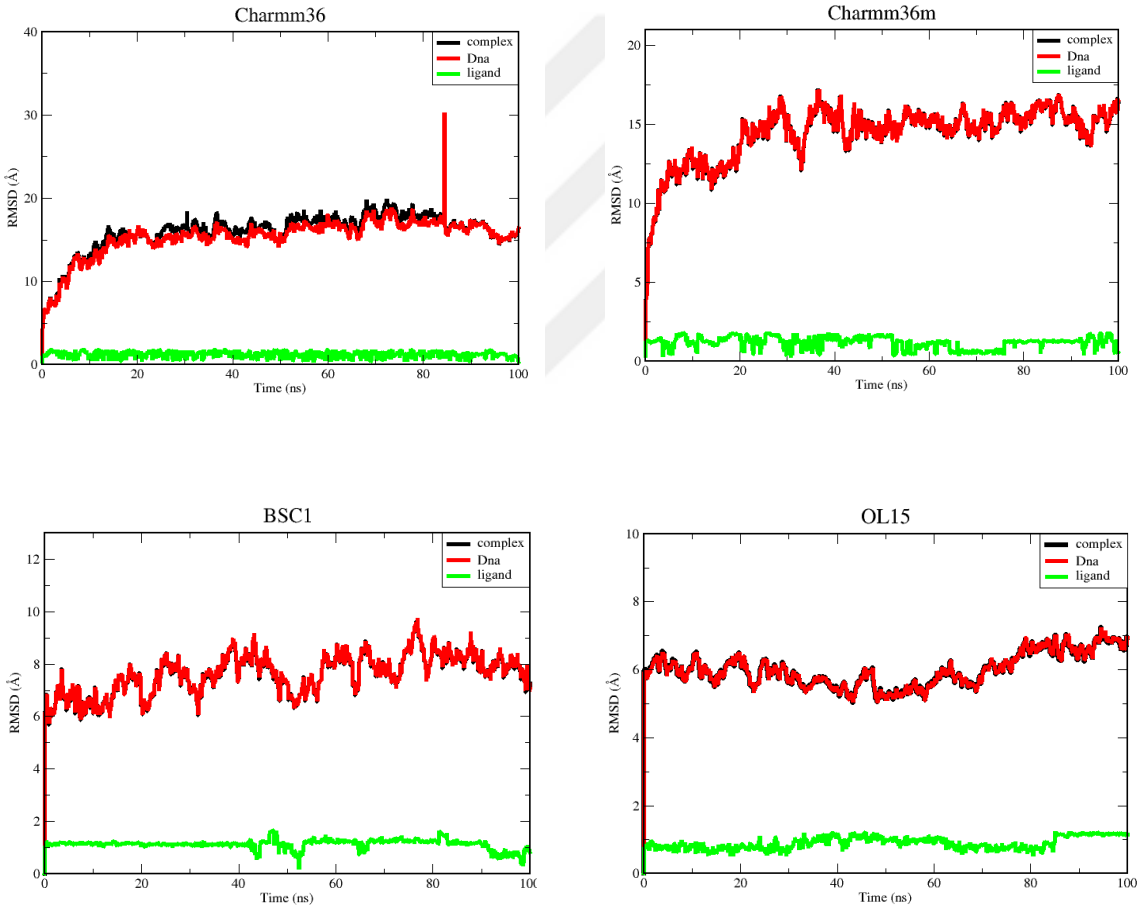

Figure 4.31.1. RMSDs of the SS-DNA-ligand complex versus 100 ns of MD simulation for each force field

Among the four complex configurations, charmm36 exhibits the maximum RMSD value, whereas the aptamer ligand located at OL15 manifests the minimum RMSD value.

Elevated RMSD values induce a substantial alteration in the conformation of the DNA-ligand complex, resulting in decreased stability. Upon examination of Figures charmm36 and charmm36m, it is evident that the RMSD value of the DNA-ligand complex structure in charmm36 is greater than that of charmm36m.

RMSD	Ligand	Dna	Complex
Charmm36	1.526	14.18	15.02
Charmm36m	1.615	10.31	10.74
BSC1	1.013	7.882	7.885
OL15	1.568	6.301	6.302

Table 4.31.1. RMSD values by force field

In the instance of charmm36, a boost in the RMSD value was shown from the initial position to 20 ns during the binding of the ligand; after 20 ns, it increased slightly to 80 ns with minimal fluctuations and did not exhibit a large conformational change during the simulation; however, around 80 ns, the dna RMSD value increased to the highest RMSD value, but from this point on, the simulation was terminated. In contrast, in charmm36m, the rmsd value increased significantly from the commencement of the simulation until 20 ns, increased further after 20 ns, and then decreased abruptly at 30 ns. Between 40 ns and 80 ns, aptamer-ligand did not undergo a significant conformational change. The complex structure underwent a significant conformational change due to ligand binding, as shown by its attainment of a maximum value at 85 ns.

Despite the fact that the DNA-ligand complex exhibits the lowest RMSD value in the OL15 instance, the disparity in the RMSD value between it and BSC1 is negligible. Upon analyzing the graphs, it is evident that the two intricate structures displayed distinct behaviors over the course of the simulation. Upon examining the Bsc1 graph, it is evident that the RMSD of the complex structure began to exhibit an upward trend after the initial 10 nanoseconds. Subsequently, the RMSD values displayed fluctuations until 80 nanoseconds, after which the complex structure failed to attain equilibrium by the conclusion of the simulation. Upon examining the Ol15 graph, it can be observed that the RMSD value remained constant until 20 ns.

However, subsequent to this time point, a decline in the RMSD value was noted between the 40 and 60 ns intervals. Following this, an increase in the RMSD value was observed after 65 ns, with a continued increase in the last 5 ns of the simulation.

Upon examination of the ligand in charmm36m, it has been observed that the ligand has exhibited displacement from the binding region in certain areas. The Charmm36 simulation reveals a modification in the binding orientation of the ligand during the final 5 nanoseconds. The Bsc1 graph indicates that the ligand remained stable within the binding region throughout the initial phase of the simulation, spanning up to 40 ns. However, between 40 and 65 ns, the ligand exited the ligand orbit and exhibited a similar trend towards the end of the simulation.

Conversely, the ol15 graph depicts the ligand's stability throughout the simulation, with no significant changes observed until 20 ns. Subsequently, the ligand's RMSD value exhibited fluctuations but ultimately reached equilibrium during the final 10 ns of the simulation, indicating good binding behavior with the aptamer.

4.31.2. Root Mean Square Fluctuation

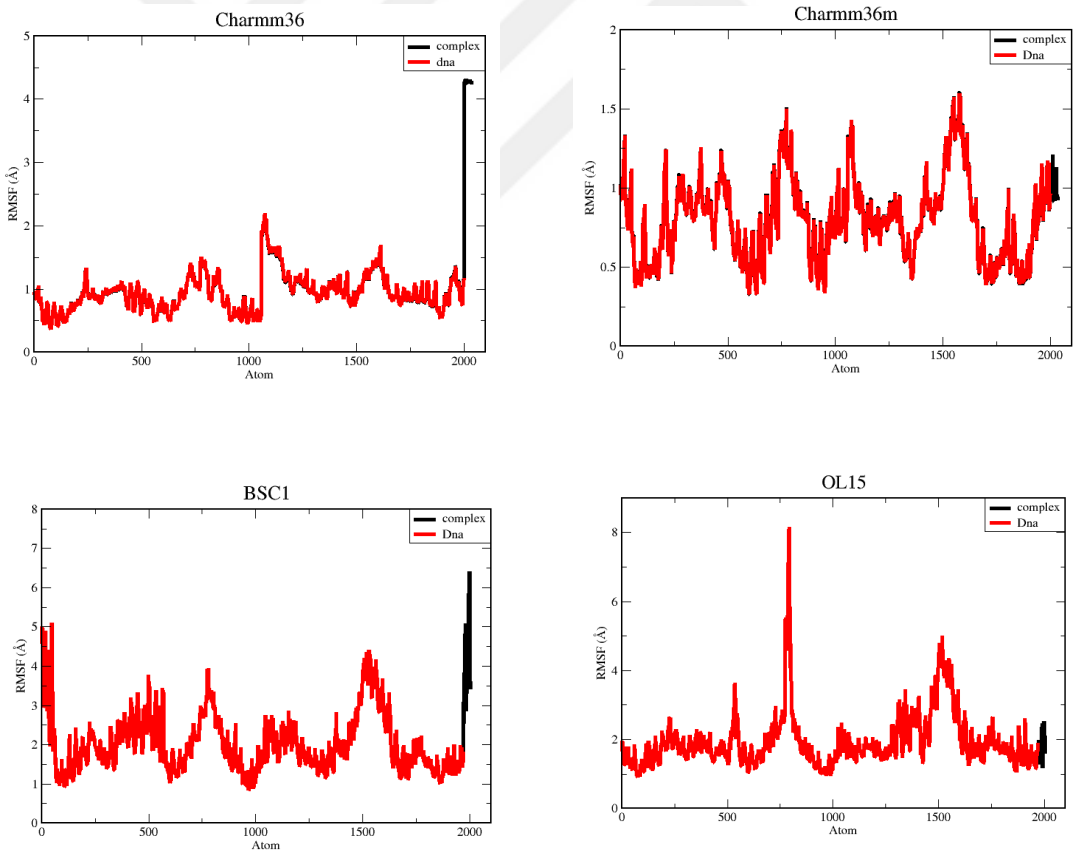

Figure 4.31.2. RMSFs of the SS-DNA-ligand complex versus 100 ns of MD simulation for each force field

Comparing the Charmm36 graph, the regions for base indices 34–36, 23–25, and 50–51 contain the most significant peaks, and the base pairs in these regions are T–A–T, A–G–C, and A–C for all three regions, respectively. The base pairs between positions 34 and 36 have the greatest RMSF value. Three of these bases with high RMSF values, the bases in the 34–36 region, are within the internal loop of the DNA aptamer structure, whereas the base pairs in the 23–25 and 50–51 regions are outside the binding site. The regions with high RMSF values in the complex structure are identical to those in the DNA structure, but the value of the RMSF value in the 5'–3' sequence is quite high in the 3' terminal residue. This is because the 3' terminal residue represents the tail of the structure, which is highly reactive and free to move, and the end of the sequence.

The -C-A- bases in the 49–50 region of the charmm36m graph have the highest RMSF peak. These bases are located in the internal loop region of the DNA aptamer structure, reduce the structure's stability, and are also located outside the binding site. The second greatest rmsf increase is the -G- base at position 24, which is located in the DNA aptamer's internal loop region. The regions with high RMSF values in the complex structure are identical to those in the DNA structure, but unlike the Charmm36 graph, the RMSF value is not as high in the 5'-3' sequence, in the 3' terminal residue, which stabilizes the structure more.

In contrast, when we look at the BSC1 and OL15 graphs, the RMSF values indicate that the significant peaks are lower. The peak with the highest RMSF value in BSC1 is located in the 5'–3' sequence and the value at the 5' terminal residue is quite high. The region between 49 and 50 displaying the second-greatest RMSF peak is -C-A. Both regions are absent from the binding region. The greatest RMSF peak in OL15 is -C and is located in region 25 of the internal loop.

4.31.3. Gyration Radius Variation

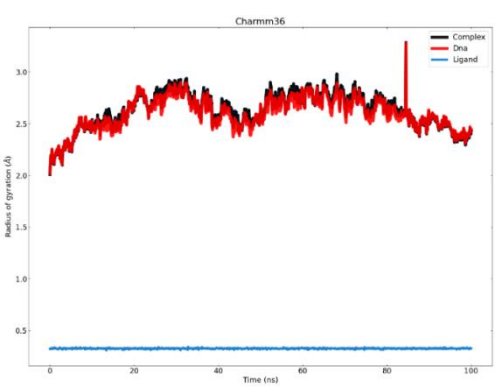

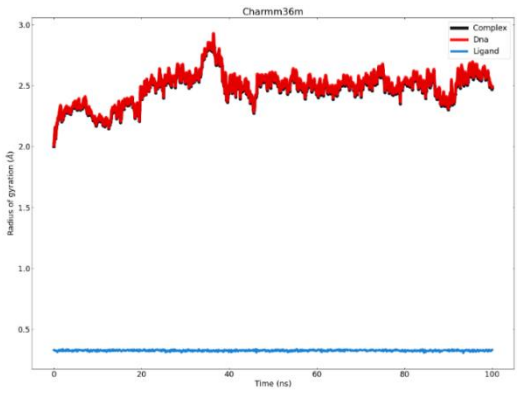

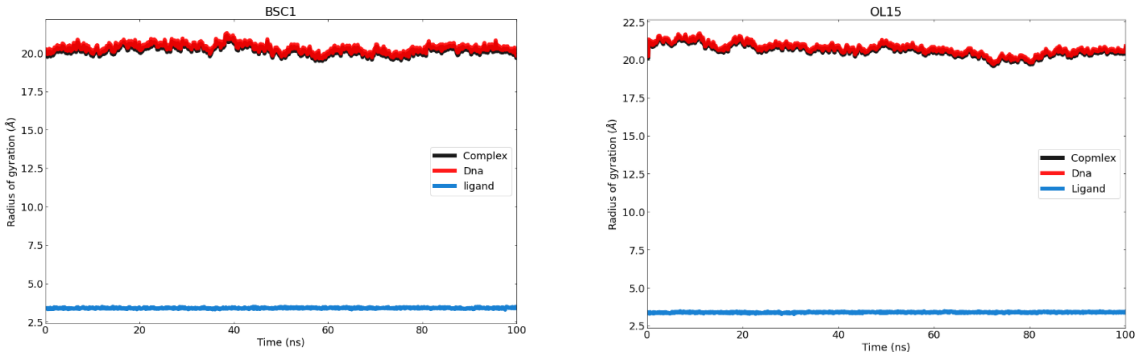

Figure 4.31.3. RGs of the SS-DNA-ligand complex versus 100 ns of MD simulation for each force field

In the Charmm36 graph, the average RG value of the DNA-ligand complex was greater than 4, and Rg values increased in both the complex system and DNA from the beginning of the simulation, with DNA exhibiting the highest RG value at 85 ns. Although the RG values of both the complex and DNA decreased between 40 and 50 ns, they continued to increase after 50 ns, with the exception of the last 10 ns of the simulation, in which the RG value decreased.

Throughout the simulation, these increases and decreases led to structural changes in the complex structure and a loss of stability. In charmm36m, the RG value of the complex system increased briefly, particularly at the outset of the simulation, before experiencing a brief decrease, particularly between 20 and 40 ns, a large increase, and reaching its maximum value. However, between 40 and 85 ns, the structure was extremely stable, indicating that the interaction between the aptamer and ligand has attained equilibrium and is extremely strong. Despite a slight rise between 85 ns and the end of the simulation, it undergoes fewer conformational changes than Charmm36.

Throughout the simulation, these increases and decreases led to structural changes in the complex structure and a loss of stability. In charmm36m, the RG value of the complex system increased briefly, particularly at the outset of the simulation, before experiencing a brief decrease, particularly between 20 and 40 ns, a large increase, and reaching its maximum value. However, between 40 and 85 ns, the structure was extremely stable, indicating that the interaction between the aptamer and ligand has attained equilibrium and is extremely strong. Despite a slight rise between 85 ns and the end of the simulation, it undergoes fewer conformational changes than Charmm36.

The average RG values of systems in BSC1 and OL15 are significantly greater than those of charmm36 and charmm36m. In the case of BSC1, the aptamer-ligand system has a lower average RG value than that of OL15, and the overall RG curve indicates that the aptamer undergoes some conformational changes but remains constant with significant fluctuations throughout the simulation time. However, the aptamer's overall compactness is slightly diminished. In contrast, in the case of OL15, both the RG value and the system endure more conformational changes during the simulation compared to BSC1, but the system reaches equilibrium in the last 10 ns of the simulation, just as it does for BSC1.

4.31.4 Hydrogen bond

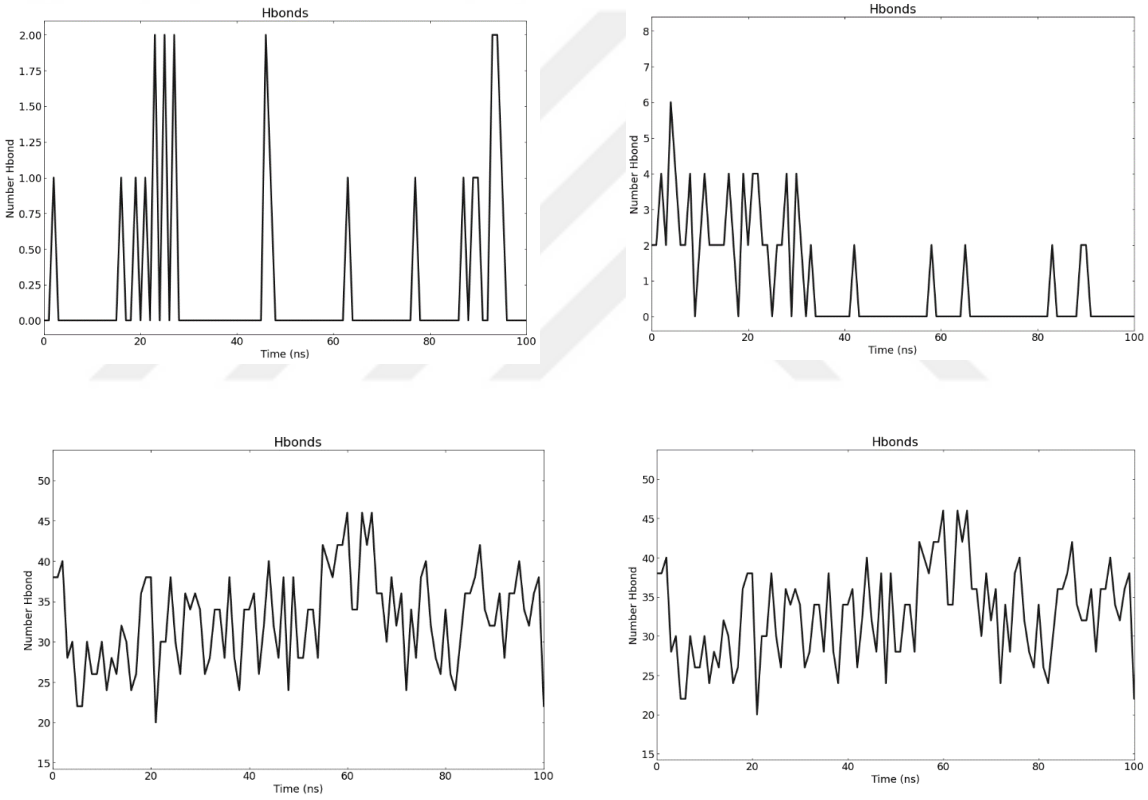

Figure 4.31.4. Hbonds of the SS-DNA-ligand complex versus 100 ns of MD simulation for each force field

As depicted in Figure 9, a dynamic pattern in the amount of hydrogen bonds present in the ligand-bound states was observed throughout the entire MD simulation. The simulation of molecular dynamics revealed that the states BSC1 and OL15 have the maximum number of hydrogen bonds between DNA and ligand.

Compared to the bsc1 and ol15 states, the charmm36 and charmm36m states exhibited significantly less hydrogen bond formation.

4.31.5 Analysis of PCA and DCCM

Charmm36-complex

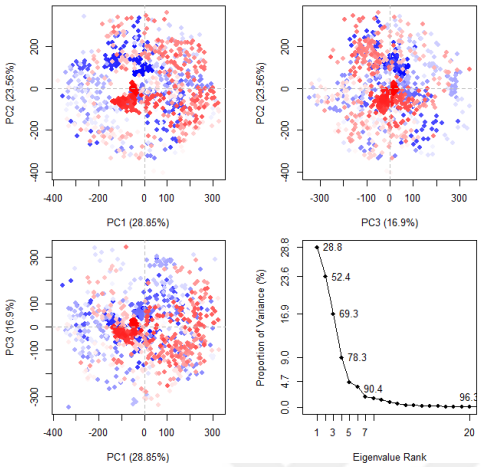

DNA

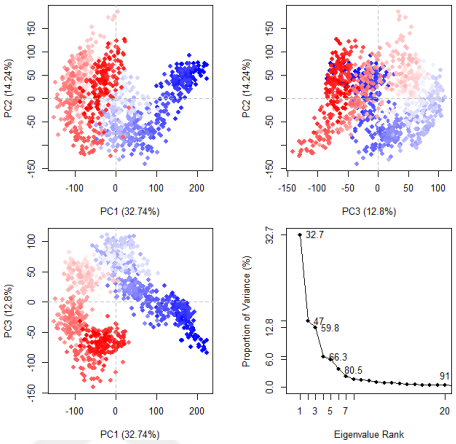

Charmm36m-complex

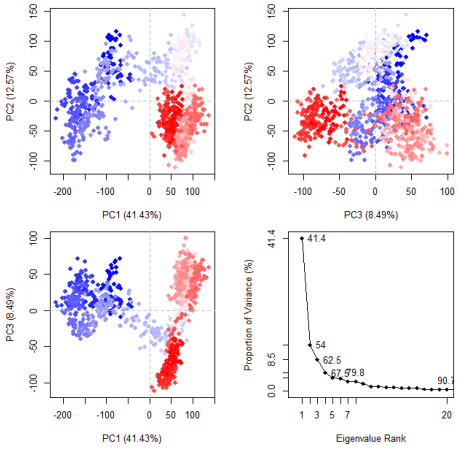

DNA

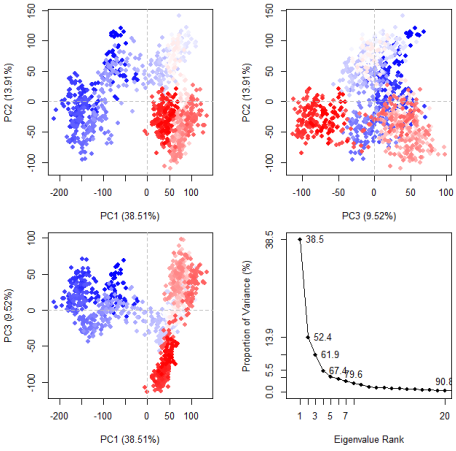

BSC1-complex DNA

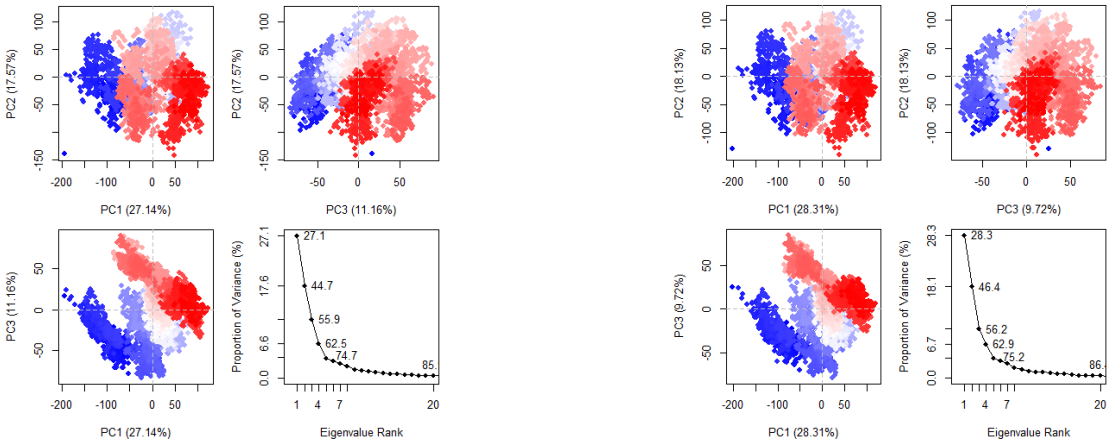

OL15-complex DNA

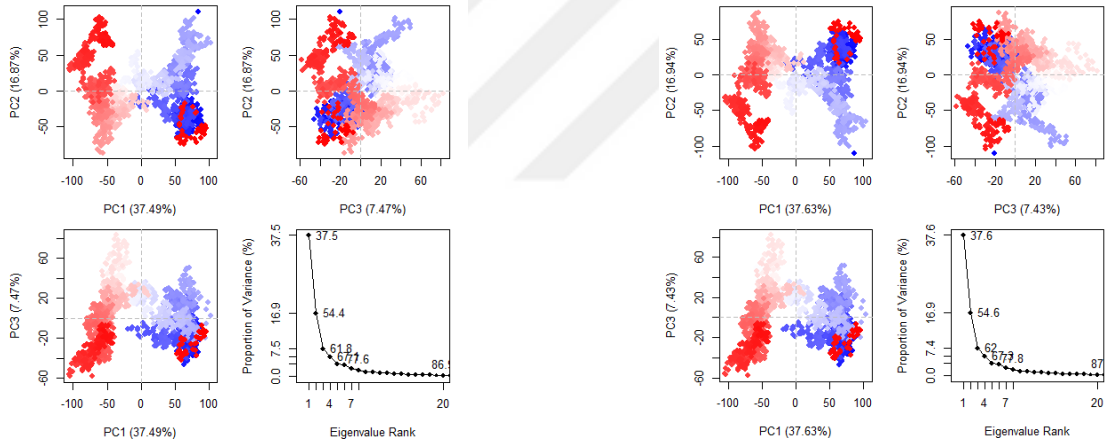

Figure 4.31.5. PCA of the SS-DNA-ligand complex versus 100 ns of MD simulation for each force field

Using a 100 ns simulation, the ranking of eigenvalues versus variance ratios of apo DNA and aptamer-ligand complexes was determined. According to the graphs, apo DNA obtained a variance of 32.7% for the first PC for charmm36. Accordingly, the variances for the second and third PCs were 12.8% and 6.0%, respectively. Compared to apo DNA, the aptamer-ligand complex for charmm36 exhibited a variance of 28.8% for the first PC, 23.6% for the second PC, and 16.8% for the third PC.

For each principal component, the variances of apo DNA are greater than those of the aptamer-ligand complex, indicating that the atoms of apo DNA leave more rapidly than those of the aptamer-ligand complex.

For Charmm36m, the variance of apo DNA was 38.5% for the 1st PC, 13.9% for the 2nd PC, and 5.5% for the 3rd PC, whereas the variance of the complex system was 41.4% and 8.5%, which was higher than that of apo DNA, indicating that apo DNA atoms move more slowly than aptamer-ligand complex atoms. These results suggest that an increase in the mobility of atoms in the aptamer-ligand system contributes to the system's adaptability. PC 1, 2, and 3 for BSC1 apo DNA displayed variances of 23.3%, 18.1%, and 6.7%, respectively, whereas the complex system displayed variances of 27.1%, 17.6%, and 6.7%. For each principal component, the variances of apo DNA are smaller than those of the aptamer-ligand complex, indicating that apo DNA atoms move more slowly than aptamer-ligand complex atoms. These results suggest that an increase in the mobility of atoms in the aptamer-ligand system contributes to the system's adaptability.

Charmm36-complex

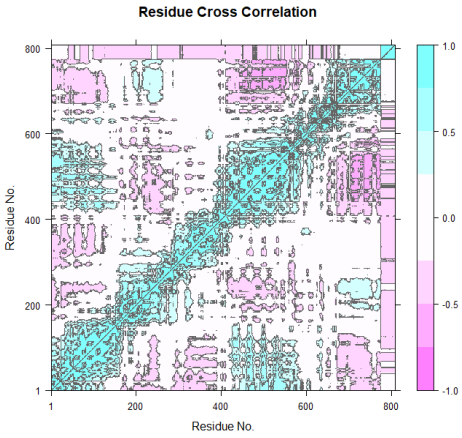

DNA

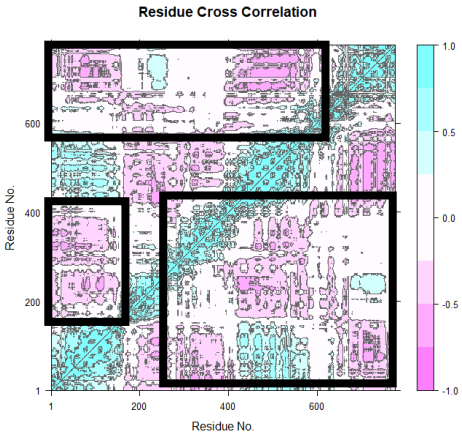

Charmm36m-complex

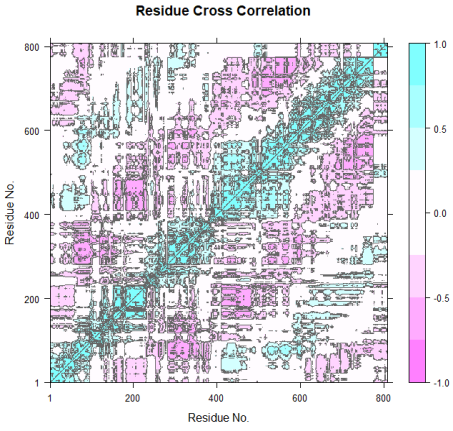

DNA

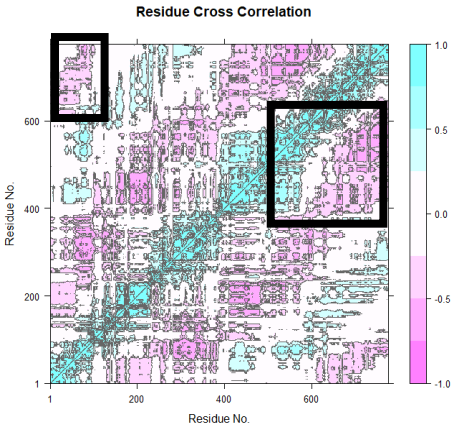

BSC1-complex

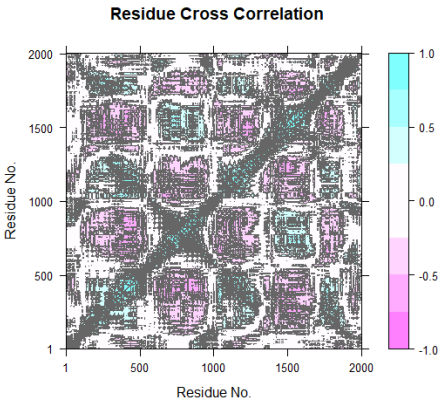

DNA

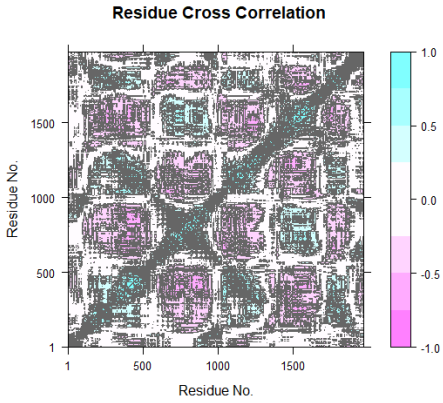

OL15-complex

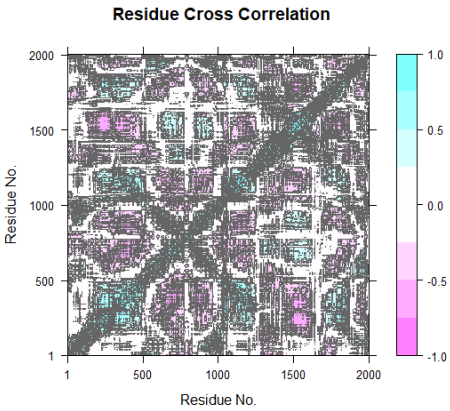

DNA

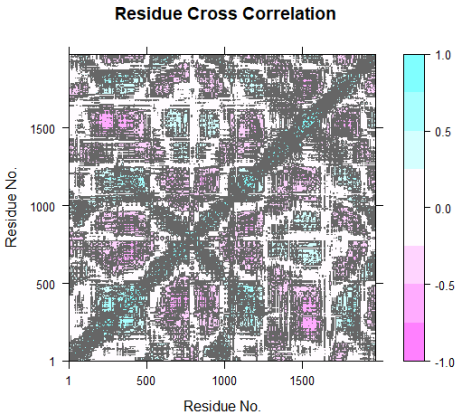

Figure 4.31.6. DCCM of the SS-DNA-ligand complex versus 100 ns of MD simulation for each force field

When analyzing the DCCM schematics of the four systems, it was discovered that the associated motions of each system were notably distinct. Significant distinctions in ligand binding exist between Charmm36's complex system and apo DNA. Positively correlated movements between apo DNA and the complex system remained relatively constant, whereas negatively correlated movements in the aptamer-ligand system decreased markedly. Positively correlated motions between apo DNA and the complex system remained relatively constant in Charmm36m, whereas negatively correlated motions in the complex system decreased slightly. Positive and negative correlated motions in the complex and apo DNA systems of BSC1 and OL15 remained relatively constant in both instances.

4.32. Molecular dynamic simulation analysis of the modeled ss-DNA aptamer from the 3dRNA server against bisphenol A

Following the molecular docking method, a complex was generated between ss-DNA and ligand, which was subsequently subjected to a 100 nanosecond molecular dynamics simulation. The simulation employed two distinct iterations of the AMBER and Charmm force fields. In addition to the examination of hydrogen bonding, an assessment was conducted on the radius of gyration, RMSD, and RMSF. Graphical representations were utilized to analyze and draw conclusions for the four force fields employed in the study

4.32.1. Analysis of RMSD

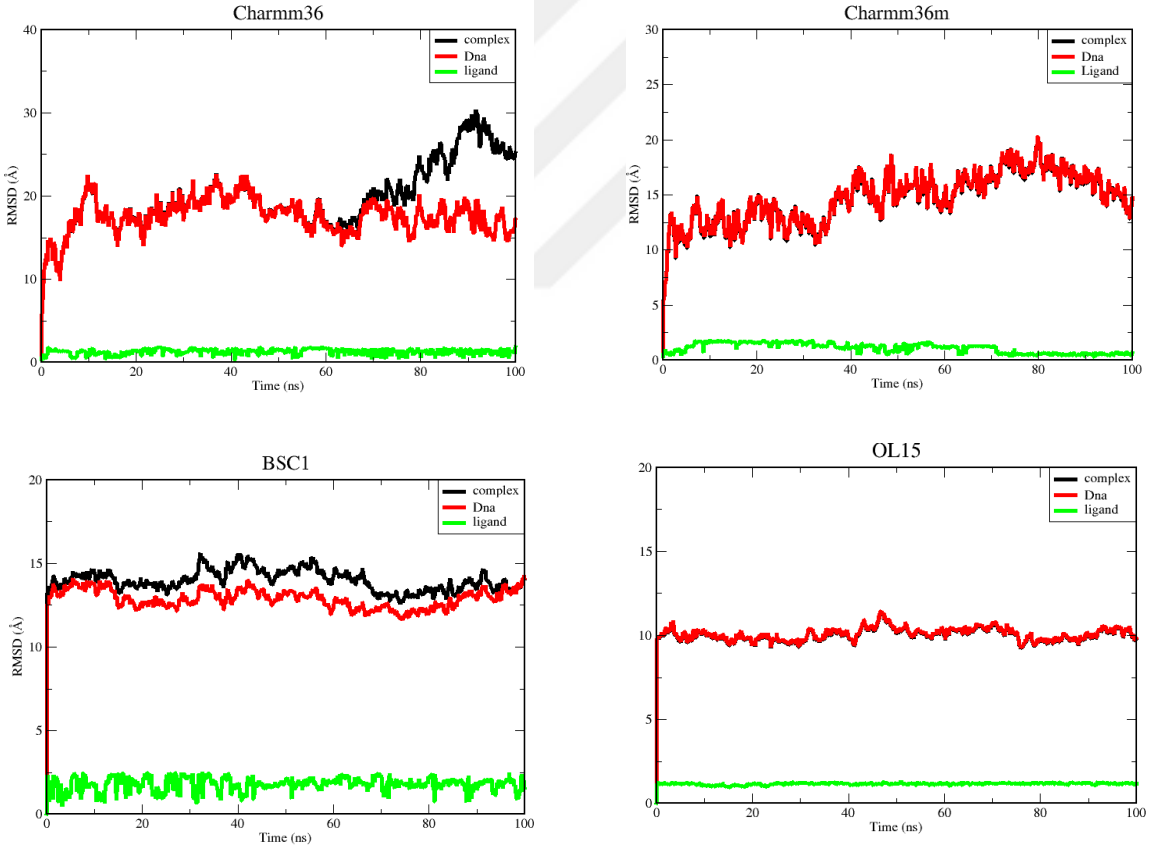

Figure 4.32.1. RMSDs of the SS-DNA-ligand complex versus 100 ns of MD simulation for each force field

Charmm36 has the highest RMSD value of the four complex structures, while the aptamer-ligand complex in OL15 has the lowest.

Comparing Figures charmm36 and charmm36m, the RMSD value of the DNA-ligand complex aptamer structure in charmm36 is greater than that of charmm36m.

RMSD	**Ligand**	**Dna**	**Complex**
Charmm36	1.163	17.48	20.37
Charmm36m	1.557	14.67	14.62
BSC1	1.796	12.93	13.92
OL15	1.781	10.039	9.990

Table 4.32.1. RMSD values by force field

In addition, the rmsd value of the complex structure increased significantly after 60 ns and continued to increase until 90 ns, indicating that the DNA aptamer-ligand structure is not particularly stable. Despite a modest decrease in the RMSD value after 90 ns, the complex system is extremely unstable.

Although the complex system in charmm36m maintained a constant value with minimal fluctuations until 30 ns, it began to rise after 30 ns and continued to rise until 80 ns. However, this increase in charmm36m is not as significant as in charmm36, and after 80 ns it began to decrease, concluding the simulation. We can conclude that Charmm36m's DNA-aptamer complex is more stable than Charmm36's.

Comparing the DNA-aptamer ligand complexes in the BSC1 and OL15 states, the system in the OL15 state is significantly more stable, with a lower rmsd value and minimal fluctuations throughout the simulation. In the case of bsc1, there is a considerably rises in the rmsd value of the complex system, particularly between 30 and 70 ns, indicating that the complex system, i.e., the DNA-aptamer, has undergone a high conformational change and that there is a continuous change in aptamer conformations, possibly as a result of the aptamer opening.

In terms of the ligands, charmm36 exhibited a smaller RMSD than charmm36m, bsc1, and ol15. However, despite the fact that the ligand binding in Charmm36 has a low RMSD value, the ligand leaves the orbit throughout the simulation and exhibits various orientations of binding. In Charmm36m, the ligand left the DNA aptamer's binding trajectory for approximately 70 ns, and although it was found in various binding orientations, in the final 20 ns, the ligand stabilized and demonstrated strong DNA-aptamer binding. Throughout the simulation of BSC1, the ligand is not in equilibrium, indicating that there are multiple binding orientations.

In contrast to the other ligands, OL15's remained stable throughout the simulation and demonstrated strong binding with the DNA aptamer.

4.32.2. Root Mean Square Fluctuation

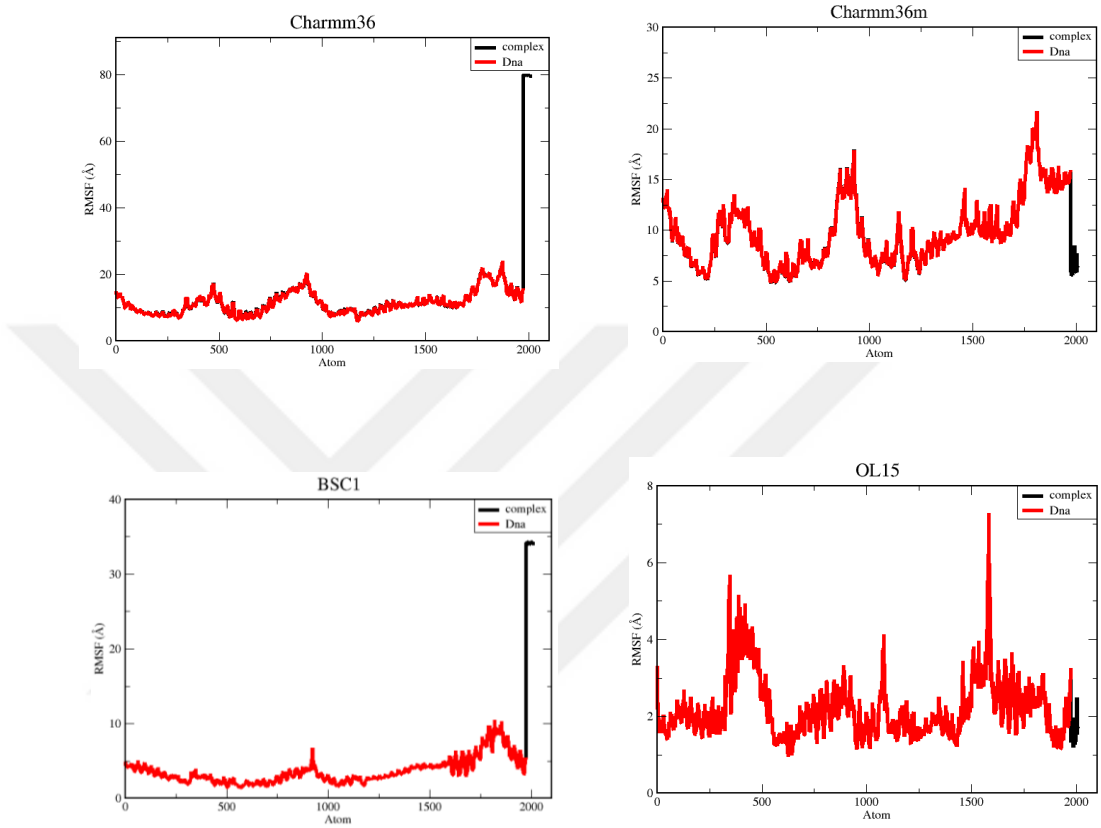

Figure 4.32.2. RMSFs of the SS-DNA-ligand complex versus 100 ns of MD simulation for each force field

Moreover, the complex rmsf values for Charmm36 and BSC1 are quite high compared to other cases. When examining the complex rmsf graph in both instances, the greatest rmsf peak exhibited high ligand state flexibility. However, the complex structures of OL15 and Charmm36m had low rmsf in the ligand state; OL15 has a lower value than Charmm36m, indicating that it forms a more stable complex system. The regions with the highest peak in charmm36m are 56–60, 29–31, and 16–17, which are located in the loop portion of the DNA aptamer structure and provide high flexibility. Comparable to Charmm36, Charmm36m possesses regions with a high degree of flexibility.

The Bsc1 regions with the most flexibility are 56–60 and 27–29. They reside within the spiral. In the loop, OL15 is located, and the region with the highest peak is 50–49.

4.32.3. Gyradition Radius Variation

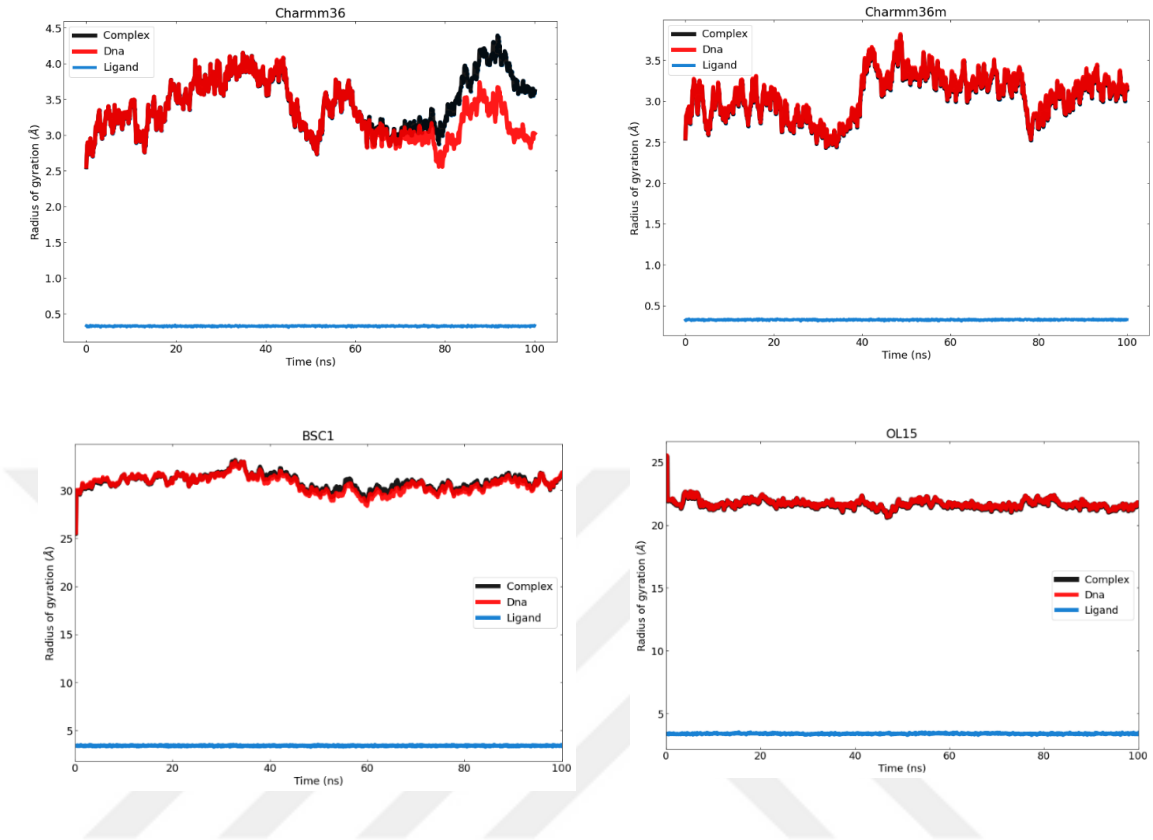

Figure 4.32.3. RGs of the SS-DNA-ligand complex versus 100 ns of MD simulation for each force field

In the Charmm36 graph, the DNA-ligand complex exhibited an average RG value greater than 4, and the RG values increased in both the complex system and DNA from the start of the simulation. At 50 ns, there was a brief decrease followed by an increase; between 60 and 80 ns, there was a state of equilibrium; however, after 80 ns, the RG value of the complex system increased significantly. Throughout the simulation, these increases and decreases represent a change in the complex structure, resulting in structural modifications and decreased stability.

In charmm36m, the compactness of the complex system continued to increase, particularly from the beginning of the simulation until 40 ns, but after 40 ns, the RG value of both DNA and the complex system increased and remained constant until 80 ns, after which it increased again. Although an abrupt decrease was observed, the final 10 ns of the simulation were more stable compared to charmm36.

The average RG values of systems in BSC1 and OL15 are significantly greater than those of charmm36 and charmm36m. Although the aptamer undergoes conformational changes, the aptamer-ligand system in the OL15 case exhibits a lower average RG value compared to BSC1, and the overall RG curve remains constant with significant fluctuations throughout the simulation time. Nonetheless, the overall compactness of the aptamer is minimally altered, whereas both the RG value and a greater number of conformational changes are observed during simulations of BSC1 compared to OL15.

4.32.4. Hydrogen bond

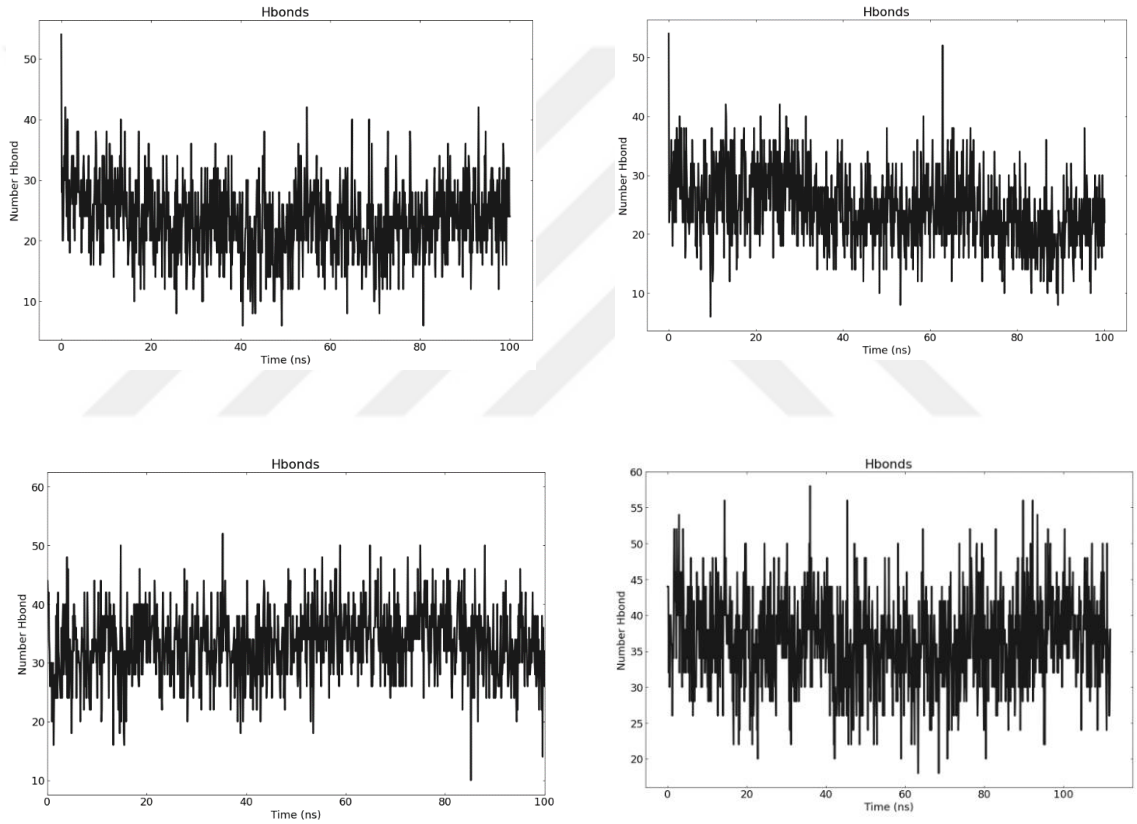

Figure 4.32.4. Hbonds of the SS-DNA-ligand complex versus 100 ns of MD simulation for each force field

The results indicate that there was a fluctuation in the amount of hydrogen bonds present in the ligand-bound states over the course of the 100 ns molecular dynamics simulation, as depicted in Figure 4.32.4. The outcomes of the MD simulation indicate that the BSC1 and OL15 states exhibit the highest quantities of hydrogen bonds between the DNA and ligand, with the OL15 state demonstrating particularly elevated levels. The states of

Charmm36 and Charmm36m demonstrated a notable reduction in hydrogen bond formation in comparison to the states of Bsc1 and Ol15.

4.32.5. Principal component analysis (PCA) and Domain cross-correlation matrix (DCCM)

Charmm36-complex

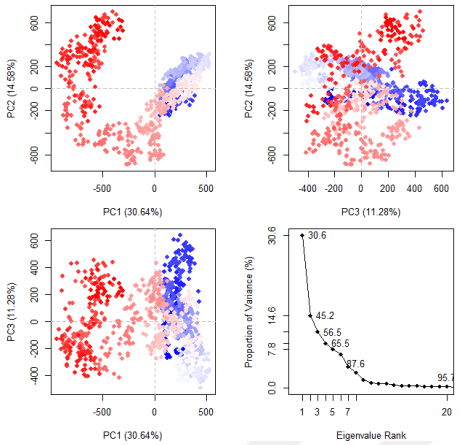

DNA

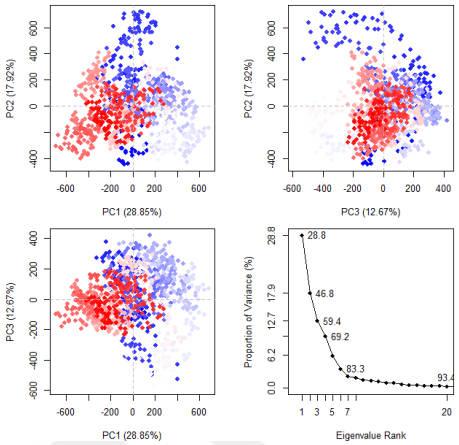

Charmm36m-complex

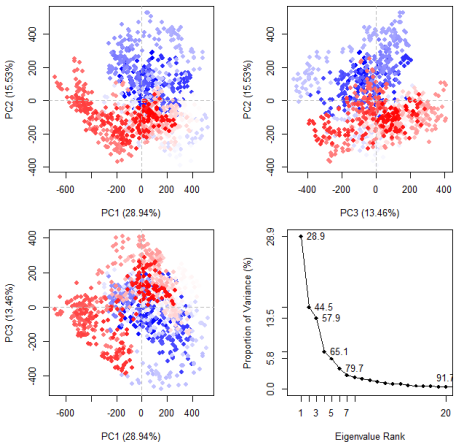

DNA

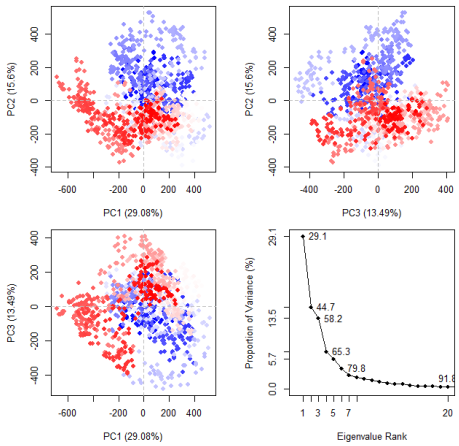

BSC1-complex DNA

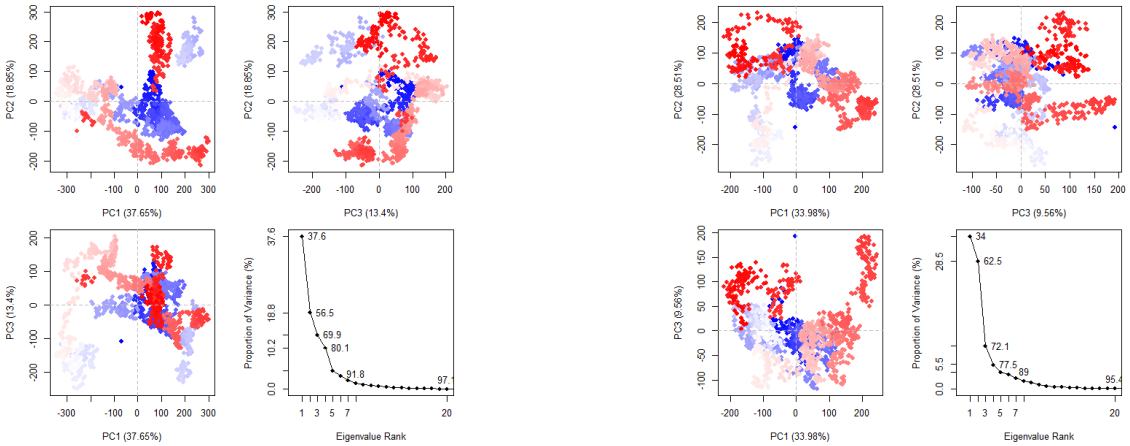

OL15-complex DNA

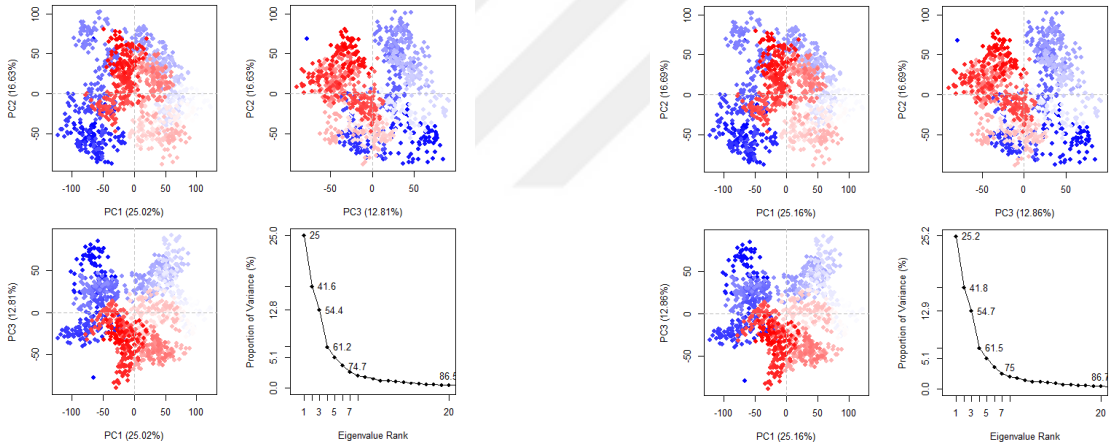

Figure 4.32.5. PCA of the SS-DNA-ligand complex versus 100 ns of MD simulation for each force field

The findings of the analysis conducted on the complex structures of all situations reveal that the initial 20 principal components (PC) of the complex-charmm36 system, charmm36m complex system, BSC1 complex system, and OL15 complex system account for 95.7%, 91.7%, 97.1%, and 86.5% of the total variance, respectively. The aforementioned observation suggests that the OL15 aptamer-DNA system exhibits a reduced degree of phase space and performance adaptability when compared to other intricate systems.

Upon comparison of the PCA plots of the complexes in charmm36 and charmm36m, it was observed that the PC1 cluster displayed the highest degree of variability, explaining 30.64% and 28.94% of the variance, respectively. The PC2 cluster demonstrated variability of 14.58% and 15.53%, respectively, whereas the PC3 cluster displayed negligible variability, representing merely 11.28% of the variance for 36m. Upon comparison of the PCA plots of the complexes in BSC1 and OL15, it was observed that the PC1 cluster displayed the highest degree of variability, explaining 37.65% and 25.02% of the variance, respectively. The OL15 dataset showed that the PC2 cluster had a variability of 18.85% and the PC3 cluster had a minimal variability of 12.81%, whereas the PC3 cluster exhibited a variability of 16.63%.

Charmm36-complex

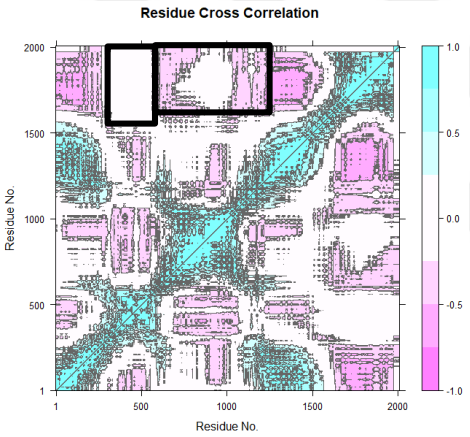

DNA

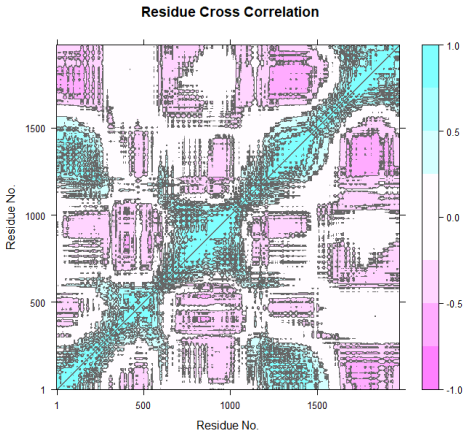

Charmm36m-complex

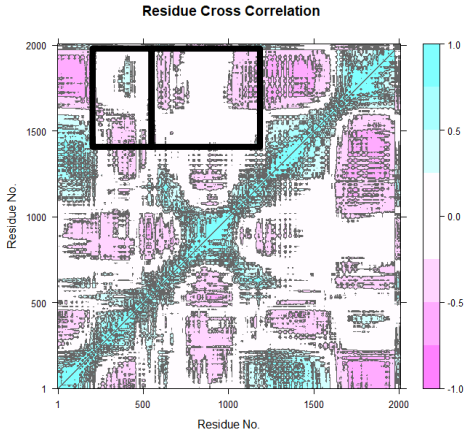

DNA

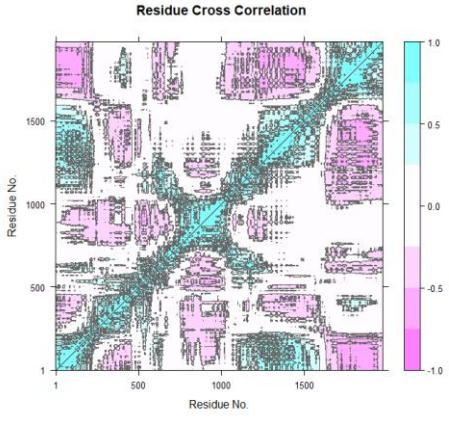

BSC1-complex DNA

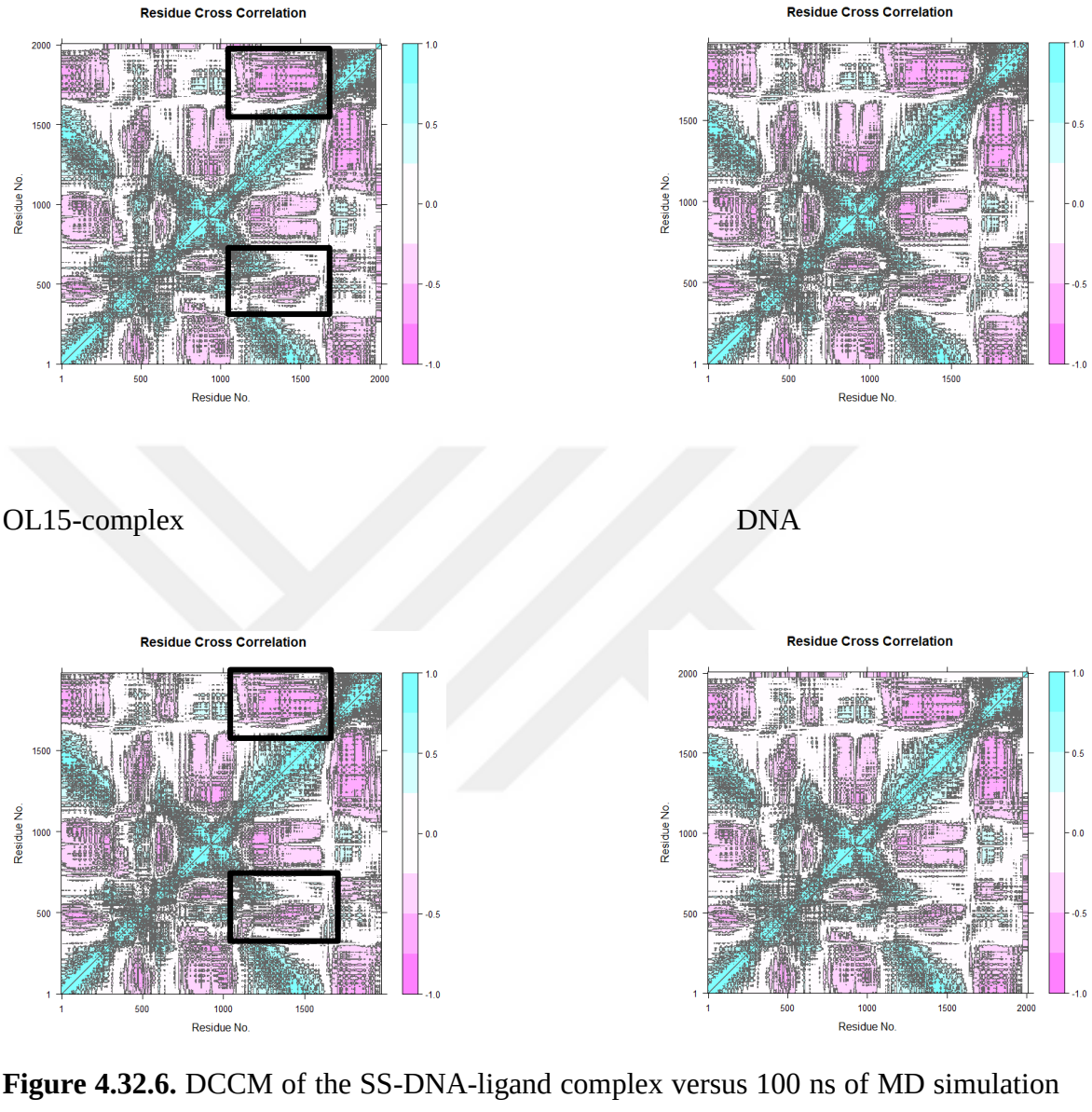

OL15-complex DNA

Figure 4.32.6. DCCM of the SS-DNA-ligand complex versus 100 ns of MD simulation for each force field

Upon analyzing the DCCM diagrams of the four systems, notable variations were observed in the correlated motions of the systems. The application of DCCM (Dynamic Cross Correlation Matrix) analysis to the complex system at charmm36m revealed noteworthy enhancements in the positive correlation motions and reductions in the negative correlation motions following ligand binding, as compared to charmm36. The complex system in the OL15 state exhibited consistent positive correlation motions subsequent to ligand binding in contrast to bsc1. However, the negative correlation motions experienced a reduction.

4.33. Molecular dynamic simulation analysis of the modeled ss-DNA aptamer from the 3D-DART server against bisphenol A

An SS-DNA-ligand complex was formed using the molecular docking technique and then simulated using molecular dynamics for 100 ns. The simulation used two versions of the force fields from Amber and Charmm. The radius of gyration, RMSD, and RMSF were evaluated in addition to hydrogen bonding. The study's four force fields were analyzed using visual representations to help draw conclusions.

4.33.1. Analysis of RMSD

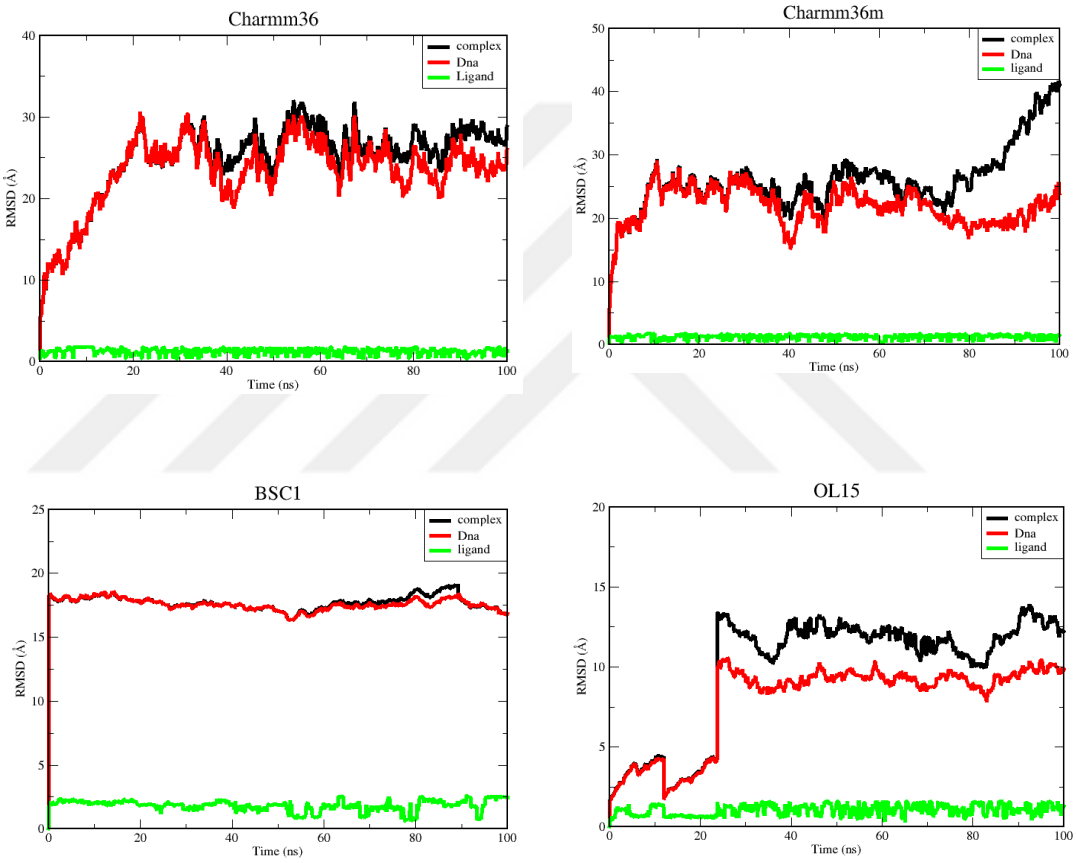

Figure 4.33.1. RMSDs of the SS-DNA-ligand complex versus 100 ns of MD simulation for each force field

Among the four complex structures, charmm36 exhibits the highest RMSD value, whereas the aptamer-ligand complex at OL15 demonstrates the lowest. Upon examination of Figures charmm36 and charmm36m, it was observed that the DNA-ligand complex aptamer structure in charmm36 exhibited a substantial rise in rmsd value during the initial 20 ns, subsequently displaying fluctuations in rmsd value from 20 ns to 90 ns,

before ultimately attaining a consistent rmsd value during the final 10 ns. The Charmm36m simulation revealed fluctuations within the complex system for a duration of 80 nanoseconds. Subsequently, a significant rise in RMSD level was observed, which persisted until the conclusion of the simulation. Throughout the simulation of BSC1, RMSD value remained constant, and the ligand exhibited superior binding affinity with the DNA structure.

4.33.2. Root Mean Square Fluctuation

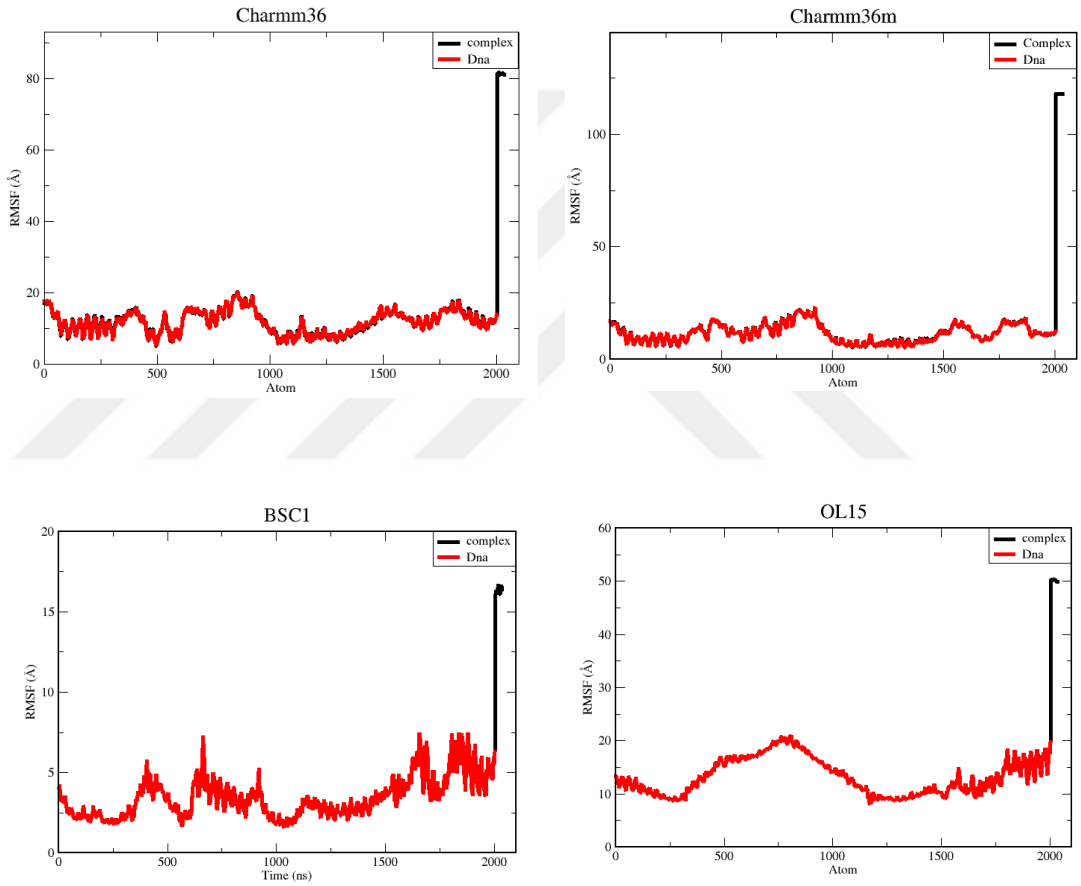

Figure 4.33.2. RMSFs of the SS-DNA-ligand complex versus 100 ns of MD simulation for each force field

The charmm36m model exhibits the highest Root Mean Square Fluctuation (RMSF) value, whereas the BSC1 model displays the lowest RMSF value. Furthermore, it is noteworthy that RMSF values in the CHARMM36m and CHARMM36 force fields exhibit relatively elevated levels in comparison to other instances. Upon examination of the intricate root mean square fluctuation (rmsf) plot in both instances, it was observed

that the most prominent rmsf peak exhibited a considerable degree of flexibility in the context of ligand binding. In the context of OL15 and BSC1, it was observed that the complex structures exhibited reduced RMSF in the existence of the ligand. Notably, BSC1 demonstrated a lower RMSF level in comparison to OL15, suggesting that it forms a more stable complex system. Upon examination of the DNA aptamer structures, it is observed that the regions exhibiting the most pronounced peak in both charmm36 and charmm36m are situated within the loop component of the DNA aptamer structure, thus imparting significant flexibility. The areas exhibiting the greatest degree of flexibility for BSC1 and OL15 are likewise situated within the loop.

4.33.3. Gyration Radius Variation

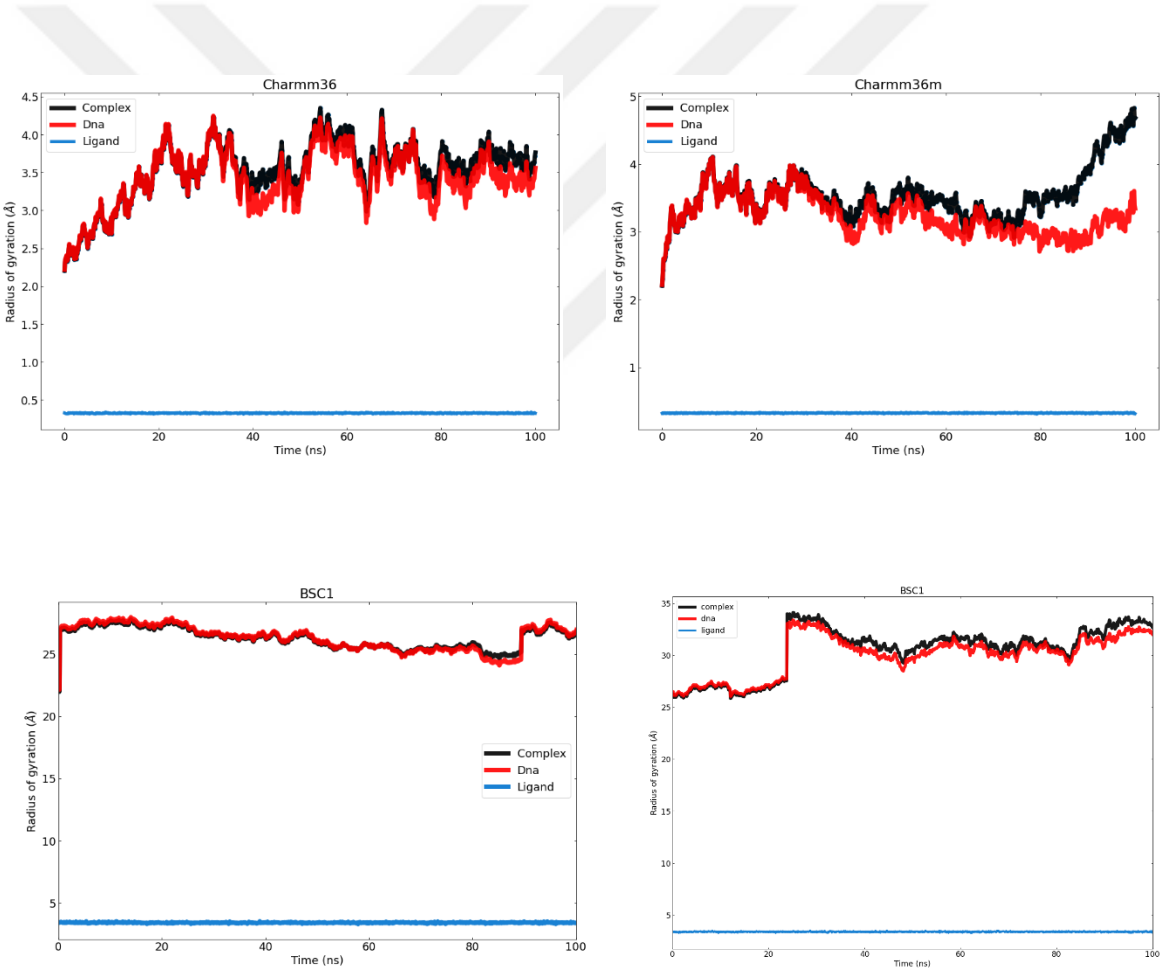

Figure 4.33.3. RGs of the SS-DNA-ligand complex versus 100 ns of MD simulation for each force field

The Charmm36 analysis indicates that the radius of gyration (Rg) values for the DNA-ligand complex exhibited an increase in both the complex system and the DNA

component. At 50 ns, the Rg values showed an initial decline and then an increase. Subsequently, the Rg value of the complex system remained constant until the completion of the simulation at 80 ns.

The Charmm36m simulation results indicate a notable increase in the RG value of the complex system, particularly during the initial phase of the simulation and up to 20 ns. Subsequently, fluctuations in the RG value persisted until 80 ns, following which a significant surge in the RG value was observed until the conclusion of the simulation.

The RG values of the systems in BSC1 and OL15 exhibit a significant increase in comparison to charmm36 and charmm36m. However, it is noteworthy that the complex system displays greater stability in the BSC1 instance.

4.33.4. Hydrogen bond

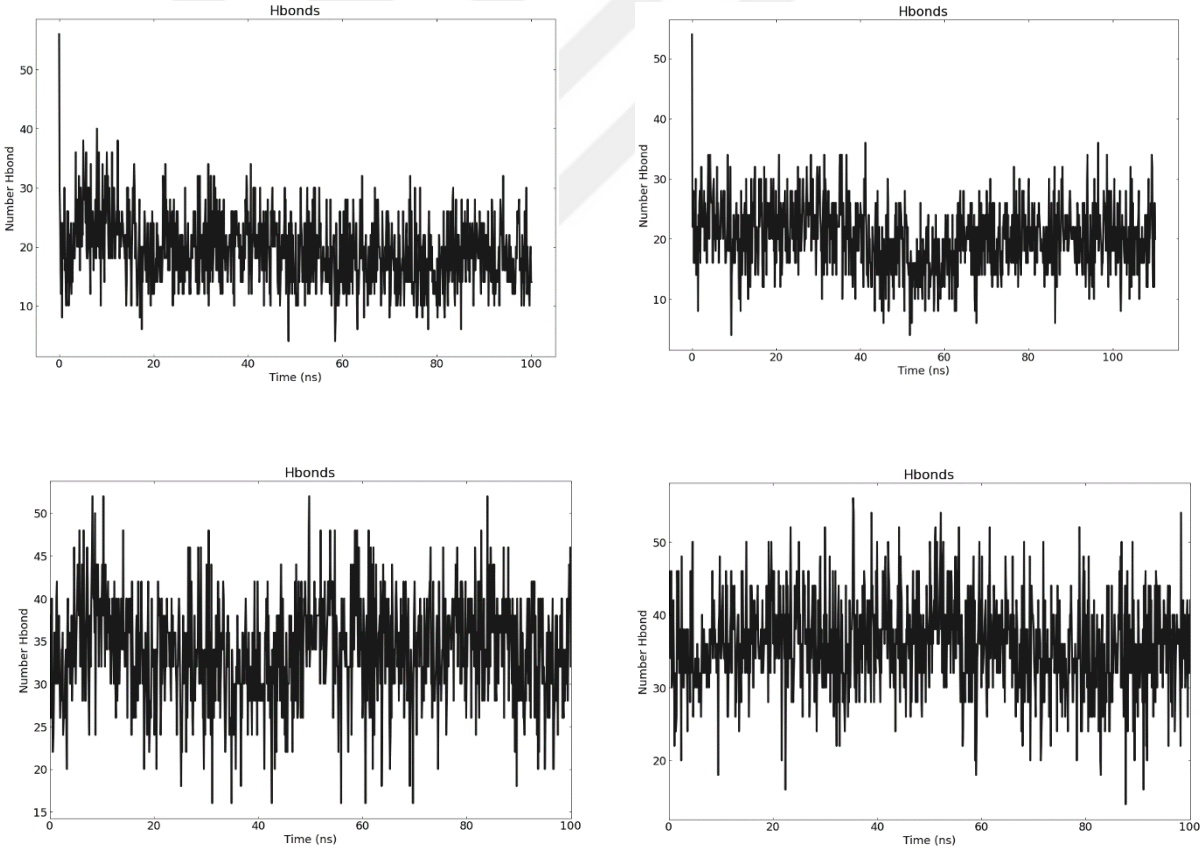

Figure 4.33.4. Hbonds of the SS-DNA-ligand complex versus 100 ns of MD simulation for each force field

Figure 9 displays the results, which reveal that the amount of hydrogen bonds in the ligand-bound states varied throughout the 100 ns molecular dynamics simulation. The findings of the molecular dynamics simulations demonstrate that the BSC1 and OL15 states have the largest levels of hydrogen bonds between the DNA and the ligand. When compared to the Bsc1 and Ol15 states, the Charmm36 and Charmm36m states displayed significantly weaker hydrogen bond formation.

4.33.5. Principal component analysis (PCA) and Domain cross-correlation matrix (DCCM)

Charmm36-complex

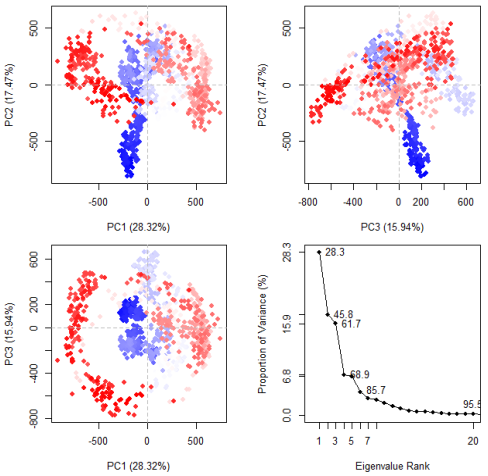

DNA

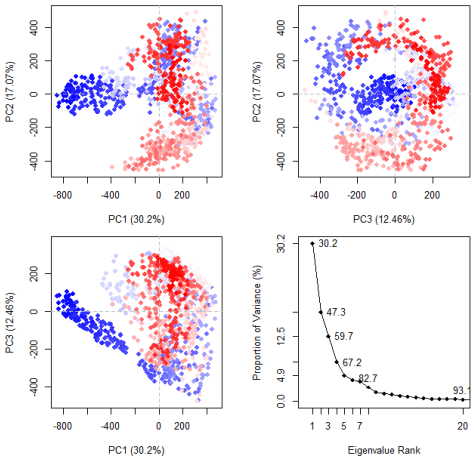

Charmm36m-complex

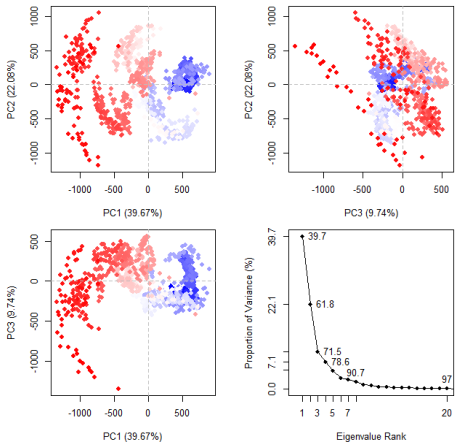

DNA

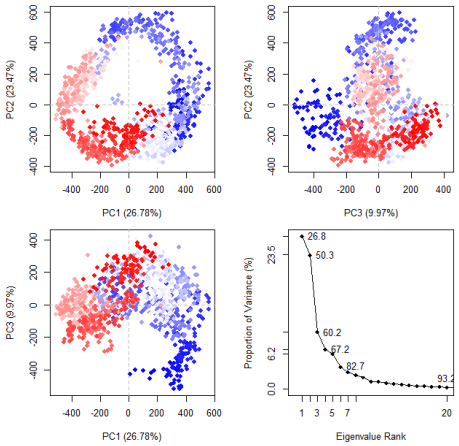

BSC1-complex DNA

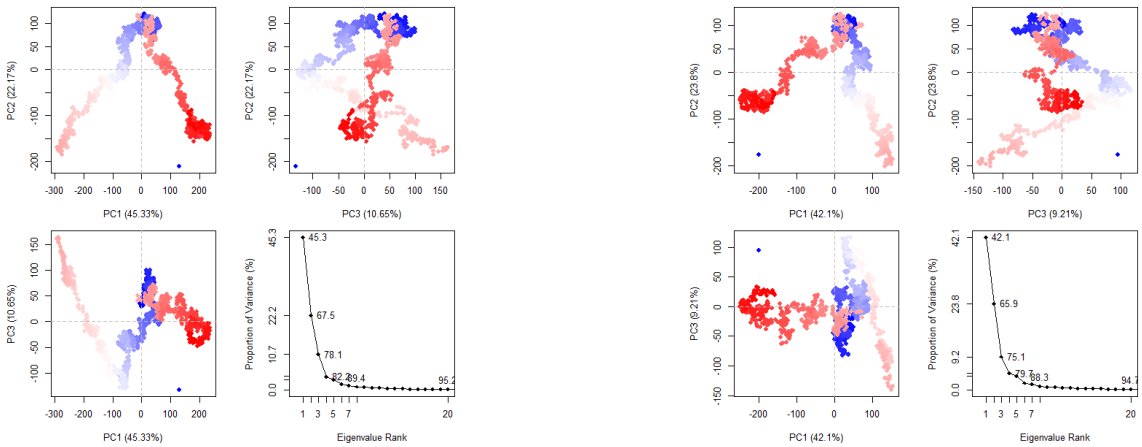

0L15-complex DNA

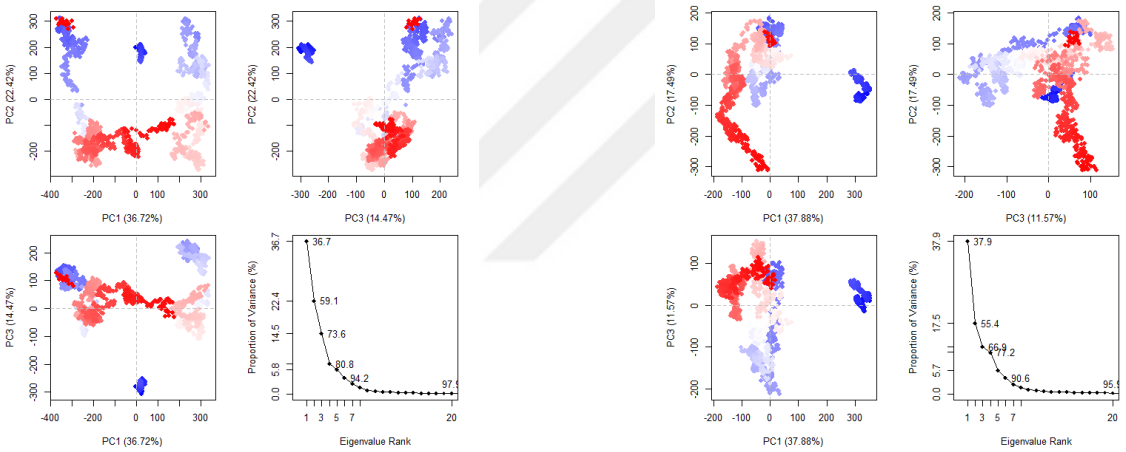

Figure 4.33.5. PCA of the SS-DNA-ligand complex versus 100 ns of MD simulation for each force field

The findings of the analysis conducted on the complex structures of all situations reveal that the initial 20 principal components (PC) of the complex-charmm36 system, charmm36m complex system, BSC1 complex system, and OL15 complex system account for 95.5%, 97%, 95.2%, and 97.5% of the total variance, respectively. The aforementioned observation suggests that the BSC1 aptamer-DNA system exhibits a reduced degree of phase space and performance adaptability when compared to other intricate systems. Upon comparison of the PCA plots of the complexes in charmm36 and charmm36m, it was observed that the PC1 cluster displayed the highest degree of variability, explaining 28.32% and 39.67% of the variance, respectively.

The PC2 cluster demonstrated variability of 17.47% and 22.08%, respectively, whereas the PC3 cluster displayed negligible variability, representing merely 9.74% of the variance for 36m. Upon comparison of the PCA plots of the complexes in BSC1 and OL15, it was observed that the PC1 cluster displayed the highest degree of variability, explaining 45.33% and 36.72% of the variance, respectively. The OL15 dataset showed that the PC2 cluster had a variability of 22.42% and the PC3 cluster had a minimal variability of 10.65%, whereas the PC3 cluster exhibited a variability of 14.47%.

Charmm36-complex

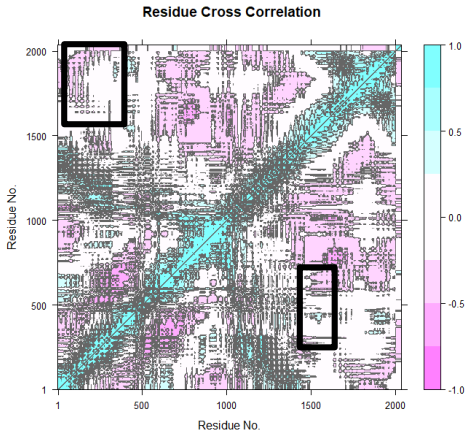

DNA

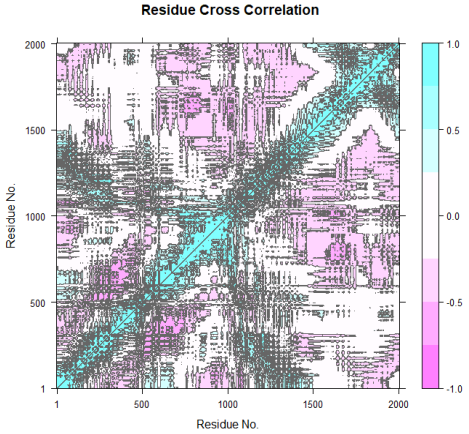

Charmm36m-complex

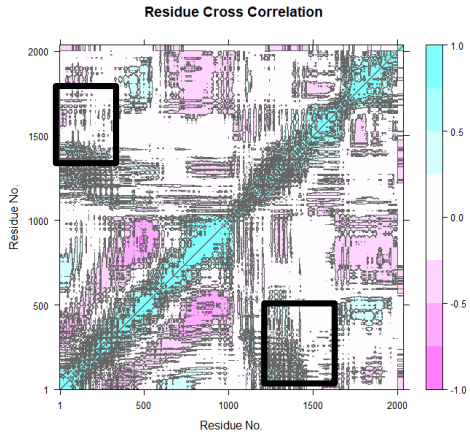

DNA

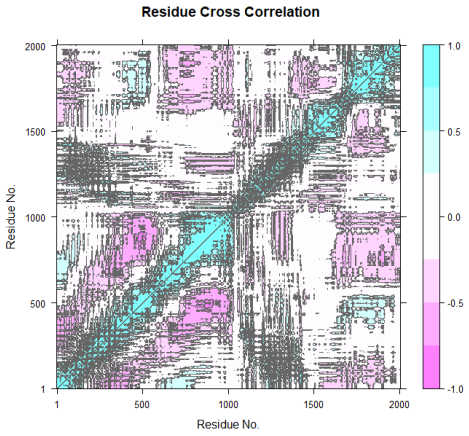

BSC1-complex DNA

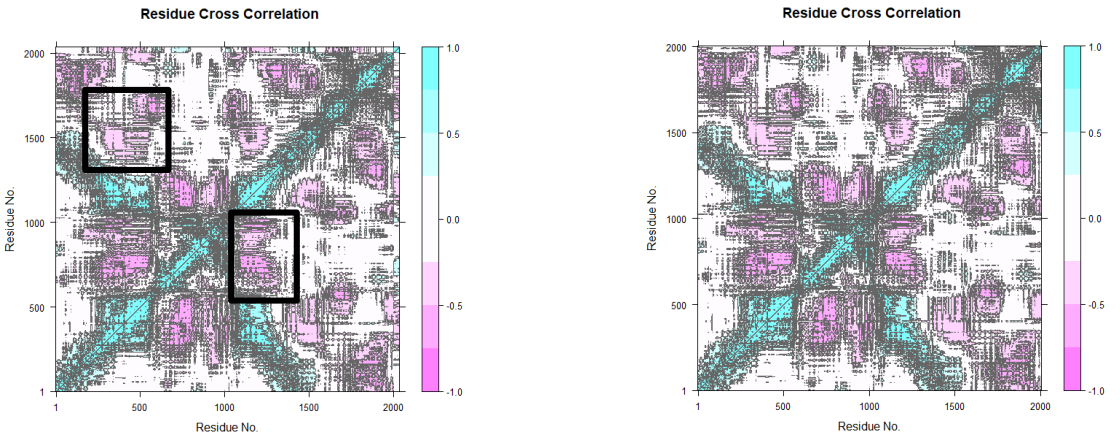

OL15-complex DNA

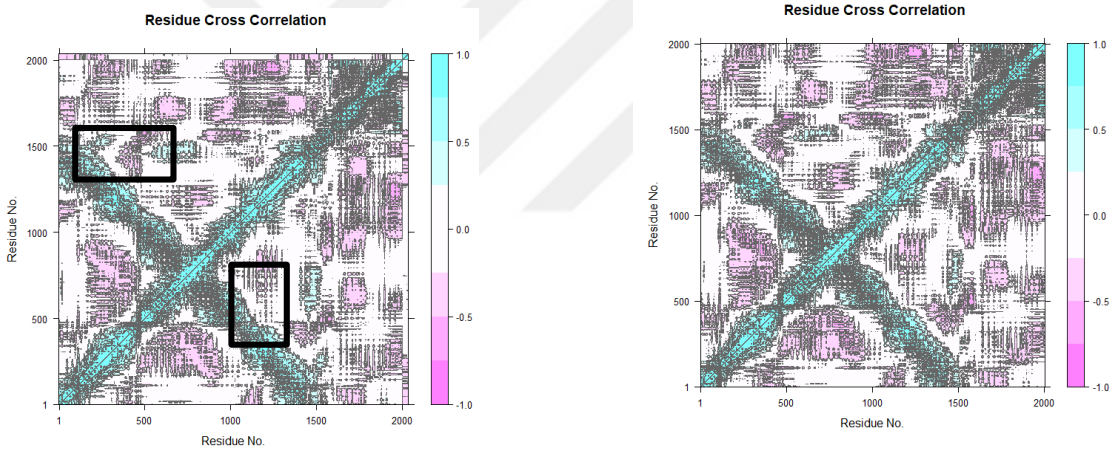

Figure 4.33.6. DCCM of the SS-DNA-ligand complex versus 100 ns of MD simulation for each force field

The utilization of dynamic cross-correlation matrix analysis on the complex system in charmm36m demonstrated significant enhancements in positive correlation motions and considerable reductions in negative correlation motions subsequent to ligand binding in contrast to charmm36. The complex system in the OL15 state manifested a persistent tendency towards positive correlation movements subsequent to ligand binding, as opposed to bsc1. Nevertheless, a reduction in motions exhibiting a negative correlation was observed.

4.34. Molecular dynamic simulation analysis of the modeled ss-DNA aptamer from the İfoldRNA server against bisphenol A

The SS-DNA-ligand complex formed using the molecular docking technique was then simulated using molecular dynamics for 100 ns. Two versions of the Amber and Charmm force fields were used in the simulation. In addition to hydrogen bonding, the radius of gyration, RMSD, and RMSF were evaluated. The four force fields of the study were analyzed using visual representations to help draw conclusions.

4.34.1. Root Mean Square Deviation (RMSD)

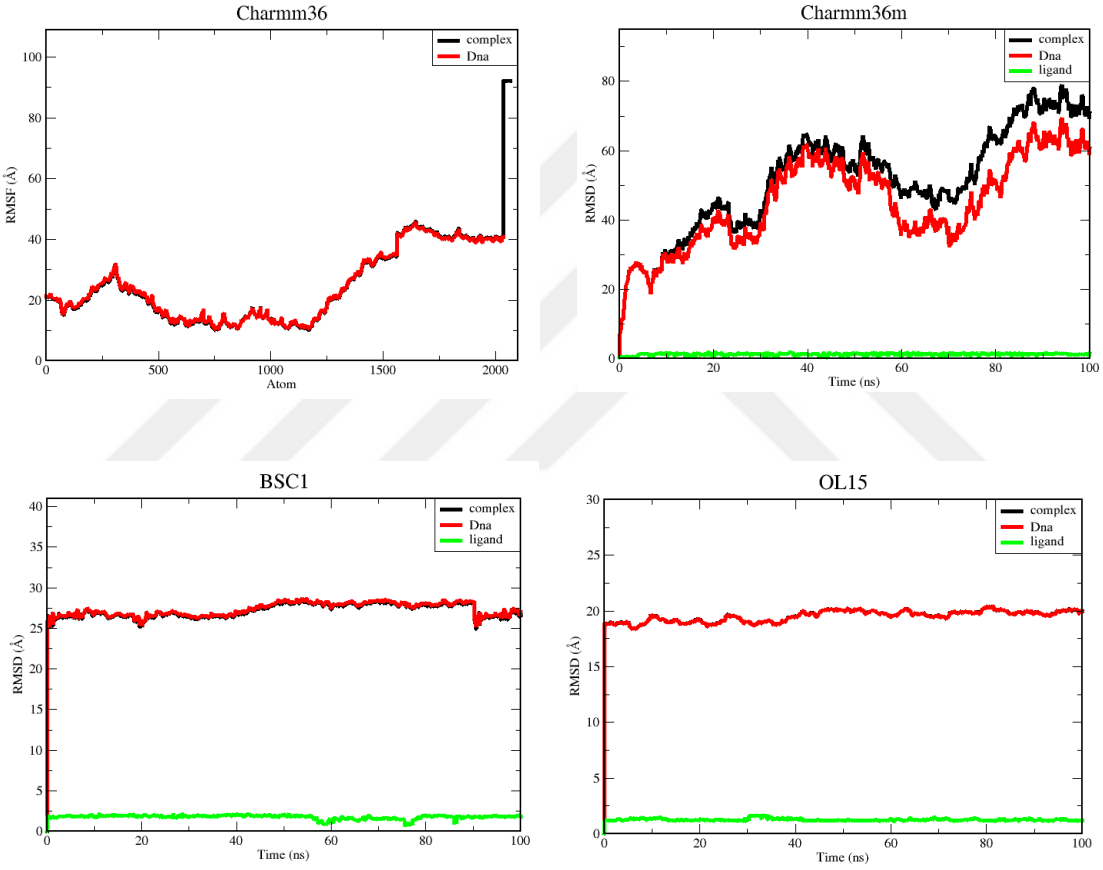

Figure 4.34.1. RMSDs of the SS-DNA-ligand complex versus 100 ns of MD simulation for each force field

Among the four complex configurations, charmm36 exhibited the highest RMSD level, whereas the aptamer-ligand complex at OL15 demonstrated the lowest. Upon examining the data pertaining to charmm36 and charmm36m figures, it was observed that the RMSD value exhibited a marked elevation, concomitant with significant conformational alterations in the DNA-ligand structures.

Upon examination of the DNA-aptamer ligand complexes in the BSC1 and OL15 instances, it is evident that the OL15 system exhibits a lower RMSD value in comparison to the BSC1 system. Additionally, the OL15 system demonstrates minimal fluctuations throughout the simulation and displays a high degree of stability. In the BSC1 instance, despite experiencing fluctuations up to 85 nanoseconds, the intricate system achieved a state of equilibrium during the final 10 nanoseconds of the simulation.

4.34.2. Root Mean Square Fluctuation

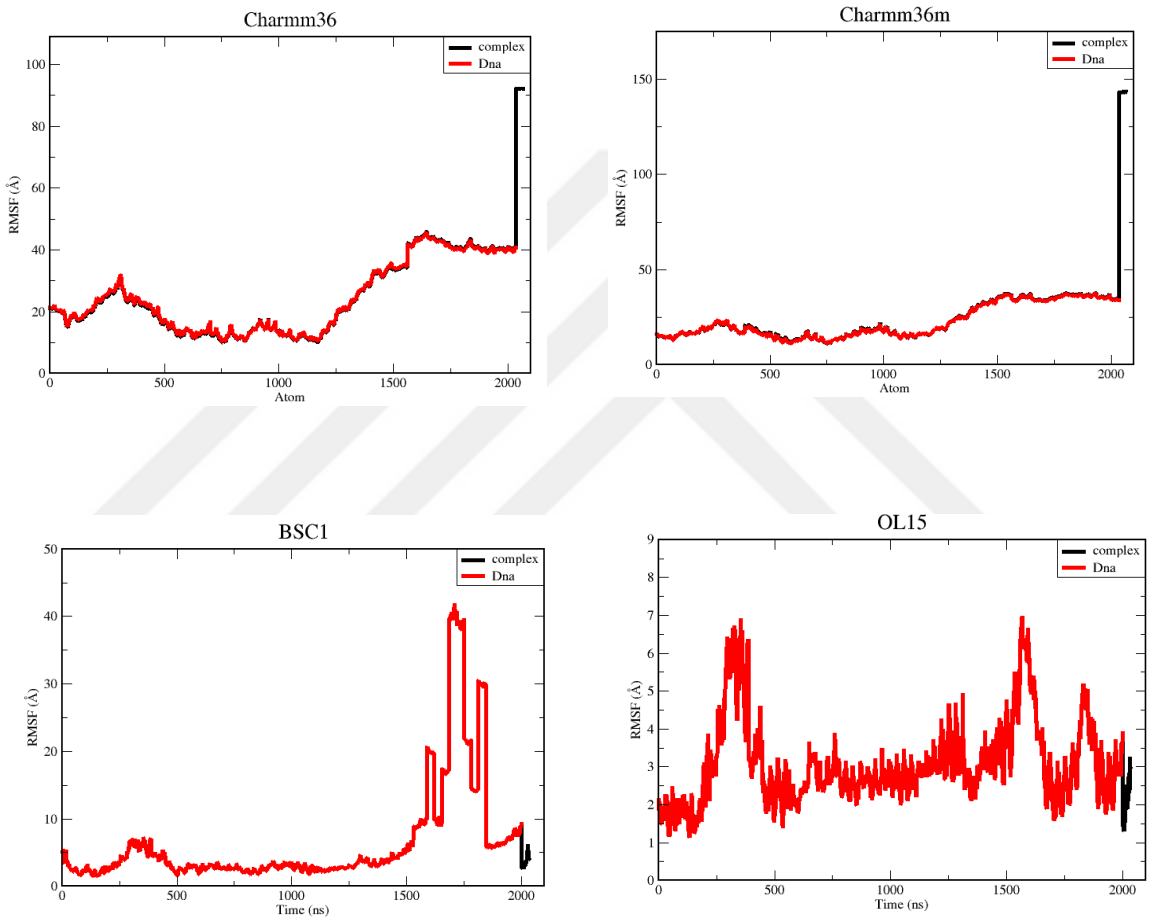

Figure 4.34.2. RMSFs of the SS-DNA-ligand complex versus 100 ns of MD simulation for each force field

Upon examination of the graphs, it can be observed that the charmm36m exhibits the highest RMSF value, whereas the ol15 displays the lowest. Furthermore, it is noteworthy that the RMSF values in charmm36 and charmm36m exhibit a relatively raised level of RMSF peak when compared to other instances.

Upon examining the complex RMSF plot in both instances, it is evident that the most prominent RMSF peak exhibited a substantial degree of flexibility in the ligand state. The complex structures of OL15 and BSC1 exhibited a reduced RMSF peak in the ligand state. Notably, OL15 demonstrated a lower value in comparison to the BSC1 state, suggesting that it forms a more stable complex system.

4.34.3. Gyration Radius Variation

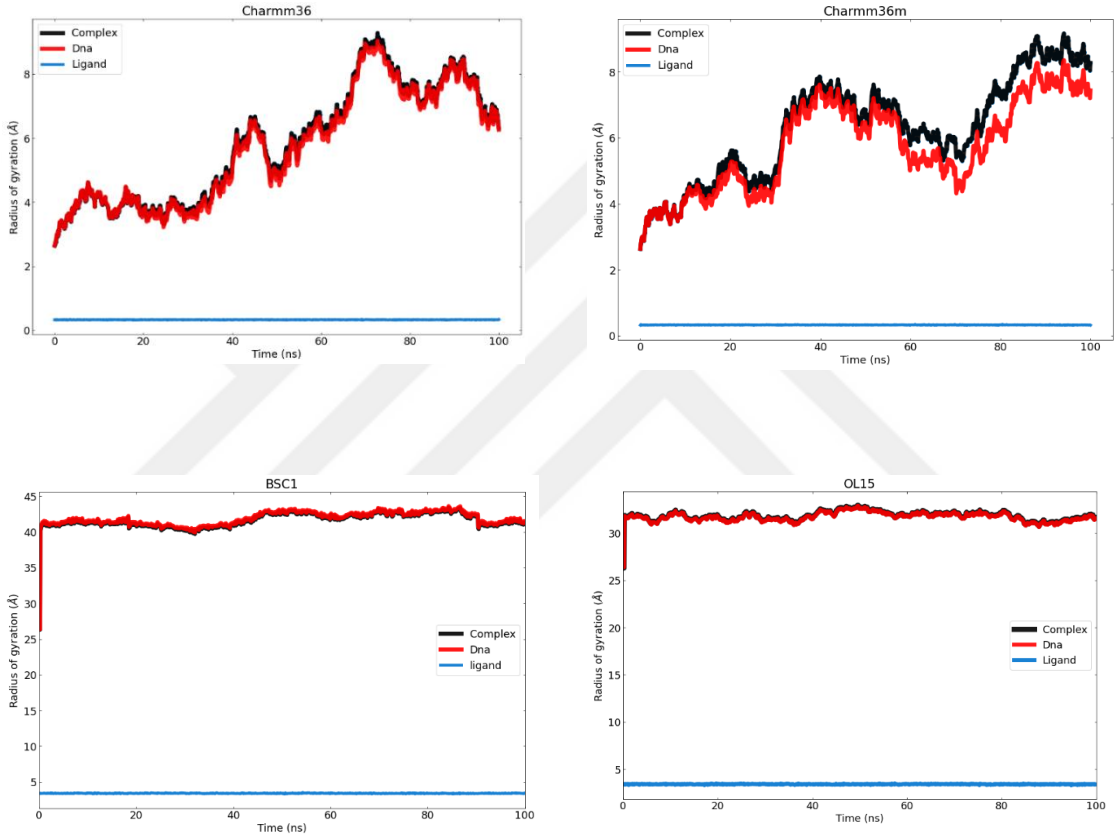

Figure 4.34.3. RGs of the SS-DNA-ligand complex versus 100 ns of MD simulation for each force field

The Charmm36 graph depicts that the RG values of both the complex system and DNA remained relatively stable with minimal fluctuations during the initial stages of the DNA-ligand simulation. However, a noticeable increase in RG values was observed after 40 ns, with the highest value being recorded at 70 ns. The Charmm36m graph shows a noticeable increase in the RG value at 30 ns, then a brief decline. However, the RG value experiences a marked increase at 70 ns and ultimately reaches its maximum value.

Despite the fact that the aptamer-ligand system in the OL15 state exhibited a reduced mean radius of gyration (RG) in comparison to BSC1, it underwent comparatively fewer conformational alterations than the BSC1 state.

4.34.4. Hydrogen bond

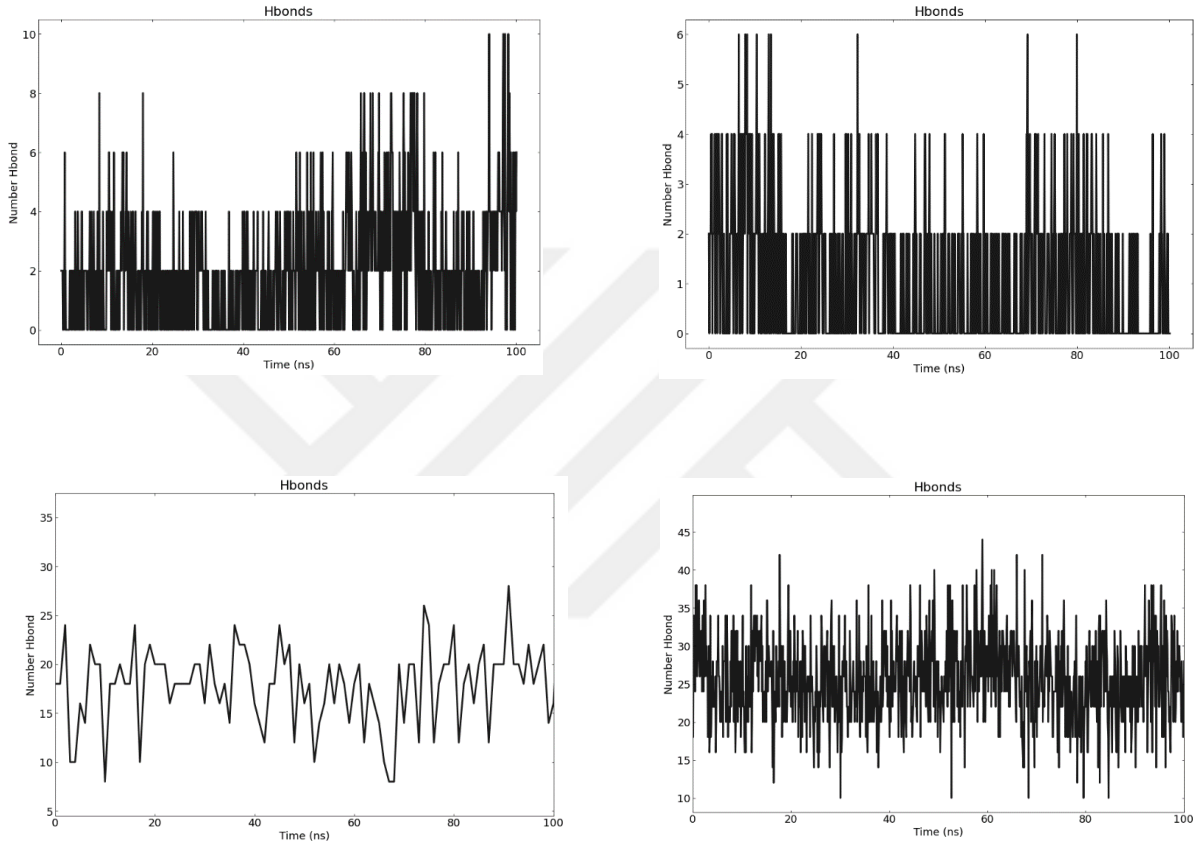

Figure 4.34.4. Hbonds of the SS-DNA-ligand complex versus 100 ns of MD simulation for each force field

Figure 4.34.4 depicts the results, indicating that the amount of hydrogen bonding in ligand-bound states varies throughout the 100 ns molecular dynamics simulation. The outcomes of the molecular dynamics simulations demonstrate that the OL15 state has the highest degree of hydrogen bonding between DNA and ligand. The amount of hydrogen bonds created in the case of Charmm36 is larger compared to Charmm36m. However, the amount of hydrogen bonds generated between DNA and ligand in the case of Bsc1 is the lowest.

4.34.5. Principal component analysis (PCA) and Domain cross-correlation matrix (DCCM)

Charmm36-complex

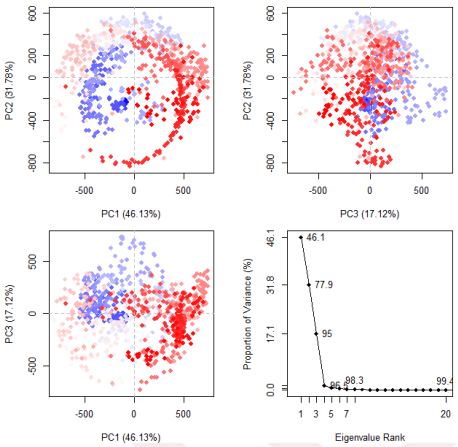

DNA

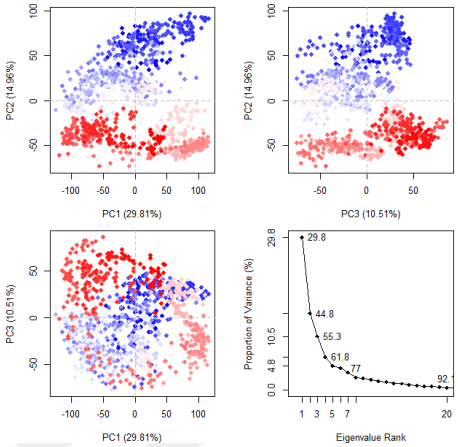

Charmm36m-complex

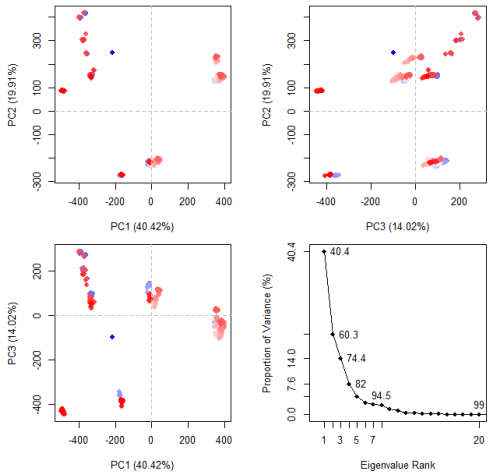

DNA

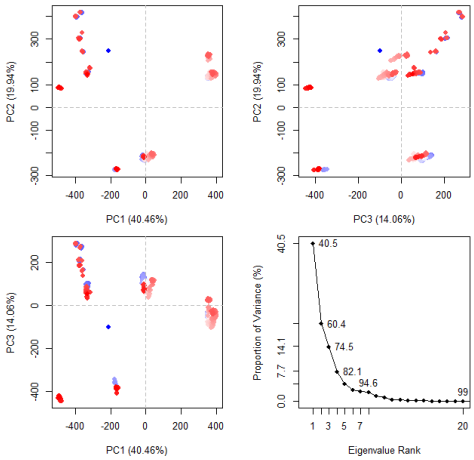

BSC1-complex DNA

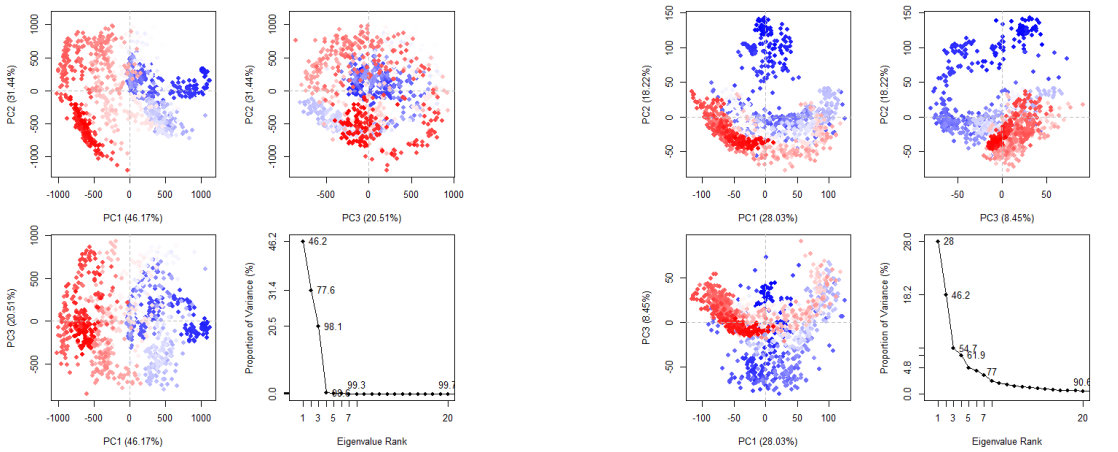

OL15-complex DNA

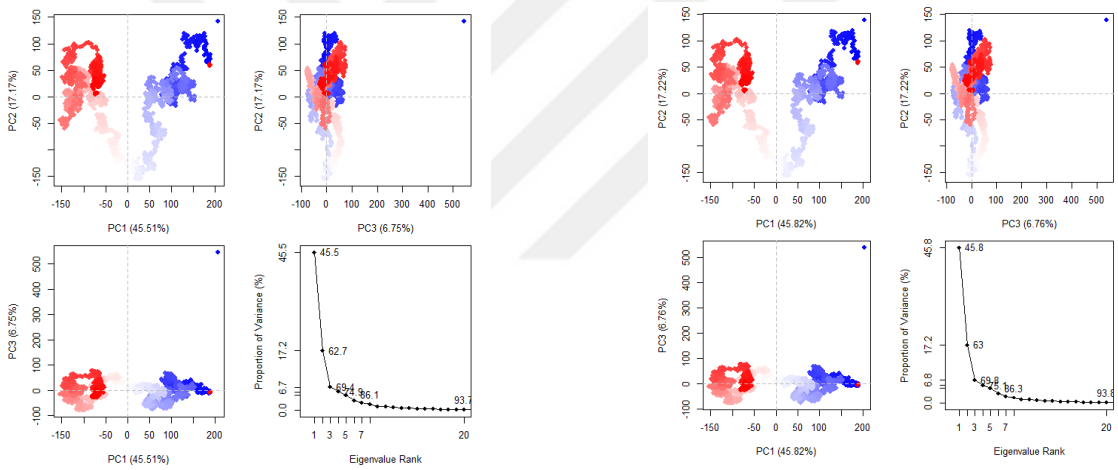

Figure 4.34.5. PCA of the SS-DNA-ligand complex versus 100 ns of MD simulation for each force field

The analysis presented for the complex structures for each case shows that the first 20 principal components (PC) of the complex-charmm36 system, charmm36m complex system, BSC1 complex system, and OL15 complex system contribute 99.4%, 99.3%, 99%, and 93% of the overall variance, respectively. This indicates that the OL15 aptamer-DNA system has a lower phase space and performance flexibility compared to other complex systems. When the PCA plots of the complexes in charmm36 and charmm36m were compared, the PC1 cluster exhibited the greatest variability, accounting for 46.13% and 46.17% of the variance, respectively.

The PC2 cluster showed 14.58% and 15.53% variability, while the PC3 cluster exhibited minimal variability, accounting for only 17.12% of the variance for 36. Comparing the PCA diagrams of the complexes in BSC1 and OL15, the PC1 cluster exhibited the greatest variability, accounting for 40.42% and 45.51% of the variance, respectively. The PC2 cluster exhibited 19.91% and 17.17% variability, while the PC3 cluster exhibited minimal variability, accounting for only 6.75% of the variance for OL15.

Charmm36-complex

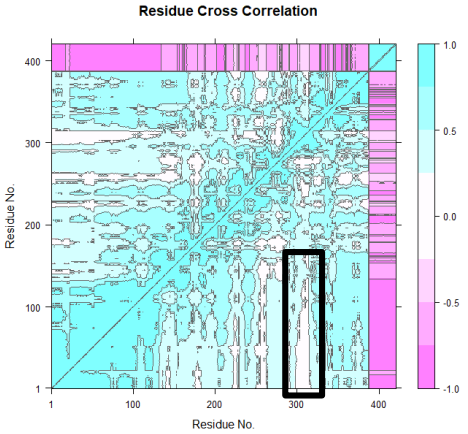

DNA

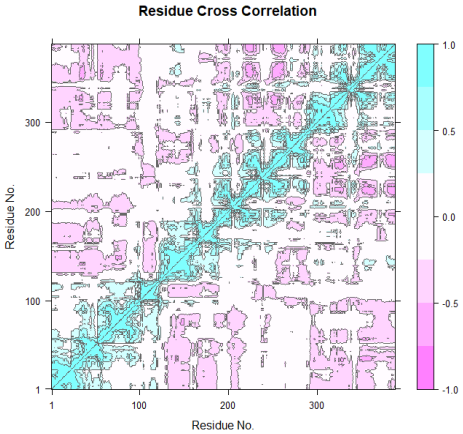

Charmm36m-complex

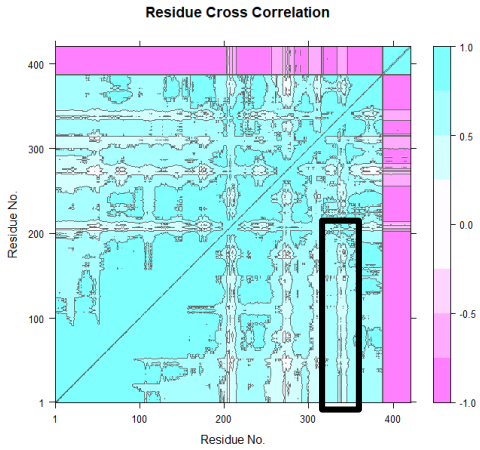

DNA

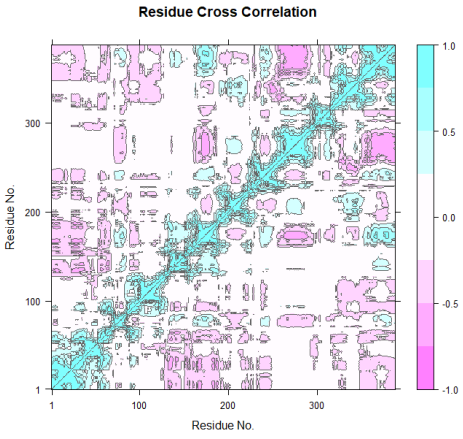

BSC1-complex DNA

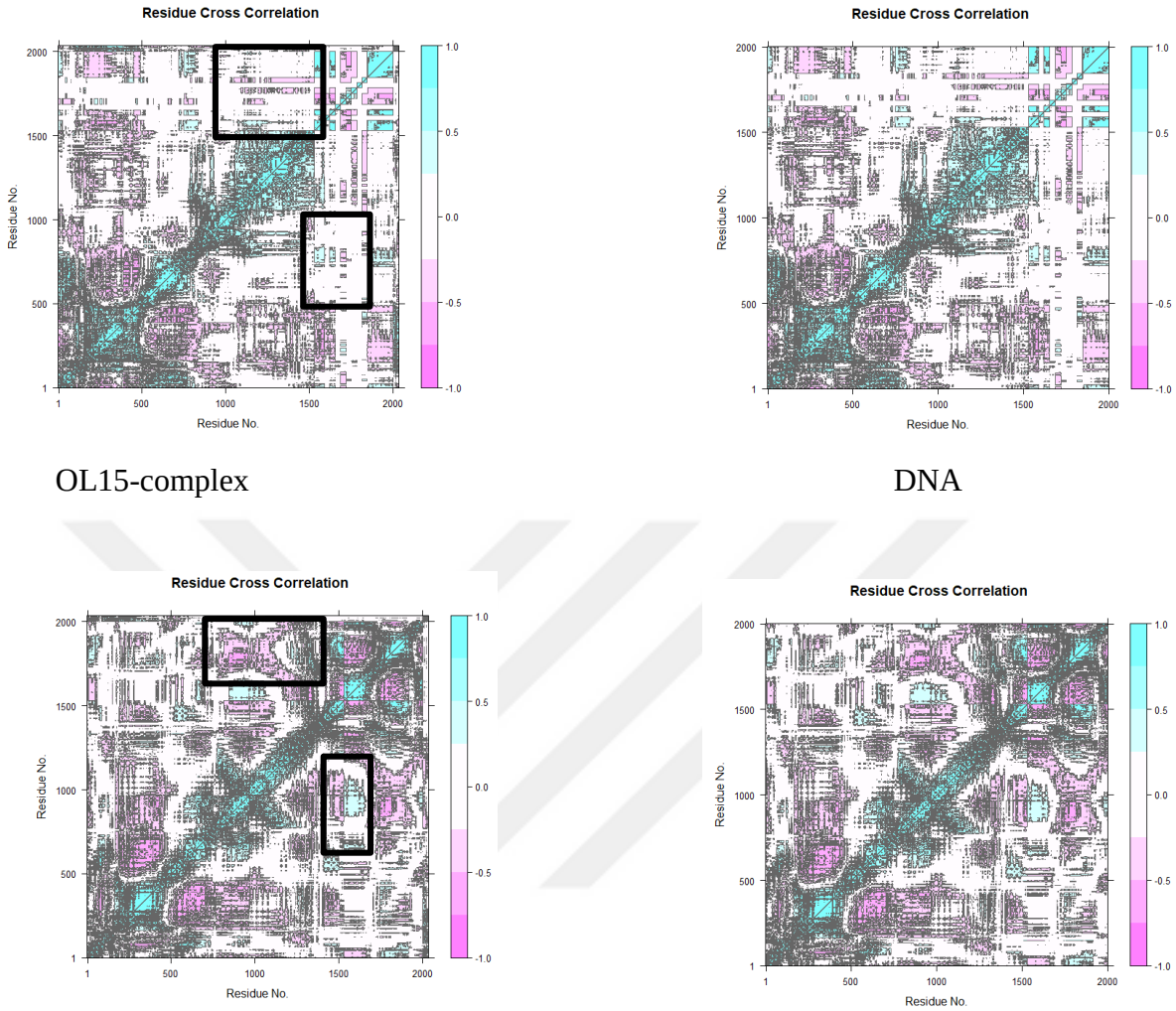

OL15-complex DNA

Figure 4.34.6. DCCM of the SS-DNA-ligand complex versus 100 ns of MD simulation for each force field

Dynamic cross-correlation matrix analysis revealed noteworthy enhancements in positively correlated movements after ligand binding in charmm36m's intricate system, which starkly contrasts with charmm36. In the case of OL15, the complex system exhibited a continuous inclination towards correlated motions in a positive direction after ligand binding, as opposed to bsc1. Furthermore, upsurges in correlated motions in a negative direction were also detected.

4.35. Molecular dynamic simulation analysis of the modeled ss-DNA aptamer from the Avogadro software against bisphenol A

The ss-dna-ligand complex that was produced via molecular docking was chosen for molecular dynamics simulation on a timescale of 100 ns in the programs NAMD and Gromacs. For this simulation, two different versions of the AMBER force field and two distinct variations of the Charmm force field were utilized. Several variables, including radius of gyration, RMSD, RMSF, and h-bond, were subjected to statistical examination. Using the four force fields that were given, comparisons are made between the plots of these values.

4.35.1. Analysis of RMSD

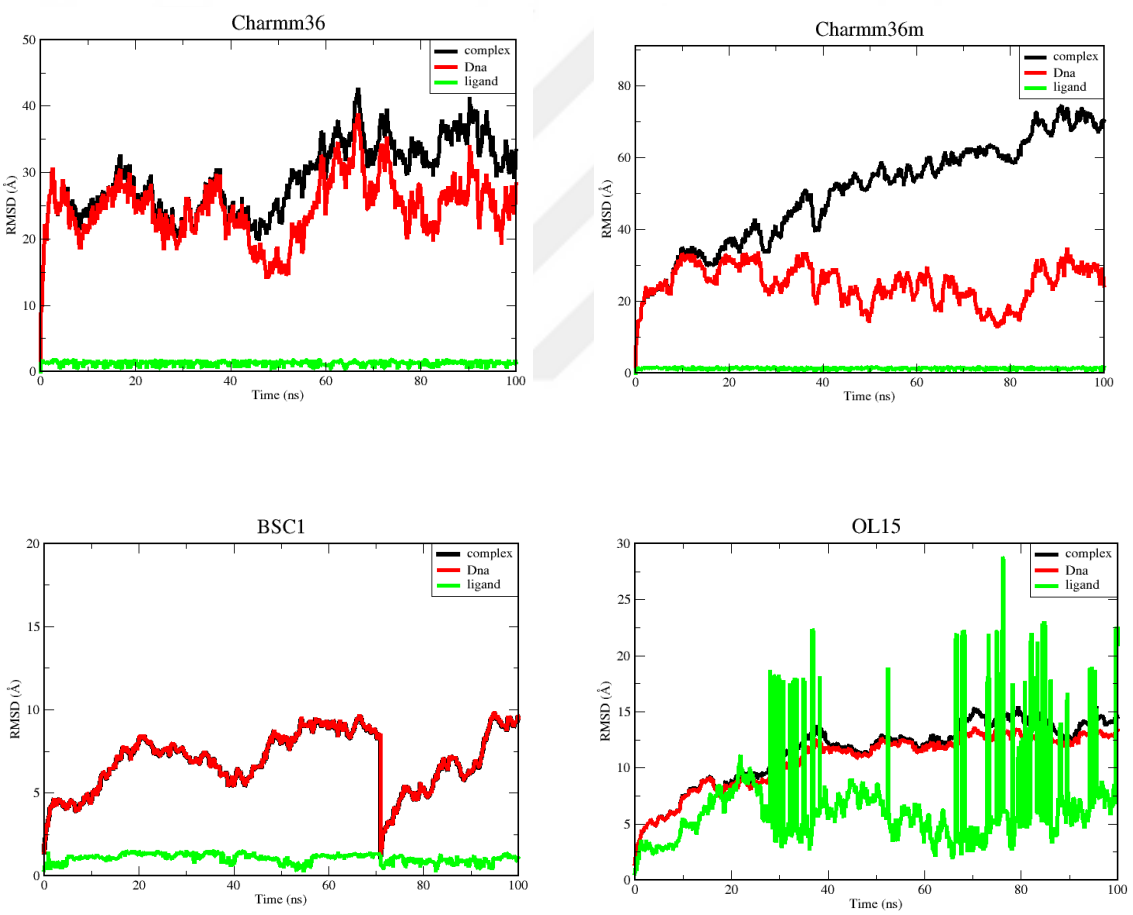

Figure 4.35.1. RMSDs of the SS-DNA-ligand complex versus 100 ns of MD simulation for each force field

Among the four complex configurations, it can be observed that charmm36m exhibits the greatest RMSD value, whereas the aptamer-ligand complex located in BSC1 displays the

lowest value. Elevated RMSD values give rise to notable alterations in the folded tate of the DNA-ligand complex, resulting in decreased stability.

RMSD		Ligand	Dna	Complex
Charmm36		1.639	24.25	35.20
Charmm36m		1.715	25.250	30.94
BSC1		1.765	6.350	9.009
OL15		15.05	8.950	11.08

Table 4.35.1. RMSD values by force field

Upon examination of Figures charmm36 and charmm36m, it was observed that the DNA-ligand complex aptamer structure in charmm36M exhibited a higher RMSD value in comparison to charmm36. Additionally, the complex structure displayed significant fluctuations throughout the simulation and failed to attain equilibrium by the conclusion of the simulation. Subsequent to the 30 nanoseconds, a notable escalation in RMSD was observed, persisting until the conclusion of the simulation. In both instances, the stability of the aptamer-ligand structure is compromised. However, it is noteworthy that the complex structure is significantly less stable in the charmm36m case compared to charmm36.

The behavior of DNA-ligand complexes in the BSC1 and OL15 states exhibits notable distinctions from those observed in the CHARMM force fields. Upon solely examining the magnitude of the RMSD, it is evident that the RMSD values of the DNA-ligand complexes in the BSC1 and OL15 states exhibit a significant reduction. Based on this magnitude, it can be inferred that the DNA aptamer-ligand complexes are comparatively more stable than the CHARMM36 and CHARMM36M complexes, as they undergo minimal conformational changes.

Upon examination of the Bsc1 graph, it is evident that there is a notable rise within the initial 5 nanoseconds of the simulation, followed by a gradual increase until the 20 nanoseconds. From 20 to 40 nanoseconds, the fluctuations were minimal. However, after 40 nanoseconds, the rmsd value experienced a subsequent increase, with a marked decrease observed at 70 nanoseconds. The simulation persisted in exhibiting fluctuations for a duration of 70 nanoseconds, culminating in the final 5 nanoseconds of the simulation. The Ol15 graph indicates that the RMSD value exhibited an initial increase during the simulation.

However, after 40 nanoseconds, the complex system demonstrated negligible fluctuations until the conclusion of the simulation. Upon examination of the ligands, it was observed

that the charmm36 ligand exhibited displacement from the binding site in certain areas, whereas the charmm36m ligand demonstrated persistent movement within its orbit throughout the simulation.

The BSC1 graph indicates that the ligand remained stable throughout the simulation, maintaining its position within the binding region for the initial 20 nanoseconds. However, a slight increase in the RMSD value was observed after this time point, although it remained constant thereafter. Conversely, the OL15 graph indicates that the ligand exhibited stability throughout the initial phase of the simulation. However, subsequent to this period, the ligand's RMSD value escalated considerably, with particularly elevated values observed between 30 and 40 ns and 70 and 90 ns.

4.35.2. Root Mean Square Fluctuation

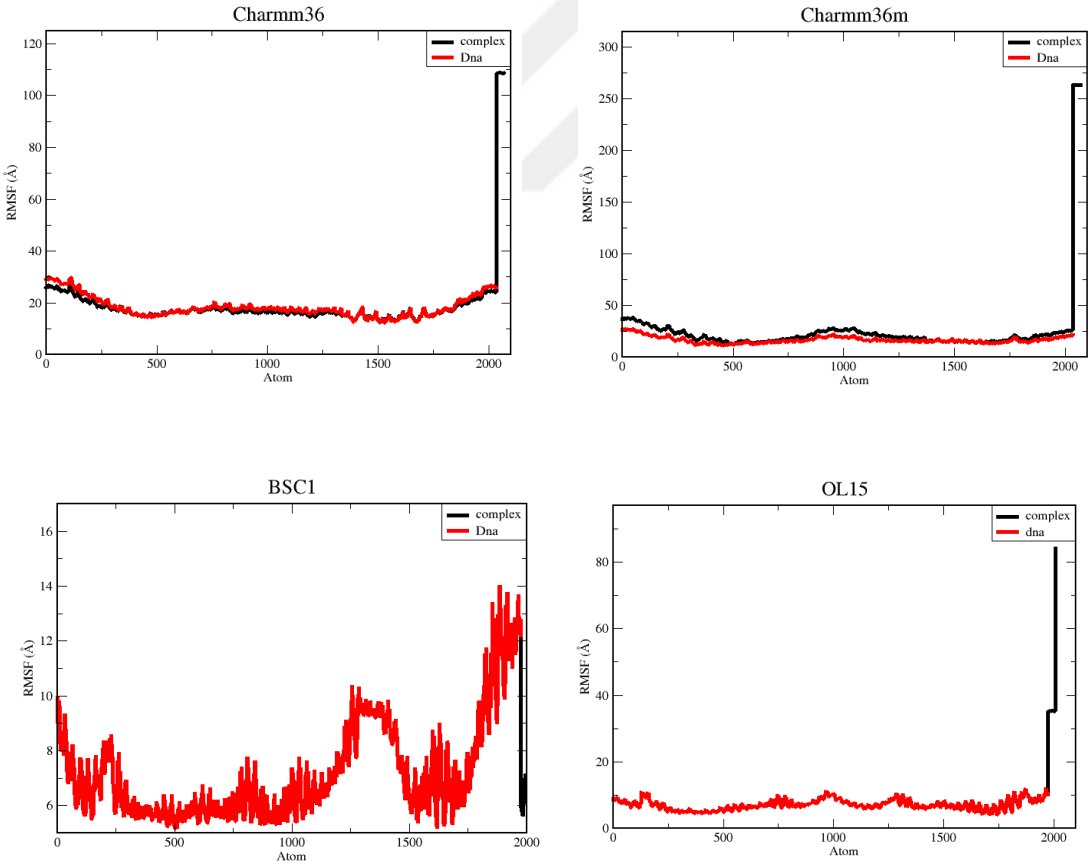

Figure 4.35.2. RMSFs of the SS-DNA-ligand complex versus 100 ns of MD simulation for each force field

Furthermore, it is noteworthy that Charmm36 and Charmm36m exhibit considerably elevated RMSF values in comparison to other instances. Upon examination of the intricate RMSF plot in both instances, it was observed that the most prominent RMSF peak exhibited a considerable degree of flexibility in the ligand state. The complex structures of OL15 and BSC1 exhibited low RMSF in the ligand state. Notably, the RMSF value of BSC1 was lower than that of OL15, indicating that BSC1 formed a more stable complex system. The analysis of the aptamer DNA structures reveals that the internal loop portion of the structure, specifically regions 56–60, 29–31, and 16–17, exhibits the most pronounced peak in charmm36m. These regions are characterized by high flexibility. The regions that exhibit notable flexibility in Charmm36m are analogous to those observed in Charmm36. The hairpin loop harbors the regions with the greatest degree of flexibility in BSC1, specifically within the range of 56–63. The OL15 location is situated within the loop and bears a resemblance to BSC1.

4.35.3. Gyration Radius Variation

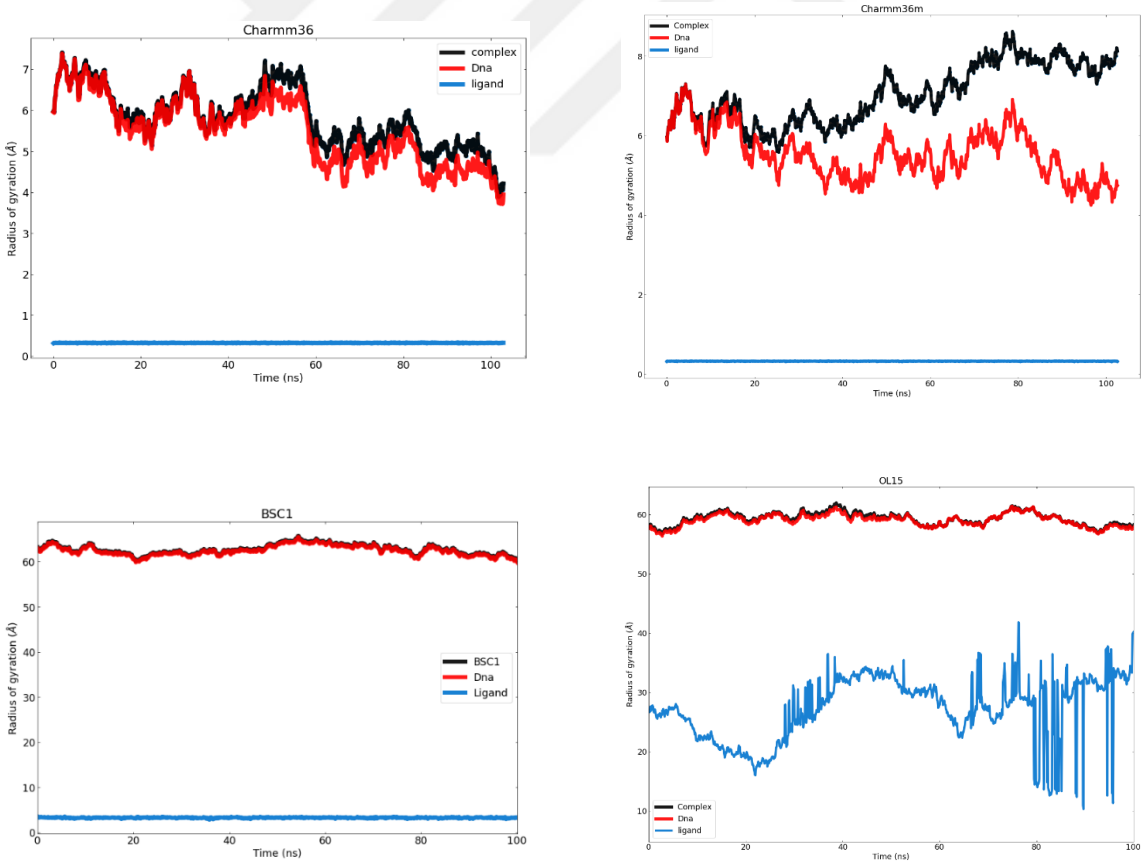

Figure 4.35.3. RGs of the SS-DNA-ligand complex versus 100 ns of MD simulation for each force field

The Charmm36 graph indicates that the DNA-ligand complex exhibited an average RG exceeding 6 Å. Throughout the simulation, both the complex system and DNA displayed an increase in RG values, with a brief decrease observed at 20 ns. Subsequently, the RG values rose once more and peaked between 40 and 60 ns. The fluctuations observed during the simulation are associated with alterations in the structural configuration, ultimately resulting in a reduction in stability. The Charmm36m simulation exhibited a notable increase in the complexity of the system, particularly during the initial stages of the simulation, and this trend persisted beyond the 20 ns until the conclusion of the simulation. The mean RG values exhibited by the systems present in BSC1 and OL15 surpass those of charmm36 and charmm36m to a significant extent. Regarding BSC1, the comprehensive RG curve indicates that the aptamer experiences conformational alterations while maintaining a consistent profile with notable fluctuations throughout the duration of the simulation. Conversely, with respect to OL15, it can be observed that both RG values exhibit a significant degree of conformational variability and have undergone more pronounced conformational alterations throughout the simulation in comparison to BSC1.

4.35.4. Hydrogen bond

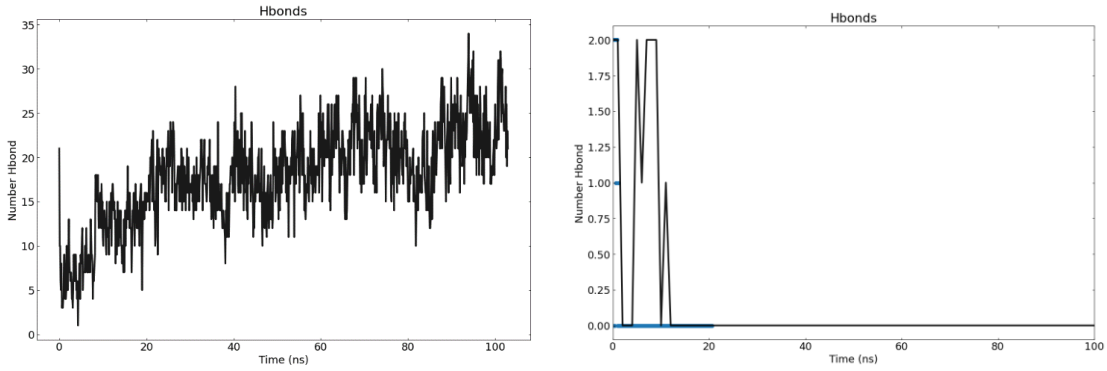

Figure 4.35.4. Hbonds of the SS-DNA-ligand complex versus 100 ns of MD simulation for each force field

The outcomes presented in Figure 4.35.5 demonstrate that the degree of hydrogen bonding in the ligand-bound states fluctuates over the course of the 100 nanosecond molecular dynamics simulation. The findings of the molecular dynamics simulations indicate that the occurrence of hydrogen bond formation between DNA and ligand is

largely absent in the instances of OL15 and BSC1. The quantity of hydrogen bonds established in Charmm36 is comparatively greater than that of Charmm36m.

4.36. Molecular dynamic simulation analysis of the modeled ss-DNA aptamer from the Schrodinger software against bisphenol A

The SS-DNA-ligand complex generated by molecular docking was selected for 100 ns of molecular dynamics simulation with the programs NAMD and Gromacs. Two distinct versions of the AMBER force field and two distinct versions of the Charmm force field were utilized for this simulation. Multiple variables, including radius of gyration, RMSD, RMSF, and h-bond, were statistically analyzed. Using the four provided force fields, comparisons are performed between these values' plots.

4.36.1. Root Mean Square Deviation (RMSD)

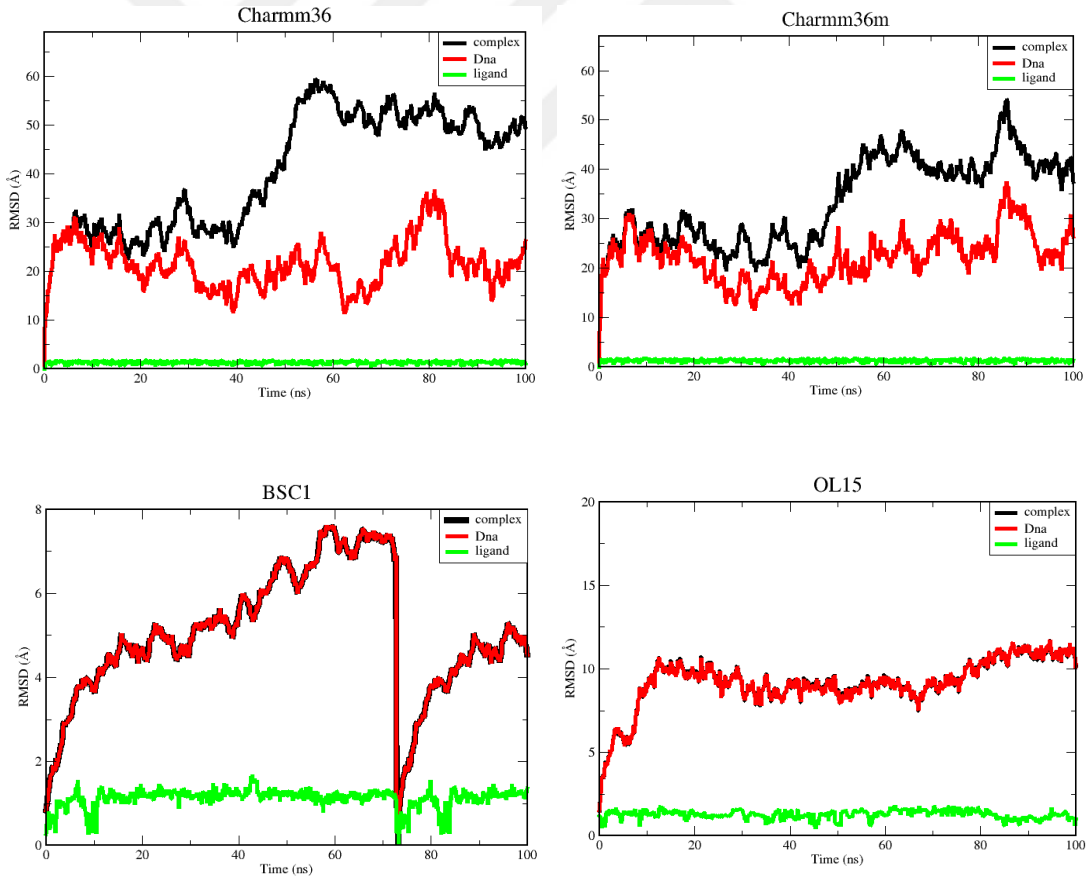

Figure 4.36.1. RMSDs of the SS-DNA-ligand complex versus 100 ns of MD simulation for each force field

Among the four complex structures, charmm36m exhibits the highest RMSD value, whereas OL15 displays the lowest. The RMSD values of the complexes observed at 36 and 36m are 20.20 Å and 20.94 Å, respectively. Upon examining Figures charmm36 and charmm36m, it can be observed that the DNA-ligand complex aptamer structure in charmm36 exhibits a greater RMSD value relative to charmm36m.

Additionally, the RMSD value of the complex structure following 50 nanoseconds displays a substantial increase and attains its maximum value. The complex system in Charmm36m exhibited fluctuations of up to 40 ns, but after 40 ns, the rmsd value increased considerably and peaked at 85 ns. After 80 ns, the value remained constant until the conclusion of the simulation.

RMSD	Ligand	Dna	Complex
Charmm36	1.718	19.25	20.20
Charmm36m	1.757	19.55	20.94
BSC1	1.761	6.329	9.009
OL15	2.01	8.904	14.08

Table 4.36.1. RMSD values by force field

Upon examination of the DNA-aptamer ligand complexes in the BSC1 and OL15 cases, it is evident that the OL15 system exhibits a high degree of stability, as evidenced by its lower rmsd value and minimal fluctuations during the simulation, in contrast to the BSC1 system. In the context of Bsc1, the complex system exhibited a notable escalation in the RMSD value, particularly beyond the 10 nanoseconds, which persisted until the 70 nanosecond interval. Despite a notable reduction in the RMSD value at 70 nanoseconds, subsequent fluctuations resulted in an increase in the RMSD value, ultimately concluding the simulation.

4.36.2. Root Mean Square Fluctuation

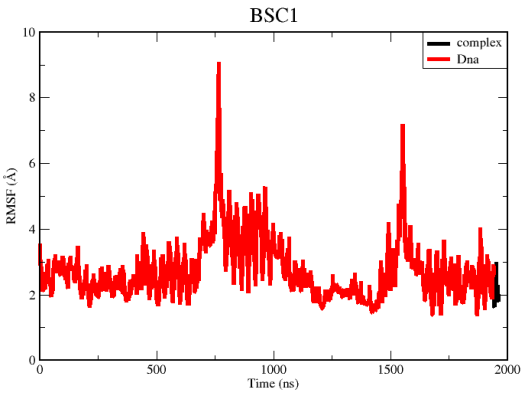

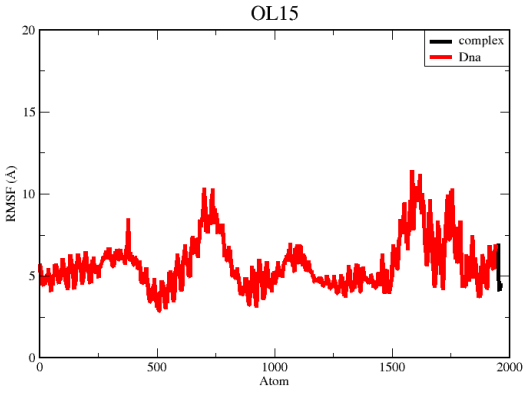

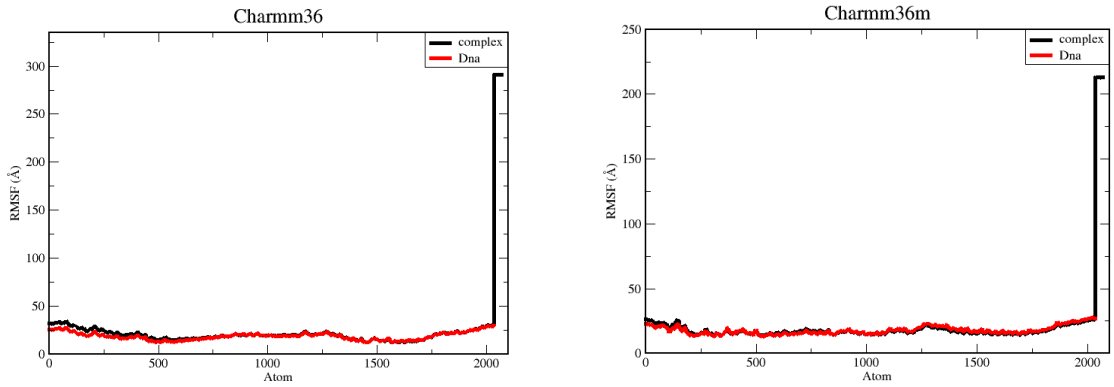

Figure 4.36.2. RMSFs of the SS-DNA-ligand complex versus 100 ns of MD simulation for each force field

Furthermore, it is noteworthy that the RMSF values in both the charmm36 and charmm36m models exhibit relatively elevated magnitudes in comparison to other possible situations. Upon examination of the complex RMSF plot in both cases, it was observed that the most prominent RMSF summit exhibited a considerable degree of flexibility in the ligand state. In the context of OL15 and BSC1, it was observed that the complex structures exhibited a minimal RMSF peak in the ligand state. Notably, OL15 demonstrated a lower value in comparison to BSC1, suggesting that it forms a more stable complex system.

4.36.3. Gyration Radius Variation

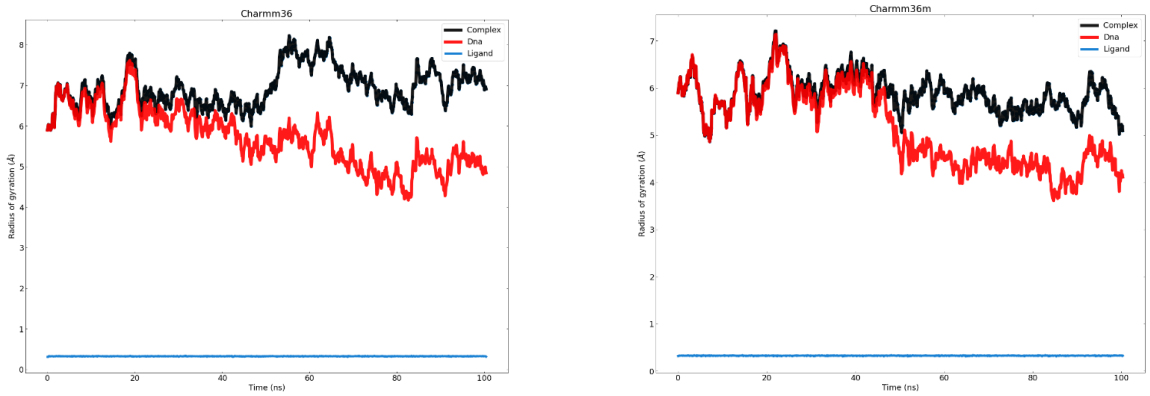

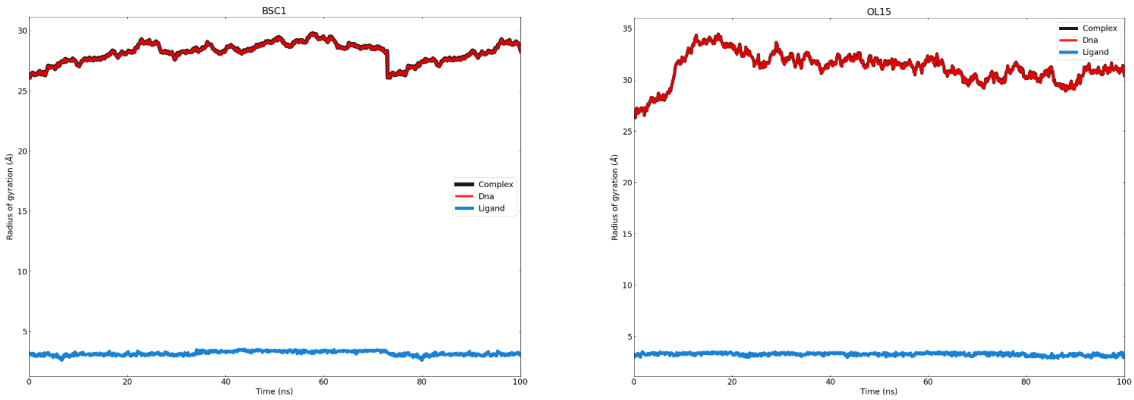

Figure 4.36.3. RGs of the SS-DNA-ligand complex versus 100 ns of MD simulation for each force field

The Charmm36 graph indicates that the DNA-ligand complex exhibited an average RG value exceeding 6 Å. Moreover, the RG values of both the complex system and DNA displayed an upward trend from the onset of the simulation. Despite exhibiting a consistent RG curve between 20 ns and 40 ns, the RG metric experienced a subsequent increase beyond 40 ns, ultimately peaking at 60 ns. Subsequent to initial variations, the fluctuations persisted until the 90 nanoseconds and ultimately stabilized at a consistent RG value during the final 10 nanoseconds.

The Charmm36m simulation demonstrated significant fluctuations within the complex system, particularly in the initial phase, spanning up to 20 nanoseconds. Nonetheless, the system exhibited a uniform RG curve within a time frame of 20 to 40 nanoseconds. The simulation demonstrated persistent fluctuations exceeding 40 nanoseconds without achieving a state of equilibrium. The RG values of the systems located in BSC1 and OL15 demonstrated a noteworthy elevation when compared to those of charmm36 and charmm36m. Nevertheless, it was noted that the interaction between DNA and ligand exhibited a relatively higher degree of effectiveness in both scenarios as opposed to the charmm force fields.

4.36.4. Hydrogen bond

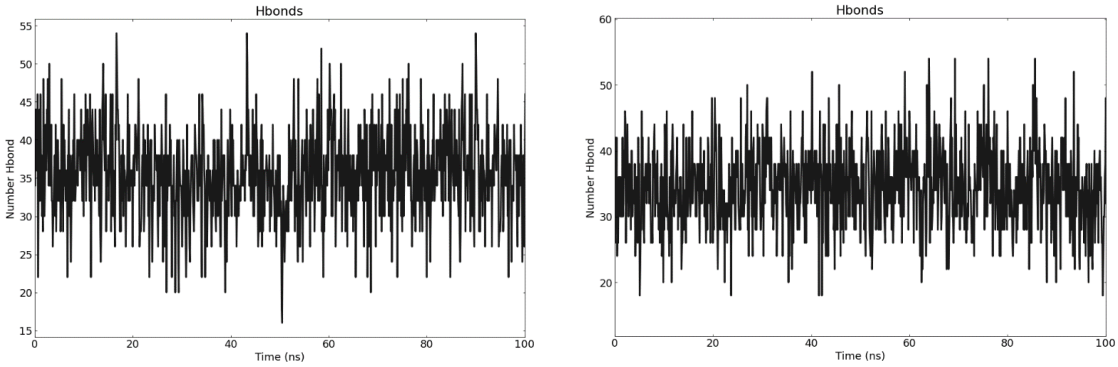

Figure 4.36.4. Hbonds of the SS-DNA-ligand complex versus 100 ns of MD simulation for each force field

Figure 4.36.4 demonstrates that the degree of hydrogen bonding in the ligand-bound states fluctuates over the course of the 100 nanosecond molecular dynamics simulation. Simulations of molecular dynamics indicate that the formation of hydrogen bonds between DNA and ligand is mainly absent in Charmm36 and Charmm36m samples. BSC1 forms a comparatively greater number of hydrogen bonds than OL15.

4.37. Molecular dynamic simulation analysis of the modeled ss-DNA aptamer from the Discovery Studio Visualizer against bisphenol A

The ss-dna-ligand complex that was generated through the process of molecular docking was selected for molecular dynamics simulation on a timescale of one hundred nanoseconds using the programs NAMD and Gromacs. For the purpose of carrying out this simulation, two distinct iterations of the AMBER force field and two distinct iterations of the Charmm force field were used. Statistical analysis was performed on a number of different variables, such as the radius of gyration, the RMSD, the RMSF, and the h-bond. The plots of these data are compared to one another, making use of the four different force fields that were provided.

4.37.1. Root Mean Square Deviation (RMSD)

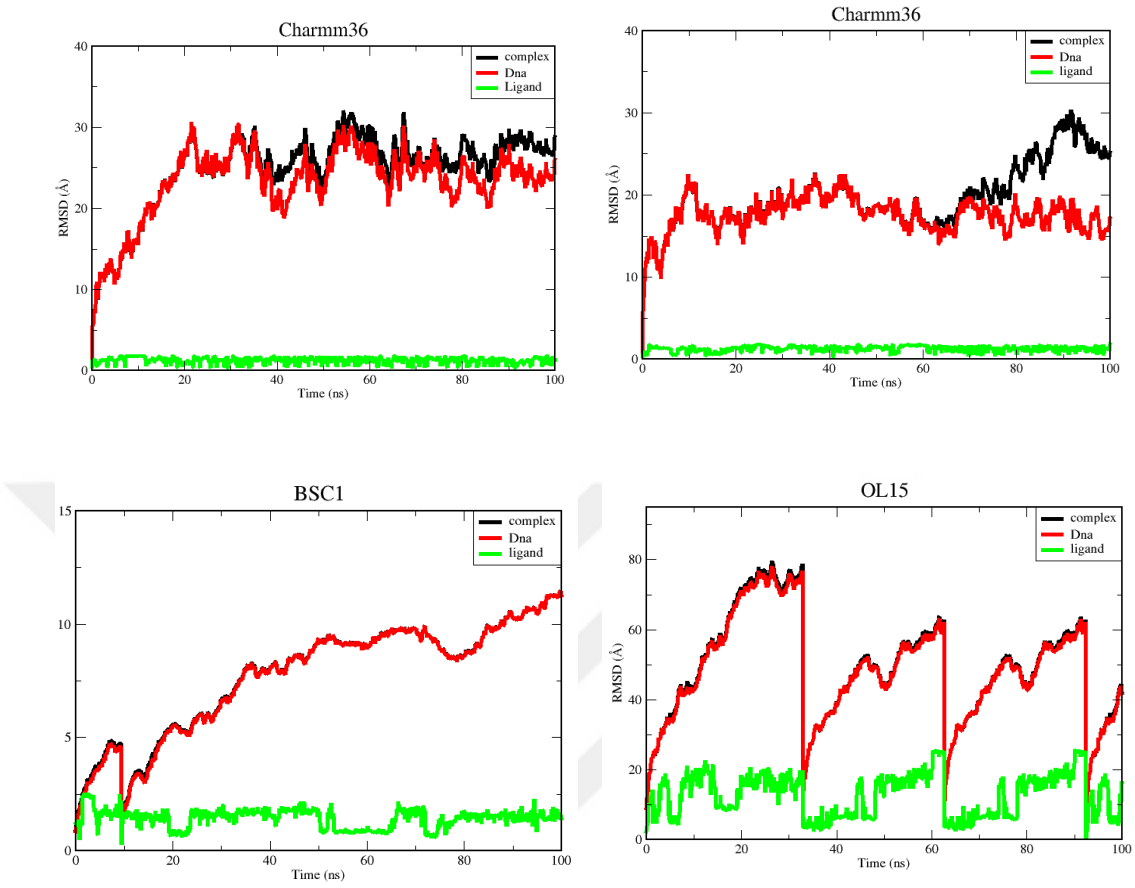

Figure 4.37.1. RMSDs of the SS-DNA-ligand complex versus 100 ns of MD simulation for each force field

The complex structure denoted as OL15 exhibits the highest RMSD value among the four structures considered, whereas the aptamer-ligand complex in BSC1 displays the lowest value. The charmm36 graph shows an initial increase in the RMSD value up to the first 20 nanoseconds, then persistent fluctuations up to 90 nanoseconds later. However, the system eventually attained equilibrium in the final 10 seconds. The Charmm36m graph shows an initial increase in the RMSD value over the first 20 nanoseconds, then relatively stable fluctuations over the following 50 nanoseconds. RMSD) of the complex system exhibited an upward trend from 50 nanoseconds until the conclusion of the simulation.Upon examination of the DNA-aptamer ligand complexes in the BSC1 and OL15 states, it was observed that the BSC1 state exhibited superior binding performance in comparison to the OL15 state.

This was evidenced by the lower RMSD values observed in the BSC1 state, as well as the reduced degree of fluctuations observed throughout the simulation. The OL15 graph exhibits abrupt declines in RMSD values, particularly at 30, 60, and 90 nanoseconds. This indicates that the system lies beyond the confines of periodic boundary conditions.

4.37.2. Root Mean Square Fluctuation

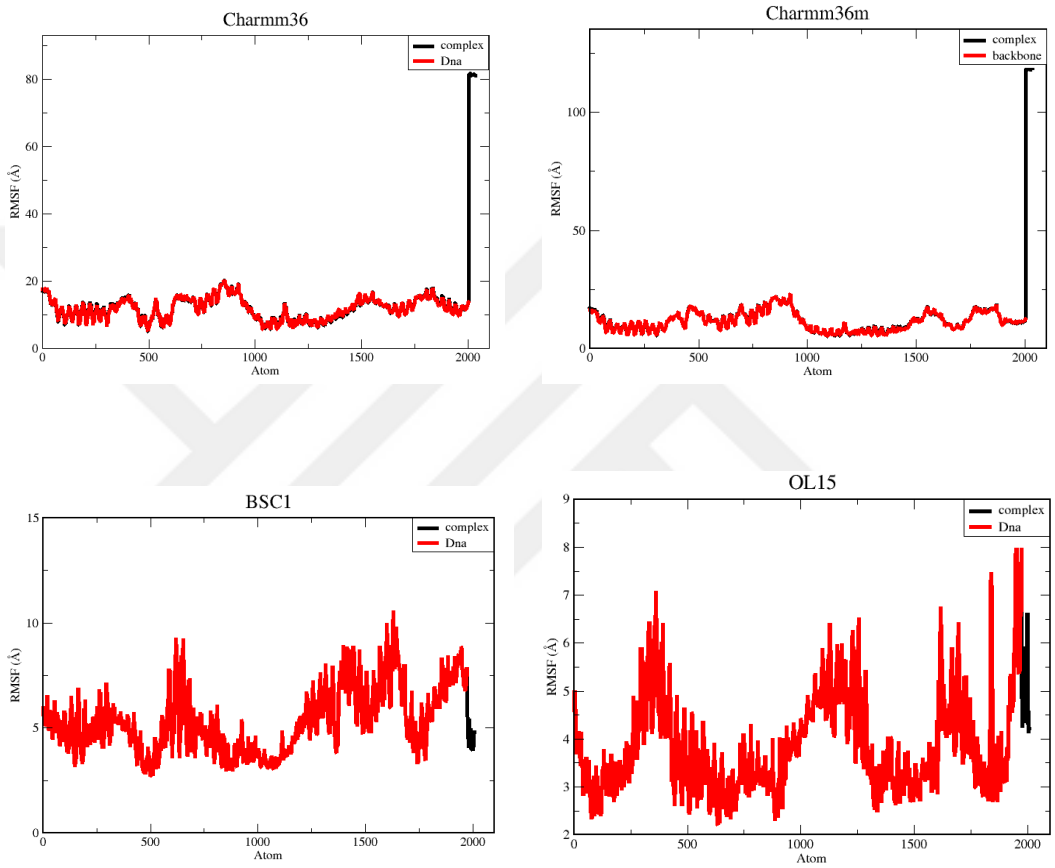

Figure 4.37.2. RMSFs of the SS-DNA-ligand complex versus 100 ns of MD simulation for each force field

It is noteworthy that Charmm36 and Charmm36m exhibit relatively elevated rmsf values in comparison to other instances. Upon examination of the complex RMSF plot in both instances, it was observed that the most prominent RMSF peak exhibited substantial flexibility in the ligand state. This suggests that the interaction between deoxyribonucleic acid (DNA) and ligands is weak. In the context of OL15 and BSC1, it was observed that the complex structures exhibited reduced rmsf in the ligand state.

Notably, BSC1 demonstrated a comparatively lower rmsf value than OL15, suggesting a higher degree of stability in the formation of the complex system.

4.37.3. Gyration Radius Variation

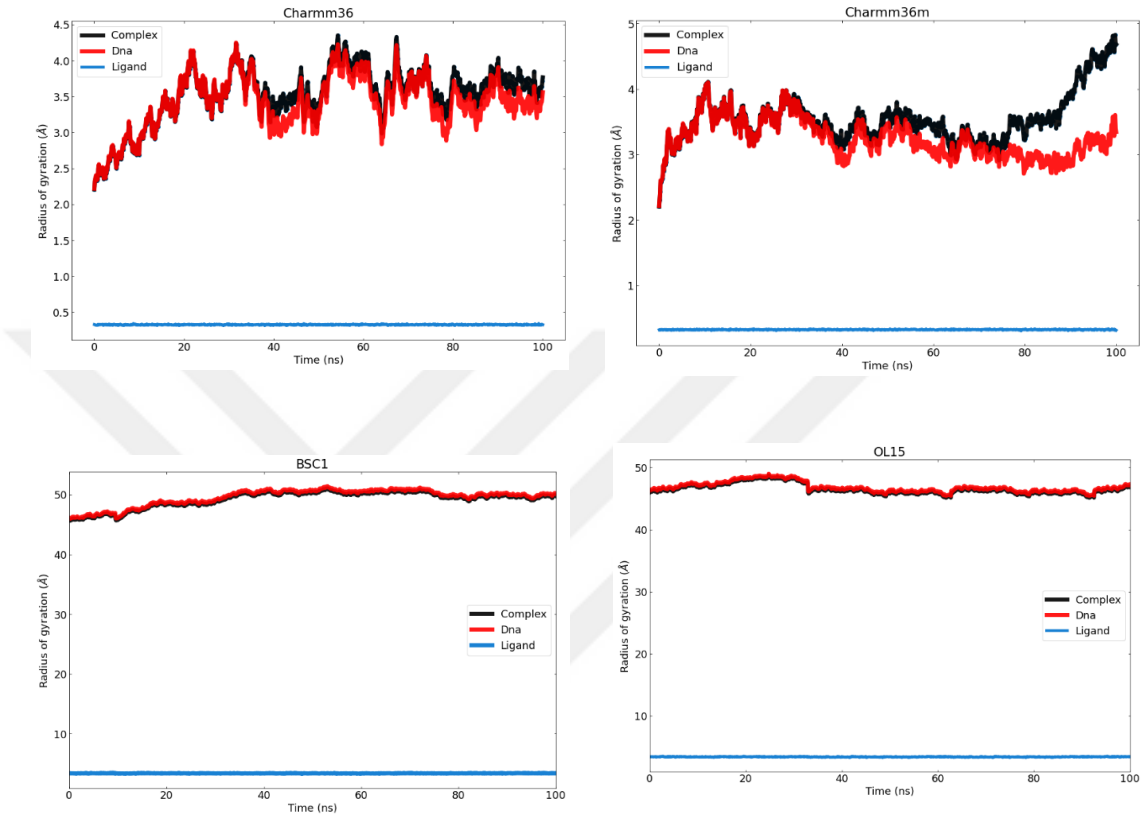

Figure 4.37.3. RGs of the SS-DNA-ligand complex versus 100 ns of MD simulation for each force field

The Charmm36 graph indicates that the DNA-ligand complex exhibited an average RG value exceeding 4. Å. Throughout the simulation, the RG values of both the complex system and DNA displayed an upward trend, with a brief decline at 40 ns. Subsequently, the RG values resumed their upward trajectory, ultimately reaching a stable RG value during the final 20 ns of the simulation. The Charmm36m simulation exhibited a notable increase in the RG value of the complex system, particularly during the initial stages of the simulation and up to the 10 ns mark. Subsequently, the RG value displayed fluctuations until 70 ns, after which it increased steadily until the conclusion of the simulation.

The mean RG values exhibited by the systems within BSC1 and OL15 are notably greater in magnitude when compared to those of charmm36 and charmm36m. In the BSC1 case, the aptamer-ligand system exhibits a lower average RG value in comparison to OL15. The RG curve of the aptamer indicates that it undergoes certain conformational changes but remains relatively constant with notable fluctuations throughout the simulation period. Nonetheless, the compactness of the aptamer is somewhat compromised, albeit to a lesser extent, in the case of OL15. This is in contrast to BSC1, where the simulation results indicate fewer conformational changes and a lower RG value.

4.37.4. Hydrogen bond

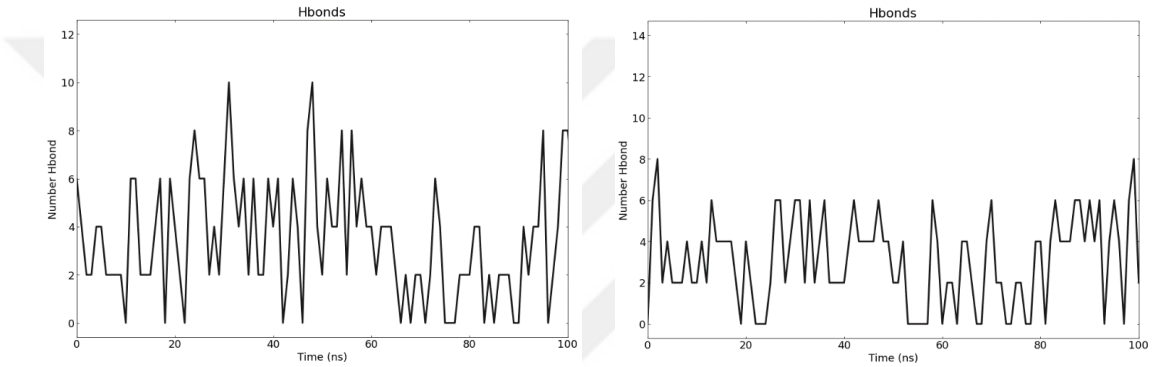

Figure 4.37.4. Hbonds of the SS-DNA-ligand complex versus 100 ns of MD simulation for each force field

The fluctuation of hydrogen bonding in the ligand-bound states was observed during the 100 nanosecond molecular dynamics simulation, as illustrated in Figure 4.37.4. The results of MD simulations suggest that the interaction between DNA and ligand is largely devoid of hydrogen bonding in Charmm36 and Charmm36m samples. BSC1 exhibits a higher propensity for hydrogen bonding in comparison to OL15.

4.38. Molecular dynamic simulation analysis of the modeled ss-DNA aptamer from the Nflex-Root software against bisphenol A

The ss-dna-ligand complex, made by molecular docking, was picked for a 100-ns molecular dynamics simulation in the programs NAMD and Gromacs. Two different versions of the AMBER force field and two different versions of the Charmm force field were used for this study.

Statistical tests were done on several factors, such as radius of gyration, RMSD, RMSF, and h-bond. Using the four force fields that were given, the plots of these numbers are compared.

4.38.1. Analysis of RMSD

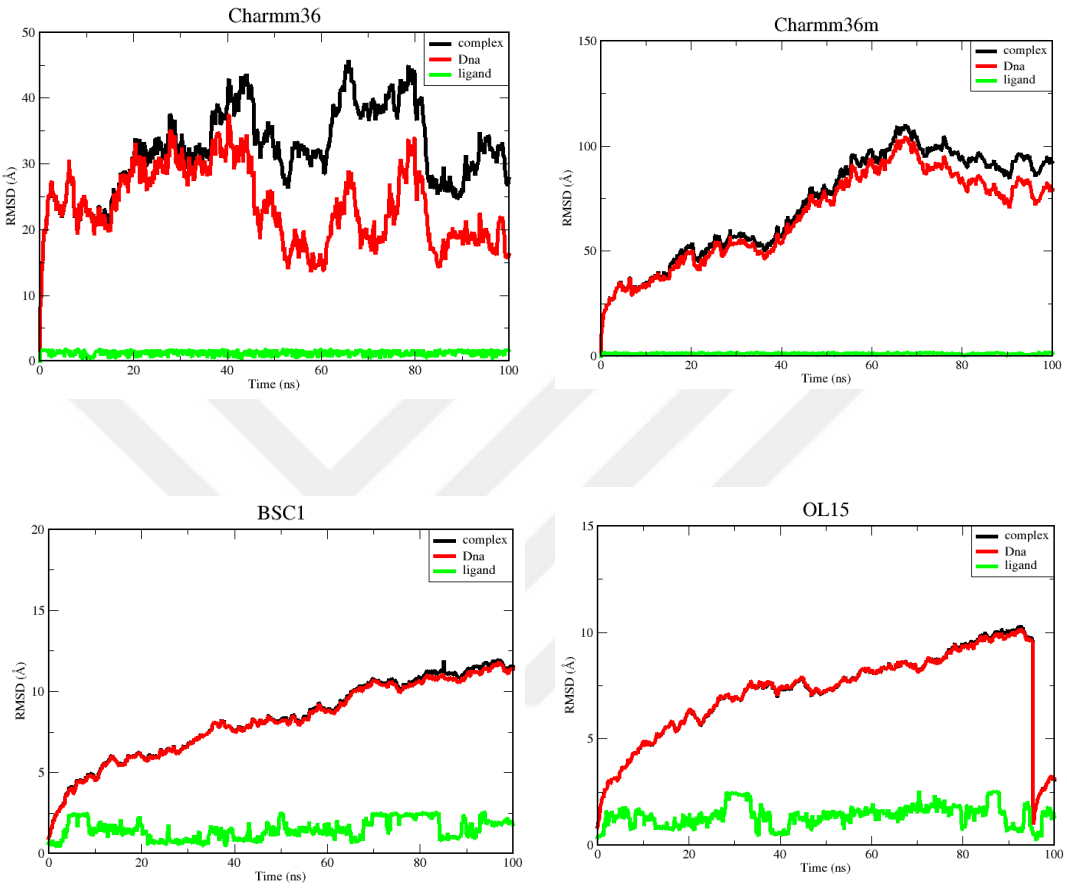

Figure 4.38.1. RMSDs of the SS-DNA-ligand complex versus 100 ns of MD simulation for each force field

Of the four complex structures examined, the charmm36m structure exhibits the greatest RMSD value, whereas the aptamer-ligand complex in BSC1 displays the lowest. Upon examination of Figures charmm36 and charmm36m, it can be observed that the RMSD value of the DNA-ligand complex aptamer structure in charmm36m is greater than that of charmm36. The Charmm36 graph exhibits notable spikes at 40 ns, 60 ns, and 80 ns, followed by an apparent decline. However, subsequent to the 80 ns, there was a rise in the observed values.

The Charmm36m simulation exhibited a consistent and stable increase in the complex system by 20 ns with negligible fluctuations.

However, subsequent to this point, the system's increase became more pronounced and persisted until 65 ns, culminating in the attainment of the maximum root-mean-square deviation value. Subsequently, the RMSD exhibited variability throughout the entirety of the simulation and demonstrated marked instability.

Upon examination of the DNA-aptamer ligand complexes in the BSC1 and OL15 instances, it is evident that the BSC1 system exhibits a reduced rmsd value in comparison to OL15. In each instance, comparable behavior was observed until the 40 nanoseconds. Subsequently, the RMSD value began to rise for both cases, but to a greater extent for the OL15 case. Furthermore, it should be noted that in the OL15 situation, the system maintained the periodic boundary conditions up to a duration of 95 nanoseconds.

4.38.2. Root Mean Square Fluctuation

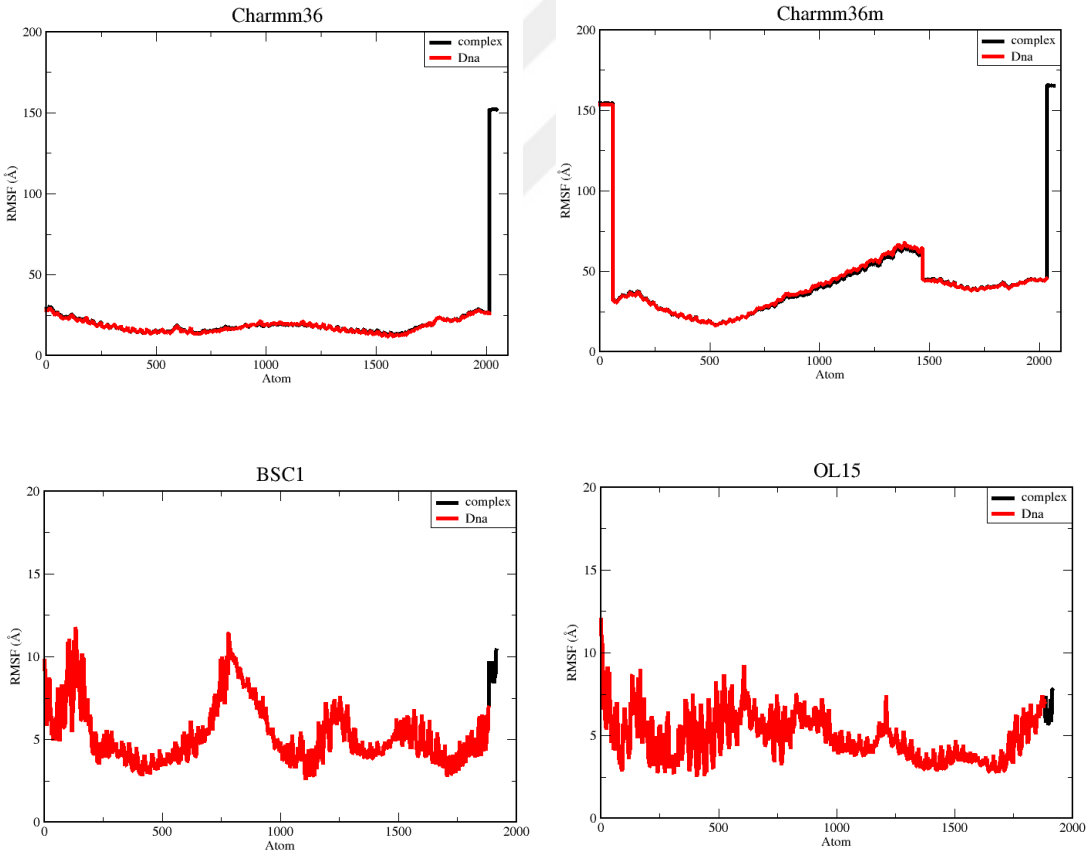

Figure 4.38.2. RMSFs of the SS-DNA-ligand complex versus 100 ns of MD simulation for each force field

A higher RMSF value is indicative of increased flexibility, whereas a lower RMSF value is suggestive of a comparatively more stable region. Consequently, an increased quantity of RMSF residues or groups signifies an elevated level of flexibility. The charmm36m model exhibits the highest RMSF value, whereas the OL15 model displays the lowest.

Furthermore, it is noteworthy that Charmm36 and Charmm36m exhibit relatively elevated rmsf values in comparison to other instances. Upon examination of the complex RMSF plot in both instances, it was observed that the maximum RMSF value exhibited a considerable degree of flexibility in the ligand state. In the context of OL15 and BSC1, it was found that the complex structures exhibited a low RMSF in the ligand state. Notably, OL15 demonstrated a lower RMSF value in comparison to BSC1, indicating that it forms a more stable complex system.

4.38.3. Gyration Radius Variation

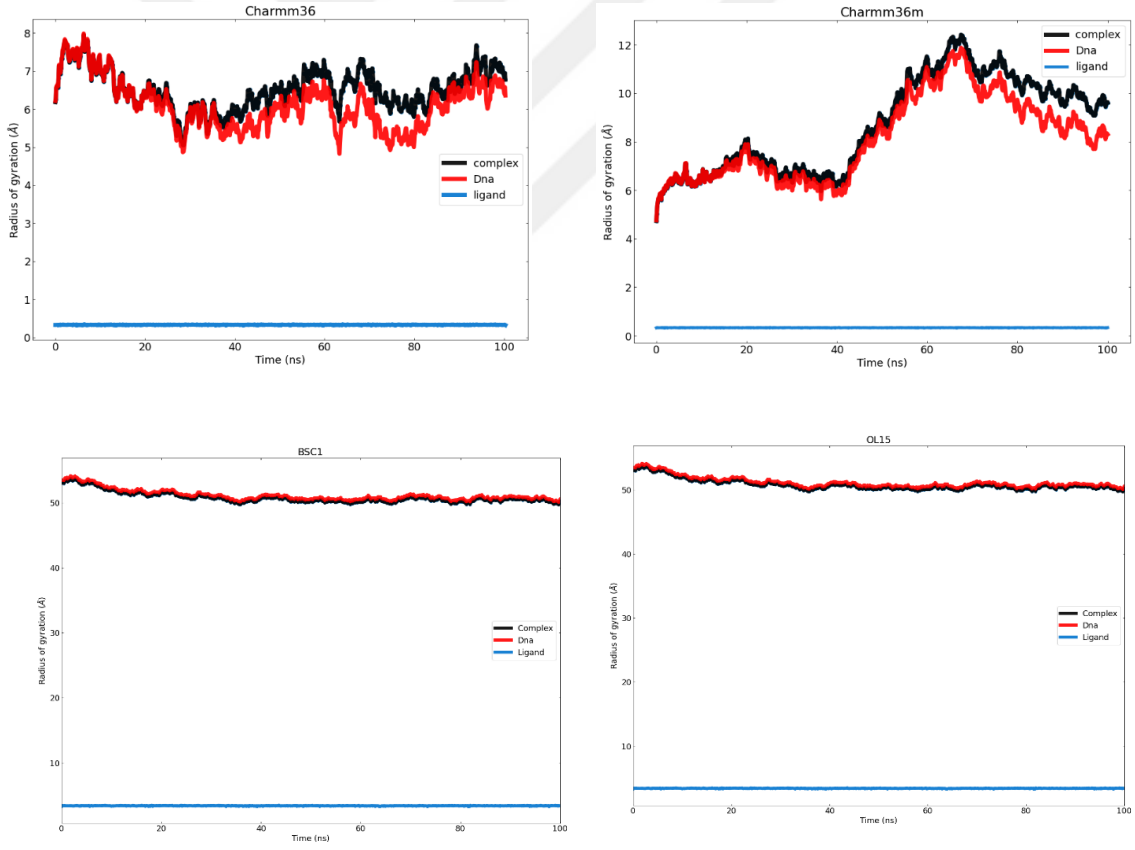

Figure 4.38.3. RGs of the SS-DNA-ligand complex versus 100 ns of MD simulation for each force field

The Charmm36 graph indicates that the DNA-ligand complex exhibited an average RG exceeding 5 Å.

While the RG value initially rose during the simulation, it subsequently declined after 10 ns, ultimately reaching a state of equilibrium, though fleetingly. The fluctuations observed during the simulation give rise to alterations in the configuration of the complex system, ultimately resulting in a reduction in its overall stability.

The Charmm36m simulation exhibited a marginal increase in the RG value during the initial stages of the complex system simulation. However, a substantial increase in the RG value was observed after 40 ns, culminating in its peak value at 70 ns. Subsequent to 70 nanoseconds, a decline in the RG value was noticed, and the simulation was concluded with negligible fluctuations.

The RG values of the systems located at BSC1 and OL15 exhibit a significant increase in comparison to those of charmm36 and charmm36m. Furthermore, it was observed that both instances exhibited negligible fluctuations over the course of the simulation and demonstrated superior coupling in comparison to charmm36 and charmm36m.

4.38.4. Hydrogen bond

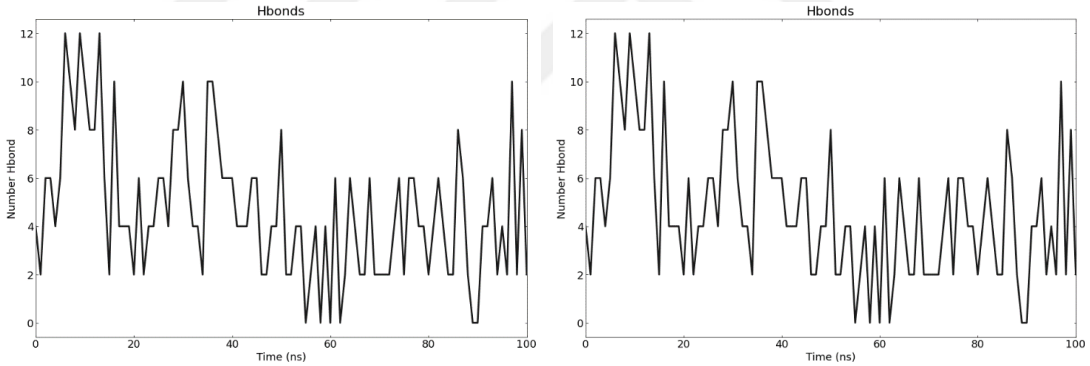

Figure 4.38.4. Hbonds of the SS-DNA-ligand complex versus 100 ns of MD simulation for each force field

The fluctuation of hydrogen bonding degree in the ligand-bound states was observed throughout the 100 nanosecond molecular dynamics simulation, as depicted in Figure 9. The Charmm36 and Charmm36m samples exhibit a notable lack of hydrogen bond formation between DNA and ligand, as evidenced by molecular dynamics simulations.

4.39. Molecular dynamic simulation analysis of the modeled ss-DNA aptamer from the X3dna software against bisphenol A

The molecular docking-formed ss-dna-ligand complex was chosen for a 100-ns molecular dynamics simulation in the programs NAMD and Gromacs. This investigation utilized two distinct versions of the AMBER force field and two distinct versions of the Charmm force field. Statistical analyses were conducted on a number of variables, including radius of gyration, RMSD, RMSF, and h-bond. Using the four provided force fields, the graphs of these numbers are compared.

4.39.1. Root Mean Square Deviation (RMSD)

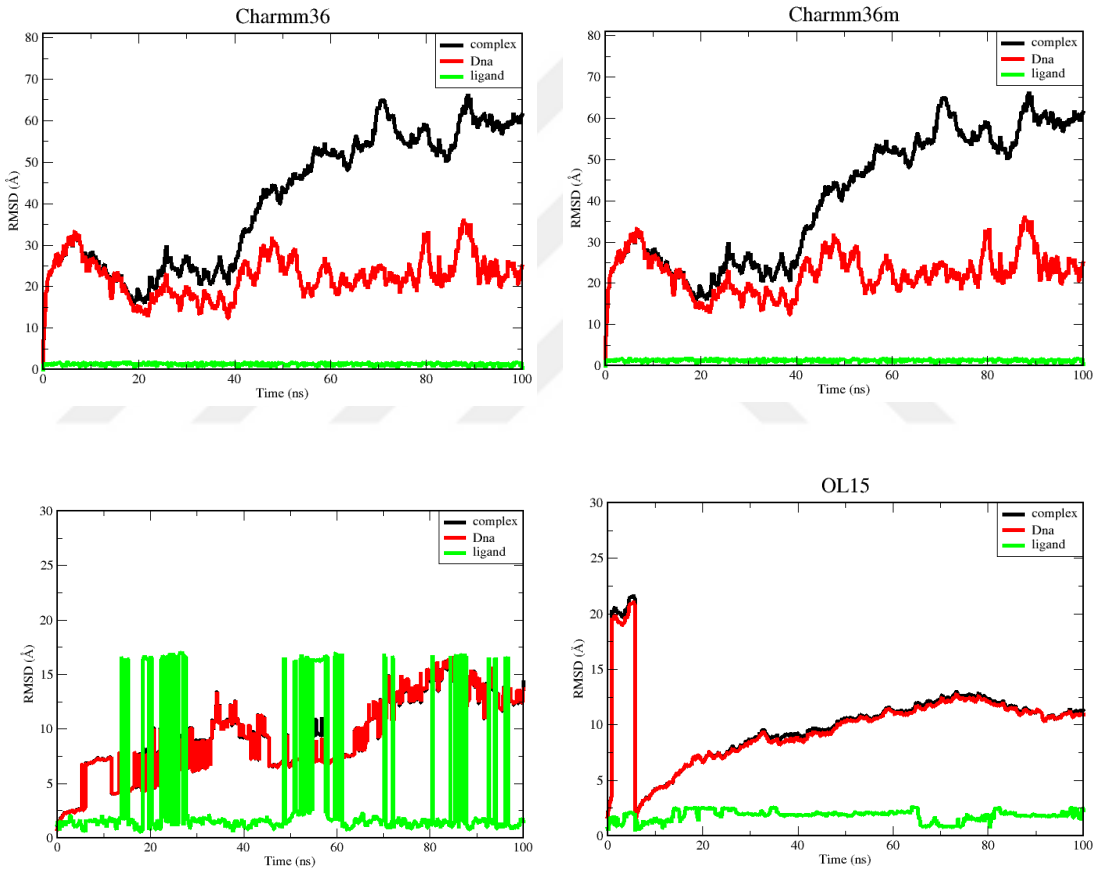

Figure 4.39.1. RMSDs of the SS-DNA-ligand complex versus 100 ns of MD simulation for each force field

The Charmm36 graph indicates that the RMSD value of the complex structure experienced a marked escalation beyond the 40 nanoseconds, ultimately peaking at its highest RMSD value and continuing to increase steadily until the 90 nanoseconds.

The findings indicate that the structural integrity of the DNA aptamer-ligand complex is somewhat weakened, but the simulation exhibited minimal fluctuations throughout the entire 90 ns duration. The Charmm36m simulation of the complex system exhibits a notable rise at the outset, followed by a period of minimal fluctuations that persists until the 55 ns mark. However, abrupt declines are observed at 55 ns and 65 ns, indicating that the system departs from the periodic boundary conditions at these points. The simulation exhibited fluctuations from 70 nanoseconds until its completion.

Regarding BSC1, the RMSD of the complex system exhibited persistent fluctuations for a duration of 90 nanoseconds. Concurrently, the ligand demonstrated a negligible affinity for DNA, as evidenced by its intermittent dissociation from orbit during the simulation. The simulation of Ol15 exhibited a notable initial rise in RMSD, followed by an abrupt decline. Subsequent to this point, RMSD measurements exhibited a persistent upward trend until the 90 nanosecond mark, followed by a period of stabilization during the final 5 nanoseconds.

4.39.2. Root Mean Square Fluctuation

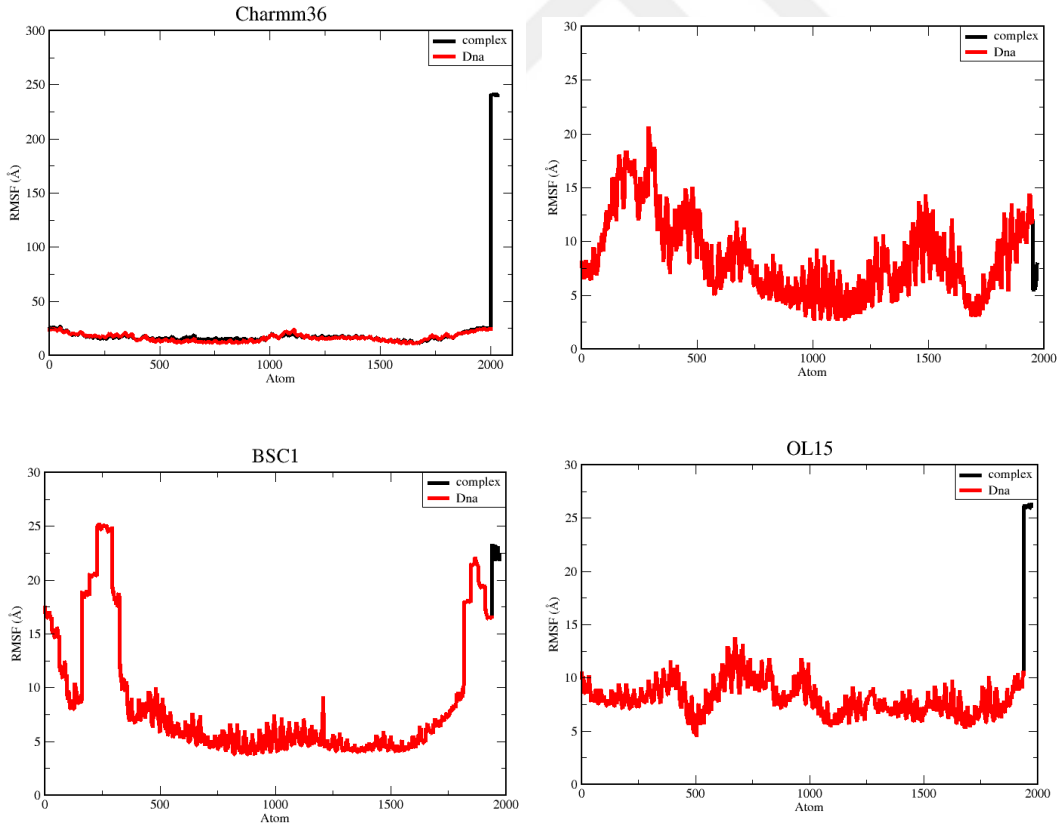

Figure 4.39.2. RMSFs of the SS-DNA-ligand complex versus 100 ns of MD simulation for each force field

The RMSF values of Charmm36 and BSC1 exhibit a relatively elevated degree of complexity in comparison to other instances. Upon examination of the intricate RMSF plot in both cases, it was noted that the most substantial RMSF spike exhibited a notable degree of pliancy in the ligand condition. In the context of OL15 and Charmm36m, it was discovered that the complex structures exhibited low RMSF in the ligand state. Notably, OL15 demonstrated a lower RMSF value in comparison to Charmm36m, suggesting that it forms a more stable complex system.

4.39.3. Gyration Radius Variation

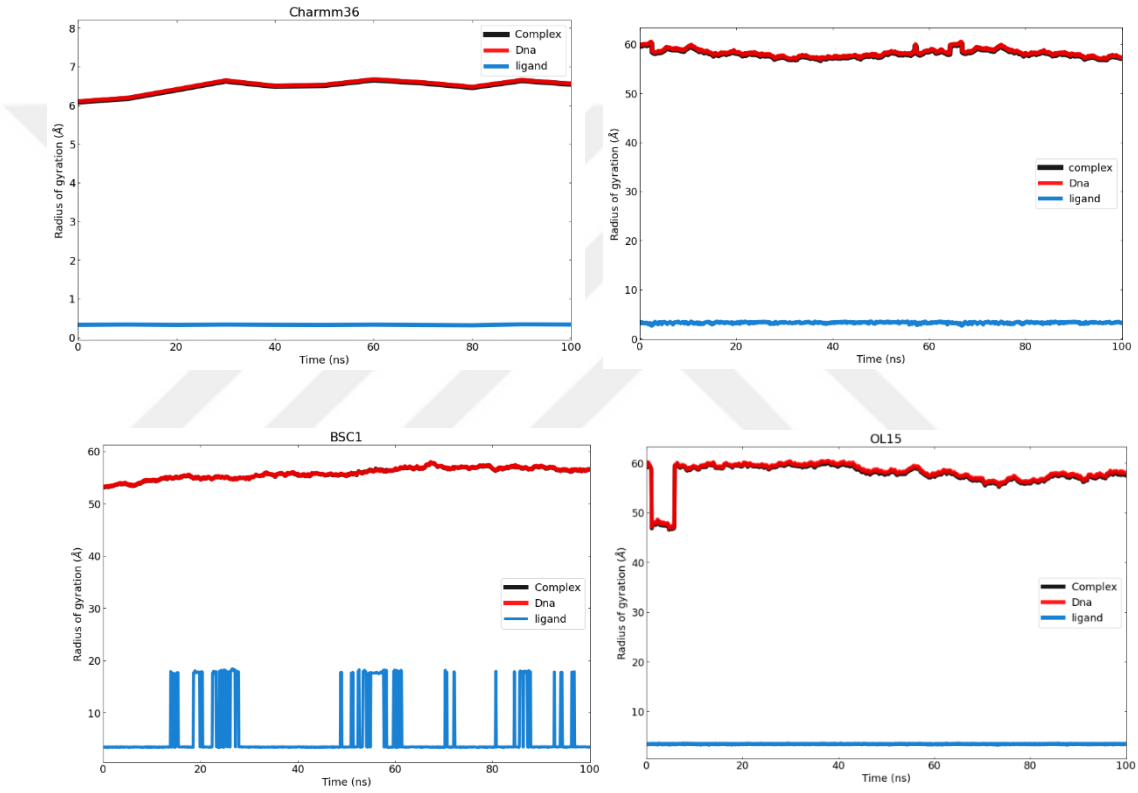

Figure 4.39.3. RGs of the SS-DNA-ligand complex versus 100 ns of MD simulation for each force field

The Charmm36 analysis revealed that the DNA-ligand complex exhibited an average radius of gyration (RG) exceeding 6 Å, with Rg values displaying an upward trend in both the complex system and DNA over the course of the simulation. Nevertheless, the RG value remained relatively constant throughout the simulation. The Charmm36m model exhibited a notable elevation in RG values, particularly at 50 ns and 70 ns, throughout the simulation of the complex system. The mean RG values exhibited by the systems located in BSC1 and OL15 demonstrate a significant increase in comparison to

those observed in charmm36 and charmm36m. Throughout the simulation, the BSC1 case exhibited minimal fluctuations in the RG value of the aptamer-ligand system. The OL15 graph indicates that while the RG value exhibited a notable decline during the initial 10 nanoseconds, it subsequently experienced an upturn and ultimately concluded with negligible fluctuations.

4.39.4. Hydrogen bond

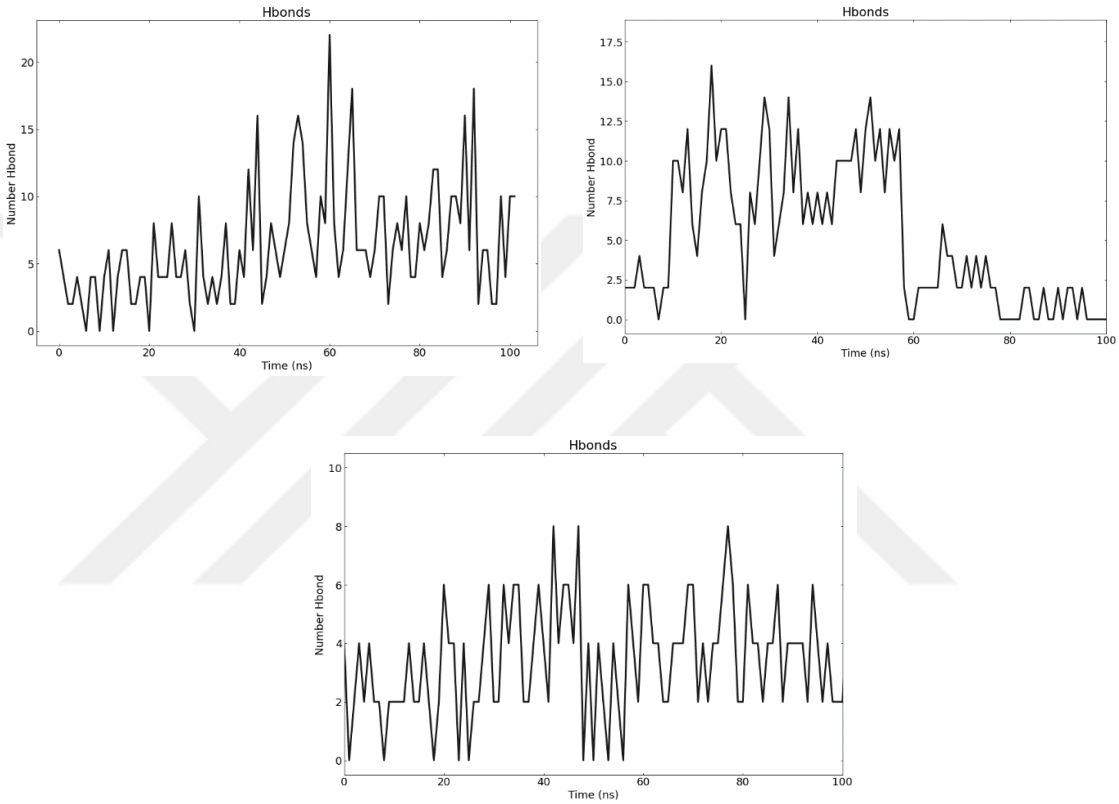

Figure 4.39.4. Hbonds of the SS-DNA-ligand complex versus 100 ns of MD simulation for each force field

Throughout the 100 nanosecond molecular dynamics simulation, Figure 9 illustrates the observation of fluctuations in the degree of hydrogen bonding in the ligand-bound states. Molecular dynamic simulations have revealed that Charmm36m does not exhibit any noteworthy hydrogen bond formation between ligand and DNA. The simulation results indicate that hydrogen bond formation occurred in both BSC1 and OL15. Furthermore, a greater number of hydrogen bonds were formed in BSC1 compared to OL15 over the course of the simulation.

4.40. Computational methods for calculating binding free energy

The evaluation of binding free energy is critical for determining the effectiveness of ligand-target binding since it offers a precise quantification of the binding potency between biomolecules. In this investigation, the free interaction energy between ligands and SS-DNA was computed using the MMPBSA.py script of the AMBER package (133). The binding free energy between the aptamer and ligand in the modeled complexes was assessed by submitting the MD trajectory of each DNA-ligand complex to the MMPBSA.py script of the AMBER package tool. The binding free energy for each complex is shown in the Tables and details are given in the appendix.

SİM-RNA complex system	ΔG Binding kj/mol
Charmm36	-8.51
Charmm36m	-0.13
BSC1	-0.42
OL15	-2.23

Table 4.40.1. The estimated free binding energy of the Sim-Rna/ligand complex for each force field using the AMBER package tool

Rosetta-Farfar complex system	ΔG Binding kj/mol
Charmm36	0.85
Charmm36m	-6.17
BSC1	-0.86
OL15	-3.09

Table 4.40.2. The estimated free binding energy of the Rosetta-Farfar/ligand complex for each force field using the AMBER package tool

Rna-Composer complex system	ΔG Binding kj/mol
Charmm36	-2.63
Charmm36m	-3.16
BSC1	1.43
OL15	-9.10

Table 4.40.3. The estimated free binding energy of the Rna-Composer/ligand complex for each force field using the AMBER package tool

Vfold3D complex system	ΔG Binding kj/mol
Charmm36	-2.41
Charmm36m	-18.68
BSC1	-11.42
OL15	-2.28

Table 4.40.4. The estimated free binding energy of the Vfold3D/ligand complex for each force field using the AMBER package tool

3dRNA complex system	ΔG Binding kj/mol
Charmm36	-0.45
Charmm36m	-25.43
BSC1	-0.53
OL15	-13.25

Table 4.40.5. The estimated free binding energy of the 3dRNA/ligand complex for each force field using the AMBER package tool

3D-DART complex system	ΔG Binding kcal/mol
Charmm36	-4.01
Charmm36m	0.00
BSC1	-13.25
OL15	-13.25

Table 4.40.6. The estimated free binding energy of the 3D-DART/ligand complex for each force field using the AMBER package tool

İfoldRNA complex system	ΔG Binding kcal/mol
Charmm36	-4.01
Charmm36m	-5.74
BSC1	-14.12
OL15	-22.82

Table 4.40.7. The estimated free binding energy of the İfoldRNA/ligand complex for each force field using the AMBER package tool

The binding energies determined will be employed in the equation Kd = Ki = Ki = exp(deltaG/(R*T)) OR ΔGExp =-RT·ln(KdExp) to find the binding affinity.

From the literature, an aptamer sequence exhibiting specific biosensor properties for BPA, an endocrine-disrupting chemical commonly detected in water samples, was obtained following a 12-step sequence by the Selex technique. The tabulated data presents the experimental results for this particular structure.

Table 4.40.8. Estimated binding affinity values of the SİM-RNA/ligand complex for each force field

Selected aptamer sequence developed using the Selex method against bisphenol a	**Target**	**Binding Affinity (Kd)**
CCGGTGGGTGGTCAGGTGGGATAGCGTTCCGCGTATGGCCCAGCGCATCACGGGTTCGCACCA	Bisphenol a	8.3 nM

Table 4.40.9. Estimated binding affinity values of the SİM-RNA/ligand complex for each force field

SİM-RNA complex system	Binding Affinity Kd
Charmm36	9.93×10^{-4} nM
Charmm36m	851 nM
BSC1	506 nM
OL15	26.7 nM

Table 4.40.10. Estimated binding affinity values of the Rosetta-Farfar/ligand complex for each force field

Rosetta-Farfar complex system	ΔG Binding kj/mol
Charmm36	3980 nM
Charmm36m	0.0444 nM
BSC1	247 nM
OL15	6.61 nM

Table 4.40.11. Estimated binding affinity values of the Rna-Composer/ligand complex for each force field

Rna-Composer complex system	ΔG Binding kj/mol
Charmm36	14 nM
Charmm36m	5.93 nM
BSC1	102 nM
OL15	3.81×10^{-4} nM

Table 4.40.12. Estimated binding affinity values of the Vfold3D/ligand complex for each force field

Vfold3D complex system	ΔG Binding kj/mol
Charmm36	20 nM
Charmm36m	6.65×10^{-11} nM
BSC1	11.8 nM
OL15	24.6 nM

Table 4.40.13. Estimated binding affinity values of the 3dRNA/ligand complex for each force field

3dRNA complex system	ΔG Binding kj/mol
Charmm36	840 nM
Charmm36m	0.0513 nM
BSC1	814 nM
OL15	5.65 nM

Table 4.40.14. Estimated binding affinity values of the 3D-DART/ligand complex for each force field

3D-DART complex system	ΔG Binding kcal/mol
Charmm36	211 nM
Charmm36m	0.00 nM
BSC1	5.82 nM
OL15	5.82 nM

Table 4.40.15. Estimated binding affinity values of the İfoldRNA/ligand complex for each force field

İfoldRNA complex system	ΔG Binding kcal/mol
Charmm36	211 nM
Charmm36m	0.00 nM
BSC1	4.15 nM
OL15	0.142 nM

Upon examination of the computed binding energy and empirical findings, it is evident that the outcomes vary across distinct complex configurations. The correlation between the binding energies of the SIM-RNA complex and the experimental data is poor when utilizing charmm36, charmm36m, and BSC1. However, upon examination of the OL15 case, it was found that the computed binding energy yielded superior outcomes compared to the empirical data.

The Rosetta-farfar complex exhibits relatively low binding energy in the charmm36m state, whereas the OL15 state demonstrates a strong binding affinity that is in close agreement with experimental data and surpasses that of other states.

The binding energy of the Rna-composer complex exhibit a significant increase in the charmm36 and charmm36m states compared to the remaining states. Although the calculated binding energy in the charmm36m state closely approximates the experimental

data, the calculated binding energy in the charmm36 state exceeds the experimental outcome. This suggests a strong binding inclination of the ligand. The Vfold3D complexes exhibited suboptimal binding affinity solely in the charmm36m state, which displayed poor correlation with the experimental outcome. In certain instances, the computed binding energies were satisfactory, particularly in the BSC1 condition where the binding energy closely approximates the experimental outcome, thereby indicating a highly effective binding. The 3D-RNA structures exhibited favorable binding energy solely in the OL15 state, which closely approximated the experimental findings. The ligand exhibited favorable binding solely in the instances of BSC1 and OL15 within 3D-DART complexes, aligning more closely with the experimental findings. Finally, Upon evaluation of the ifoldRNA complex structures, it is observed that the calculated binding energy for the BSC1 situation exhibits a significant increase compared to the other instances and is in closer proximity to the experimental outcome.

5. DISCUSSION and CONCLUSION

Antibodies have been widely utilized in various biomolecular applications throughout history and to the present day. However, it is important to note that while antibodies offer significant benefits, they also possess certain drawbacks. The primary benefit of the indispensability of antibodies is their ability to exhibit highly sensitive binding to the intended target. However, because they are costly and time-consuming, scientists have investigated novel biomolecules and designed alternative biomolecules. Aptamers have emerged as the most beneficial alternative biomolecules. Aptamers have competed with antibodies over the past decade, and in many applications, they have been favored over antibodies due to their ability to bind to multiple targets, high specificity, low cost, and quick production. Owing to their elevated specificity, they are particularly favored as the bio-recognition element that constitutes the fundamental basis of the biosensor.

In recent years, there has been an integration of aptamer structures into biosensor devices, resulting in improved sensitivity in environmental analysis. The aptamers generated through the conventional Selex method for aptamer production may not exhibit sufficient affinity and specificity towards the target. Additionally, it may not always be feasible to isolate the optimal aptamer sequence. Hence, bioinformatics methodologies have been employed to enhance the binding affinity of aptamers.

In order to investigate the relationships among a ligand and an aptamer structure, a comprehensive methodology was developed. The methodology involved the utilization of a well-established aptamer sequence that was previously employed in the biosensor application of this study.

In this study, we initially introduced methodologies for forecasting the tridimensional configurations of the aptamer nucleotide sequence. In the realm of in silico applications, the emphasis on three-dimensional structure predictions is primarily directed toward proteins. Despite the existence of extensive databases containing the three-dimensional structures of nearly all proteins, the same cannot be said for aptamers. In fact, only a small number of aptamers have had their structures experimentally determined. Various software models have been employed in the literature to estimate the three-dimensional structures of aptamers, with each study utilizing a distinct model.

Given the absence of a crystal structure, the reliability of the software employed remains a subject of debate. In our study, extant software was utilized to model the aptamer sequence for the intended purpose.

We attempted to determine which model produced the best results by categorizing this software. Upon assessing the outcomes of the software employed, it has been observed that the aptamer models, which are derived from the primary sequence and progress towards obtaining 2D structures and, subsequently, three-dimensional structures, exhibit greater stability in comparison to the aptamer models that solely rely on the primary sequence to obtain the three-dimensional structures. Upon conducting molecular dynamics simulations at 100 nanoseconds, our analysis revealed that the aforementioned model structures exhibited greater stability as evidenced by their respective RMSD, RMSF, and RG values. The aptamer structures, which were modeled from primary sequence using various software tools such as Avogadro, X3dna, Discovery studio visualizer, Schrodinger, and Nflex-root, exhibited significant instability during molecular dynamics simulation analyses and failed to attain equilibrium.

The utilization of algorithms that enable the modeling of a more stable aptamer structure, starting from primary sequences and reaching the secondary structure, followed by the modeling of a three-dimensional structure, would facilitate the design of aptamers with stronger binding affinities. Furthermore, accurate conformations were anticipated through the implementation of molecular docking techniques, which involved the aptamer structures we generated and the corresponding ligand. The results obtained from the docking analysis indicate a reduced level of interaction between the ligands and aptamer structures that were modeled from primary sequences. To gain a more comprehensive understanding of the target structure and aptamer structures, molecular dynamics simulations were conducted to analyze their internal dynamics. The present investigation scrutinized the binding behavior of bp via the bp-specific aptamer, and meticulously observed the ensuing interactions. The assessment of the stability of each simulation was conducted through the analysis of diverse parameters.

Ultimately, through the computation of binding energies within our overarching methodology, it was determined the degree to which the intended configuration interacts and its level of conformity with empirical findings. The obtained binding energy outcomes exhibited a strong correlation with the experimental findings. there are even complex structures that give better bonding results.

The in vitro validation of the aptamers was accomplished through in silico predictions, resulting in the stabilization of the desired conformations and an enhancement of the aptamers' binding affinity towards their target analytes.

Furthermore, the utilization of the Bioinformatics methodology will facilitate forthcoming investigations in enhancing both aptamers and the process of aptamer selection. Our findings will pave the way for future efforts to broaden the scope of our method to include different aptamer forms.

6. REFERENCES

(1) Diamanti-Kandarakis E, Bourguignon J-P, Giudice LC, Hauser R, Prins GS, Soto A. M, Zoeller R. T, Gore A. C. Endocrine-disrupting chemicals: An Endocrine society scientific statement. Endocr Rev 2009;*30* (4):293–342.

(2) World Health Organization. Regional Office for Europe. Identification of Risks from Exposure to Endocrine-Disrupting Chemicals at the Country Level; World Health Organization. Regional Office for Europe, 2014.

(3) Kumar M, Sarma D. K., Shubham S, Kumawat M.,Verma V, Prakash A, Tiwari R. Environmental Endocrine-Disrupting Chemical Exposure: Role in non-communicable diseases. Front. Public Health 2020;*8*:553850.

(4) Jeddi I, Saiz L. Three-dimensional modeling of single stranded DNA hairpins for aptamer-based biosensors. Scientific Reports. 2017;7(1):1178

(5) Song K-M, Lee S, Ban C. Aptamers and Their Biological Application. PMC. 2009;30(4):293-342.

(6) Li Y-C, E.; Lee I-C. The Current Trends of Biosensors in Tissue Engineering. Biosensors (Basel). 2020;10 (8):88.

(7) Newman J. D, Turner A. P. F. In Handbook of Biosensors and Biochips. Marks R. S, Cullen D. C, Karube I, Lowe C. R, Weetall H. H., Eds.; John Wiley & Sons, Ltd. Chichester, UK, 2008:p.hbb002.

(8) Bhalla N, Jolly P, Formisano N, Estrela P. Introduction to Biosensors. Essays Biochem. 2016;60 (1):1–8.

(9) Rai V, Acharya S, Dey N. Implications of Nanobiosensors in Agriculture. JBNB 2012;03 (02):315–324.

(10) Clark Jr. L. C, Lyons C. Electrode Systems for Continuous Monitoring in Cardiovascular Surgery. Annals of the New York Academy of Sciences. 1962;102 (1):29–45.

(11) Kovacs, Gregory T. A. Micromachined transducers sourcebook. McGraw-Hill series in electrical and computer engineering; WCB/McGraw-Hill:Boston, 1998.

(12) Mohanty S.P. Biosensors: A survey report. [Electronic Journal]. . http://biocapteurs.wikispa- ces.com/file/view/BiosensorSurveyReport.pdfaccessed. June;2001

(13) Soleymani L, Li F. Mechanistic Challenges and Advantages of Biosensor Miniaturization into the Nanoscale. ACS Sens. 2017;2 (4):458–467.

(14) Njagi J. I, Kagwanja S. M. The Interface in Biosensing: Improving Selectivity and Sensitivity. In ACS Symposium Series; Helburn, R., Vitha, M. F., Eds.; American Chemical Society: Washington, DC, 2011; Vol. 1062, pp 225–247.

(15) Ali J, Najeeb J, Asim Ali M, Farhan Aslam M, Raza A. Biosensors: Their Fundamentals, Designs, Types and Most Recent Impactful Applications: A Review. J Biosens Bioelectron. 2017;08 (01).

(16) Saha K, Agasti S. S, Kim C, Li X, Rotello V. M. Gold Nanoparticles in Chemical and Biological Sensing. Chem. Rev. 2012;112 (5):2739–2779.

(17) Wang Y, Knoll W, Dostalek J. Bacterial Pathogen Surface Plasmon Resonance Biosensor Advanced by Long Range Surface Plasmons and Magnetic Nanoparticle Assays. Anal. Chem. 2012;84 (19):8345–8350.

(18) Wilkins E, Atanasov P. Glucose Monitoring: State of the Art and Future Possibilities. Medical Engineering & Physics. 1996;18 (4):273–288.

(19) Nguyen H. H, Lee S. H, Lee U. J, Fermin C. D, Kim M. Immobilized Enzymes in Biosensor Applications. Materials (Basel). 2019;12 (1):121. https://doi.org/10.3390/ma12010121.

(20) Mairal T, Ozalp V, Lozano S. P, Mir M, Katakis I, O'Sullivan C. Aptamers: Molecular Tools for Analytical Applications. Analytical and bioanalytical chemistry. 2008;390:989–1007.

(21) Ibupoto Z, Khun K, Willander M. Development of a Disposable Potentiometric Antibody Immobilized ZnO Nanotubes Based Sensor for the Detection of C-Reactive Protein. *S*ensors and Actuators B: Chemical. 2012;166–167:809–814.

(22) Omidfar K, Khorsand F, Darziani Azizi M. New Analytical Applications of Gold Nanoparticles as Label in Antibody Based Sensors. Biosens. Bioelectron. 2013; 43:336–347.

(23) Cordeiro C. A, de Vries M. G, Ngabi W, Oomen P. E, Cremers T. I. F. H, Westerink B. H. C. In Vivo Continuous and Simultaneous Monitoring of Brain Energy Substrates with a Multiplex Amperometric Enzyme-Based Biosensor Device. Biosensors and Bioelectronics. 2015;67:677–686..

(24) Syshchyk O, Skryshevsky V. A, Soldatkin O. O, Soldatkin A. P. Enzyme Biosensor Systems Based on Porous Silicon Photoluminescence for Detection of Glucose, Urea and Heavy Metals. Biosensors and Bioelectronics. 2015;66:89–94.

(25) Baker B. R, Lai R. Y, Wood M. S, Doctor E. H, Heeger A. J, Plaxco K. W. An Electronic, Aptamer-Based Small-Molecule Sensor for the Rapid, Label-Free Detection of Cocaine in Adulterated Samples and Biological Fluids. J. Am. Chem. Soc. 2006;128 (10):3138–3139.

(26) Bouchet-Spinelli A, Reuillard B, Coche-Guérente L, Armand, S, Labbé P, Fort S. Oligosaccharide Biosensor for Direct Monitoring of Enzymatic Activities Using QCM-D. Biosens Bioelectron. 2013;49:290–296.

(27) Bhand S. G, Soundararajan S, Surugiu-Wärnmark I, Milea J. S, Dey E. S, Yakovleva M, Danielsson B. Fructose-Selective Calorimetric Biosensor in Flow Injection Analysis. Analytica Chimica Acta 2010;668 (1):13–18.

(28) Ballesta-Claver J, Ametis-Cabello J, Morales-Sanfrutos J, Megía-Fernández A, Valencia-Mirón M. C, Santoyo-González F, Capitán-Vallvey L. F. Electrochemiluminescent Disposable Cholesterol Biosensor Based on Avidin–Biotin Assembling with the Electroformed Luminescent Conducting Polymer Poly(Luminol-Biotinylated Pyrrole). Analytica Chimica Acta 2012;754:91–98.

(29) Yan Z, Yang M, Wang Z, Zhang F, Xia J, Shi G, Xia L, Li Y. H, Xia Y, Xia L. A. Label-Free Immunosensor for Detecting Common Acute Lymphoblastic Leukemia Antigen (CD10) Based on Gold Nanoparticles by Quartz Crystal Microbalance. Sensors and Actuators B: Chemical. 2015;210.

(30) Ellington A. D, Conrad R. Aptamers as Potential Nucleic Acid Pharmaceuticals. In Biotechnology Annual Review. El-Gewely M. R, Ed, Elsevier, 1995; Vol. 1, pp 185–214.

(31) Stoltenburg R, Reinemann C, Strehlitz B. FluMag-SELEX as an advantageous method for DNA aptamer selection. Anal Bioanal Chem. 2005;383(1):83-91.

(32) Sampson T. Aptamers and SELEX: The Technology. World Patent Information. 2003;25 (2):123–129.

(33) Hermann T, Patel DJ. Adaptive recognition by nucleic acid aptamers. Science. 2000 Feb 4;287(5454):820-5.

(34) Stoltenburg R, Reinemann C, Strehlitz B. SELEX Evolutionary Method to Generate High-Affinity Nucleic Acid Ligands. Biomol Eng. 2007;24 (4):381–403.

(35) Tuerk C, Gold L. Systematic Evolution of Ligands by Exponential Enrichment: RNA Ligands to Bacteriophage T4 DNA Polymerase. Science. 1990;249 (4968): 505–510.

(36) Ellington A. D, Szostak J. W. In Vitro Selection of RNA Molecules That Bind Specific Ligands. Nature. 1990;346 (6287):818–822.

(37) Ellington A. D, Szostak J. W. Selection in Vitro of Single-Stranded DNA Molecules That Fold into Specific Ligand-Binding Structures. Nature. 1992;355 (6363):850–852.

(38) Darmostuk M, Rimpelova S, Gbelcova H, Ruml T. Current Approaches in SELEX: An Update to Aptamer Selection Technology. Biotechnology Advances. 2015;33 (6, Part 2):1141–1161.

(39) Mosing R.K, Mendonsa S.D, Bowser M.T. Capillary electrophoresis-SELEX selection of aptamers with affinity for HIV-1 reverse transcriptase. Anal Chem. 2005; 77(19):6107-12.

(40) Joyce G. F. Amplification, Mutation and Selection of Catalytic RNA. Gene. 1989;82 (1):83–87.

(41) Baldrich E, Campàs M, O`Sullivan C. Aptamers: Powerful Molecular Tools for Therapeutics and Diagnostics. 2004;193–217.

(42) Mayer G, Ahmed MS, Dolf A, Endl E, Knolle PA, Famulok M. Fluorescence-activated cell sorting for aptamer SELEX with cell mixtures. Nat Protoc. 2010 ;5(12):1993-2004.

(43) Yu H, Alkhamis O, Canoura J, Liu Y, Xiao Y. Advances and Challenges in Small-Molecule DNA Aptamer Isolation, Characterization, and Sensor Development. Angew Chem Int Ed Engl. 2021;60(31):16800-16823.

(44) Hoinka J, Przytycka T. AptaPLEX - A dedicated, multithreaded demultiplexer for HT-SELEX data. Methods. 201;106:82-5.

(45) McKeague M, Wong R. S, Smolke C. D. Opportunities in the Design and Application of RNA for Gene Expression Control. Nucleic Acids Res. 2016;44 (7): 2987–2999.

(46) Buglak A. A, Samokhvalov A. V, Zherdev A. V, Dzantiev B. B. Methods and Applications of In Silico Aptamer Design and Modeling. Int J Mol Sci. 2020;21 (22):8420.

(47) Lee S. J, Cho J, Lee B-H., Hwang D, Park J-W. Design and Prediction of Aptamers Assisted by In Silico Methods. Biomedicines**.** 2023;11 (2):356.

(48) Bauer M, Strom M, Hammond D. S, Shigdar S. Anything You Can Do, I Can Do Better: Can Aptamers Replace Antibodies in Clinical Diagnostic Applications. Molecules. 2019;24 (23):4377.

(49) Chushak Y, Stone M. O. In Silico Selection of RNA Aptamers. Nucleic Acids Res. 2009;37 (12):e87.

(50) Domin G, Findeiß S, Wachsmuth M, Will S, Stadler P. F, Mörl M. Applicability of a Computational Design Approach for Synthetic Riboswitches. Nucleic Acids Res. 2017;45 (7):4108–4119.

(51) Ilgu M, Yan S, Khounlo R. M, Lamm M. H, Nilsen-Hamilton M. Common Secondary and Tertiary Structural Features of Aptamer-Ligand Interaction Shared by RNA Aptamers with Different Primary Sequences. Molecules. 2019;24 (24): 4535.

(52) Jokar M, Safaralizadeh M. H, Hadizadeh F, Rahmani F, Kalani M. R. Apta-Nanosensor Preparation and in Vitro Assay for Rapid Diazinon Detection Using a Computational Molecular Approach. J Biomol Struct Dyn. 2017;35 (2):343–353.

(53) Hilder T. A, Hodgkiss J. M. The Bound Structures of 17β-Estradiol-Binding Aptamers. ChemPhysChem. 2017;18 (14):1881–1887.

(54) Zhao M, Li W, Liu K, Li H, Lan X. C4-HSL aptamers for blocking qurom sensing and inhibiting biofilm formation in Pseudomonas aeruginosa and its structure prediction and analysis. PLoS One. 2019 Feb 19;14(2):e0212041. 6.

(55) Navien T. N, Thevendran R, Hamdani H. Y, Tang T-H, Citartan M. In Silico Molecular Docking in DNA Aptamer Development. Biochimie. 2021;180:54–67.

(56) Wang T, Chen C, Larcher L. M, Barrero R. A, Veedu R. N. Three Decades of Nucleic Acid Aptamer Technologies: Lessons Learned, Progress and Opportunities on Aptamer Development. Biotechnol Adv. 2019;37 (1):28–50.

(57) Sabri M. Z, Abdul Hamid A, Hitam S, Abdul Rahim M. Z. In-Silico Selection of Aptamer: A Review on the Revolutionary Approach to Understand the Aptamer Design and Interaction Through Computational Chemistry. Materials Today: Proceedings. 2019;19:1572–1581.

(58) Chen J, Zhou J, Peng Y, Xie Y, Xiao Y. Aptamers: A prospective tool for infectious diseases diagnosis. J Clin Lab Anal. 2022;36(11):e24725.

(59) Kanwar J. R, Roy K, Kanwar R. K. Chimeric Aptamers in Cancer Cell-Targeted Drug Delivery. Crit Rev Biochem Mol Biol. 2011;46 (6):459–477.

(60) Simmons SC, McKenzie EA, Harris LK, Aplin JD, Brenchley PE, Velasco-Garcia MN, Missailidis S. Development of novel single-stranded nucleic acid aptamers against the pro-angiogenic and metastatic enzyme heparanase (HPSE1). PLoS One. 2012;7(6):e37938.

(61) Kim, K. S, Lee H-S, Yang J-A, Jo M-H, Hahn S. K. The Fabrication, Characterization and Application of Aptamer-Functionalized Si-Nanowire FET Biosensors. Nanotechnology. 2009;20 (23):235501.

(62) Shigdar S, Ward A. C, De A, Yang C. J, Wei M, Duan W. Clinical Applications of Aptamers and Nucleic Acid Therapeutics in Haematological Malignancies. Br J Haematol. 2011;155 (1):3–13.

(63) Famulok M, Hartig JS, Mayer G. Functional aptamers and aptazymes in biotechnology, diagnostics, and therapy. Chem Rev. 2007;107(9):3715-43.

(64) Khan H, Missailidis S. Aptamers in oncology: A diagnostic perspective. Genes Ther. Mol. Biol. 2008;12:111–128

(65) Savory N, Abe K, Sode K, Ikebukuro K. Selection of DNA Aptamer against Prostate Specific Antigen Using a Genetic Algorithm and Application to Sensing. Biosensors and Bioelectronics. 2010;26 (4):1386–1391.

(66) Zhu D, Zhou X., Xing D. A New Kind of Aptamer-Based Immunomagnetic Electrochemiluminescence Assay for Quantitative Detection of Protein. Biosens Bioelectron. 2010;26 (1):285–288.

(67) Green L. S, Bell C, Janjic N. Aptamers as Reagents for High-Throughput Screening. Biotechniques. 2001;30 (5):1094–1096, 1098, 1100.

(68) Proske D, Blank M, Buhmann R, Resch A. Aptamers--basic research, drug development, and clinical applications. Appl Microbiol Biotechnol. 2005;69(4):367-74.

(69) Ravelet C, Grosset C, Peyrin E. Liquid Chromatography, Electrochromatography and Capillary Electrophoresis Applications of DNA and RNA Aptamers. J Chromatogr A. 2006;1117 (1):1–10.

(70) Gutsaeva D. R, Parkerson J. B, Yerigenahally S. D, Kurz J. C, Schaub R. G, Ikuta T, Head C. A. Inhibition of Cell Adhesion by Anti–P-Selectin Aptamer: A New Potential Therapeutic Agent for Sickle Cell Disease. Blood. 2011;117 (2):727–735.

(71) Faryammanesh, R.; Lange, T.; Magbanua, E.; Haas, S.; Meyer, C.; Wicklein, D.; Schumacher, U.; Hahn, U. SDA, a DNA Aptamer Inhibiting E- and P-Selectin Mediated Adhesion of Cancer and Leukemia Cells, the First and Pivotal Step in Transendothelial Migration during Metastasis Formation. PLoS One 2014;*9* (4): e93173..

(72) Cywiński P. J., Olejko L, Löhmannsröben H-G. A Time-Resolved Luminescent Competitive Assay to Detect L-Selectin Using Aptamers as Recognition Elements. Anal Chim Acta. 2015;887:209–215.

(73) Zhu Q, Liu G, Kai M. DNA Aptamers in the Diagnosis and Treatment of Human Diseases. Molecules. 2015;20 (12):20979–20997.

(74) Chang YM, Donovan MJ, Tan W. Using aptamers for cancer biomarker discovery. J Nucleic Acids. 2013;2013:817350.

(75) Marro M. L, Daniels D. A, McNamee A, Andrew D. P, Chapman T. D, Jiang M. S, Wu Z, Smith J. L, Patel K. K,Gearing K. L. Identification of Potent and Selective RNA Antagonists of the IFN-γ-Inducible CXCL10 Chemokine. Biochemistry. 2005;44 (23):8449–8460.

(76) Rusconi CP, Roberts JD, Pitoc GA, Nimjee SM, White RR, Quick G Jr, Scardino E, Fay WP, Sullenger BA. Antidote-mediated control of an anticoagulant aptamer in vivo. Nat Biotechnol. 2004;22(11):1423-8.

(77) Chandola C, Kalme S, Casteleijn M. G, Urtti A, Neerathilingam M. Application of Aptamers in Diagnostics, Drug-Delivery and Imaging. J Biosci. 2016;*41* (3):535–561.

(78) Zhang, H.; Zhang, C.; Li, Z.; Li, C.; Wei, X.; Zhang, B.; Liu, Y. A New Method of RNA Secondary Structure Prediction Based on Convolutional Neural Network and Dynamic Programming. Frontiers in Genetics. 2019;*10*.

(79) Kim M, Kim DM, Kim KS, Jung W, Kim DE. Applications of Cancer Cell-Specific Aptamers in Targeted Delivery of Anticancer Therapeutic Agents. Molecules. 2018;23(4):830.

(80) Pfeiffer F, Mayer G. Selection and Biosensor Application of Aptamers for Small Molecules. Front Chem. 2016;4:25.

(81) Tu D, Garza J. T, Coté G. L. A SERS Aptasensor for Sensitive and Selective Detection of Bis(2-Ethylhexyl)Phthalate. RSC Adv. 2019;9 (5):2618–2625.

(82) Wei Y, Zhou Y, We Y, Dong C, Wang L. A Fluorescent Aptasensor Based on Berberine for Ultrasensitive Detection of Bisphenol A in Tap Water. Anal. Methods. 2021;13 (15):1816–1822.

(83) González-González, R. B.; Flores-Contreras, E. A.; Parra-Saldívar, R.; Iqbal, H. M. N. Bio-Removal of Emerging Pollutants by Advanced Bioremediation Techniques. Environ Res. 2022;214 (Pt 2):113936.

(84) Guedes-Alonso R, Sosa-Ferrera Z, Santana-Rodríguez J. J. Determination of Steroid Hormones in Fish Tissues by Microwave-Assisted Extraction Coupled to Ultra-High Performance Liquid Chromatography Tandem Mass Spectrometry. Food Chemistry. 2017;237:1012–1020.

(85) Desbrow C, Routledge E. J, Brighty G. C, Sumpter J. P, Waldock M. Identification of Estrogenic Chemicals in STW Effluent. 1. Chemical Fractionation and in Vitro Biological Screening. Environ. Sci. Technol. 1998,;32 (11):1549–1558.

(86) Isobe, T, Shiraishi H, Yasuda M, Shinoda A, Suzuki H, Morita M. Determination of Estrogens and Their Conjugates in Water Using Solid-Phase Extraction Followed by Liquid Chromatography-Tandem Mass Spectrometry. J Chromatogra. 2003;984 (2):195–202.

(87) Zhang W, Yang F, Ou D, Lin G, Huang A, Liu N, Li P. Prediction, Docking Study and Molecular Simulation of 3D DNA Aptamers to Their Targets of Endocrine Disrupting Chemicals. Journal of Biomolecular Structure and Dynamics. 2019;37 (16):4274–4282.

(88) Wang, L.; Wang, H.; Tizaoui, C.; Yang, Y.; Ali, J.; Zhang, W. Endocrine Disrupting Chemicals in Water and Recent Advances on Their Detection Using Electrochemical Biosensors. Sensors and Diagnostics. 2022.

(89) Acconcia F, Pallottini V, Marino M. Molecular Mechanisms of Action of BPA. Dose Response. 2015;13 (4):1559325815610582.

(90) Niu X, Yang W, Wang G, Ren J, Guo H, Gao J. A. Novel Electrochemical Sensor of Bisphenol A Based on Stacked Graphene Nanofibers/Gold Nanoparticles Composite Modified Glassy Carbon Electrode. Electrochimica Acta. 2013;98:167–175.

(91) Kim Y. S, Jung H. S, Matsuura T, Lee H. Y, Kawai T, Gu M. B. Electrochemical Detection of 17β-Estradiol Using DNA Aptamer Immobilized Gold Electrode Chip. Biosensors and Bioelectronics. 2007;22 (11):2525–2531.

(92) Yin G. G, Kookana R. S, Ru Y. J. Occurrence and Fate of Hormone Steroids in the Environment. Environ Int. 2002;28 (6):545–551.

(93) Huy G. D, Jin N, Yin B. C, Ye B. C. A Novel Separation and Enrichment Method of 17β-Estradiol Using Aptamer-Anchored Microbeads. Bioprocess Biosyst Eng**.** 2011;34 (2):189–195.

(94) Delbès G, Levacher C, Habert R. Estrogen Effects on Fetal and Neonatal Testicular Development. Reproduction. 2006;132 (4):527–538.

(95) Adeel M, Song X, Wang Y, Francis D, Yang Y. Environmental Impact of Estrogens on Human, Animal and Plant Life: A Critical Review. Environ Int. 2017;99:107–119.

(96) Pessoa G. P, de Souza N. C, Vidal C. B, Alves J. A. C, Firmino P. I. M, Nascimento R. F, dos Santos A. B. Occurrence and Removal of Estrogens in Brazilian Wastewater Treatment Plants. Sci Total Environ**.** 2014;490:288–295.

(97) Jacobson J. L, Jacobson S. W. Intellectual Impairment in Children Exposed to Polychlorinated Biphenyls in Utero. N Engl J Med 1996, *335* (11), 783–789.

(98) Rocheleau C. M., Bertke S. J, Deddens J. A, Ruder A. M., Lawson C. C, Waters M. A, Hopf N. B, Riggs M. A, Whelan E. A. Maternal Exposure to Polychlorinated Biphenyls and the Secondary Sex Ratio: An Occupational Cohort Study. Environmental Health 2011;10 (1):20.

(99) Thomas H. Book Review of Quantum Chemistry, 2nd Edition. American Chemical Society. 2010

(100) Leach A. R. Molecular Modelling: Principles and Applications; Prentice Hall, Harlow, England. 2001;788

(101) Kohn W, Becke A. D, Parr R. G. Density Functional Theory of Electronic Structure. J. Phys. Chem. 1996;100 (31):12974–12980.

(102) Sabin J. R, Santry D. P., Weiss K. CNDO [Complete Neglect of Differential Overlap] Molecular Orbital Calculations. Invariance of Methods for Second Row Elements. J. Am. Chem. Soc. 1972;94 (19):6651–6652.

(103) Spanget-Larsen J. INDO Calculations with Inclusion of an Effective Solvent Field. Application to Benzosemiquinones. Theoret. Chim. Acta. 1978;47 (4):315–328.

(104) Hehre W. J. MINDO/3. Evaluation of Its Usefulness as a Structural Theory. *J.* Am. Chem. Soc. 1975;97 (18):5308–5310.

(105) Mantz Y. A, Musselman R. L. ZINDO Calculations of the Ground State and Electronic Transitions in the Tetracyanonickelate Ion, $Ni(CN)_4^{2-}$. Inorg. Chem. 2002;41 (22):5770–5777.

(106) Dewar M. J. S, Zoebisch E. G, Healy E. F, Stewart J. P. Development and use of quantum mechanical molecular models. 76. AM1: A New general purpose quantum mechanical molecular model. J.Am. Chem. Soc. 1985;107:3902-3909.

(107) Repasky M. P, Chandrasekhar J, Jorgensen W. L. PDDG/PM3 and PDDG/MNDO: Improved Semiempirical Methods. Journal of Computational Chemistry. 2002;23 (16):1601–1622.

(108) Mayer I. The Hartree-Fock Method. In Simple Theorems, Proofs, and Derivations in Quantum Chemistry; Mayer, I., Ed.; Mathematical and Computational Chemistry; Springer US: Boston, MA, 2003; pp 165–225.

(109) Chakraborty, A. Exploring Chemistry with Electronic Structure Methods. **1996**.

(110) Muzomwe M, Maes G, Kasende O. E. Theoretical DFT(B3LYP)/6-31+G(d) Study on the Prediction of the Preferred Interaction Site of 3-Methyl-4-Pyrimidone with Different Proton Donors. Natural Science. 2012;4 (5):286–297.

(111) Jeffrey R. R. Computational Methods for Large Systems: Electronic Structure Approaches for Biotechnology and Nanotechnology. Wiley & Sons Ltd, September,2011:688.

(112) Gaussian 16, Revision C.01, Frisch M. J, Trucks G. W, Schlegel H. B, Scuseria G. E, Robb M. A, Cheeseman J. R, Scalmani G, Barone V, Petersson G. A, Nakatsuji H, Li X, Caricato M, Marenich A.V, Bloino J, Janesko B. G, Gomperts R, Mennucci B, Hratchian H. P, Ortiz J. V, Izmaylov A. F, Sonnenberg J. L, Williams-Young D, Ding F, Lipparini F, Egidi F, Goings J, Peng B, Petrone A, Henderson T, Ranasinghe D, Zakrzewski V. G, Gao J, Rega N, Zheng G, Liang W, Hada M, Ehara M, Toyota K, Fukuda R, Hasegawa J, Ishida M, Nakajima T, Honda Y, Kitao O, Nakai H, Vreven T, Throssell K, Montgomery J. A. Jr, Peralta J. E, Ogliaro F, Bearpark M. J, Heyd J. J, Brothers E. N, Kudin K. N, Staroverov V. N, Keith T. A, Kobayashi R, Normand J, Raghavachari K, Rendell A. P, Burant J. C, Iyengar S. S, Tomasi J, Cossi M, Millam J. M, Klene M, Adamo C, Cammi R, Ochterski J. W, Martin R. L, Morokuma K, Farkas O, Foresman J. B, Fox D. J. Gaussian, Inc., Wallingford CT. 2016.

(113) Jo M, Ahn J.-Y, Lee J, Le S, Hong S. W, Yoo J.-W, Kang J, Dua P, Lee D, Hong S, Kim S. Development of Single-Stranded DNA Aptamers for Specific Bisphenol A Detection. Oligonucleotides. 2011;21 (2):85–91.

(114) Zuker M. Mfold Web Server for Nucleic Acid Folding and Hybridization Prediction. Nucleic Acids Res. 2003;31 (13):3406–3415.

(115) Gruber A. R, Lorenz R, Bernhart S. H, Neuböck R, Hofacker I. L. The Vienna RNA Websuite. Nucleic Acids Res. 2008;36 (Web Server issue):W70-74.

(116) Li J, Fu A, Zhang L. An Overview of Scoring Functions Used for Protein-Ligand Interactions in Molecular Docking. Interdiscip Sci. 2019;11(2):320-328.

(117) Quiroga R, Villarreal MA. Vinardo: A Scoring Function Based on Autodock Vina Improves Scoring, Docking, and Virtual Screening. PLoS One. 2016;11(5):e0155183.

(118) Sherman M, Contreras L. Computational Approaches in Design of Nucleic Acid-Based Therapeutics. Current Opinion in Biotechnology 2018;53:232–239.

(119) Phillips J. C, Hardy D. J, Maia J. D. C, Stone J. E, Ribeiro J. V, Bernardi R. C, Buch R, Fiorin G, Hénin J, Jiang W, McGreevy R, .Melo M. C. R, Radak B. K, Skeel R. D, Singharoy A, Wang Y, Roux B, Aksimentiev A, Luthey-Schulten Z, Kalé L. V, Schulten K, Chipot C, Tajkhorshid E. Scalable Molecular Dynamics on CPU and GPU Architectures with NAMD. J Chem Phys. 2020;153 (4):044130.

(120) Lindahl; Abraham; Hess; Spoel, van der. GROMACS 2020 Manual. 2020.

(121) Case D. A, Cheatham III T. E, Darden T, Gohlke H, Luo R, Merz Jr. K. M, Onufriev A, Simmerling C, Wang B, Woods R. J. The Amber Biomolecular Simulation Programs. Journal of Computational Chemistry. 2005;26 (16):1668–1688.

(122) Ivani I, Dans P. D, Noy A, Pére A, Faustino I, Hospital A, Walther J, Andrio P, Goñi R, Balaceanu A, Portella G, Battistini F, Gelpí J. L, González C, Vendruscolo M, Laughton C. A, Harris S. A, Case D. A. Orozco, M. PARMBSC1: A REFINED FORCE-FIELD FOR DNA SIMULATIONS. Nat Methods. 2016;13 (1):55–58.

(123) Zgarbová M, Šponer J, Otyepka M, Cheatham T. E, Galindo-Murillo R, Jurečka, P. Refinement of the Sugar-Phosphate Backbone Torsion Beta for AMBER Force Fields Improves the Description of Z- and B-DNA. J Chem Theory Comput**.** 2015; 11 (12):5723–5736.

(124) Vanommeslaeghe K, Hatcher E, Acharya C, Kundu S, Zhong S, Shim J, Darian E, Guvench O, Lopes P, Vorobyov I, MacKerell A. D. CHARMM General Force Field (CGenFF): A Force Field for Drug-like Molecules Compatible with the CHARMM All-Atom Additive Biological Force Fields. J Comput Chem. 2010;31 (4):671–690.

(125) Brooks BR, Brooks CL 3rd, Mackerell AD Jr, Nilsson L, Petrella RJ, Roux B, Won Y, Archontis G, Bartels C, Boresch S, Caflisch A, Caves L, Cui Q, Dinner AR, Feig M, Fischer S, Gao J, Hodoscek M, Im W, Kuczera K, Lazaridis T, Ma J, Ovchinnikov V, Paci E, Pastor RW, Post CB, Pu JZ, Schaefer M, Tidor B, Venable RM, Woodcock HL, Wu X, Yang W, York DM, Karplus M. CHARMM: the biomolecular simulation program. J Comput Chem. 2009;30(10):1545-614.

(126) Case D. A, Cheatham T. E, Darden T, Gohlke H, Luo R, Mer K. M, Onufrlev A, Sımmerlıng C, Wang B, Woods R. J. The Amber Biomolecular Simulation Programs. J Comput Chem. 2005;26 (16):1668–1688.

(127) Ivani I, Dans P. D, Noy A, Pérez A, Faustino I, Hospital A, Walther J, Andrio P, Goñi R, Balaceanu A, Portella G, Battistini F, Gelpí J. L, González C, Vendruscolo M, Laughton C. A, Harris S. A., Case D. A, Orozco M. PARMBSC1: A REFINED FORCE-FIELD FOR DNA SIMULATIONS. Nat. Methods. 2016;13 (1), 55–58.

(128) Zgarbová M, Šponer J, Otyepka M, Cheatham T. E, Galindo-Murillo R, Jurečka P. Refinement of the Sugar-Phosphate Backbone Torsion Beta for AMBER Force Fields Improves the Description of Z- and B-DNA. J. Chem. Theory Comput. 2015;11 (12):5723–5736.

(129) Vanommeslaeghe K, Hatcher E, Acharya C, Kundu S, Zhong S, Shim J, Darian E, Guvench O, Lopes P, Vorobyov I, MacKerell A. D. CHARMM General Force Field (CGenFF): A Force Field for Drug-like Molecules Compatible with the CHARMM All-Atom Additive Biological Force Fields. J. Comput. Chem. 2010;31 (4):671–690.

(130) Charmm: The biomolecular simulation program - Brooks - 2009 - Journal of Computational Chemistry - Wiley Online Library.

(131) Case D. A, Cheatham T. E, Darden T, Gohlke H, Luo R, Merz K. M, Onufrlev A, Simmerling C, Wang B, Woods R. J. The Amber Biomolecular Simulation Programs. J. Comput. Chem. 2005;26 (16):1668–1688.

(132) Grant B.J, Rodrigues A.P, ElSawy K.M, McCammon J.A, Caves L.S. Bio3d: an R package for the comparative analysis of protein structures. Bioinformatics. 2006;22(21):2695-6.

(133) Wang E, Sun H, Wang J, Wang Z, Liu H, Zhang JZH, Hou T. End-Point Binding Free Energy Calculation with MM/PBSA and MM/GBSA: Strategies and Applications in Drug Design. Chem Rev. 2019;119(16):9478-9508.

APPENDICE

APPENDIX 1 : Parameter file of the MD simulation for the internal MD generation step in Gromacs for the DNA-ligand complex

Equilibration

```
define                  = DNA-Ligand
integrator              = md-vv; leap-frog integrator
dt                      = 0.001; 1 fs
nsteps                  = 125000
nstxtcout               = 5000; save energies every 10.0 ps
nstvout                 = 5000
nstfout                 = 5000
nstcalcenergy           = 100
nstenergy               = 1000
nstlog                  = 1000
;
cutoff-scheme           = Verlet
nstlist                 = 20
rlist                   = 1.2
vdwtype                 = Cut-off
vdw-modifier            = Force-switch
rvdw_switch             = 1.0
rvdw                    = 1.2
coulombtype             = PME
rcoulomb                = 1.2
;
tcoupl                  = v-rescale
tc_grps                 = SOLU SOLV
tau_t                   = 1.0 1.0
ref_t                   = 310 310
;
constraints             = h-bonds
constraint_algorithm    = LINCS
;
nstcomm                 = 100
comm_mode               = linear
comm_grps               = SOLU SOLV
;
gen-vel                 = yes
gen-temp                = 310
gen-seed                = -1
```

MD simulation production

```
integrator              = md-vv
dt                      = 0.002
nsteps                  = 50000000
nstxtcout               = 50000
nstvout                 = 50000
nstfout                 = 50000
nstcalcenergy           = 100
nstenergy               = 1000
nstlog                  = 1000
;
cutoff-scheme           = Verlet
nstlist                 = 20
vdwtype                 = Cut-off
vdw-modifier            = Force-switch
rvdw_switch             = 1.0
rvdw                    = 1.2
rlist                   = 1.2
rcoulomb                = 1.2
coulombtype             = PME
;
tcoupl                  = v-rescale
tc_grps                 = SOLU SOLV
tau_t                   = 1.0 1.0
ref_t                   = 310 310
;
pcoupl                  = Parrinello-Rahman
pcoupltype              = isotropic
tau_p                   = 5.0
compressibility         = 4.5e-5
ref_p                   = 1.0
;
constraints             = h-bonds
constraint_algorithm    = LINCS
continuation            = yes
;
nstcomm                 = 100
comm_mode               = linear
comm_grps               = SOLU SOLV
;
```

APPENDIX 2 : Parameter file of the MD simulation for the internal MD generation step in NAMD for the DNA-ligand complex

```
#set inpname      md_01_inp
#set outname      md_01_out

#============================================================
# initial config
cwd             ./

#velocities
#temperature     310K

#during reading a restart
#firsttimestep  15000

#============================================================
#  input
parmfile              complex2_wat.prmtop
ambercoor             complex2_wat.inpcrd
amber           on
readexclusions          yes
#coordinates            2O3M_1.pdb
#paraTypeCharmm         on
#parameters             par_all27_na.prm
#============================================================
#from restart files
binCoordinates         md_equ_300_out.rst.coor
binVelocities          md_equ_300_out.rst.vel # uncomment only
if temp. if off
ExtendedSystem         md_equ_300_out.rst.xsc

#============================================================
# output params
outputname      md_01.pdb
##  or use $outname
binaryoutput    no
restartname     md_01.rst
##  or use $outname.restart
restartfreq     2000
restartsave     no
DCDfile         md_01.dcd
##  or use  $outname.dcd
DCDfreq         2000
outputPressure  2000

#============================================================
# dyanmics params
timestep               2.0
numsteps               50000000
nonbondedFreq          1

#============================================================
#SHAKE H
rigidBonds      all
```

```
rigidIterations 500

#=============================================================
# Force field params
exclude                 scaled1-4
1-4scaling              0.833333
cutoff                  14
switching               On
switchdist              12
pairlistdist            16
margin                  1.0

#=============================================================
# PME (for full-system periodic electrostatics)
PME                 yes
#PMEInterpOrder      6
PMEGridSizeX        100
PMEGridSizeY        100
PMEGridSizeZ        100
#these values are multiple of 4 and are taken from PBC vector

#=============================================================
## Temperature control Berendsen
#tCouple         on
#tCoupleTemp     310K
#tCoupleFile     HTpep_couple.pdb
#tCoupleCol      B

#=============================================================
## Constant Pressure Control (variable volume)
#useGroupPressure      yes
## needed for rigidBonds
#useFlexibleCell       no
#useConstantArea       no

#=============================================================
##langevinPiston       on
#langevinPistonTarget  1.01325
##  in bar -> 1 atm
#langevinPistonPeriod  100.
#langevinPistonDecay   50.
#langevinPistonTemp    310

#=============================================================
langevin                on      # do langevin dynamics
langevinTemp            310
langevinDamping         5       # damping coefficient (gamma) of
1-5/ps
langevinHydrogen        off
useFlexibleCell         no
langevinPiston          on
langevinPistonTarget    1.01325 #  in bar -> 1 atm
langevinPistonPeriod    100
langevinPistonDecay     50
langevinPistonTemp      310
```

```
#============================================================
# Periodic Boundary Conditions
#cellBasisVector1     -126.0         0.0          0.0
#cellBasisVector2      0.0     -138.0             0.0
#cellBasisVector3      0.0      0.0         -145.0
#cellOrigin           64.67230224609375 70.6960220336914
74.10343170166016

#take these values from vmd *.prmtop *.rst.coor by calling
#set t [atomselect top all]
#measure minmax $t
#measure center $t
#vecsub{min}{max}

#============================================================
wrapAll             on
wrapwater            on
wrapNearest          on

#============================================================
outputEnergies      500
# 100 steps = every 0.2 ps
outputTiming        500

#============================================================
#fixed atoms
fixedAtoms          off
#fixedAtoms          on
#fixedAtomsFile     min_all_out.coor
#fixedAtomsCol      O

#============================================================
twoAwayX yes
```

APPENDIX 3 : Parameter file for Binding Energy Calculation

```
Sample input file for PB calculation
&general
startframe=100,
endframe=1381,
keep_files=2,
temperature=310,
interval=10,
#strip_mask=":WAT,Na+",

# In gmx_MMPBSA v1.5.0 we have added a new PB radii set named
charmm_radii. This radii set should be used only
# with systems prepared with CHARMM force fields. Uncomment the
line below to use charmm_radii set
PBRadii=4,
/
&pb
# calculation
istrng=0.100,inp=1, fillratio=4.0, radiopt=0,
```

APPENDIX 4 : Results file for Binding Energy Calculation

Sim-RNA Complex-Charmm36

Delta (Complex - Receptor - Ligand):

Energy Component	Average	SD(Prop.)	SD	SEM(Prop.)	SEM
Î”BOND	-0.00	2.53	0.00	0.35	0.00
Î”ANGLE	-0.00	2.08	0.00	0.29	0.00
Î”DIHED	0.00	2.10	0.00	0.29	0.00
Î”UB	0.00	0.70	0.00	0.10	0.00
Î”IMP	0.00	0.00	0.00	0.00	0.00
Î”CMAP	0.00	0.00	0.00	0.00	0.00
Î”VDWAALS	-12.98	4.36	11.45	0.61	1.60
Î”EEL	-8.55	2.96	10.22	0.41	1.43
Î”1-4 VDW	-0.00	1.78	0.00	0.25	0.00
Î”1-4 EEL	-0.00	0.83	0.00	0.12	0.00
Î”EPB	14.50	4.44	12.17	0.62	1.70
Î”ENPOLAR	-1.49	0.37	1.15	0.05	0.16
Î”EDISPER	0.00	0.00	0.00	0.00	0.00
Î”GGAS	-21.53	5.31	19.69	0.74	2.76
Î”GSOLV	13.02	4.46	11.27	0.62	1.58
Î”TOTAL	-8.51	6.94	11.21	0.97	1.57

Sim-RNA Complex-Charmm36m

Delta (Complex - Receptor - Ligand):

Energy Component	Average	SD(Prop.)	SD	SEM(Prop.)	SEM
Î”BOND	0.00	2.34	0.00	0.24	0.00
Î”ANGLE	0.00	1.90	0.00	0.19	0.00
Î”DIHED	0.00	1.84	0.00	0.19	0.00
Î”UB	0.00	0.55	0.00	0.06	0.00
Î”IMP	0.00	0.00	0.00	0.00	0.00
Î”CMAP	0.00	0.00	0.00	0.00	0.00
Î”VDWAALS	-2.25	2.41	4.68	0.25	0.48
Î”EEL	-0.99	0.17	5.33	0.02	0.54
Î”1-4 VDW	-0.00	1.69	0.00	0.17	0.00
Î”1-4 EEL	-0.00	0.97	0.00	0.10	0.00
Î”EPB	3.52	0.34	5.86	0.03	0.60
Î”ENPOLAR	-0.41	0.10	0.70	0.01	0.07
Î”EDISPER	0.00	0.00	0.00	0.00	0.00
Î”GGAS	-3.23	2.47	8.68	0.25	0.89
Î”GSOLV	3.11	0.35	5.34	0.04	0.54
Î”TOTAL	-0.13	2.50	4.07	0.26	0.42

Sim-RNA Complex-BSC1

Delta (Complex - Receptor - Ligand):

Energy Component	Average	SD(Prop.)	SD	SEM(Prop.)	SEM
Î”BOND	0.00	1.88	0.00	0.12	0.00
Î”ANGLE	-0.00	2.30	0.00	0.14	0.00
Î”DIHED	-0.00	2.18	0.00	0.14	0.00
Î”VDWAALS	-0.58	0.88	2.77	0.05	0.17
Î”EEL	0.82	0.56	3.36	0.04	0.21
Î”1-4 VDW	-0.00	0.85	0.00	0.05	0.00
Î”1-4 EEL	0.00	0.83	0.00	0.05	0.00
Î”EPB	-0.59	0.30	3.86	0.02	0.24
Î”ENPOLAR	-0.07	0.06	0.31	0.00	0.02
Î”EDISPER	0.00	0.00	0.00	0.00	0.00
Î”GGAS	0.24	1.04	4.56	0.07	0.28
Î”GSOLV	-0.66	0.30	3.71	0.02	0.23
Î”TOTAL	-0.42	1.09	1.73	0.07	0.11

Sim-RNA Complex-OL15

Delta (Complex - Receptor - Ligand):

Energy Component	Average	SD(Prop.)	SD	SEM(Prop.)	SEM
Î”BOND	-0.00	2.16	0.00	0.07	0.00
Î”ANGLE	-0.00	2.68	0.00	0.09	0.00
Î”DIHED	-0.00	1.96	0.00	0.06	0.00
Î”VDWAALS	-0.03	1.17	0.25	0.04	0.01
Î”EEL	0.75	0.75	2.29	0.02	0.08
Î”1-4 VDW	0.00	0.87	0.00	0.03	0.00
Î”1-4 EEL	0.00	0.80	0.00	0.03	0.00
Î”EPB	-2.94	0.23	2.94	0.01	0.10
Î”ENPOLAR	-0.00	0.02	0.05	0.00	0.00
Î”EDISPER	0.00	0.00	0.00	0.00	0.00
Î”GGAS	0.72	1.39	2.37	0.05	0.08
Î”GSOLV	-2.95	0.23	2.93	0.01	0.10
Î”TOTAL	-2.23	1.41	1.70	0.05	0.06

Rosetta-Farfar Complex-Charmm36

Delta (Complex - Receptor - Ligand):

Energy Component	Average	SD(Prop.)	SD	SEM(Prop.)	SEM
Î”BOND	-0.00	2.09	0.00	0.19	0.00
Î”ANGLE	0.00	2.35	0.00	0.21	0.00
Î”DIHED	-0.00	1.77	0.00	0.16	0.00
Î”UB	-0.00	0.61	0.00	0.05	0.00
Î”IMP	0.00	0.00	0.00	0.00	0.00
Î”CMAP	0.00	0.00	0.00	0.00	0.00
Î”VDWAALS	-1.96	1.29	4.13	0.12	0.37
Î”EEL	-1.45	1.25	6.12	0.11	0.54
Î”1-4 VDW	-0.00	1.84	0.00	0.16	0.00
Î”1-4 EEL	-0.00	0.81	0.00	0.07	0.00
Î”EPB	4.62	0.93	6.33	0.08	0.56
Î”ENPOLAR	-0.36	0.01	0.60	0.00	0.05
Î”EDISPER	0.00	0.00	0.00	0.00	0.00
Î”GGAS	-3.41	1.90	8.50	0.17	0.76
Î”GSOLV	4.26	0.93	5.94	0.08	0.53
Î”TOTAL	0.85	2.11	3.38	0.19	0.30

Rosetta-Farfar Complex-Charmm36m

Delta (Complex - Receptor - Ligand):

Energy Component	Average	SD(Prop.)	SD	SEM(Prop.)	SEM
Î”BOND	-0.00	2.19	0.00	0.31	0.00
Î”ANGLE	-0.00	2.34	0.00	0.33	0.00
Î”DIHED	-0.00	1.41	0.00	0.20	0.00
Î”UB	0.00	0.56	0.00	0.08	0.00
Î”IMP	0.00	0.00	0.00	0.00	0.00
Î”CMAP	0.00	0.00	0.00	0.00	0.00
Î”VDWAALS	-10.96	4.92	10.71	0.69	1.50
Î”EEL	-5.83	4.44	9.26	0.62	1.30
Î”1-4 VDW	0.00	1.63	0.00	0.23	0.00
Î”1-4 EEL	0.00	0.96	0.00	0.13	0.00
Î”EPB	11.77	5.61	11.21	0.79	1.57
Î”ENPOLAR	-1.15	0.05	1.04	0.01	0.15
Î”EDISPER	0.00	0.00	0.00	0.00	0.00
Î”GGAS	-16.78	6.65	17.96	0.93	2.52
Î”GSOLV	10.61	5.61	10.37	0.79	1.45
Î”TOTAL	-6.17	8.70	8.49	1.22	1.19

Rosetta-Farfar Complex-BSC1

Delta (Complex - Receptor - Ligand):

Energy Component	Average	SD(Prop.)	SD	SEM(Prop.)	SEM
Î”BOND	-0.00	2.31	0.00	0.36	0.00
Î”ANGLE	-0.00	2.79	0.00	0.43	0.00
Î”DIHED	-0.00	1.48	0.00	0.23	0.00
Î”VDWAALS	-0.00	0.86	0.00	0.13	0.00
Î”EEL	0.77	0.31	1.89	0.05	0.29
Î”1-4 VDW	0.00	0.85	0.00	0.13	0.00
Î”1-4 EEL	0.00	0.56	0.00	0.09	0.00
Î”EPB	-1.63	0.17	1.90	0.03	0.29
Î”ENPOLAR	0.00	0.01	0.00	0.00	0.00
Î”EDISPER	0.00	0.00	0.00	0.00	0.00
Î”GGAS	0.76	0.91	1.89	0.14	0.29
Î”GSOLV	-1.63	0.17	1.90	0.03	0.29
Î”TOTAL	-0.86	0.93	0.95	0.14	0.15

Rosetta-Farfar Complex-OL15

Delta (Complex - Receptor - Ligand):

Energy Component	Average	SD(Prop.)	SD	SEM(Prop.)	SEM
Î”BOND	-0.00	1.59	0.00	0.19	0.00
Î”ANGLE	-0.00	2.49	0.00	0.30	0.00
Î”DIHED	0.00	1.23	0.00	0.15	0.00
Î”VDWAALS	-0.00	0.98	0.00	0.12	0.00
Î”EEL	1.06	0.88	1.79	0.10	0.21
Î”1-4 VDW	0.00	0.87	0.00	0.10	0.00
Î”1-4 EEL	-0.00	0.92	0.00	0.11	0.00
Î”EPB	-4.15	0.12	2.32	0.01	0.28
Î”ENPOLAR	-0.00	0.02	0.00	0.00	0.00
Î”EDISPER	0.00	0.00	0.00	0.00	0.00
Î”GGAS	1.06	1.32	1.79	0.16	0.21
Î”GSOLV	-4.15	0.12	2.32	0.01	0.28
Î”TOTAL	-3.09	1.32	1.39	0.16	0.16

Rna-Composer Complex-Charmm36

Delta (Complex - Receptor - Ligand):

Energy Component	Average	SD(Prop.)	SD	SEM(Prop.)	SEM
Î”BOND	-0.00	2018526.45	0.00	395865.61	0.00
Î”ANGLE	-0.00	88.15	0.00	17.29	0.00
Î”DIHED	0.00	2.84	0.00	0.56	0.00
Î”UB	-0.00	421866.23	0.00	82734.77	0.00
Î”IMP	0.00	0.00	0.00	0.00	0.00
Î”CMAP	0.00	0.00	0.00	0.00	0.00
Î”VDWAALS	-3.49	1.80	6.05	0.35	1.19
Î”EEL	-4.91	4.98	7.52	0.98	1.48
Î”1-4 VDW	-0.00	3.36	0.00	0.66	0.00
Î”1-4 EEL	0.00	5.22	0.00	1.02	0.00
Î”EPB	6.22	0.02	9.43	0.00	1.85
Î”ENPOLAR	-0.45	0.14	0.75	0.03	0.15
Î”EDISPER	0.00	0.00	0.00	0.00	0.00
Î”GGAS	-8.40	421866.23	13.13	82734.77	2.57
Î”GSOLV	5.77	0.14	8.70	0.03	1.71
Î”TOTAL	-2.63	421866.23	4.84	82734.77	0.95

Rna-Composer Complex-Charmm36m

Delta (Complex - Receptor - Ligand):

Energy Component	Average	SD(Prop.)	SD	SEM(Prop.)	SEM
Î”BOND	0.00	2.91	0.00	0.41	0.00
Î”ANGLE	0.00	2.18	0.00	0.31	0.00
Î”DIHED	0.00	2.01	0.00	0.28	0.00
Î”UB	-0.00	0.64	0.00	0.09	0.00
Î”IMP	0.00	0.00	0.00	0.00	0.00
Î”CMAP	0.00	0.00	0.00	0.00	0.00
Î”VDWAALS	-4.38	0.65	6.81	0.09	0.95
Î”EEL	-2.44	0.65	7.17	0.09	1.00
Î”1-4 VDW	0.00	1.91	0.00	0.27	0.00
Î”1-4 EEL	-0.00	0.96	0.00	0.13	0.00
Î”EPB	4.14	0.54	8.74	0.08	1.22
Î”ENPOLAR	-0.49	0.37	0.75	0.05	0.10
Î”EDISPER	0.00	0.00	0.00	0.00	0.00
Î”GGAS	-6.81	1.12	12.99	0.16	1.82
Î”GSOLV	3.65	0.65	8.13	0.09	1.14
Î”TOTAL	-3.16	1.30	5.52	0.18	0.77

Rna-Composer Complex-BSC1

Delta (Complex - Receptor - Ligand):

Energy Component	Average	SD(Prop.)	SD	SEM(Prop.)	SEM
Î”BOND	-0.00	1.93	0.00	0.17	0.00
Î”ANGLE	-0.00	2.34	0.00	0.20	0.00
Î”DIHED	0.00	1.89	0.00	0.17	0.00
Î”VDWAALS	-0.10	1.26	0.37	0.11	0.03
Î”EEL	-0.66	0.18	4.89	0.02	0.43
Î”1-4 VDW	0.00	0.67	0.00	0.06	0.00
Î”1-4 EEL	0.00	0.75	0.00	0.07	0.00
Î”EPB	2.21	1.03	5.56	0.09	0.49
Î”ENPOLAR	-0.02	0.01	0.11	0.00	0.01
Î”EDISPER	0.00	0.00	0.00	0.00	0.00
Î”GGAS	-0.76	1.27	5.02	0.11	0.44
Î”GSOLV	2.19	1.03	5.52	0.09	0.48
Î”TOTAL	1.43	1.64	3.67	0.14	0.32

Rna-Composer Complex-OL15

Delta (Complex - Receptor - Ligand):

Energy Component	Average	SD(Prop.)	SD	SEM(Prop.)	SEM
Î”BOND	0.00	2.03	0.00	0.28	0.00
Î”ANGLE	0.00	2.10	0.00	0.29	0.00
Î”DIHED	-0.00	1.91	0.00	0.27	0.00
Î”VDWAALS	-12.26	0.79	4.51	0.11	0.63
Î”EEL	-15.59	3.68	11.97	0.52	1.68
Î”1-4 VDW	0.00	0.85	0.00	0.12	0.00
Î”1-4 EEL	-0.00	0.84	0.00	0.12	0.00
Î”EPB	20.42	3.18	11.28	0.45	1.58
Î”ENPOLAR	-1.66	0.26	0.46	0.04	0.06
Î”EDISPER	0.00	0.00	0.00	0.00	0.00
Î”GGAS	-27.85	3.76	14.03	0.53	1.96
Î”GSOLV	18.76	3.19	10.96	0.45	1.53
Î”TOTAL	-9.10	4.93	4.62	0.69	0.65

Vfold3D Complex-Charmm36

Delta (Complex - Receptor - Ligand):

Energy Component	Average	SD(Prop.)	SD	SEM(Prop.)	SEM
Î”BOND	-0.00	1.66	0.00	0.17	0.00
Î”ANGLE	0.00	1.74	0.00	0.17	0.00
Î”DIHED	0.00	2.02	0.00	0.20	0.00
Î”UB	0.00	0.53	0.00	0.05	0.00
Î”IMP	0.00	0.00	0.00	0.00	0.00
Î”CMAP	0.00	0.00	0.00	0.00	0.00
Î”VDWAALS	-5.41	4.32	8.86	0.43	0.88
Î”EEL	-3.35	4.51	7.25	0.45	0.72
Î”1-4 VDW	-0.00	1.71	0.00	0.17	0.00
Î”1-4 EEL	0.00	0.91	0.00	0.09	0.00
Î”EPB	6.97	8.58	11.52	0.85	1.15
Î”ENPOLAR	-0.61	0.71	0.97	0.07	0.10
Î”EDISPER	0.00	0.00	0.00	0.00	0.00
Î”GGAS	-8.77	6.27	14.59	0.62	1.45
Î”GSOLV	6.35	8.61	10.67	0.86	1.06
Î”TOTAL	-2.41	10.65	5.93	1.06	0.59

Vfold3D Complex-Charmm36m

Delta (Complex - Receptor - Ligand):

Energy Component	Average	SD(Prop.)	SD	SEM(Prop.)	SEM
Î”BOND	-0.00	2.99	0.00	0.42	0.00
Î”ANGLE	-0.00	2.08	0.00	0.29	0.00
Î”DIHED	0.00	1.93	0.00	0.27	0.00
Î”UB	0.00	0.79	0.00	0.11	0.00
Î”IMP	0.00	0.00	0.00	0.00	0.00
Î”CMAP	0.00	0.00	0.00	0.00	0.00
Î”VDWAALS	-30.02	0.50	3.69	0.07	0.52
Î”EEL	-16.91	0.44	7.04	0.06	0.99
Î”1-4 VDW	0.00	2.08	0.00	0.29	0.00
Î”1-4 EEL	-0.00	1.05	0.00	0.15	0.00
Î”EPB	30.97	0.61	7.23	0.08	1.01
Î”ENPOLAR	-2.73	0.03	0.20	0.00	0.03
Î”EDISPER	0.00	0.00	0.00	0.00	0.00
Î”GGAS	-46.92	1.03	8.15	0.14	1.14
Î”GSOLV	28.24	0.61	7.14	0.08	1.00
Î”TOTAL	-18.68	1.19	4.63	0.17	0.65

Vfold3D Complex-BSC1

Delta (Complex - Receptor - Ligand):

Energy Component	Average	SD(Prop.)	SD	SEM(Prop.)	SEM
Î”BOND	-0.00	1.57	0.00	0.21	0.00
Î”ANGLE	-0.00	2.73	0.00	0.36	0.00
Î”DIHED	0.00	1.90	0.00	0.25	0.00
Î”VDWAALS	-20.29	0.87	4.50	0.12	0.60
Î”EEL	-21.34	0.33	12.48	0.04	1.67
Î”1-4 VDW	-0.00	0.73	0.00	0.10	0.00
Î”1-4 EEL	0.00	0.71	0.00	0.09	0.00
Î”EPB	32.56	0.04	10.70	0.01	1.43
Î”ENPOLAR	-2.35	0.04	0.32	0.01	0.04
Î”EDISPER	0.00	0.00	0.00	0.00	0.00
Î”GGAS	-41.63	0.93	13.32	0.12	1.78
Î”GSOLV	30.21	0.06	10.51	0.01	1.40
Î”TOTAL	-11.42	0.93	4.93	0.12	0.66

Vfold3D Complex-OL15

Delta (Complex - Receptor - Ligand):

Energy Component	Average	SD(Prop.)	SD	SEM(Prop.)	SEM
Î”BOND	0.00	2.08	0.00	0.29	0.00
Î”ANGLE	0.00	2.41	0.00	0.34	0.00
Î”DIHED	-0.00	2.16	0.00	0.30	0.00
Î”VDWAALS	-31.06	0.74	2.31	0.10	0.32
Î”EEL	-20.00	0.01	4.95	0.00	0.69
Î”1-4 VDW	-0.00	0.79	0.00	0.11	0.00
Î”1-4 EEL	0.00	0.74	0.00	0.10	0.00
Î”EPB	51.87	2.45	7.89	0.34	1.11
Î”ENPOLAR	-3.08	0.02	0.06	0.00	0.01
Î”EDISPER	0.00	0.00	0.00	0.00	0.00
Î”GGAS	-51.06	0.74	4.36	0.10	0.61
Î”GSOLV	48.78	2.45	7.88	0.34	1.10
Î”TOTAL	-2.28	2.56	7.51	0.36	1.05

3dRNA Complex Charmm36

Delta (Complex - Receptor - Ligand):

Energy Component	Average	SD(Prop.)	SD	SEM(Prop.)	SEM
Î”BOND	-0.00	5546271.16	0.00	1087713.26	0.00
Î”ANGLE	-0.00	229.05	0.00	44.92	0.00
Î”DIHED	-0.00	13.64	0.00	2.68	0.00
Î”UB	-0.00	749104.08	0.00	146911.40	0.00
Î”IMP	0.00	0.00	0.00	0.00	0.00
Î”CMAP	0.00	0.00	0.00	0.00	0.00
Î”VDWAALS	-0.43	1.54	2.03	0.30	0.40
Î”EEL	-1.76	16.74	21.89	3.28	4.29
Î”1-4 VDW	-0.00	3.97	0.00	0.78	0.00
Î”1-4 EEL	0.00	7.71	0.00	1.51	0.00
Î”EPB	1.68	22.02	21.63	4.32	4.24
Î”ENPOLAR	-0.06	0.35	0.28	0.07	0.05
Î”EDISPER	0.00	0.00	0.00	0.00	0.00
Î”GGAS	-2.19	749104.08	22.30	146911.40	4.37
Î”GSOLV	1.62	22.02	21.58	4.32	4.23
Î”TOTAL	-0.57	749104.08	1.47	146911.40	0.29

3dRNA Complex Charmm36m

Delta (Complex - Receptor - Ligand):

Energy Component	Average	SD(Prop.)	SD	SEM(Prop.)	SEM
Î”BOND	0.00	2.58	0.00	0.36	0.00
Î”ANGLE	0.00	1.72	0.00	0.24	0.00
Î”DIHED	0.00	1.73	0.00	0.24	0.00
Î”UB	0.00	0.78	0.00	0.11	0.00
Î”IMP	0.00	0.00	0.00	0.00	0.00
Î”CMAP	0.00	0.00	0.00	0.00	0.00
Î”VDWAALS	-36.00	0.91	3.00	0.13	0.42
Î”EEL	-15.16	0.06	5.32	0.01	0.75
Î”1-4 VDW	0.00	1.97	0.00	0.28	0.00
Î”1-4 EEL	0.00	0.84	0.00	0.12	0.00
Î”EPB	28.60	0.44	5.21	0.06	0.73
Î”ENPOLAR	-2.88	0.01	0.10	0.00	0.01
Î”EDISPER	0.00	0.00	0.00	0.00	0.00
Î”GGAS	-51.15	1.20	5.04	0.17	0.71
Î”GSOLV	25.73	0.44	5.20	0.06	0.73
Î”TOTAL	-25.43	1.28	3.45	0.18	0.48

3dRNA Complex BSC1

Delta (Complex - Receptor - Ligand):

Energy Component	Average	SD(Prop.)	SD	SEM(Prop.)	SEM
Î”BOND	-0.00	2.32	0.00	0.26	0.00
Î”ANGLE	0.00	2.27	0.00	0.25	0.00
Î”DIHED	0.00	1.96	0.00	0.22	0.00
Î”VDWAALS	-1.51	0.92	4.04	0.10	0.45
Î”EEL	-2.00	0.48	6.04	0.05	0.67
Î”1-4 VDW	0.00	0.73	0.00	0.08	0.00
Î”1-4 EEL	0.00	0.77	0.00	0.09	0.00
Î”EPB	3.16	0.21	7.66	0.02	0.85
Î”ENPOLAR	-0.18	0.18	0.47	0.02	0.05
Î”EDISPER	0.00	0.00	0.00	0.00	0.00
Î”GGAS	-3.51	1.04	9.13	0.12	1.01
Î”GSOLV	2.98	0.28	7.27	0.03	0.81
Î”TOTAL	-0.53	1.08	2.40	0.12	0.27

3dRNA Complex OL15

Delta (Complex - Receptor - Ligand):

Energy Component	Average	SD(Prop.)	SD	SEM(Prop.)	SEM
Î”BOND	0.00	1.78	0.00	0.29	0.00
Î”ANGLE	-0.00	2.06	0.00	0.34	0.00
Î”DIHED	0.00	1.83	0.00	0.30	0.00
Î”VDWAALS	-26.21	0.57	2.95	0.09	0.48
Î”EEL	-23.06	0.74	12.08	0.12	1.99
Î”1-4 VDW	0.00	0.85	0.00	0.14	0.00
Î”1-4 EEL	0.00	0.68	0.00	0.11	0.00
Î”EPB	38.83	0.28	7.51	0.05	1.24
Î”ENPOLAR	-2.81	0.01	0.09	0.00	0.01
Î”EDISPER	0.00	0.00	0.00	0.00	0.00
Î”GGAS	-49.27	0.93	11.17	0.15	1.84
Î”GSOLV	36.02	0.28	7.48	0.05	1.23
Î”TOTAL	-13.25	0.97	5.55	0.16	0.91

3D-DART Complex Charmm36

Delta (Complex - Receptor - Ligand):

Energy Component	Average	SD(Prop.)	SD	SEM(Prop.)	SEM
Î”BOND	0.00	3.27	0.00	0.46	0.00
Î”ANGLE	0.00	2.19	0.00	0.31	0.00
Î”DIHED	-0.00	2.34	0.00	0.33	0.00
Î”UB	-0.00	0.53	0.00	0.07	0.00
Î”IMP	0.00	0.00	0.00	0.00	0.00
Î”CMAP	0.00	0.00	0.00	0.00	0.00
Î”VDWAALS	-7.12	0.94	7.18	0.13	1.01
Î”EEL	-4.44	0.26	6.76	0.04	0.95
Î”1-4 VDW	-0.00	1.73	0.00	0.24	0.00
Î”1-4 EEL	0.00	0.65	0.00	0.09	0.00
Î”EPB	8.47	0.72	8.98	0.10	1.26
Î”ENPOLAR	-0.91	0.42	0.89	0.06	0.12
Î”EDISPER	0.00	0.00	0.00	0.00	0.00
Î”GGAS	-11.57	1.11	11.53	0.16	1.61
Î”GSOLV	7.55	0.83	8.30	0.12	1.16
Î”TOTAL	-4.01	1.39	4.32	0.19	0.60

3D-DART Complex Charmm36m

Delta (Complex - Receptor - Ligand):

Energy Component	Average	SD(Prop.)	SD	SEM(Prop.)	SEM
Î”BOND	-0.00	2473066.12	0.00	346298.52	0.00
Î”ANGLE	-0.00	235.85	0.00	33.03	0.00
Î”DIHED	0.00	7.67	0.00	1.07	0.00
Î”UB	-0.00	261754.82	0.00	36653.01	0.00
Î”IMP	0.00	0.00	0.00	0.00	0.00
Î”CMAP	0.00	0.00	0.00	0.00	0.00
Î”VDWAALS	-0.19	1.25	0.65	0.17	0.09
Î”EEL	-2.52	2.95	8.02	0.41	1.12
Î”1-4 VDW	0.00	3.58	0.00	0.50	0.00
Î”1-4 EEL	0.00	3.88	0.00	0.54	0.00
Î”EPB	2.75	7.83	8.06	1.10	1.13
Î”ENPOLAR	-0.04	0.28	0.15	0.04	0.02
Î”EDISPER	0.00	0.00	0.00	0.00	0.00
Î”GGAS	-2.71	261754.82	8.09	36653.01	1.13
Î”GSOLV	2.71	7.84	8.04	1.10	1.13
Î”TOTAL	0.00	261754.82	0.64	36653.01	0.09

3D-DART Complex BSC1

Delta (Complex - Receptor - Ligand):

Energy Component	Average	SD(Prop.)	SD	SEM(Prop.)	SEM
Î”BOND	0.00	1.78	0.00	0.29	0.00
Î”ANGLE	-0.00	2.06	0.00	0.34	0.00
Î”DIHED	0.00	1.83	0.00	0.30	0.00
Î”VDWAALS	-26.21	0.57	2.95	0.09	0.48
Î”EEL	-23.06	0.74	12.08	0.12	1.99
Î”1-4 VDW	0.00	0.85	0.00	0.14	0.00
Î”1-4 EEL	0.00	0.68	0.00	0.11	0.00
Î”EPB	38.83	0.28	7.51	0.05	1.24
Î”ENPOLAR	-2.81	0.01	0.09	0.00	0.01
Î”EDISPER	0.00	0.00	0.00	0.00	0.00
Î”GGAS	-49.27	0.93	11.17	0.15	1.84
Î”GSOLV	36.02	0.28	7.48	0.05	1.23
Î”TOTAL	-13.25	0.97	5.55	0.16	0.91

3D-DART Complex OL15

Delta (Complex - Receptor - Ligand):

Energy Component	Average	SD(Prop.)	SD	SEM(Prop.)	SEM
Î”BOND	0.00	1.78	0.00	0.29	0.00
Î”ANGLE	-0.00	2.06	0.00	0.34	0.00
Î”DIHED	0.00	1.83	0.00	0.30	0.00
Î”VDWAALS	-26.21	0.57	2.95	0.09	0.48
Î”EEL	-23.06	0.74	12.08	0.12	1.99
Î”1-4 VDW	0.00	0.85	0.00	0.14	0.00
Î”1-4 EEL	0.00	0.68	0.00	0.11	0.00
Î”EPB	38.83	0.28	7.51	0.05	1.24
Î”ENPOLAR	-2.81	0.01	0.09	0.00	0.01
Î”EDISPER	0.00	0.00	0.00	0.00	0.00
Î”GGAS	-49.27	0.93	11.17	0.15	1.84
Î”GSOLV	36.02	0.28	7.48	0.05	1.23
Î”TOTAL	-13.25	0.97	5.55	0.16	0.91

İfoldRNA Complex Charmm36

Delta (Complex - Receptor - Ligand):

Energy Component	Average	SD(Prop.)	SD	SEM(Prop.)	SEM
Î”BOND	0.00	2.58	0.00	0.08	0.00
Î”ANGLE	0.00	2.36	0.00	0.07	0.00
Î”DIHED	0.00	2.02	0.00	0.06	0.00
Î”UB	-0.00	0.64	0.00	0.02	0.00
Î”IMP	0.00	0.00	0.00	0.00	0.00
Î”CMAP	0.00	0.00	0.00	0.00	0.00
Î”VDWAALS	-10.26	0.43	10.59	0.01	0.33
Î”EEL	-6.19	0.58	9.16	0.02	0.29
Î”1-4 VDW	-0.00	1.93	0.00	0.06	0.00
Î”1-4 EEL	-0.00	0.90	0.00	0.03	0.00
Î”EPB	11.92	0.16	10.76	0.00	0.34
Î”ENPOLAR	-1.27	0.27	1.10	0.01	0.03
Î”EDISPER	0.00	0.00	0.00	0.00	0.00
Î”GGAS	-16.45	0.96	17.48	0.03	0.55
Î”GSOLV	10.64	0.31	9.89	0.01	0.31
Î”TOTAL	-5.81	1.01	9.36	0.03	0.30

İfoldRNA Complex Charmm36m

Delta (Complex - Receptor - Ligand):

Energy Component	Average	SD(Prop.)	SD	SEM(Prop.)	SEM
Î”BOND	0.00	2.65	0.00	0.28	0.00
Î”ANGLE	-0.00	2.22	0.00	0.23	0.00
Î”DIHED	0.00	2.16	0.00	0.23	0.00
Î”UB	0.00	0.67	0.00	0.07	0.00
Î”IMP	0.00	0.00	0.00	0.00	0.00
Î”CMAP	0.00	0.00	0.00	0.00	0.00
Î”VDWAALS	-9.49	3.09	10.64	0.32	1.12
Î”EEL	-7.15	0.75	9.76	0.08	1.02
Î”1-4 VDW	0.00	1.89	0.00	0.20	0.00
Î”1-4 EEL	-0.00	0.81	0.00	0.09	0.00
Î”EPB	12.07	1.49	11.72	0.16	1.23
Î”ENPOLAR	-1.17	0.07	1.11	0.01	0.12
Î”EDISPER	0.00	0.00	0.00	0.00	0.00
Î”GGAS	-16.65	3.25	18.56	0.34	1.95
Î”GSOLV	10.90	1.49	10.80	0.16	1.13
Î”TOTAL	-5.74	3.58	9.80	0.38	1.03

İfoldRNA Complex BSC1

Delta (Complex - Receptor - Ligand):

Energy Component	Average	SD(Prop.)	SD	SEM(Prop.)	SEM
Î”BOND	0.00	1.78	0.00	0.35	0.00
Î”ANGLE	-0.00	2.89	0.00	0.57	0.00
Î”DIHED	0.00	2.30	0.00	0.45	0.00
Î”VDWAALS	-25.35	0.48	3.64	0.10	0.71
Î”EEL	-11.51	1.63	5.83	0.32	1.14
Î”1-4 VDW	-0.00	0.75	0.00	0.15	0.00
Î”1-4 EEL	0.00	0.89	0.00	0.17	0.00
Î”EPB	25.24	1.96	4.89	0.38	0.96
Î”ENPOLAR	-2.50	0.01	0.13	0.00	0.02
Î”EDISPER	0.00	0.00	0.00	0.00	0.00
Î”GGAS	-36.86	1.71	6.78	0.33	1.33
Î”GSOLV	22.74	1.96	4.85	0.38	0.95
Î”TOTAL	-14.12	2.60	3.80	0.51	0.74

İfoldRNA Complex OL15

Delta (Complex - Receptor - Ligand):

Energy Component	Average	SD(Prop.)	SD	SEM(Prop.)	SEM
Î”BOND	0.00	1.47	0.00	0.29	0.00
Î”ANGLE	0.00	2.17	0.00	0.42	0.00
Î”DIHED	-0.00	1.90	0.00	0.37	0.00
Î”VDWAALS	-33.33	1.08	1.53	0.21	0.30
Î”EEL	-10.78	0.14	6.11	0.03	1.20
Î”1-4 VDW	0.00	1.02	0.00	0.20	0.00
Î”1-4 EEL	0.00	0.67	0.00	0.13	0.00
Î”EPB	23.99	0.47	5.93	0.09	1.16
Î”ENPOLAR	-2.70	0.01	0.06	0.00	0.01
Î”EDISPER	0.00	0.00	0.00	0.00	0.00
Î”GGAS	-44.11	1.09	6.06	0.21	1.19
Î”GSOLV	21.29	0.47	5.92	0.09	1.16
Î”TOTAL	-22.82	1.19	2.13	0.23	0.42